Energie & Umwelt
Energy & Environment
246

Nanostructured Si-alloys for silicon solar cells

Kaining Ding

Member of the Helmholtz Association

Energie & Umwelt / Energy & Environment
Band / Volume 246
ISBN 978-3-95806-024-1

JÜLICH
FORSCHUNGSZENTRUM

Nanostructured Si-alloys for silicon solar cells

Kaining Ding

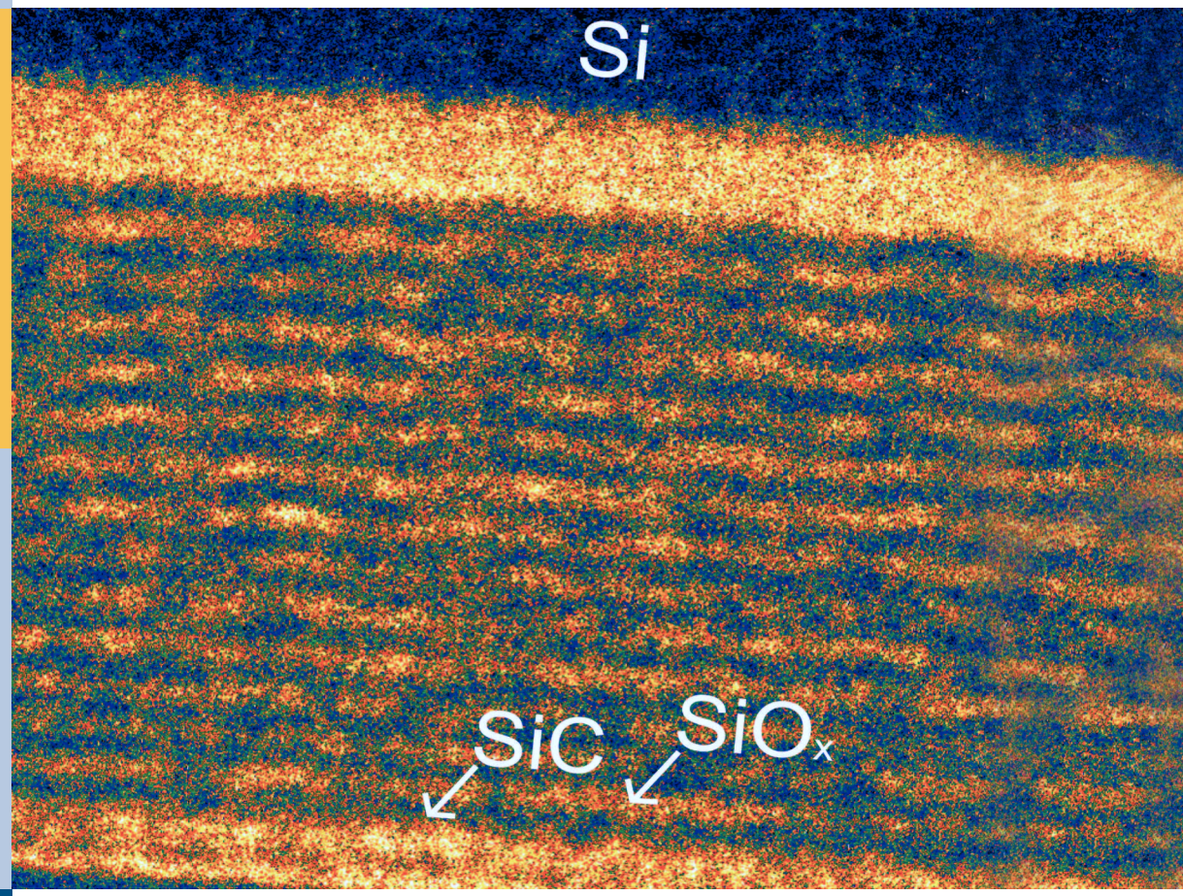

Energie & Umwelt / Energy & Environment
Band / Volume 246
ISBN 978-3-95806-024-1

JÜLICH
FORSCHUNGSZENTRUM

Schriften des Forschungszentrums Jülich
Reihe Energie & Umwelt / Energy & Environment Band / Volume 246

Forschungszentrum Jülich GmbH
Institute of Energy and Climate Research
IEK-5 Photovoltaics

Nanostructured Si-alloys for silicon solar cells

Kaining Ding

Schriften des Forschungszentrums Jülich
Reihe Energie & Umwelt / Energy & Environment Band / Volume 246

ISSN 1866-1793 ISBN 978-3-95806-024-1

Bibliographic information published by the Deutsche Nationalbibliothek.
The Deutsche Nationalbibliothek lists this publication in the Deutsche
Nationalbibliografie; detailed bibliographic data are available in the
Internet at http://dnb.d-nb.de.

Publisher and Distributor: Forschungszentrum Jülich GmbH
Zentralbibliothek
52425 Jülich
Tel: +49 2461 61-5368
Fax: +49 2461 61-6103
Email: zb-publikation@fz-juelich.de
www.fz-juelich.de/zb

Cover Design: Grafische Medien, Forschungszentrum Jülich GmbH

Printer: Grafische Medien, Forschungszentrum Jülich GmbH

Schriften des Forschungszentrums Jülich
Reihe Energie & Umwelt / Energy & Environment, Band / Volume 246

D 82 (Diss. RWTH Aachen University, 2014)

ISSN 1866-1793
ISBN 978-3-95806-024-1

The complete volume is freely available on the Internet on the Jülicher Open Access Server (JuSER)
at www.fz-juelich.de/zb/openaccess.

Contents

Abstract

In order to initiate further progress in silicon (Si) photovoltaics, a next-generation of Si solar cell concepts targeting both high performance and low-cost production needs to emerge. The objective of this thesis is to fabricate and characterize Si nanostructures embedded in a Si alloy matrix and implement these novel materials into Si based photovoltaic devices. In particular, silicon quantum dots (Si-QDs) in a silicon carbide (SiC)/Si-rich silicon oxide (SiO_x) hetero-superlattice (HSL) structure as top cell absorber in all-Si tandem solar cells and nanocomposite microcrystalline silicon oxide (µc-SiO_x:H) as contact layers in silicon heterojunction (SHJ) solar cells have been investigated. The main focus of the Si-QD absorber topic lies on the fundamental understanding of the material properties, whereas for the SHJ solar cell topic, developments on device level are the key aspect.

Due to the competing nature of charge carrier confinement requiring high band offset and charge carrier transport demanding low band offset between Si-QDs and the embedding material, the choice of different materials for matrix and barrier is indicated. The novel Si-QD absorber approach based on HSL with near-stoichiometric SiC (low band offset) as vertical barrier layer and Si-rich SiO_x (high band offset) as lateral matrix layer is motivated by pointing out the technical and theoretical difficulties of Si-QD formation in SiC matrix. After the successful development of laterally uniform, low rate and fully compatible plasma-enhanced chemical vapor depositions of high quality SiC and SiO_x single layers, the processes were transfered into an automatic deposition sequence, which allows for the fabrication of SiC/SiO_x HSL structures with excellent control over the sublayer composition and thickness. Even though the SiO_x was found to fulfill the requirements for a matrix material upon high-temperature annealing (Si precipitation and crystallization, well passivated Si-QDs exhibiting clear signature of quantum confinement, remaining

amorphous SiO_2 phase after annealing), the SiC revealed several drawbacks that limit the usability of the SiC/SiO_x HSL as a Si-QD absorber: (i) The Si-QDs extended into adjacent SiC layers especially with smaller SiO_x sublayer thickness or higher silicon excess, which suggests that SiC is an insufficient Si diffusion barrier. (ii) The hydrogen release from SiC sublayers gave rise to the decrease of the optical band gap, the increase of the defect density and the increase of the sub-band gap absorption in HSL. (iii) The defects in the carbide layers seem to open non-radiative recombination paths for carriers generated in Si-QDs. (iv) The annealing-induced doping character of SiC is expected to increase recombination in these layers during carrier transport. The systematic analysis of HSL and single layers of SiC and SiO_x annealed at various temperatures and passivated by various techniques using a number of characterization methods yielded a consistent picture of the fundamental differences between SiC and SiO_x. The hydrogen effusion mechanisms during annealing and the hydrogen reincorporation mechanisms during passivation in HSL are well understood. The stronger increase of spin density upon annealing in SiC as compared to SiO_x is ascribed to the effusion of a higher amount of hydrogen and the less efficient atomic diffusion. The much lower optical band gap and the significantly higher sub-band gap absorption of SiC in the annealed state as compared to SiO_x can be traced back to the lower flexibility of its relatively dense 4-fold coordinated atomic structure. The less efficient stress relaxation in SiC increases the probability of creating strained bonds that additionally contributes to the sub-band gap absorption.

Doped μc-SiO_x:H, consisting of a phase mixture of Si crystallites and a-SiO_x:H tissue, is an attractive contact layer material due to its high conductivity upon doping and at the same time high optical band gap and favorable refractive index. After finding out that the passivation quality of μc-SiO_x:H is insufficient, an intrinsic amorphous silicon oxide (a-SiO_x:H) buffer layer was inserted between the wafer and the doped layers yielding the first SHJ solar cells involving all buffer layers made from a-SiO_x:H and all contact layers made from μc-SiO_x:H materials. The advantages of a-SiO_x:H, e.g., high optical band gap and high thermal stability were independently confirmed by analyzing the optical properties of a-SiO_x:H layers and by showing good surface passivation on material and device level upon annealing, respectively. Implied open circuit voltages up to 742 mV achieved using a-SiO_x:H

passivation layers demonstrate a good reachability of high quality a-SiO_x:H passivation within a low O content range. In addition, preconditioning by a-SiO_x:H cover layer depositions after any change in the system was found to be crucial for the reproducibility of the passivation quality as well as the controlling of the buffer layer thickness. In fact, SHJ solar cells with front and rear a-SiO_x layer thicknesses varying within a nanometer range showed largely deviating efficiency values. Structural, optical, electrical and passivation properties of the n- and p-type µc-SiO_x:H layers deposited under various deposition conditions were consistently correlated to the cell results with the support of device simulations. The best SHJ solar cell using optimized a-SiO_x:H and µc-SiO_x:H layers on flat p-type wafer yielded an active area efficiency $\eta_{\mathrm{act}} = 19.0\%$ with open circuit voltage $V_{\mathrm{oc}} = 667$ mV, short curcuit current density $J_{\mathrm{sc}} = 35.8$ mA/cm^2 and fill factor $FF = 79.6$ %, which is up to now the highest efficiency shown for SHJ solar cells with µc-SiO_x:H contact layers. In addition, the present work was able to provide several hints to explain the buffer layer thickness dependence of the surface passivation by a model, which assumes electrons and holes, generated in the crystalline silicon absorber, to be able to walk through the buffer layer and recombine at the next defect-rich interface.

Zusammenfassung

Um die Forschung auf dem Gebiet der Silizium (Si) Photovoltaik weiter voranzutreiben, ist eine neue Generation von Si Solarzellen-Konzepten vonnöten, welche hohe Effizienz und niedrige Produktionskosten vereinen können. Gegenstand dieser Doktorarbeit ist die Herstellung und Charakterisierung von Si-Nanostrukturen eingebettet in einer Si-Legierungsmatrix, sowie deren Anwendungen in Si-basierten Solarzellen. Im Speziellen wurden Si-Quantenpunkte (Si-QDs) in kombinierter Matrix aus Siliziumkarbid (SiC) und Si-reichem Siliziumoxid (SiO_x) als Absorber einer oberen Teilzelle in all-Si Tandem-Solarzellen sowie das Nanomischmaterial mikrokristallines Siliziumoxid (μc-SiO_x:H) zur Verwendung in Kontaktschichten für Si-Heterostruktur (SHJ) Solarzellen untersucht. Während sich der Teil über Si-QD Absorber in erster Linie auf das fundamentale Verständnis der Materialeigenschaften konzentriert, beschäftigt sich der Beitrag zu SHJ Solarzellen hauptsächlich mit den Entwicklungen auf Bauteil-Ebene.

Aufgrund der konkurrierenden Anforderungen von Ladungsträgerlokalisierung, die einen hohen Bandversatz zwischen Si-QDs und dem Einbettungsmaterial benötigt, und Ladungsträgertransport, der einen niedrigen Bandversatz voraussetzt, ist der Einsatz von unterschiedlichen Materialien für Matrix und Barriere angebracht. Der innovative Si-QD Ansatz basierend auf Hetero-Übergitter (HSL) mit nahezu stöchiometrischem SiC (niedriger Bandversatz) als vertikaler Barriereschicht und Si-reichem SiO_x (hoher Bandversatz) als lateraler Matrixschicht wird motiviert, indem die technischen und theoretischen Schwierigkeiten der Realisierung von Si-QDs in SiC Matrix aufgezeigt werden. Nach der erfolgreichen Entwicklung von Prozessen zur langsamen und vollkompatiblen Abscheidung von homogenen SiC und SiO_x Einzelschichten wurden diese Prozesse auf eine automatische Depositionssequenz übertragen, welche die Herstellung von SiC/SiO_x HSL-Strukturen mit ausgezeich-

neter Kontrolle über die Komposition und die Dicke der individuellen Schichten erlaubt. Obwohl SiO_x während des Hochtemperatur-Prozesses ein für ein Matrixmaterial günstiges Verhalten zeigt (Ausscheidung und Kristallisation von Si, Si-QDs mit guter Oberflächenpassivierung und klaren Anzeichen von Quanten-Confinement, Hochtemperaturbeständigkeit der amorphen SiO_2 Phase), weist SiC mehrere Nachteile auf, die die Nutzbarkeit von SiC/SiO_x HSL als potenziellem Si-QD Absorber einschränkt: (i) Die Si-QDs breiten sich in die benachbarten SiC Schichten aus, insbesondere für dünne SiO_x Schichten mit hoher Si-Überschuß, was darauf hindeutet, dass SiC als Si-Diffusionsbarriere eher ungeeignet ist. (ii) Das Entweichen von Wasserstoff aus den SiC Schichten resultierte in einer Abnahme der optischen Bandlücke und einer Zunahme der Defektdichte sowie der Absorption unterhalb der Bandlücke in HSL. (iii) Die Defekte in den SiC Schichten scheinen neue, nichtstrahlende Rekombinationspfade für die generierten Ladungsträger in Si-QDs zu eröffnen. (iv) Die thermisch induzierte Dotierung von SiC kann zu einer Zunahme der Rekombination in diesen Schichten führen. Die systematische Untersuchung von HSL und Einzelschichten aus SiC und SiO_x, die bei unterschiedlichen Temperaturen getempert, mittels verschiedenen Methoden passiviert und mithilfe einer Reihe von Charakterisierungsmethoden analysiert wurden, ergab ein konsistentes Bild der fundamentalen Unterschiede zwischen SiC und SiO_x. Die Wasserstoffeffusionsmechanismen während des Temperns sowie die Wasserstoffeinbringungsmechanismen während der Passivierung sind für HSL weitgehend verstanden. Die stärkere Zunahme von Spindichten nach dem Tempern in SiC verglichen mit SiO_x wird der Effusion von einer größeren Menge von Wasserstoff und der weniger effizienten atomaren Diffusion zugeschrieben. Die viel kleinere optische Bandlücke und die deutlich höhere Absorption unterhalb der Bandlücke im getemperten SiC lassen sich auf die geringere Flexibilität seiner 4-fach koordinierten Gitterstruktur zurückführen. Die schlechtere Spannungsrelaxation in SiC erhöht die Wahrscheinlichkeit der Ausbildung von verspannten Bindungen, die zusätzlich zur Absorption unterhalb der Bandlücke beitragen.

Dotiertes µc-SiO_x:H, bestehend aus einem Phasengemisch aus Si Kristalliten und a-SiO_x:H Matrix, stellt aufgrund seiner hohen Leitfähigkeit nach dem Dotieren und gleichzeitig hohen optischen Bandlücke sowie seines vorteilhaften Brechungsindices ein attraktives Kontaktschichtmaterial dar. Nachdem es sich herausstellte, dass die Passivierqualität von µc-SiO_x:H unzureichend ist, wurde zwischen dem

Wafer und den dotierten Schichten eine Pufferschicht aus intrinsischem, amorphem Siliziumoxid (a-SiO_x:H) eingeführt. Damit entstanden die ersten SHJ-Solarzellen mit allen Pufferschichten aus a-SiO_x:H und allen Kontaktschichten aus µc-SiO_x:H Materialien. Die Vorteile von a-SiO_x:H - wie z.B. hohe optische Bandlücke und hohe thermische Stabilität - wurden unabhängig bestätigt mittels der Analyse der optischen Eigenschaften von a-SiO_x:H sowie durch das Aufzeigen von guter Passivierqualität nach dem Tempern auf Material- und Bauteil-Ebenen. Implizite offene Klemmspannungen bis zu 742 mV wurden erreicht mit a-SiO_x:H Schichten, was die Realisierbarkeit von a-SiO_x:H Passivierung hoher Qualität in einem niedrigen Sauerstoffgehalt-Bereich demonstriert. Außerdem hat sich die Deposition von a-SiO_x:H Deckschichten zum Vorkonditionieren der Depositionsanlage nach jeglicher Umstellung an letzterer als äußerst wichtig erwiesen für die Reproduzierbarkeit der Passivierqualität und für die Kontrolle der Pufferschichtdicken. Tatsächlich zeigten SHJ-Solarzellen mit im Nanometerbereich variierenden a-SiO_x:H Schichtdicken auf der Vorder- und der Rückseite stark variierende Effizienzwerte. Strukturelle, optische, elektrische und passivierende Eigenschaften von n- und p-Typ µc-SiO_x:H Schichten, die unter verschiedenen Depositionsbedingungen hergestellt worden sind, konnten mit den Solarzellen-Ergebnissen korreliert werden unter Zuhilfenahme von Bauelementsimulationen. Außerdem konnte die vorliegende Arbeit mehrere Hinweise liefern zur Erklärung der Pufferschichtdickenabhängigkeit der Oberflächenpassivierung mit einem Modell, das annimmt, dass Elektronen und Löcher in der Lage sind, aus dem kristallinen Si-Absorber durch die Pufferschicht zu dringen und an der nächsten Defekt-reichen Grenzfläche zu rekombinieren. Die beste SHJ-Solarzelle mit den optimierten a-SiO_x:H und µc-SiO_x:H Schichten erreichte eine Effizienz des aktiven Bereichs $\eta_{\mathrm{act}} = 19.0\%$ bei offener Klemmspannung $V_{\mathrm{oc}} = 667$ mV, Kurzschlussstromdichte $J_{\mathrm{sc}} = 35.8$ mA/cm^2 und Füllfaktor $FF = 79.6$ %, was die bislang höchste auf SHJ-Solarzellen mit µc-SiO_x:H Kontaktschichten erzielte Effizienz darstellt.

1. Introduction

The enormous demand for electricity worldwide is still primarily covered by the combustion of fossil energy sources. Since this kind of energy gain is pollutive and the fossil fuel resources will be exhausted someday, alternative concepts to generate clean and renewable energy need to be introduced and promoted. Among the existing alternative concepts, e.g. solar energy, wind energy, hydro power and biomass, photovoltaics represent the most direct way to convert solar energy, which is the origin of almost all forms of energy on earth, into electrical power. Today, a large variety of photovoltaic devices using different materials and designs coexist, among which silicon (Si) based solar cells are most sustainable for terrestrial applications due to the non-toxicity and abundance of the Si semiconductor. The first generation of Si solar cells is based on the use of mono- or polycrystalline Si, for which the main drawback concerns its high fabrication cost due to the relatively high energy and material consumption. The aim of the second generation of Si solar cells is to reduce the fabrication and material cost through the large-area deposition of Si thin-films at low temperatures. Since the electrical quality of Si wafer based absorbers outreaches that of Si thin-film absorbers, Si thin-film solar cells give solar energy conversion efficiencies below those of Si wafer solar cells.

As the research is proceeding on future technologies, a next-generation of Si solar cells targeting both high performance and low-cost production needs to emerge to initiate further progress in Si photovoltaics. One possibility is to develop new concepts, which are capable of increasing the efficiency while relying on the cost-efficient thin-film fabrication. Green et al. proposed novel third generation Si solar cell concepts based on Si nanostructures in thin-films with the potential to overcome the Shockley-Queisser-limit [1]. The so called all-Si multi-junction solar cell making use of Si quantum dot (Si-QD) arrays, that are periodically aligned Si nanocrys-

tals (Si-NCs) embedded in a Si dielectric compound, is one of the most promising candidate being proposed [2]. Meanwhile, another promising concept based on amorphous Si (a-Si)/crystalline Si (c-Si) heterojunctions combining both Si wafer and Si thin-film technologies has attracted considerable interest. This concept follows the idea of decreasing the fabrication cost while relying on the high efficiency c-Si wafer technology. The appearance of these so called Silicon Heterojunction (SHJ) solar cells is a direct consequence of matured first generation and second generation Si technologies and thus can be considered as a third generation Si solar cell as well, however, not within the meaning of Ref. [1].

This work deals with the fabrication and characterization of novel Si based nanostructures for implementation in next-generation solar cells. In particular, this work is divided in two topics. The first topic deals with Si-QD absorber material consisting of periodically aligned, mono-disperse Si-NCs in a silicon carbide (SiC)/Si-rich silicon oxide (SiO_x) multilayer structures. For the second topic, the focus lies on the implementation of contact material based on a nanocomposite phase mixture of Si crystallites in a silicon oxide matrix for SHJ solar cells with intrinsic a-SiO_x:H buffer layers. Even though the two material systems are designed for different applications in different devices, they share the similarity of being exclusively made of Plasma Enhanced Chemical Vapor Deposition (PECVD) grown Si dielectric compounds with other abundant elements e.g. oxygen(O) and carbon (C). The significance of hydrogenation is another common ground of the two topics. In order to ensure good solar cell performance, hydrogen is needed to saturate defect states either at the heterojunction interface of the SHJ solar cell or within the absorber material of the all-Si tandem solar cell. Therefore, analysis of the passivation properties at SHJ solar cell interface and in Si-QD absorber forms a important part of this work. It is worthwhile to stress that the main focus of the Si-QD absorber topic lies on the fundamental understanding of the material properties, whereas for the SHJ solar cell topic, technical development on device level is the key aspect.

Chapter 2, divided in two sections, briefly reviews basic aspects and literature on all-Si tandem and SHJ solar cells. Section 2.1 starts with a general description of the all-Si tandem solar cell concept, followed by a closer look at state-of-the-art superlattice approaches towards the fabrication of Si-QD absorbers. Section

2.2 describes the development of SHJ solar cells during the last decades. Different strategies to reduce heterojunction interface recombination, which is one of the most critical issues, are presented. The literature on the research of novel materials as functional layers in SHJ solar cells is shortly summarized. Analytical techniques used to characterize materials and solar cells in this work are introduced in Chapter 3. Due to the large number of characterization methods used, the description of each technique is kept short and material unspecific. Details on the evaluation and interpretation of the measurement results are annotated later when presenting the respective data. Section 3.1 provides an overview of the characterization techniques for the investigation of the structural properties. Section 3.2 describes the methods for characterization of the optoelectronic as well as the c-Si surface passivation properties. Section 3.3 contains information on the characterization of solar cells. Summary and outlook are given in Chapter 6.

Chapter 4 and 5 form the major part of this work. Chapter 4 investigates the applicability of SiC material as barrier layer in SiC/SiO_x Hetero-Superlattice (HSL) structure for implementation in, e.g., all-Si tandem solar cells. Section 4.1 introduces and motivates the novel HSL approach. The technical and theoretical constrains of Si-QD formation in SiC matrix were pointed out. Section 4.2 reports on the material and process development of SiC and SiO_x single layers taking into account critical compatibility issues for later HSL fabrication. Section 4.3 analyses the structural and optical properties of HSL layers with varying SiC thicknesses, SiO_x thicknesses and SiO_x compositions. In Sec. 4.4, the study on the formation of annealing induced defects in SiC/SiO_x HSL were presented, which includes the interpretation of structural, optical and electrical changes in these materials during thermal annealing and hydrogen passivation. Chapter 5 deals with the development of SHJ solar cells exclusively based on hydrogenated silicon oxide (SiO_x:H) functional layers. Section 5.1 provides information on the c-Si surface passivation using intrinsic a-SiO_x:H buffer layers from both technical and materials science point of view. In Sec. 5.2, the dependence of the doped microcrystalline silicon oxide (µc-SiO_x:H) layer properties in terms of microstructure, optoelectronics and passivation on the PECVD deposition conditions are presented and discussed. Section 5.3 presents the initial development of silicon oxide SHJ solar cells, which involves, among others, the testing of a prototype SiO_x emitter SHJ solar cell. Section 5.4 presents the

optimization of PECVD grown SiO_x:H layers towards state-of-the-art full SiO_x SHJ solar cells.

2. Literature review

2.1. All-silicon tandem solar cell

The all-Si tandem solar cell concept comprises the stacking of several Si based individual cells of different band gap connected in series, starting with the largest band gap cell and ending with the lowest band gap cell. A schematic drawing of a triple junction all-Si tandem solar cell stack is illustrated in Fig. 2.1. As light enters the device, the uppermost cell will absorb the highest energy photons and allow lower energy photons to pass through to underlying cells. With an infinite number of current-matched individual cells, the light absorption within the device is perfectly adjusted to the solar spectrum and thus strongly reduces thermalization and transmission losses. Even with tandem stacks of two or three cells, the radiative efficiency limit increases from 29 % for a single junction Si cell to 42.5 % and 47.5 %, respectively [3]. Using c-Si as the bottom cell, the optimal band gap of the top cell to maximize conversion efficiency is around 1.8 eV for a 2-cell tandem and 1.5 eV and 2.0 eV for the middle and upper cells for a 3-cell tandem, respectively [4]. To date, a similar all-Si tandem approach has already been realized and commercialized in the Si thin-film branch by stacking a-Si:H cell with an optical band gap of around 1.8 eV on top of μc-Si:H cell with an optical band gap of around 1.1eV [5].

2.1.1. Silicon quantum dot superlattice

A new silicon-based material to form top cell above the c-Si cell can be engineered via the fabrication of Si-NCs embedded in a Si dielectric compounds with other abundant elements e.g. Si oxides, nitrides or carbides [3]. The quantum confinement due to carrier localization within the Si-NCs of few nanometers in diameter results in

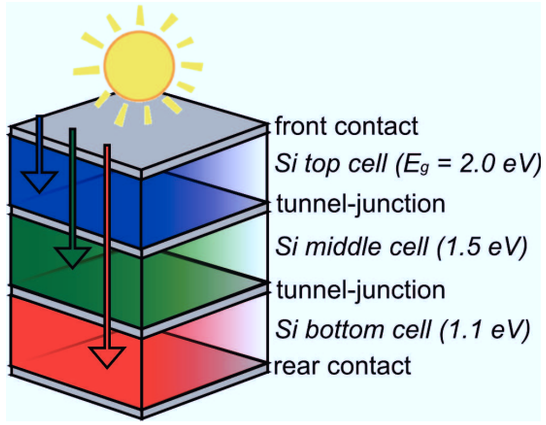

Figure 2.1.: *Schematic drawing of a triple junction all-Si tandem solar cell stack. As light enters the device, the uppermost cell will absorb the highest energy photons and allow lower energy photons to pass through to underlying cells. Using c-Si as the bottom cell, the optimal band gap of the top cell to maximize conversion efficiency is* 1.5 eV *and* 2.0 eV *for the middle and upper cells for the* 3*-cell tandem solar cell [4].*

a widening of the optical band gap tunable by changing the size of the Si-NCs. These Si-NCs showing quantum size effect are refered to as Si quantum dots (Si-QDs). In addition, the carrier localization relaxes the momentum conservation during optical transitions and thus increases the optical absorption, thereby overcoming a major drawback of the indirect band gap of c-Si. As a very first approximation, a Si-QD is described as a cubic potential box (Fig. 2.2(a)) [6]. Using the effective mass approximation, the Schrödinger equation for an electron confined in the potential box gives [7]

$$E_{\mathrm{n}} \approx 3\frac{\pi^2\hbar^2}{m^* a^2} n^2 \left(1 + \frac{2\hbar\sqrt{2m^* V_0}}{a}\right)^{-2} \tag{2.1}$$

where E_{n} is the confinement energy of the n-th electron state, m^* the reduced electron mass, $\hbar$ the reduced Plank constant, a the width of the potential box (Si-QD size) and V_0 electron potential barrier (conduction band offset). This equation, also applicable for holes, predicts that the energy of the carrier will decrease with

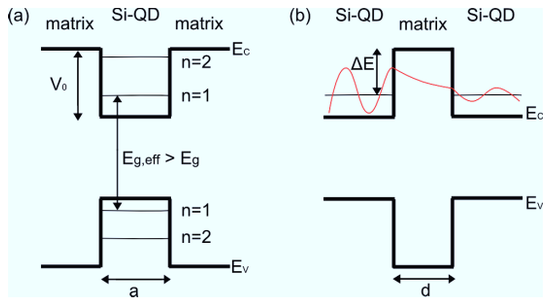

Figure 2.2.: *(a) Quantum confinement in Si-QD as a potential box surrounded by a matrix material providing a potential barrier. The energy of the carrier is expected to decrease with the Si-QD size and with the band offset. (b) Tunneling of an electron (red curve: electron wavefunction) through the matrix from one Si-QD to another Si-QD. The overlap of the wavefunctions needed for carrier transport is increased by placing the dots close to each other and/or by lowering the barrier in-between, however, at the cost of quantum confinement.*

the Si-QD size and with the band offset.

However, the carrier transport within this kind of devices containing isolating matrices is challenging. Fortunately, the carriers have a certain probability to exit the potential box via tunneling. Figure 2.2(b)) shows the wavefunction (red curve) of the electrons coming from the left Si-QD, spreading into the barrier and tunneling to the right Si-QD. The probability of find electrons on the other side of the barrier is given by the approximate relation [7]

$$T_{\mathrm{e}} \approx 16 \exp\left(-d\sqrt{\frac{8m_*}{\hbar^2}\Delta E}\right) \tag{2.2}$$

where T_{e} is the tunneling probability, d the barrier width (spacing between Si-QDs) and ΔE the energy difference between the conduction band edge of the matrix and the confined energy level of the quantum dots. Hence, the tunnel current, which is proportional to T_{e}, will exponentially decrease with the Si-QD spacing and the band offset. Based on the principle of resonant tunneling, a new transport path via mini-band states will arise [8], if the Si-QDs are arranged periodically and

there is a significant overlap of the wavefunctions localized on adjacent dots. These ordered Si-QD structures showing mini-band formation are denoted as quantum dot superlattices. Pronounced overlap of the wavefunctions is facilitated by placing the dots close to each other and/or by lowering the barrier in-between, however, at the cost of quantum confinement. Details on the fundamental physics of quantum confinement and mini-band formation can be found in Ref. [9].

Si-NCs can be fabricated by depositing a sub-stoichiometric Si dielectric material with an excess of Si. A high temperature annealing step after the deposition is required to induce the precipitation and crystallization of the excess Si. By applying this approach to multilayer structures made of 20 - 50 bilayers of alternating thin layers of Si-rich and stoichiometric Si alloys, Si-QD superlattices can be realized. Ideally, the Si-QDs formation is constrained to the layers with Si excess. Thus, the Si-rich layer thickness determines the size of the Si-QDs and consequently the band gap energy. The stoichiometric layer thickness corresponds to the vertical spacing between the Si-QDs and is consequently related to the mini-band formation. The variation of Si excess allows for the controlling of the Si-QD density independent from the Si-QD size [10]. Doping of the Si-QD superlattice is important to form junctions with a built-in electric field for the carrier selectivity and tunnel junctions connecting two individual cells. However, doping of Si-NCs is not yet fully understood. It is not clear whether the dopants for bulk Si like phosphorus and boron still act as shallow impurities and not as deep defects [11]. Moreover, impurity doping of Si-NCs may be energetically unfavorable due to higher formation energy of dopants [12].

2.1.2. Alternative superlattice concepts

In the following, the research to date on the fabrication of Si-QD superlattice materials and solar cells based on the high temperature annealing of silicon oxide, carbide and nitride multilayers is reviewed. As the first multilayer annealing approach to accurately engineer size, position and density of Si-NCs, the preparation of a-Si in silicon dioxide (SiO_2) superlattices was suggested [13]. However, the annealed a-Si layers became polycrystalline and Si-NCs touched each other. Inspired by this approach, Zacharias et al. [10] could demonstrate good control of the Si-NC alignment

on a Silicon Rich Oxide (SRO)/SiO_2 structure. More importantly, strong photoluminescence indicated good Si-NC surface passivation, and a size dependent shift of the luminescence energy is an evidence for quantum confined states in Si-NCs. This excellent finding has encouraged considerable work in this research area. Similar systems were realized by reactive evaporation [14], magnetron sputtering [15] and PECVD [16]. The effects of different annealing methods [17] in different ambients [18] have been investigated. Furthermore, successful doping of the Si-NCs has been reported despite of the above mentioned theoretical difficulties [11, 19]. Nowadays, the phase separation and crystallization of Si-QDs in SRO/SiO_2 superlattices [20], their optical properties [21] and the defect passivation [22] are already well understood. However, it is a major challenge to achieve charge carrier transport through a network of Si-QDs embedded in a SiO_2 matrix, namely due to high barrier and disorder-related carrier localization. As an alternative matrix to SiO_2 (band gap $E_g = 9.0$ eV), Si based host matrices such as silicon nitride (Si_3N_4) with $E_g = 5.3$ eV [23–26] or SiC with $E_g = 2.5$ eV [27–30] that feature lower band offset with respect to the Si band edge, have drawn the interest. The SiC matrix provides even lower barrier offset towards Si and hence better electronic transport properties than the Si_3N_4 matrix. However, the lower barrier height decreases the quantum confinement and consequently the band gap widening for the same Si-QD size (Eq. 2.1).

It was shown that Si-NCs can be obtained in thick layers of Silicon Rich Nitride (SRN) [31] or Silicon Rich Carbide (SRC) [32] fabricated in a very similar process to that of SRO, when annealed at high temperatures. However, unlike for SRO and SRN, the crystallization of Si in SiC matrix depends on the Si excess [32]. This is attributed to the fact, that the length and polarity of the Si-Si bonds in the SiC matrix are lower than in the SiO_2 or Si_3N_4 matrix, which complicates the phase separation and precipitation of Si-NCs in the SiC matrix [33, 34]. The nitride matrix shows a lower persistence of its amorphous phase at high temperatures as compared to oxide, since its crystallization is observed already at temperatures above 1150 °C [35]. In contrary to the oxide and nitride matrix, Si- and SiC-NCs are formed simultaneously in SRC by high temperature annealing, indicating an even lower persistence of the amorphous SiC matrix [36]. The crystalline matrix consists of crystallites of different orientations at the Si-QDs interface, where strong

fluctuation of the barrier height may occur.

Multilayered structures of alternating SRN and stoichiometric Si_3N_4 [23] or alternating SRC and stoichiometric SiC [29] result in Si-NC formation with more controlled size and position of the Si-NCs. However, Si-NCs with diameters greater than the SRC layer thickness are observed, which is attributed to Si inter-diffusion into the stoichiometric SiC layers resulting in growth of Si-NCs also in these layers. Another problem concerning the SRC/SiC superlattice is the drastically increasing dark conductivity of the stoichiometric SiC films with increasing annealing temperature, which was believed to increase the leakage current. The increase of the dark conductivity was attributed to the formation of SiC crystals [37]. Kurokawa et al. incorporated nitrogen [38] or oxygen [37] atoms into the stoichiometric SiC layers using molecular nitrogen (N_2) or carbon dioxide (CO_2) gases in the gas phase, respectively. Suppression of the SiC crystallization as well as reduction of the dark conductivity to an intrinsic level were demonstrated. However, the incorporation of nitrogen (N) and oxygen (O) atoms may also introduce a large number of defects. Wan et al. [39] introduced an approach to circumvent the SiC conductivity issue by fabricating SRC/Si_3N_4 multilayers. The Si_3N_4 layer with a lower Si diffusion coefficient than SiC inhibits the Si diffusion and enables good spacial confinement of the Si-NCs. Di et al. [40] reported on the formation of Si-QDs in a similar hybrid matrix using SRO/Si_3N_4 multilayers. Here, the Si_3N_4 layer is not only a good diffusion barrier but also a more efficient electronic transport layer as compared to SiO_2.

Si-QDs grown in situ during PECVD deposition have also been reported for Si-QD in a Si_3N_4 matrix [41] or in a SiC matrix [34]. Even though the control over the size, position and shape of the Si-QDs is problematic, omitting the high temperature step, which rather makes the Si-QD absorber a high-cost material, is highly attractive. Adjusting the deposition conditions to avoid agglomeration of Si-NCs might also be challenging.

Before being able to demonstrate the benefit of quantum confinement based absorbers in a tandem solar cell, the applicability of the high temperature annealing approach has to be shown on device level. Cho et al. [42] fabricated a heterojunction solar cell using phosphorus (P) doped Si-QDs in a SiO_2 matrix as a emitter layer on

a p-type c-Si wafer. The authors obtained a reasonable open circuit voltage (V_{oc}) of 556 mV, which indicates a formation of a Si-QD/c-Si n-p junction and the transport of carriers through the Si-QDs. However, the photovoltaic active material in this single junction device is still the c-Si wafer. Yamada et al. [43] presented intrinsic Si-QDs in a SiC matrix as the absorber of a p-i-n structure with a thick, heavily doped a-Si as back contact on quartz glass. The authors achieved a V_{oc} of 518 mV. However, it is difficult to separate the contribution of the Si-QD layer from that of the thick contact layer, which underwent the phase transition from amorphous to crystalline during the thermal treatment. Perez-Wurfl et al. [44] realized an p-i-n solar cell exclusively made of Si-QDs in a SiO_2 matrix on quartz glass, which guarantees measurements free of bulk Si contributions. The authors in situ doped the top layers of their Si-QD superlattice structure with boron (B) and the bottom layers with P. The solar cell gives a V_{oc} of 492 mV. However, the strong interdiffusion of dopants as impurities during annealing are assumed to deteriorate the electronic quality and limit the device performance. Loeper et al. [45] presented a device structure in which the c-Si substrate is locally removed by chemical etching. The thin P and B doped sub-stoichiometric silicon carbide (a-SiC_x:H) contact layers sandwiching the intrinsic Si-QDs in a in a SiC matrix were deposited after the annealing and etching steps. By doing so, dopant diffusion and bulk Si layers are avoided. The authors demonstrated a V_{oc} of 370 mV on their quantum dot membrane solar cell.

2.2. Silicon heterojunction solar cell

Minimizing the surface recombination of charge carriers is a key issue for high efficiency c-Si solar cells. Thermally grown SiO_2, well known from the microelectronics, exhibits excellent c-Si surface passivation properties [46, 47]. The Passivated Emitter and Rear Locally diffused (PERL) cells for example, achieving efficiencies up to 25% [48], use thermal SiO_2 for c-Si passivation (Fig. 2.3). However, the thermal oxidation implies an energy-consuming high-temperature step. PECVD grown, low-temperature Si-rich silicon nitride (a-SiN_x:H) thin films are presently the most commonly used surface passivation and antireflection coatings for c-Si solar cell

Figure 2.3.: *Schematic of the passivated emitter, rear locally diffused (PERL) cell structure. The passivated emitter refers to the high quality oxide at the front surface that significantly lowers the number of carriers recombining at the surface. The rear doping is locally diffused only at the metal contacts to minimize recombination at the rear while maintaining good electrical contact. Figure from "http://www.pveducation.org".*

packaging due to their excellent physical and chemical properties, such as high refractive index, low surface recombination velocity [49–51] and good resistance to oxidation [52]. Optionally, a very thin thermal SiO_2 prior a-SiN_x:H deposition helps to reduce parasitic shunting [53] induced by fixed charges in the nitride film [50]. Recently, PECVD grown off-stoichiometric aluminum oxide (a-AlO_x:H) featuring high passivation quality has also attracted the attention of the photovoltaic community [54–56].

Since these dielectric layers are insulating, contact to the electronically active absorber is realized by firing the metal through the passivation layer [57] or by locally laser-opening the passivation layer [58]. A simpler approach is to use a multifunctional layer, preferably grown at low temperatures, which simultaneously fulfills the requests for passivation and contact. Furthermore, replacing the diffused emitter and Back Surface Field (BSF) by doped PECVD thin films allows for further reduction of energy consumption during production. Already in 1974, Fuhs et al. [59] published the first SHJ solar cell using doped amorphous Si as a passivating contact

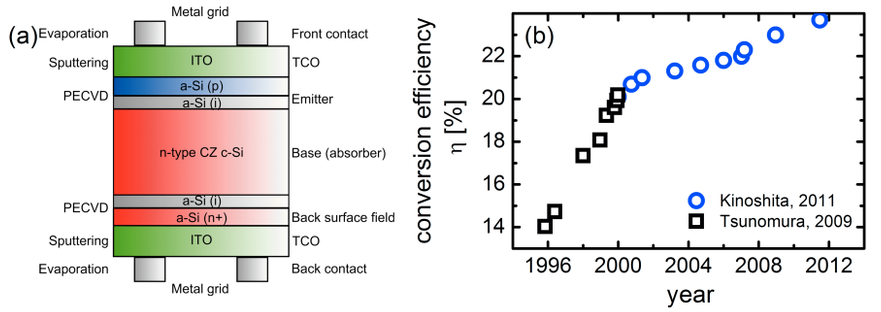

Figure 2.4.: *(a) Schematic illustration of the Sanyo HIT bifacial solar cell structure on n-type CZ c-Si wafer. Its random texture is not included in the schematic. The very thin, intrinsic a-Si:H buffer layer between wafer and doped layers is characteristic for this device. (b) Progress in the conversion efficiency of HIT solar cells at R&D stage from Ref. [63, 64].*

layer. The research was readopted and continued by the Sanyo Electronics group in the 90th [60–62].

2.2.1. Heterojunction with intrinsic thin-layers

Recently, after 20 years of continuous advancement [65, 66], the so called Heterojunction with Intrinsic Thin layer (HIT) solar cells, now using a bifacial structure, reached a highest conversion efficiency of 23.7% on 100 cm^2 n-type Czochralski (CZ) wafer [64] (Fig. 2.4). The very high V_{oc} of 745 mV clearly demonstrates the excellent electronic c-Si surface passivation. It is important to note that these results were achieved on 98 µm thin wafers that are not processable anymore with c-Si technology based on diffused emitter and BSF. This is an enormous advantage of SHJ solar cells as compared to conventional c-Si solar cells, expecially with the current industry trend towards thinner wafers. In addition, SHJ solar cells provides better temperature characteristics than conventional c-Si solar cells resulting in higher energy yield in outdoor conditions for the same nominal conversion efficiency [67]. The SHJ solar cells combining c-Si wafer with a-Si thin-film technology benefits from both the high quality of the c-Si absorber and the formation of the junctions

at low temperature making it truely one of the most promising candidate for high efficiency and low cost Si photovoltaic device designed for mass production. Details on the working principle of heterojunction solar cells can be found in Ref. [68, 69].

From a general point of view, the boosts in efficiency are due to a number of achievements in reducing optical, recombination and resistive losses in the device at the same time. The wafer surface pretreatment, e.g., ensures undamaged, contamination-free, chemically stable and reproducible substrate surfaces and thus is one of the most crucial steps in minimizing interface recombination losses. Partial hydrogen-termination of surface dangling bonds (DBs) during the wafer cleaning adds to the surface quality. The wet-chemical cleaning procedures was adapted from the microelectronics device technology [70] and optimized for solar cell manufacturing [71]. Since c-Si surface was textured to optimize light trapping properties, wet-chemical smoothing of sharp edges [72] were necessary to maintain good passivation by a-Si:H layers.

It turned out that it is mandatory to include a very thin (low resistive loss), intrinsic, high quality a-Si:H buffer layer between wafer and doped layers to realize effective passivation of defects on the c-Si surface [60]. The main reason is that the defect density in a-Si:H and consequently the defect density at the a-Si/c-Si interface increases with doping, which results in high surface recombination [73]. The a-Si:H deposition parameters were adjusted to give uniform layers with a precise thickness control [62] and suppressed epitaxial growth [74]. Low plasma and/or thermal damage to the c-Si surface is another important demand, not only during a-Si:H but also during Transparent Conducting Oxide (TCO) and metal contact deposition. Thermal annealing at temperatures below 200 °C was found to yield an improved surface passivation [75]. Besides the reduction of the surface state density via chemical passivation, the reduction of wrong free carriers at the surface via an electrical field built up by the doped a-Si:H layers adds to the minimization of recombination losses. Optical losses such as grid electrode shadow loss can be reduced by screen printing metal grids with high aspect ratio provided that the resistive loss remains low. Metal grids with high aspect ratio were realized by, e.g., optimizing the viscosity and rheology of the silver (Ag) paste as well as the process parameters in screen printing [63]. Absorption in the a-Si:H and TCO layers can

be reduced by using wide-gap Si alloys (Sec. 2.2.2) and highly transparent TCO, respectively [66]. Again, the conductivity of these layers have to be sufficiently high to ensure low resistive loss.

2.2.2. Alternative materials for silicon heterojunction solar cells

As a consequence of the successful Sanyo HIT concept, research groups are encouraged to develop advanced alternative materials for SHJ solar cells. One possibility to improve the cell performance is to reduce the optical losses in the intrinsic and/or doped a-Si:H layers. Pysch et al. [76] used phosphorus-doped a-SiC_x:H as a wide-gap emitter on p-type wafer omitting the intrinsic buffer layer. However, the surface passivation was insufficient unless a thin a-Si:H buffer layer was inserted [77]. On the contrary, intrinsic a-SiO_x:H seems to be more promising not only because of its high optical band gap. Mueller et al. [78] reported on excellent surface passivation of both n- and p-type wafers exceeding those of record SiO_2 and a-SiN_x:H. Fujiwara et al. [79] stated that during the growth of a-SiO_x:H, the epitaxial growth of Si that degrades the solar cell performance severely [74] is suppressed due to the presence of oxygen in the plasma. Hence, there is more freedom in changing the deposition parameter to optimize the material. Moreover, Einsele et al. [80] demonstrated an outstanding thermal stability of the a-SiO_x:H passivation up to 400°C. Recently, a conversion efficiency of about 21% with an V_{oc} of 705 mV was reported for SHJ solar cells using a-SiO_x:H buffer layers.

Conductive materials like doped µc-Si:H, µc-SiC:H and µc-SiO_x:H have the potential to replace the doped a-Si:H layers. The µc-Si:H, a composite material that consists of crystalline and amorphous Si phases, possesses a lower absorption coefficient in the short wavelength range and a much higher conductivity than a-Si:H [81], when doped with phosphorus or boron. The higher conductivity allows for thinner µc-Si:H contact layers, which in turn further reduces optical losses in these layers. Quantum efficiencies of SHJ solar cells using µc-Si:H contact layers exhibiting a distinct increase in the blue part of the solar spectrum have been reported [82]. An even more transparent material is the highly crystalline, stoichiometric µc-SiC:H containing large SiC crystallites, which give rise to the high optical band gap [83]. With its refractive index between the c-Si absorber and the TCO layer [84], the

μc-SiC:H can efficiently in-couple light at the front side and back-reflect light at the rear side of the SHJ solar cell. The μc-SiC:H is highly conductive either in its native n-type form without intentional doping or after overcompensation with intentional aluminum p-type doping [85]. However, the large amount of atomic hydrogen, which are needed to produce highly crystalline μc-SiC:H, results in low deposition rate and causes significant etching damage to the underlying material. Nevertheless, an active area efficiency of 19.1% was realized on flat p-type SHJ solar cells using μc-SiC:H emitter, where the authors applied a two-step process starting with a soft a-SiC layer deposition [86].

The μc-SiO_x:H, a phase mixture of Si crystallites and a-SiO_x:H matrix, is also an attractive contact layer material due to its high conductivity upon doping and at the same time high optical band gap and favorable refractive index. The material properties can be varied strongly depending on the fraction of c-Si and a-SiO_x:H phases. The less conductive a-SiO_x:H phase gives rise to the more beneficial optical properties, whereas the less transparent c-Si phase, easily doped with P and B, contributes to the high conductivity via c-Si percolation paths. This material is fabricated at less aggressive conditions, which enables a wider field of application in Si based solar cells as compared to μc-SiC:H. In Si thin-film solar cells, it is standardly used as intermediate reflector [87] or wide-gap window layer [88]. Partial implementation as emitter [89, 90] or back contact material [91] in n- and p-type SHJ solar cells has already been reported. Nevertheless, an active area efficiency of 18.5% was achived on flat p-type SHJ solar cell with p-type μc-SiO_x:H BSF [91] without intrinsic buffer at the rear side.

3. Characterization methods

This chapter addresses the experimental methods used to characterize the materials and the solar cells in this work. The first section provides an overview of the characterization techniques for the investigation of the structural properties. The second section describes the methods for characterization of the optoelectronic as well as the c-Si surface passivation properties. The last section contains information on the characterization of solar cells.

3.1. Investigation of structural properties

Thickness The precise determination of the film thickness is crucial for the calculation of some material properties, e.g., the absorption coefficient α or the electrical conductivity σ. The film thickness was mechanically measured by a step profiling system (Vecco DEKTAK 6M Stylus Profiler). Before each deposition, one or more dots were planted on the substrates using a permanent marker. After deposition, these dots were then carefully scratched away using a scalpel and subsequently cleaned with 2-Propanol. This procedure creates a sharp step between substrate and film. The corresponding height difference, scanned with a fine probe tip, gives the thickness of the film. The deposition rate was then acquired by dividing the measured thickness by the deposition time. The thicknesses of the films deposited in this work were all below 1 µm.

Rutherford Backscattering Spectrometry (RBS) RBS was used to determine the composition of silicon oxide and silicon carbide films by measuring the elastic backscattering of a beam of high kinetic energy helium ions (He^{2+}) accelerated at a sample. Since these ions interact with the atom nuclei of the sample, the number of

back scattered ions is proportional to the square of the ordinal number of the target atoms. By detecting the particle energy, which is correlated to the energy loss at the scattering, information on the mass of the target atoms is obtained. Since RBS is insensitive to the microscopic structure of the material, inhomogeneous mixture of amorphous or crystalline silicon and silicon alloy phases does not affect the resulting stoichiometry. The RBS measurements were carried out on the 1.7 MW Tandetron accelerator in the Peter Grünberg Institute, Forschungszentrum Jülich [92]. For less conductive films on isolating substrates, a 2 nm sputtered platinum layer on top of the film was required to suppress charging effects.

Secondary Ion Mass Spectrometry (SIMS) In this work, SIMS was performed to measure in-depth profiles of relative element distributions (silicon, oxygen, carbon and hydrogen). For a SIMS measurement, an primary cesium ion (Cs^+) beam is accelerated towards the film. Part of the sputtered material are charged secondary ions, which are separated in a time of flight mass spectrometer in a field-free drift path according to their velocity. Since all secondary ions have the same kinetic energy, the velocity and therefore the time of flight varies according to the ion mass, allowing the identification of chemical elements present. In order to ensure high depth resolution for multilayer systems with sublayer thicknesses in the range of few nm, a low primary ion energy of 1 keV was used. The SIMS in-depth profiles were measured on the Tof-SIMS in the Central Division of Analytical Chemistry, Forschungszentrum Jülich.

X-ray Photoelectron Spectroscopy (XPS) XPS is a surface-sensitive method for the quantitative investigation of elemental composition and chemical states. During the irradiation of a sample with an X-ray beam of discrete energy, electrons are excited out of the atomic shell with a certain kinetic energy, which corresponds to the difference between the excitation and the binding energy of the electron. Since the binding energies are specific to both elements and bonding conditions, the detected energy spectrum of the photoelectrons identifies the chemical elements and the bonding states of the sample. The XPS data for O 1s, C 1s and Si 2p lines were provided by the Institute for Silicon Photovoltaics, Helmholtz-Zentrum Berlin using a Mg-Kα source with a photon energy of 1253.6 eV [93]. XPS in-depth profiling by

applying an additional Ar sputter gun during measurement was carried out in the Central Division of Analytical Chemistry, Forschungszentrum Jülich.

Grazing Incidence X-Ray Diffraction Spectroscopy (GI-XRD) The crystalline structure of the synthesized films was investigated using an X-ray diffractometer (Bruker D8 Advance) in graze-angle mode. During the measurement, the photons with a characteristic X-ray spectrum containing the intense Cu-Kα line at the wavelength of 0.154 nm encounter the sample under a constant flat angle. The impinging photons are diffracted at the electrons surrounding the atom nuclei, which are periodically ordered in lattice planes in case of crystalline structure. The diffraction of X-ray at lattice planes with material specific spacings creates interference patterns, which are detected by varying the detector position within the corresponding scatter angles. Information on the presence of Si and SiC crystallites in silicon carbide and/or silicon oxide materials were obtained from GIXRD data. The average size of the crystals were calculated using the Scherrer formula neglecting strain effects [94]. More details on the measurement setup and the evaluation of GIXRD data can be found in Ref. [95].

Raman Spectroscopy Raman spectroscopy is a fast and non-destructive measurement, which was used to estimate the Si crystalline volume fraction on the layer systems. This method is based on the inelastic scattering of a photon while creating or absorbing a phonon. The intensity of the emitted light is detected as function of energy loss, which correlates with the material and structure specific lattice oscillation energy. Ref. [96] is recommended for further readings. The samples were deposited on glass substrates and measured with a Renishaw inVia Raman Microscope with 532 nm Nd:YAG laser. Since transparency and thin silicon alloy films were under investigation, the impinging photons might penetrate into the substrate and contribute to Raman signals, which needs to be checked before evaluation. Even though a chromium coating between film and substrate prevents substrate Raman signals by effectively reflecting the light back to the film, the cracking of this coating during annealing experiments limits its applicability to as-deposited samples. A detailed description of the determination of the crystalline Si volume ratio from Raman measurements can be found in Ref. [97].

Fourier Transform Infrared Spectroscopy (FTIR) In the infrared spectroscopy, incident light is absorbed due to excitation of electric dipoles in the material. The oscillation frequencies of the induced molecular vibrations are determined by the bonding and the dielectric constant, thus, give information on the bonding structure and its close environments. The FTIR spectra of the samples on polished Si wafer substrates were recorded using a Nicolet 5700 Fourier transform infrared spectrometer. The measurement chamber was purged with nitrogen during the recording of the spectrum for the sample and the Si wafer reference. After normalizing the sample spectrum to the reference spectrum, the absorption coefficient as a function of the photon energy was calculated using the film thickness. The absorption coefficient was multiplied with the empirical correction factor $\kappa = 1/(1.72 - 0.0011kd)$ for all $\kappa < 1$ to correct the absorption coefficient values for films with thicknesses below 1 µm, where k is the corresponding wavenumber and d the film thickness [98].

Transmission Electron Microscopy (TEM) Cross-sectional TEM images allow for direct visualization of layer structures on an atomic scale. In TEM, part of the electron beam passing through the sample is used for imaging. In order to perform TEM analysis very thin lamellas have to be prepared from the samples. In this work, such lamellas were produced either using focused ion beam instrument or by mechanical grinding, polishing and dimpling followed by argon ion (Ar^+) milling. The contrast of a High Resolution Transmission Electron Microscopy (HRTEM) image originates from the coherent superposition of primary and of scattered electron beams in the image plane, which is related to the atomic structure of crystallites. However, only crystallographic lattices with orientations allowing the electrons to channel along the atom columns are observed, which should be kept in mind to avoid misinterpretation. The HRTEM studies were conducted on a FEI Titan 80 - 300 TEM and a FEI Titan 60 - 300 Pico in the ER-C, Forschungszentrum Jülich as well as on a JEM 4010 TEM in the Interdisziplinäres Zentrum für Materialwissenschaften, MLU Halle-Wittenberg. Energy Filtered Transmission Electron Microscopy (EFTEM) is an analytical method to determine the spacial distribution of elements (silicon, oxygen and carbon). It bases on the detection of the energy loss of transmitted electrons, where the elementally sensitive image emerges by adjusting a slit only allowing electrons of a specific amount of energy loss to reach the detector. The

EFTEM measurements were carried out on a JEOL JEM 2000 FX II microscope in Gemeinschaftslabor für Elektronenmikroskopie, RWTH Aachen University.

Hydrogen Effusion In the hydrogen effusion experiment, the sample on c-Si substrate was heated up to 1050 °C inside a permanently evacuated vacuum quartz tube with a constant heating rate of 20 K/min. During the heating, hydrogen is released from the material network into the vacuum. The hydrogen partial pressure as a measure of the hydrogen effusion rate was detected with a quadrupole mass spectrometer as a function of time. In principle, the mass analyzer allows for the investigation of any escaping gaseous compounds e.g. O-H and C-H molecules. The measured hydrogen effusion rate as a function of annealing temperature enables interpretation of the hydrogen transport mechanisms of the sample, which again depend on the micro structure of the material. The measuring procedure and the data interpretation is described in Ref. [99].

Electron Spin Resonance (ESR) ESR was used to gain information on the quality of the materials in terms of paramagnetic defect states. In a magnetic field, the magnetic moment of a electron orients itself parallel or antiparallel to the field with these two alignments having different energies. An unpaired electron can switch between the two energy levels by either absorbing or emitting electromagnetic radiation of energy. During a ESR measurement, the magnetic field strength is varied and the loss of microwave power at resonance condition is recorded. Paramagnetic defect states were investigated by a conventional continuous wave X-band ESR spectrometer (Bruker ESP E580) at room temperature. A sputtered amorphous silicon with a known spin number of 2×10^{15} and g-value of 2.00565 was used as a standard to calculate the spin densities and g-values of the samples [100].

3.2. Optical, electrical and passivation properties

Photoluminescence (PL) PL is a powerful tool to investigate the electronic structure of material providing information for defect identification and band gap determination. A laser beam with energy larger than the band gap of the material gener-

ates electron-hole pairs, which then radiatively recombine with a certain probability. The detected emission spectrum contains information about the energy levels of the recombination centers, e.g., band-to-band recombination or defect recombination. From the luminescence intensity, information on the competing process, the non-radiative recombination, can also be deduced. The PL measurements were carried out on a μ-PL setup with a diode-pumped solid-state laser for the excitation at 532 nm and a silicon detector cooled with liquid nitrogen for the detection in an energy range of 1.2 eV - 2.2 eV. The PL spectra were background subtracted and system corrected in a subsequent evaluation procedure.

Photothermal Deflection Spectroscopy (PDS) The spectral optical absorption was investigated by PDS. This method stands out for its high sensitivity for absorption coefficients over many orders of magnitudes, thus, the optical band gap as well as the absorption in band tails and in the sub-band gap energy range are simultaneously obtained [101]. The measurement setup consists of a cavity filled with an optically transparent CCl_4 fluid surrounding the sample. The sample is illuminated with a monochromatic light in the wavelength range between 310 nm (halogen lamp) and 2600 nm (high pressure xenon lamp). This technique makes use of the heat generation in the sample due to the absorption of the monochromatic light and the heat transfer to the CCl_4 fluid. The refractive index of the fluid changes with temperature, therefore the temperature difference between the sample and the fluid creates a refractive index profile, which can be detected by the deflection of a passing laser beam. A phase correction procedure using chopped light and lock-in technique is applied to reduce contribution of glass substrate by delaying the substrate signal.

Optical photometry The spectral transmittance $T(\lambda)$ and reflectance $R(\lambda)$ of the films on glass substrates were obtained from measurements using a calibrated spectrometer (Perkin Elmer LAMBDA 950) with a spectral band width of 250 nm - 2500 nm. An integrating sphere with highly reflective and diffuse internal coating is installed to include scattered light. For the transmittance measurement, the sample is positioned before the optical entrance of the sphere, which gathers and guides the transmitted light into the detector. For the reflectance measurement, the sample is positioned on the opposite side of the optical entrance. The spectral absorptance

is then calculated as $A(\lambda) = 1 - T(\lambda) - R(\lambda)$. Using an optical simulator (Scout), the spectral refractive index $n(\lambda)$ was obtained by fitting the transmittance and reflectance data with an appropriate layer stack model consisting of the substrate and the film of known thickness. The cell reflectance was also measured with this technique.

Coplanar conductivity Lateral electrical conductivity was measured at room temperature in vacuum between two thermally evaporated coplanar silver contacts with 0.5 mm inter-electrode gap. No thermal treatment at 440 K is required for SiC and SiO_x materials according to comparison between conductivity values with and without heating before measurement. A major advantage of this technique is the by orders of magnitudes smaller cross section of current flow lateral in the thin film as compared to that vertically through the contacts and the films, therefore the contact resistance becomes negligible. A drawback of this technique is the fact that the vertical conductivity through the film, which is relevant in solar cells, might differ significantly from the measured lateral conductivity. We tested different concepts to determine the vertical conductivity, however, the contact resistance tends to dominate over the resistance of those conductive layers, since the cross section of current flow through the contact and the film are necessarily the same. For doped contact materials, only the conductivity in the dark σ_{dark} was measured, whereas for intrinsic absorber materials, the conductivity under illumination σ_{illum} with a halogen lamp was additionally obtained in order to calculate the photo sensitivity $(\sigma_{\text{illum}} - \sigma_{\text{dark}})/\sigma_{\text{dark}}$.

Transfer Length Method (TLM) In this work, TLM was used to measure the contact resistance between TCO and silver. A TLM structure consisting of silver dots of 2 mm diameter with 8 mm spacing between two adjacent dots was thermally evaporated on a TCO film. The resistance between dots of different distance was measured using the four point probe technique to suppress the parasitic resistance introduced by the probe. By plotting the resistance versus the contact separation, the contact resistance is read from the intersection between the linear interpolation and the y-axes. The slope of the linear interpolation gives the sheet resistance of the TCO film.

Quasi Steady-State Photo Conductance (QSSPC) The effective lifetime $\tau_{\text{eff}}(t)$ of the minority carriers in Si wafer is performed on a Sinton Consulting WTC-120 QSSPC setup [102]. In the QSS mode, the sample is illuminated by a slowly decaying pulse of light, which is considered to be stationary at each time as compared to the lifetime of photo generated excess free charge carriers in the range of few µs to ms. Since the IR light is removed by an IR filter, the intensity of the light pulse measured with a light sensor is converted into a generation rate $G(t)$. Simultaneously the conductivity of the sample is detected using a RF coil and converted into a excess charge carrier density $\Delta n(t)$. The τ_{eff} is calculated from the continuity equation $d\Delta n(t)/dt = G(t) - \Delta n(t)/\tau_{\text{eff}}(t)$. Under the reasonable assumption that the bulk lifetime $\tau_{\text{bulk}}(t)$ is much larger than the surface lifetime $\tau_{\text{surface}}(t)$, the $\tau_{\text{eff}}(t)$ is a direct measure for $\tau_{\text{surface}}(t)$, which is related to the c-Si surface passivation quality of the films on both sides of the Si wafer. Ref. [103] is recommended for further readings.

3.3. Characterization of solar cells

Current-Voltage (IV) characteristics The current density versus voltage (JV) characteristics of solar cells are measured by means of a class A double source Air-Mass (AM) 1.5 solar simulator (WACOM-WXS-140S-Super) at standard test conditions (AM1.5G, 100 mW/cm^2, 25 °C). While the dark JV characteristic gives the diode quality factor n and the saturation current density J_0, the JV curve under illumination delivers the open circuit voltages V_{oc} at $V(J = 0\ \text{mA/cm}^2)$, the short circuit current densities J_{sc} at $J(V = 0\ \text{V})$ and the fill factors $FF = (V_{\text{mpp}} \cdot J_{\text{mpp}})/(V_{\text{oc}} \cdot J_{\text{sc}})$, where V_{mpp} and J_{mpp} denote the voltage and current density at the maximum power point. The solar energy conversion efficiency η is defined as the ratio between the maximum power ($P_{\text{mpp}} = V_{\text{mpp}} \cdot J_{\text{mpp}} = V_{\text{oc}} \cdot J_{\text{sc}} \cdot FF$) and the power of the sun simulator ($P_{\text{solar}} = 100\ \text{mW/cm}^2$). The slopes of the JV characteristic under illumination at J_{sc} and V_{oc} are a measure for the shunt (R_{sh}) and series resistance (R_{s}), respectively. Ref. [69] is recommended for further readings.

Quantum efficiency The spectrally resolved quantum efficiency provides detailed insight into the optical absorption and carrier extraction in solar cells. The External Quantum Efficiency (EQE) is defined as the ratio between the number of charge carriers collected by the solar cell and the number of photons falling vertically on a solar cell area for each wavelength. Unlike the EQE, the Internal Quantum Efficiency (IQE) $IQE = EQE/(1-R)$ excludes optical loss arising from cell reflectance allowing the independent observation of losses within the solar cell. The comparison between EQE measure at the bias voltage of 0 V and that under reverse bias separates to some extend electrical losses from optical losses, since a reverse bias reduces the charge carrier recombination due to enhanced internal electrical field and, thus, increases the charge carrier collection. A detailed description of the setup is given in Ref. [104].

Capacitance Voltage Measurement (CV) The CV measurement is a common technique for characterizing a wide range of semiconductor materials and devices. The procedure for taking CV measurements involves the application of DC bias voltage across the capacitor while making the measurement with an AC signal. In this work, the voltage dependent capacitance $C(V)$ of the SHJ solar cells were determined at an excitation frequency $f = 100$ kHz using a HP 4284A Precision LCR Meter. The acceptor base doping concentration N_{A} of the used Si wafer was extracted from the Mott-Schottky-plot by reading the slope of the linear range. This method is explained in Ref. [103] in more detail.

4. Silicon carbide layers in silicon quantum dot superlattices

This chapter focuses on the fabrication and characterization of SiC containing Si-QD absorbers for implementation in, e.g., all-silicon tandem solar cells. In particular, the applicability of SiC material as barrier layer in SiC/SiO_x HSL structure was investigated. The first section revises the reported technical difficulties of Si-QD formation in SiC matrix and their theoretical impact on quantum confinement. Based on these considerations, the novel SiC/SiO_x hetero-superlattice approach as an alternative candidate for high quality Si-QD absorber was introduced and motivated. The second section reviews the development of SiC and SiO_x single layers with specific consideration on the process and material compatibility during later HSL fabrication. The third section analyses the structural and optical properties of HSL layers with varying SiC thicknesses, SiO_x thicknesses and SiO_x compositions. In the last section, the investigation of the formation of annealing-induced defects in SiC and SiO_x materials and their multilayer systems is presented.

4.1. Feasibility of Si-QD absorber using silicon carbide matrix

The high-temperature approach to realize Si-QDs embedded in an ideally stoichiometric SiC matrix presumes the decomposition of silicon-rich carbide (SRC) as well as the crystallization of Si precipitates upon annealing [105]. Even though these thermally activated processes seem to progress easily in silicon-rich oxide (SRO) materials [10], they have to be reappraised in the case of SRC, which is, despite the

similarity of being a Si alloy, a completely different material with different micro structure and bonding configurations than SRO. This section first targets this issue by investigating the Si crystallization process in SRC layers with varying Si excess. Then, theoretical limitations of Si-QD absorbers with SiC as matrix material are discussed in addition to the experimental evaluations. In the last part, the novel SiC/SiO_x hetero-superlattice approach is introduced and motivated.

4.1.1. Crystal formation in SiC matrix

As-deposited SiC single layers

The a-SiC:H samples were fabricated in a multi-chamber deposition system built by MRG Inc.. It contains three PECVD chambers, one Hot-Wire Chemical Vapor Deposition (HWCVD) chamber and one load lock chamber mounted around the robot chamber. Details on the systems were introduced elsewhere [106]. In particular, the PECVD chamber usually utilized to deposit p-type material was used for a-SiC:H growth. This chamber provides the required precursor gases monomethylsilane (MMS) H_3SiCH_3, silane SiH_4 and hydrogen H_2. The development of a-SiC:H material is presented in Sec. 4.2.1. In order to investigate the Si crystallization process in SRC layers with varying Si excess, single layers were prepared under different SiH_4 gas flow ratio r_{SiH_4} (100 %, 80 %, 60 %, 40 %, 20 % and 0 %), which is defined as the ratio between SiH_4 gas flow rate f_{SiH_4} and the sum of MMS and SiH_4 gas flow rate $f_{MMS} + f_{SiH_4}$. Other deposition parameters can be found in Sec. 4.3.2. The RBS carbon content c_C of these SRC samples were 0 %, 3 %, 11.5 %, 23.1 %, 33.3 % and 41.2 %, respectively.

Figure 4.1 displays the FTIR absorption coefficient plotted versus the wave number k for the as-grown SRC samples of different c_C. The peak positions of the Si-C, Si-H and C-H stretching (S) and bending (B) vibration modes according to Ref. [107] are indicated. While the a-Si:H reference sample with $c_C = 0$ % shows Si-H vibration-related absorption only, the Si-C (S) signal rising with increasing c_C denotes an increase of Si-C bond density. The increase of Si-H (S) and C-H (S) absorption indicates a higher amount of incorporated hydrogen with increasing c_C. At the same time, the Si-H (S) peak position shifts continuiously to higher wave

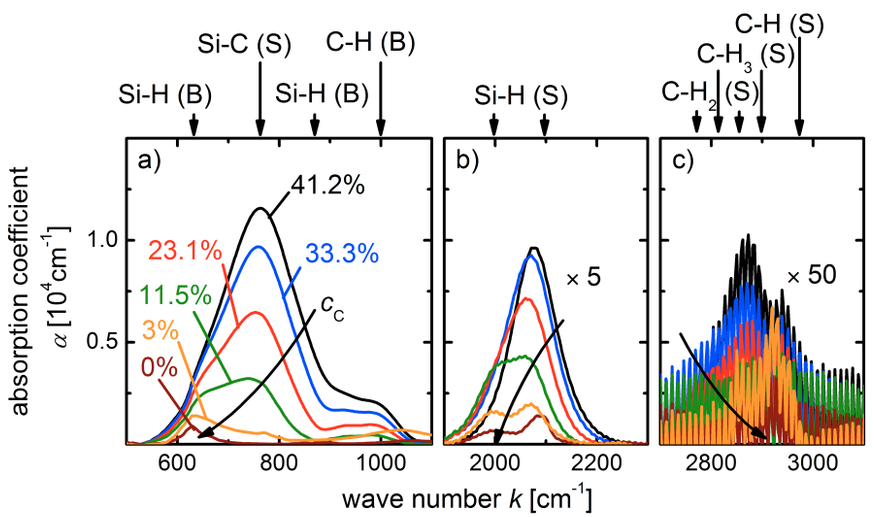

Figure 4.1.: *FTIR absorption coefficient versus the wave number k for the as-grown SRC samples of different c_C. The peak positions of the Si-C, Si-H and C-H stretching (S) and bending (B) vibration modes are indicated according to Ref. [107]. The Si-C (S) signal rising with increasing c_C denotes an increase of Si-C bond density. The increase of Si-H (S) and C-H (S) absorption indicates a higher amount of incorporated hydrogen with increasing c_C.*

number due to back bonded carbon at the Si site [108]. Thus, SRC materials with different compositions were successfully fabricatd by the variation of $r_{\mathrm{SiH_4}}$.

Crystal formation during annealing

After deposition, the SRC samples were annealed at 950 °C or 1050 °C each for 1 h (Sec. 4.2.4) and characterized with GIXRD measurements together with the as-deposited samples. Figure 4.2 shows the GIXRD pattern (symbol) as well as the deconvolution (lines) of the $c_{\mathrm{C}} = 23.1$ % sample after annealing at 1050 °C. The signals centered around the diffraction angles $2\theta = 35.4$ °, 60.0 ° and 71.8 ° are assigned to (111), (220) and (311) oriented cubic SiC crystals, respectively, whereas the reflexes appearing around $2\theta = 28.5$ °, 47.6 ° and 56.3 ° are ascribed to (111),

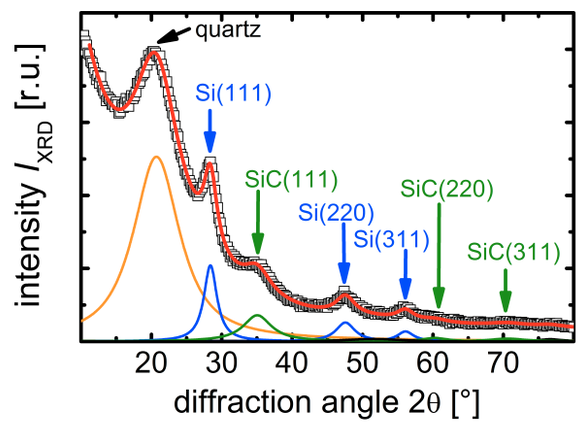

Figure 4.2.: *Measured GIXRD pattern (symbol) and the deconvolution (lines) of the* $c_C = 23.1$ *% sample after annealing at* 1050 °C. *The signals centered around* $2\theta = 35.4$ °, 60.0 ° *and* 71.8 ° *are assigned to (111), (220) and (311) oriented cubic SiC crystals. The reflexes appearing around* $2\theta = 28.5$ °, 47.6 ° *and* 56.3 ° *are ascribed to (111), (220) and (311) oriented Si crystals. From the integrated intensity ratio* $I_{c\text{-}Si}/I_{total}$ *and* $I_{c\text{-}SiC}/I_{total}$, *the c-Si and c-SiC volume fractions* $f_{c\text{-}Si}$ *and* $f_{c\text{-}SiC}$ *could be estimated. The coherence lengths of SiC and Si crystals could be determined from the corresponding (111) diffraction peaks using the Scherrer formula (Eq. 4.1).*

(220) and (311) oriented Si crystals, respectively [29]. The pronounced peak centered at 21.0 ° originates from the amorphous quartz substrate. For the sake of clarity, the much weaker and broader amorphous Si and SiC signals are not included in Fig. 4.2. The GIXRD patterns could be fitted without taking into account contributions from a graphitic phase.

The c-Si and c-SiC volume fractions $f_{\text{c-Si}}$ and $f_{\text{c-SiC}}$ could be estimated from the integrated intensity ratio $I_{\text{c-Si}}/I_{\text{total}}$ and $I_{\text{c-SiC}}/I_{\text{total}}$, respectively, where I_{total} is the sum of the integrated intensities from a-Si, c-Si, a-SiC and c-SiC peaks. The coherence lengths of SiC and Si crystals, which roughly indicate their average crystal sizes $d_{\text{c-Si}}$ and $d_{\text{c-SiC}}$, were determined from the corresponding (111) diffraction peaks using the Scherrer formula

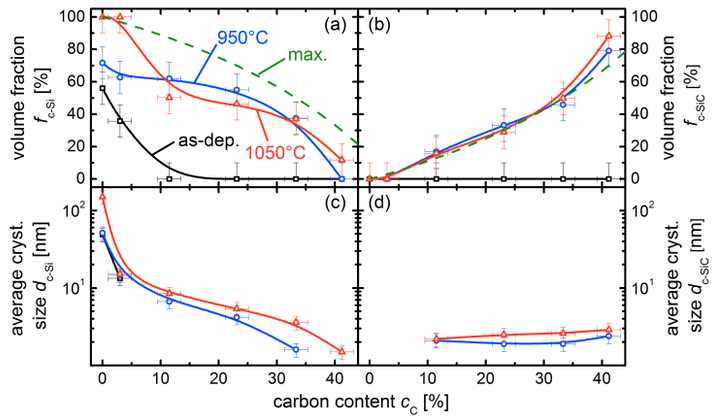

Figure 4.3.: *Volume fractions (a) $f_{c\text{-}Si}$ and (b) $f_{c\text{-}SiC}$ as well as the average crystal sizes (c) $d_{c\text{-}Si}$ and (d) $d_{c\text{-}SiC}$ versus carbon content c_C for SRC samples before and after annealing. The dashed lines in (a,b) represent the theoretical maximum of $f_{c\text{-}Si}$ and $f_{c\text{-}SiC}$ at a given c_C assuming completed phase separation and crystallization. An upper limit of Si crystallization below the theoretical maximum due to carbon-related inhibition of Si crystal formation is suggested, whereas phase separation and SiC crystallization seem to be completed already at* 950 °C.

$$d = 57.3 \frac{k\lambda}{w \cos(\theta)} \tag{4.1}$$

neglecting strain effects [30]. In Eq. 4.1, k is a geometry factor which is usually set to 0.9 for SiC and Si nanocrystals [94, 109], λ is the wavelength of the used x-ray radiation (0.154 nm) and w is the full width at half maximum of the (111) reflexes, which was corrected by the instrumental broadening [110]. θ is the single diffraction angle of the (111) peak position and 57.3 is the angle conversion factor from radian to degree.

Figure 4.3 presents the volume fractions $f_{\text{c-Si}}$ and $f_{\text{c-SiC}}$ as well as the average crystal sizes $d_{\text{c-Si}}$ and $d_{\text{c-SiC}}$ plotted versus carbon content c_{C} for SRC samples before and after annealing. The dashed lines represent the theoretical maximum of $f_{\text{c-Si}}$ and $f_{\text{c-SiC}}$ at a given c_{C} assuming completed phase separation and crystallization.

Prior to the annealing, the SRC layers consist of amorphous phase only except for the two samples with lowest c_C, which additionally exhibit a remarkable amount of c-Si phase. This decrease of $f_{c\text{-}Si}$ with increasing c_C was also observed in Ref. [34], where the composition variation was generated by changing the hydrogen dilution. Hence, the inhibition of Si crystal growth from the gas phase is likely linked to the incorporation of carbon.

The $f_{c\text{-}SiC}$ values of samples annealed at 1050 °C were comparable with those annealed at 950 °C both showing excellent correlation with the theoretical maximum. This correlation strongly suggests a complete phase separation and SiC crystallization already at 950 °C. This agrees with the observation that stoichiometric SiC is either amorphous or fully crystalline, as a clear mixture of both phases could not be identified [111]. The increase of $f_{c\text{-}SiC}$ with higher c_C is then simply due to a higher amount of C atoms that allows for the formation of SiC.

On the contrary, the theoretical $f_{c\text{-}Si}$ maximum was only reached by the c_C = 0 % and 3 % samples that were annealed at 1050 °C. Thus, the Si crystallization in all other samples might be unfinished, since phase separation is assumed to be completed at these temperatures (see above). In other words, the phase separation is unlikely the limiting factor for the formation of Si-NCs in SRC. In addition, the $f_{c\text{-}Si}$ does not increase further by annealing at 1050 °C as compared to 950 °C for $c_C \geq 11.5$ %, which might indicate an upper limit of Si crystallization below the theoretical maximum due to carbon-related inhibition of Si crystal formation. A certain volume fraction of a-Si phase, which is represented by the difference between $f_{c\text{-}Si}$ and the corresponding theoretical maximum, seems unavoidable at the presence of more than 3 % C in the material. This statement, however, should be verfied by annealing SRC samples at even higher temperatures, which was not carried out in this work due to the limitation of the annealing temperature to 1050 °C (Sec. 4.2.4). One reasonable configuration to explain the incomplete crystallization would be the surrounding of Si-NC by an a-Si phase that was not able to fully crystallize due to influences from adjacent SiC matrix. In this case, the quantum confinement is expected to be weak due to the low band offset between c-Si and a-Si.

The Si-NC size (Fig. 4.3(c)) decreases significantly with increasing c_C for both as-deposited and annealed samples. From c_C = 0 % to 41.2 %, the $d_{c\text{-}Si}$ of, e.g.,

the 1050 °C samples decreased by two orders of magnitude. As the temperature increases from 950 °C to 1050 °C, larger Si-NCs were formed irrespective of the carbon content. Since the $f_{\text{c-Si}}$ did not increase at the same time, a lower density of these larger Si-NCs is expected, which might be a consequence of higher diffusion coefficient at higher temperature giving rise to larger but less Si agglomerates. At $c_{\text{C}} = 41.2$ % and 33.3 %, the Si-NC size was constrained to $d_{\text{Si}} = 1.5$ nm and 3.6 nm after annealing at the highest available annealing temperature of 1050 °C. Thus, it might be challenging to tune the Si-QD size in SRC/SiC superlattices by defining the SRC layer thickness larger than 1.5 nm and 3.6 nm, if SRC material with $c_{\text{C}} =$ 41.2 % and 33.3 % were used, respectively. On the contrary, lateral growth of Si-QDs within the SRC layers despite vertically constrained dot size by the SRC layer thickness might occur for SRC with low carbon content. The SiC-NC size (Fig. 4.3(d)) remained almost constant at 1.9 nm − 2.9 nm. Thus, the crystalline matrix consists of many small crystallites of different orientations at the Si-QDs interface, where barrier height fluctuation may occur that can negatively affect the mini-band formation and thus its carrier transport properties.

4.1.2. Theoretical considerations

Estimation of matrix composition and band gap

Despite the above mentioned technical obstacles in realizing Si-QD absorbers based on SRC/SiC superlattices, an theoretical estimation of the quantum confinement was performed on the basis of the assumptions illustrated in Fig. 4.4(a). It considers the decomposition of an as-deposited SRC layer with a homogeneously distributed carbon content $c_{\text{C,initial}}$ into perfectly spherical, periodically aligned Si-QDs and amorphous matrix with a homogeneously distributed carbon content $c_{\text{C,matrix}}$ (no c-SiC or a-Si phases). The Si-QD size d_{dot} is determined by the SRC layer thickness assuming the stoichiometric SiC layers as perfect Si crystallization stop. Different possible sets of d_{dot} and Si-QD spacing d_{sp} give different Si-QD volume ratios, which determines the $c_{\text{C,matrix}}$ of the matrix for a given $c_{\text{C,initial}}$ (see below). An unit cell used for calculations is highlighted by the red rectangle. The $c_{\text{C,matrix}}$ was translated into a band gap E_{g} of the matrix (see below). From d_{sp}, d_{dot} and E_{g}, the effective

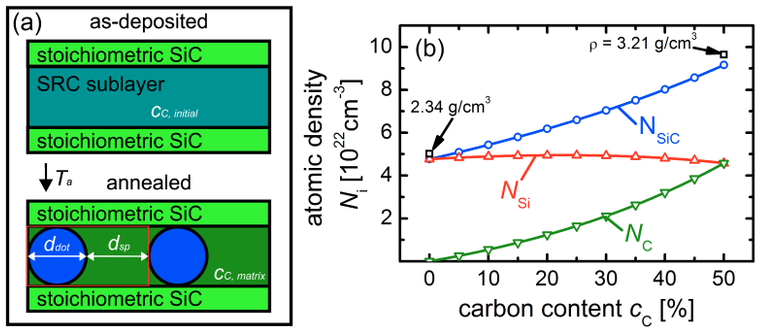

Figure 4.4.: *(a) Schematic drawing of the decomposition of an as-deposited SRC layer with a homogeneously distributed carbon content $c_{C,initial}$ into perfectly spherical, periodically aligned Si-QDs and amorphous matrix with a homogeneously distributed carbon content $c_{C,matrix}$. It is assumed that c-SiC or a-Si phases are not formed during the annealing. (b) Atomic density N_i versus the carbon content c_C, where N_{SiC}, N_{Si} and N_C denote the atomic density of Si+C, Si and C elements, respectively. The atomic density of crystalline Si and crystalline SiC were derived from the corresponding mass densities ρ of* 2.34 g/cm^3 *and* 3.21 g/cm^3*, respectively.*

band gap energy $E_{\mathrm{g,eff}}$ of the Si-QDs was calculated using a theoretical model (see below).

The composition of the matrix can be derived from the number of Si and C atoms within the unit cell before annealing and the consumption of Si atoms by Si-QD formation as well as the left-over of Si atoms in the matrix after annealing. The calculation of Si and C atoms in different phases requires information on the atomic densities of these phases. Figure 4.4(b) shows the atomic density N_{i} plotted versus the carbon content c_{C}. The atomic density of crystalline Si (5.0×10^{22} cm^{-3}) and crystalline SiC (9.6×10^{22} cm^{-3}) were derived from the corresponding mass densities ρ of 2.34 g/cm^3 and 3.21 g/cm^3, respectively. The ρ_{SiC} and consequently the N_{SiC} of amorphous SiC layers was obtained by assuming a mass density that linearly increases with c_{C} and is 5 % lower than in ordered crystalline materials [112]. With N_{SiC} provided, the individual Si and C atomic densities N_{Si} and N_{C} could be determined from the c_{C} values. Figure 4.5 summarizes the calculated $c_{\mathrm{C,matrix}}$ as a function of d_{sp} and d_{dot} for various initial carbon contents $c_{\mathrm{C,initial}}$ in form of contour

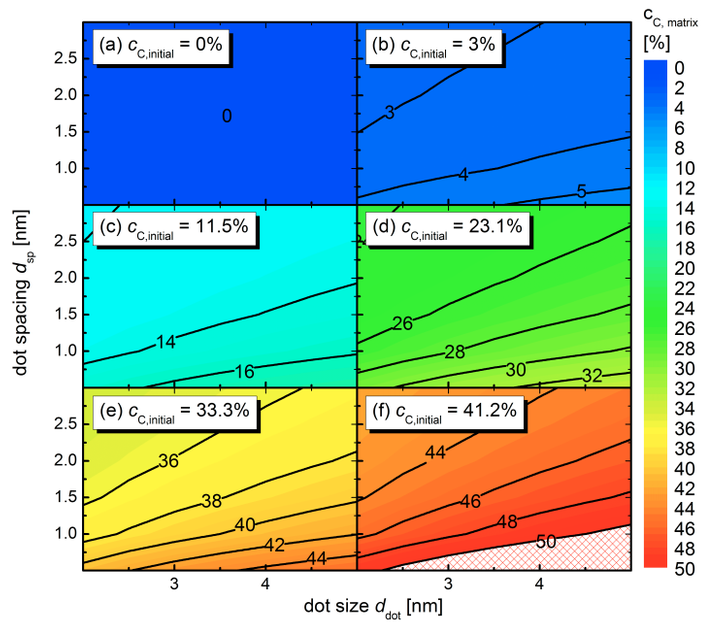

Figure 4.5.: *Calculated $c_{C,matrix}$ as a function of d_{sp} and d_{dot} for various initial carbon contents $c_{C,initial}$ in form of contour maps. Matrix carbon content values above 50 % (shaded area in (f)) are not considered.*

maps. For example, the consumption of excess Si to form Si-QDs is higher for a larger Si-QD volume ratio (large d_{dot} and small d_{sp}) giving rise to higher carbon concentration of the matrix, and vice versa. Matrix carbon content values above 50 % (shaded area in Fig. 4.5(f)) are not considered in this work.

Figure 4.6 shows the band gap energy E_{g} as a function of the carbon content c_{C} in the material, compiled from several publications. The open symbols represent experimentally obtained E_{g} values of hydrogenated a-SiC:H material from Ref. [114–116]. The authors used the E_{04} gap, defined as the energy with an absorption coefficient $\alpha = 10^4$ cm^{-1}, as a measure for the band gap energy. In all three publications, the E_{04} increases with increasing c_{C}, which is due to the replacement of Si-Si bonds with the stronger Si-C bonds according to Ref. [113]. The discrepancy in the slope of the increase is attributed to the variable ratios of sp^2

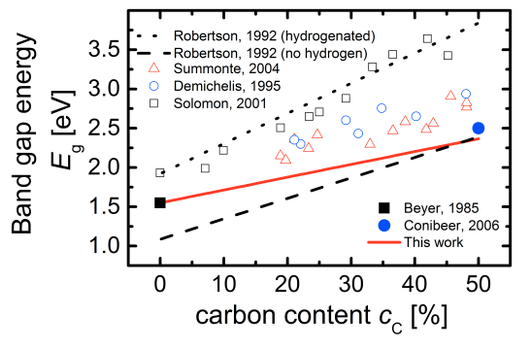

Figure 4.6.: *Band gap energy E_g as a function of the carbon content c_C in the material, compiled from several publications. The theoretical E_g values of a-SiC material with (dotted line) and without (dashed line) hydrogen incorporation were obtained by using the tight-binding method [113]. This work regards the averaged $E_{04}(c_C)$ values from Ref. [114–116] (open symbol) as the band gap energies of hydrogenated SiC material, on which basis a reduction of E_g by 18 % after complete dehydrogenation was assumed for the entire composition range (continuous line). The factor 18 % was derived from Ref. [117] (filled square) for a-Si:H. The stoichiometric a-SiC E_g value used by Conibeer et al. [2] is included for comparison.*

(graphite-like) and sp^3 (diamond-like) local structure of carbon [114]. A higher amount of sp^3 bonds tends to give a wider gap in spite of comparable total carbon content. Robertson [113] calculated the theoretical E_g values of sp^2-free a-SiC material with (dotted line) and without (dashed line) hydrogen incorporation using the tight-binding method. The hydrogen widens the E_g over the entire composition range by a recession of the valence band, known as the hydrogen chemical alloying effect (Sec. 4.3.2). The increase of E_g upon hydrogenation is more pronounced for a-SiC:H with higher c_C because of its larger H content [118]. Beyer et al. [117] also reported on the reduction of E_{04} with annealing-induced dehydrogenation in a-Si:H materials, reaching a E_{04} value of 1.55 eV at 0 % hydrogen (filled square), which is however higher than that determined by tight-binding [113]. Thus, the network structure after dehydrogenation via thermal annealing might be less ordered than assumed in the tight-binding model for hydrogen-free a-SiC material.

This work regards the averaged $E_{04}(c_C)$ values from Ref. [114–116] as the

band gap energies of hydrogenated SiC material, on which basis a reduction of E_g by 18 % after complete dehydrogenation was assumed for the entire composition range (continuous line). Hydrogen effusion due to the high-temperature annealing step required for the Si-QD formation is discussed in Sec. 4.4.2. The factor 18 % was derived from Ref. [117] for a-Si:H. Applying this factor to a-SiC:H is justfied by the aforementioned statement that hydrogen has a more pronounced effect on E_g in a-SiC:H with higher c_C because of larger H incorporation. It is interesting to note that the obtained E_g as a function of c_C is in excellent agreement with the empirical equation $E_g(c_C) = E_g(0) + 1.68 c_C$ proposed by Ref. [119]. In addition, the stoichiometric a-SiC E_g value used by Conibeer et al. [2] is included for comparison. From the obtained curve, the band gap energy E_g of the matrix was extracted for each given $c_{C,matrix}$.

Estimation of Si-QD effective band gap

The effective band gap energy $E_{g,eff}$ was calculated by solving the effective mass equation (Sec. 2.1) using the three-dimensional superposition of the one-dimensional Kronig-Penny model [8, 120]. In the lateral two dimensions, where the Si-QDs are surrounded by the amorphous matrix, a band gap E_g corresponding to the $c_{C,matrix}$ (Fig. 4.6) were taken into account. In the vertical one dimension, a 2 nm thick stoichiometric a-SiC barrier layer was applied providing a E_g of 2.4 eV (Fig. 4.6). In all three dimensions, symmetrical conduction and valence band offsets towards the band gap of Si-QD (1.1 eV) were assumed. Figure 4.7 displays the contour map of $E_{g,eff}$ plotted versus d_{dot} and d_{sp} for various $c_{C,initial}$. In general, $E_{g,eff}$ decreases with larger d_{dot} and smaller d_{sp} due weaker quantum confinement [121]. The Si-QD size has a more significant impact on $E_{g,eff}$ than the Si-QD spacing. Especially at large d_{sp}, the cross-talk between the wavefunctions of adjacent Si-QDs is negligibly small and, thus does not affect the quantum confinement.

The deterioration of $E_{g,eff}$ with increasing d_{dot} and decreasing d_{sp} dominates over the expected increase of $E_{g,eff}$ with rising $c_{C,matrix}$ and therefore E_g of the matrix at larger d_{dot} and smaller d_{sp} (Fig. 4.5). Nevertheless, the comparison between different $c_{C,initial}$ scenarios shows an increase of E_g for higher $c_{C,initial}$ values. The aspired $E_{g,eff} \approx 1.8$ eV (Sec. 2.1) is theoretically achievable only for $c_{C,initial} = 41.2$ %,

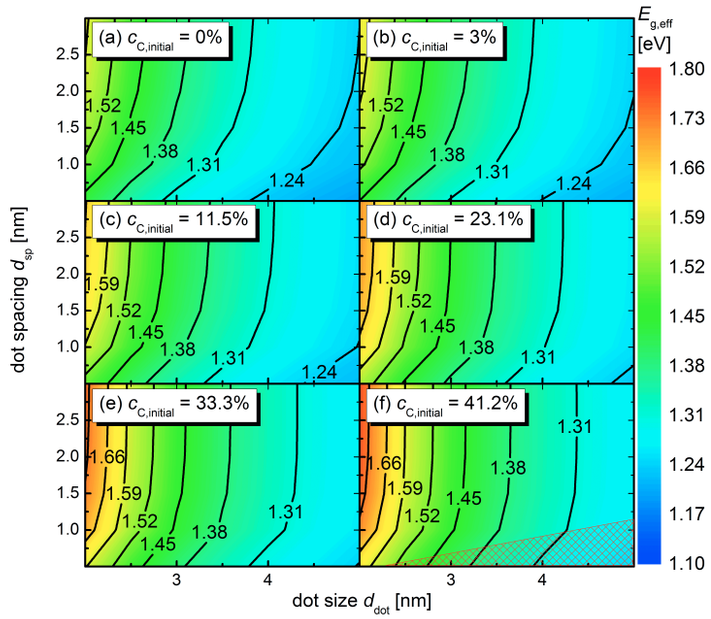

Figure 4.7.: *Contour map of effective band gap energy $E_{g,eff}$ plotted versus d_{dot} and d_{sp} for various $c_{C,initial}$. The $E_{g,eff}$ was calculated by solving the effective mass equation using the three-dimensional superposition of the one-dimensional Kronig-Penny model [8, 120]. In general, $E_{g,eff}$ decreases with larger d_{dot} and smaller d_{sp} due weaker quantum confinement [121]. The conflict between high quantum confinement (small d_{dot} and large d_{sp}) and sufficient Si-QD density (large d_{dot} and small d_{sp}) makes it impossible to produce usable Si-QD absorber material with $E_{g,eff} \approx 1.8$ eV with SiC matrix.*

$d_{\mathrm{dot}} = 2$ nm and $d_{\mathrm{sp}} \geq 2$ nm. Si-QD sizes smaller than 2 nm were not taken into account not only because of deficient reliability of the underlying effective mass approach for such small Si-QDs [121], but also due to technical difficulties in precise controlling of the SRC layer thicknesses below 2 nm. However, the determining drawback of the combination of small d_{dot} and large d_{sp} is the very low density of Si-QDs in the material, which is unsuitable for application as a absorber material. For example, while the Si-NC volume fraction is 39 % for $d_{\mathrm{dot}} = 5$ nm and $d_{\mathrm{sp}} = 0.5$ nm, it decreases to 3 % for $d_{\mathrm{dot}} = 2$ nm and $d_{\mathrm{sp}} = 3$ nm. Thus, the conflict between quantum confinement and Si-QD density makes it impossible to produce usable Si-

QD absorber material with $E_{g,eff} \approx 1.8$ eV with SiC matrix. A further increase of $c_{C,initial}$ would shift d_{dot} and d_{sp} that are required to realize $E_{g,eff} \approx 1.8$ eV to smaller values and thus provide a better compromise between quantum confinement and Si-QD density. However, it is not possible to produce sufficiently large Si-QDs with small spacing at higher $c_{C,initial}$ due to the lack of Si excess, if the carbon content of the matrix does not exceed 50 %. In other words, the extension of the shaded area (Fig. 4.7(f)) will become another decisive limitation at $c_{C,initial}$ approaching 50 %. It is important to stress that the situation is considerably relaxed in the case of silicon oxide matrix material due to its significantly higher E_g and therefore higher band offsets towards Si than silicon carbide (Sec. 4.3.2).

4.1.3. Introducing SiC/SiO_x hetero-superlattice

Motivation of the HSL approach

Due to the competing nature of charge carrier confinement requiring high band offset and charge carrier transport demanding low band offset between Si-QDs and the embedding material, the choice of different materials for matrix and barrier is indicated. This work introduces the novel SiC/SiO_x HSL with near-stoichiometric SiC as vertical barrier layer and silicon-rich SiO_x as lateral matrix layer for the quantum dot formation. The SiO_x is considered a promising matrix due to the thermodynamically favored phase separation into Si and SiO_2 [122], the high persistence of the amorphous SiO_2 phase at high temperatures [123], the pronounced band offset giving rise to high quantum confinement [121] and the excellent Si/SiO_2 interface quality [22]. The SiC with low band gap should lead to low band offset between Si and SiC and thus give rise to high tunnel probability and easy carrier transport. Figure 4.8(a) illustrates this idea of having Si-QDs surrounded by SiO_2 laterally in 2D and separated by SiC in the vertical 1D direction. Correspondingly, Fig. 4.8(b-d) visualize simulated Si-QD electron wavefunctions (lowest three orders) that solely extend into the adjacent SiC layers as a consequence of good confinement with silicon oxide and low barrier towards silicon carbide. In Si-QD superlattice, the overlap of the Si-QD electron wavefunctions within the SiC layers will form mini-bands as new transport path [8].

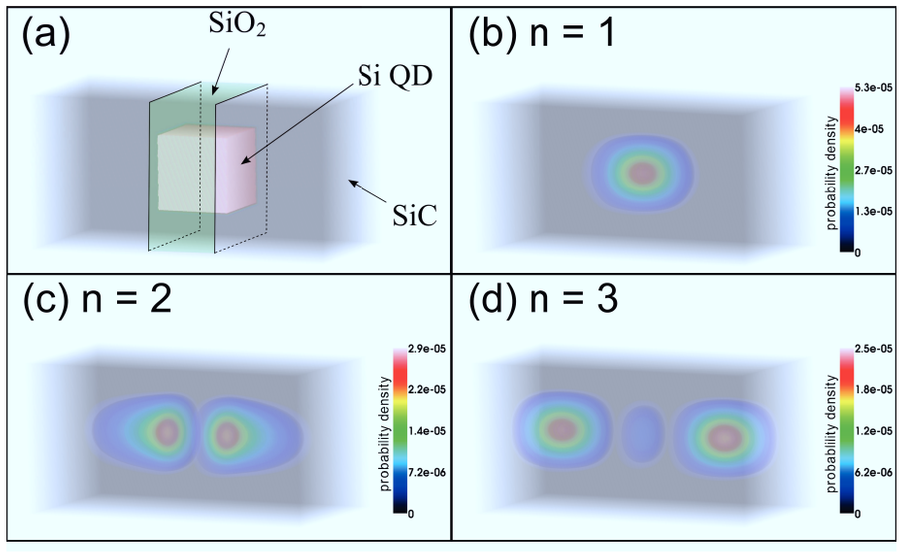

Figure 4.8.: *(a) Schematic illustration of Si-QDs surrounded by SiO_2 laterally in 2D and separated by SiC in the vertical 1D direction. (b-d) Visualization of simulated Si-QD electron wavefunctions (lowest three orders) that only extend into the adjacent SiC layers as a consequence of good confinement with silicon oxide and low barrier towards silicon carbide. In Si-QD superlattice, the overlap of the Si-QD electron wavefunctions within the SiC layers will form mini-bands as new transport path [8].*

Processing the HSL structure

Figure 4.9 shows the schematic drawing of as-deposited, high-temperature annealed and hydrogen passivated SiC/SiO_x HSL structures. The SiC/SiO_x multilayer can be realized by the alternating deposition of a-SiC:H and a-SiO_x:H thin layers using PECVD for low-cost production on top of crystalline Si or amorphous quartz substrates. The precise control of the sublayer thicknesses and compositions is technically challenging and has to be monitored carefully (Sec. 4.2). During the high-temperature annealing, phase separation of SiO_x should result in Si-QDs laterally surrounded by a SiO_2 matrix. Experiments should clarify whether the SiC sublayers can fulfill their function as a stop for Si crystallization from the SiO_x sublayers (Sec. 4.3). Nevertheless, the crystallization of SiC upon annealing should be less critical

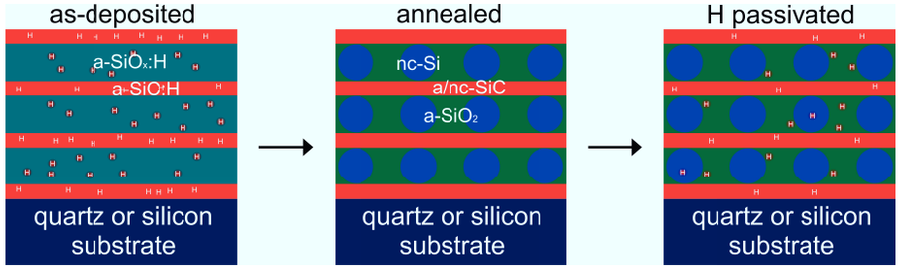

Figure 4.9.: *Schematic drawing of as-deposited, high-temperature annealed and hydrogen passivated SiC/SiO_x HSL structures. The alternating a-SiC:H and a-SiO_x:H thin layers were deposited onto crystalline Si or amorphous quartz substrates using PECVD for low-cost production. During the high-temperature annealing, phase separation of SiO_x should result in Si-QDs laterally surrounded by a SiO_2 matrix. Hydrogen reincorporation is necessary to passivate defects that were activated due to the escape of hydrogen during annealing.*

for the Si-QDs, since the Si/SiC contact area is rather limited. Experiments should also clarify whether the increase in dark conductivity [37] is related to defects that were activated due to the escape of hydrogen from the material during annealing and whether a post-annealing hydrogen reincorporation procedure can passivate these defects (Sec. 4.4).

4.2. Process and material development for SiC/SiO_x HSL

This section reviews the development of a-SiC:H and a-SiO_x:H single layers designed for HSL application. The focus lies on the critical requirements for these layers from the technical point of view, which include, e.g., the precise control of thickness and composition during deposition. The first part deals with the deposition parameter adjustment for homogeneous and low rate growth of high quality a-SiC:H material. Then, the a-SiO_x:H layers were checked before and after annealing for their compositional properties in as-grown states and the Si-NC formation behavior upon annealing. In addition, an automatic deposition sequence was adapted for the sake

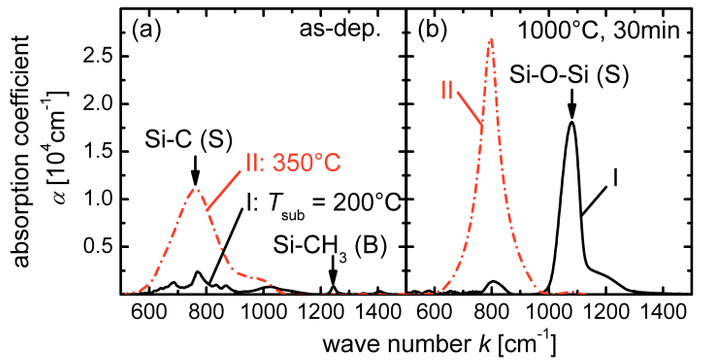

Figure 4.10.: *FTIR results of two of the first a-SiC:H single layers on c-Si substrates (a) before and (b) after annealing at* 1000 °C *for* 30 min *under* N_2 *gas flow. The samples I and II were deposited at a substrate temperature* T_{sub} *of* 200 °C *and* 350 °C*, respectively. The presence of the Si-*CH_3 *(B) vibration peak centered at* $\lambda = 1245$ nm *[119] accompanied by a weak Si-C (S) peak intensity indicates a preferable incorporation of* CH_3*, which is known to result in highly disordered and void-rich a-SiC:H materials [124]. The appearance of a dominant Si-O-Si (S) vibration peak centered at* $\lambda = 1080$ nm *[125] suggests an strong Si oxidation during the thermal treatment, which is in agreement with the idea of a porous material structure.*

of good reproducibility and low expenditure of human labor. The last part describes the optimization of the annealing procedure in the course of this work.

4.2.1. Deposition of a-SiC:H single layers

High quality a-SiC:H material

The first step aims at the development of high quality, near-stoichiometric a-SiC:H material. Since Si-C bonds already exist in the MMS molecule, the formation of stoichiometric a-SiC:H is expected to be easier using MMS than a mixture of SiH_4 and methane CH_4 [126]. The SiH_4 precursor gas was not needed for near-stoichiometric a-SiC:H growth. Figure 4.10 shows the FTIR results of two of the first a-SiC:H single layers on c-Si substrates before and after annealing at 1000 °C for 30 min under N_2 gas flow. The sample I was deposited at a power density P of 13.3 mW/cm^2,

a plasma frequency f of 13.56 MHz, a deposition pressure p of 5.00 mbar, a substrate temperature T_{sub} of 200 °C, an electrode spacing d_{ele} of 12 mm, a MMS gas flow f_{MMS} of 4.5 sccm and a H_2 gas flow of 85.5 sccm. In the as-deposited state, the presence of the Si-CH_3 (B) vibration peak centered at $\lambda = 1245$ nm [119] accompanied by a weak Si-C (S) peak intensity indicates a preferable incorporation of monomethyl CH_3, which is known to result in highly disordered and void-rich a-SiC:H materials [124]. After annealing, the appearance of a dominant Si-O-Si (S) vibration peak centered at $\lambda = 1080$ nm [125] suggests an strong Si oxidation during the thermal treatment, which is in agreement with the idea of an porous material structure. Individually varying the power density, deposition pressure, electrode spacing, H_2 gas flow and plasma frequency only results in minor change in CH_3 incorporation during deposition and SiO formation during annealing. Solely with the increase of T_{sub} of 200 °C to 350 °C (sample II), a pronounced increase of the Si-C (S) intensity and the disappearance of the Si-CH_3 (B) peak were observed before annealing. More importantly, the Si-O-Si (S) peak intensity remained on a negligible level upon annealing. Thus, the substrate temperature is a key parameter to produce more ordered and dense a-SiC:H material with more Si-C bonds and less H incorporation. This might be due to the higher energy provided by the higher substrate temperature that enhances the probability of dissociating C-H bonds by forming gaseous H_2 molecules on the surface.

Homogeneity and deposition rate

Thickness homogeneity on 10 cm $\times$ 10cm glass substrate was investigated as well, which is a crucial prerequisite to evaluate experimental results of HSL samples. The linking of different measurements carried out on specimen cut out from different spots of the same sample is only valid if the individual layers of the multilayer stack have excellent thickness homogeneity, especially when the thicknesses are in the range of a few nanometers and their deviation affects the final results as in the case of Si-QD absorber. The combination of $p = 0.25$ mbar, $d_{\mathrm{ele}} = 16$ mm and $f = 81.40$ MHz achieved the best thickness homogeneity with a deviation below ± 0.5 %. In addition, the Very High Frequency (VHF) mode was found to yield a more stable plasma than the Radio Frequency (RF) mode presumably due to the

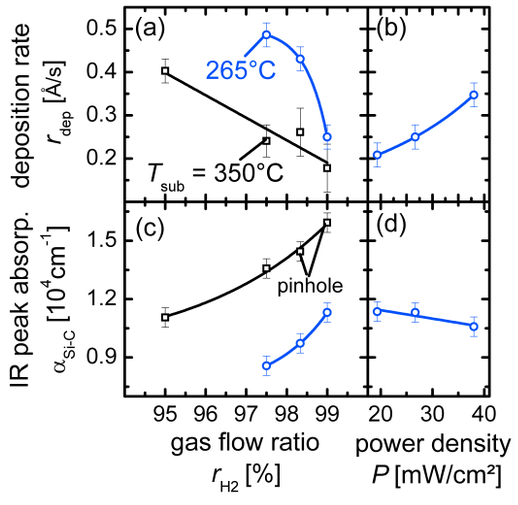

Figure 4.11.: *(a,b) Deposition rate r_{dep} and (c,d) IR peak absorption of the Si-C (S) vibration mode $\alpha_{Si\text{-}C}$ plotted versus the H_2 gas flow ratio r_{H_2} and/or the power density P for two a-SiC:H series deposited at $T_{sub} = 265$ °C and 350 °C. The optimum combination of p, d_{ele} and f was applied to these samples. During the r_{H_2} variation, the P was kept constant at 26.6 mW/cm^2, while the r_{H_2} was kept constant at 99 % during the P variation. Pinholes were observed on a-SiC:H samples of the $T_{sub} = 350$ °C series for $r_{H_2} > 97.5$ %.*

higher degree of gas ionization in the former.

Besides a dense material and a laterally homogeneous deposition, a lowest possible deposition rate r_{dep} is mandatory for a precise thickness control of the very thin individual layers in HSL. Figure 4.11 displays the r_{dep} and the IR peak absorption of the Si-C (S) vibration mode $\alpha_{\mathrm{Si\text{-}C}}$ plotted versus the H_2 gas flow ratio $r_{\mathrm{H_2}}$ and/or P for two a-SiC:H series deposited at $T_{\mathrm{sub}} = 265$ °C and 350 °C. The aforementioned optimum combination of p, d_{ele} and f was applied to these samples. During the $r_{\mathrm{H_2}}$ variation, the P was kept constant at 26.6 mW/cm^2, while the $r_{\mathrm{H_2}}$ was kept constant at 99 % during the P variation. The $r_{\mathrm{H_2}}$ is defined as the ratio between $f_{\mathrm{H_2}}$ and the total gas flow rate f_{total}. Since all samples from the 350 °C series had a comparable carbon content c_{C} of around 45 % according to RBS measurements, the pronounced variation of their $\alpha_{\mathrm{Si\text{-}C}}$ cannot be attributed

to an increase of the total amount of carbon atoms in the material but an increase in Si-C bond density. Thus, $\alpha_{\text{Si-C}}$ is considered a measure for the compactness of the a-SiC:H material in this particular study. A comparison between $T_{\text{sub}} = 265$ °C and 350 °C samples shows lower r_{dep} and higher $\alpha_{\text{Si-C}}$ for the latter. Thus, the higher energy provided by the higher substrate temperature does not only enhances the probability of C-H bond dissociation (higher $\alpha_{\text{Si-C}}$) but also the probability of radicals desorption from the surface (lower r_{dep}). In either case, a higher T_{sub} is more advantageous than a lower one. However, the T_{sub} is limited to 350 °C by the deposition system.

For both series, the r_{dep} decreases and the $\alpha_{\text{Si-C}}$ increases with increasing r_{H_2}, which might be explained by the hydrogen etching effect [127]. The increase of r_{H_2} adds to the removal of embedded material by an increasing number of hydrogen impinging on the surface and consequently lowers the r_{dep}. Since the Si-C bonds feature higher bonding energy than the C-H bonds in an amorphous network [128], the incorporated H atoms are more likely to be removed by hydrogen etching, giving rise to more ordered material with higher Si-C bond density. However, pinholes were observed on a-SiC:H samples of the $T_{\text{sub}} = 350$ °C series with $r_{\text{H}_2} > 97.5$ %, making them ineligible for later application. With decreasing P, the r_{dep} decreases, while the $\alpha_{\text{Si-C}}$ silightly increases. The lower r_{dep} is likely due to the lower amount of radicals accelerated onto the substrate surface. Consequently, the higher $\alpha_{\text{Si-C}}$ might arise from the fact that these radicals have more time to diffuse along the surface, find suitable docking states and dissociate the C-H bonds before subsequently arriving materials inmobilize them. However, the plasma could not be stabilized with further decrease of P under the given conditions. Hence, the deposition power should be as low as possible under the precondition that a stable plasma is guaranteed. As already indicated above, it was not possible to produce perfectly stoichiometric a-SiC:H material. Since all a-SiC:H layers fabricated in this work contain a Si excess, a partial cracking of the Si-C bond within the H_3SiCH_3 molecule as well as the release of CH_3 group into the gas phase can be assumed. Nevertheless, the near-stoichiometric a-SiC:H with a maximum $c_{\text{C}} = 45$ % achieved in this work is still considered a suitable barrier material due to the previous observation that Si crystallization hardly take place upon high temperature annealing at these SiC compositions (Sec. 4.1.1).

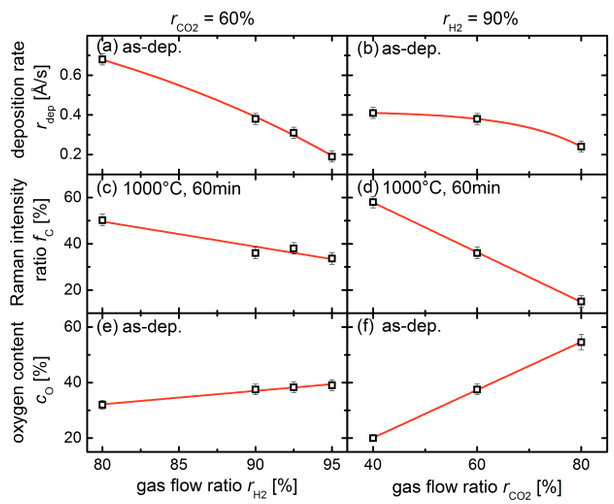

Figure 4.12.: *(a,b) Deposition rate r_{dep}, (c,d) Raman intensity ratio f_c and (e,f) RBS oxygen content c_O of two a-SiO_x:H series with varying r_{H_2} and r_{CO_2}. The r_{dep} and c_O were measured on as-deposited samples. The f_c belongs to samples annealed at* 1000 °C *for* 60 min *under N_2 gas flow. The r_{dep} and f_c values decrease with increasing r_{H_2} and r_{CO_2}, while the c_O increase.*

4.2.2. Deposition of a-SiO_x:H single layers

Deposition rate and oxygen content

Like a-SiC:H deposition, a homogeneous and slow growth of a-SiO_x:H layer with good material quality is crucial for its successful implementation in HSL structures. In addition, the a-SiO_x:H deposition needs to be fully compatible with the a-SiC:H process, since system changes between the deposition of alternating carbide and oxide layers are not feasible due to the large number of individual layers in HSL. Hence, the a-SiO_x:H layers were deposited in the same chamber and under the same conditions as the optimized a-SiC:H layers (Sec. 4.2.1). A power density P of 18.0 mW/cm^2, a plasma frequency f of 81.40 MHz, a deposition pressure p of 0.25 mbar, a substrate temperature T_{sub} of 350 °C, an electrode spacing d_{ele} of 16 mm were used. Using these deposition parameters, a stable plasma could be maintained and the a-SiO_x:H layers achieved a lateral thickness homogeneity as good as that

of a-SiC:H layers. The variation of the oxygen composition c_O was realized by, e.g., varying the CO_2 gas flow ratio r_{CO_2}, which is defined as the ratio between CO_2 gas flow rate f_{CO_2} and the sum of CO_2 and SiH_4 gas flow rate $f_{CO_2} + f_{SiH_4}$.

Figure 4.12 shows the deposition rate r_{dep}, the Raman intensity ratio f_c as a measure for the crystalline Si volume ratio (Sec. 3.1) and the RBS oxygen content c_O of two a-SiO$_x$:H series each with varying r_{H_2} and r_{CO_2}. While the r_{dep} and c_O were measured on as-deposited samples, the f_c belongs to samples annealed at 1000 °C for 60 min under N_2 gas flow. Prior to the annealing, all samples consist of amorphous phase only according to Raman spectroscopy. The r_{dep} values, in a comparable range as those for a-SiC:H, decrease with increasing r_{H_2} and r_{CO_2}, while the c_O values increase at the same time. Similar trends were observed and discussed during the development of intrinsic a-SiO$_x$:H passivation layers for SHJ solar cells. For more details, the readers are referred to Sec. 5.1. The $r_{CO_2} = 80$ % sample features a c_O of 55 %, which is within the required oxygen content range needed to produce Si-QDs with reasonable quantum confinement (Sec. 4.3.2). Besides, a corresponding deposition rate of 0.24 Å/s stands for a good compromise between sufficient thickness control and justifiable deposition time (e.g., 3 nm in 125 s). As c_O increases, the Si excess decreases with increasing r_{H_2} and giving rise to decreased f_c in annealed states. The presence of crystalline Si suggests a phase separation of SiO$_x$ into Si and SiO_2 phases during the thermal treatment [129]. It is worthwhile to stress that the $c_O = 55$ % sample also exhibits a c-Si fraction despite its high oxygen content.

Surface-sensitive XPS measurements (Sec. 3.1) were carried out on the as-deposited a-SiO$_x$:H layer directly after the removal of surface native oxide using a hydrofluoric acid. The a-SiO$_x$:H samples were deposited at $r_{CO_2} = 70$ %, 75 % and 80 %, respectively, which are within a smaller r_{CO_2} range as compared to the series shown above. These layers feature c_O values that are more relevant for HSL application (Sec. 4.3.2). Figure 4.13 illustrates the deconvolution of the characteristic XPS spectra of the Si(2p) photoelectrons for all three a-SiO$_x$:H samples using parameter correlation proposed by Ref. [130]. The Gaussian peaks centered at −99.8 eV, −100.7 eV, −102.0 eV, −103.1 eV and −104.4 eV are assigned to the photoelectrons from Si^{0+}, Si^{1+}, Si^{2+}, Si^{3+} and Si^{4+} nuclei with 0, 1, 2, 3 and 4 O atoms as bonding

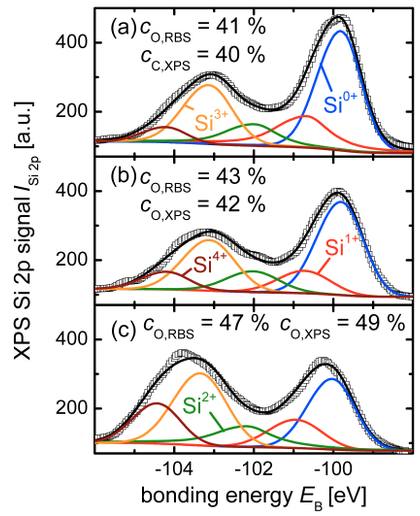

Figure 4.13.: *deconvolution of the characteristic XPS spectra of the Si(2p) photoelectrons for three a-SiO_x:H samples deposited at (a) $r_{CO_2} = 70$ %, (b) 75 % and (c) 80 %. The experimental data is shown in symbols and the fitted data are shown in lines. The Gaussian peaks centered at −99.8 eV, −100.7 eV, −102.0 eV, −103.1 eV and −104.4 eV are assigned to the photoelectrons from Si^{0+}, Si^{1+}, Si^{2+}, Si^{3+} and Si^{4+} nuclei with 0, 1, 2, 3 and 4 O atoms as bonding partners, respectively. The oxygen contents determined from the integrated peak intensities of the different Si(2p) signals are in good agreement with those from RBS measurements.*

partners, respectively.

The experimental data (symbol) accords with the sum of the individual signals (line). The oxygen contents determined from the integrated peak intensities of the different Si(2p) signals are in good agreement with those from RBS measurements and thus confirm the reliability of the RBS results. The XPS results reveal that even though the differences in the overall c_O were not significant, the distribution of the Si(2p) peaks changed noticeably between the three a-SiO_x:H layers. With increasing c_O, the Si^{0+} peak intensity decreased, while the Si^{3+} and Si^{4+} peak intensities increased. Most surprisingly, the deconvolved Si(2p) signals show that all as-deposited samples already possess a partial decomposition, which is indicated by,

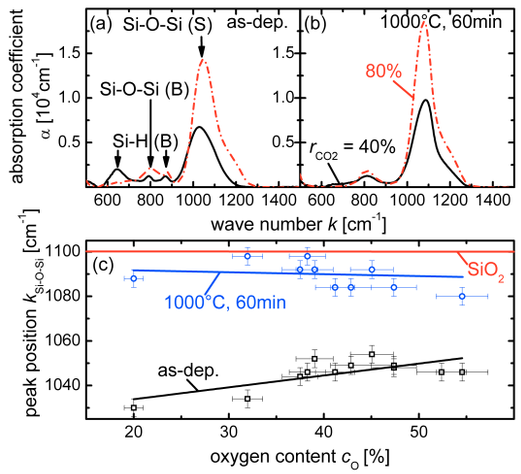

Figure 4.14.: *FTIR spectra of two samples with $r_{CO_2} = 40$ % and 80 % (a) before and (b) after annealing. (c) Si-O-Si (S) peak positions $k_{Si\text{-}O\text{-}Si}$ plotted versus c_O for the a-SiO_x:H samples in as-deposited and annealed states. The phase separation seems to be still uncomplete after annealing at 1000 °C for 60 min, since the composition of the O-rich phases still deviates from that of SiO_2 according to the comparison between $k_{Si\text{-}O\text{-}Si}$ values for SiO_2 and annealed a-SiO_x:H samples.*

e.g., the smaller fraction of the Si^{2+} intensity as compared to that of the Si^{3+} intensity. This material property is especially beneficial for the later Si-QD formation via thermally induced phase separation.

Phase separation upon annealing

In order to check whether and/or to which extent phase separation took place during the high temperature annealing, FTIR measurements were performed on a number of a-SiO_x:H samples on c-Si substrates deposited at different gas flow ratios before and after annealing. Figure 4.14(a,b) shows exemplarily the FTIR spectra of two samples with $r_{CO_2} = 40$ % and 80 % from the previous r_{CO_2} series before and after annealing. The peaks centered at around $k = 650$ cm^{-1} and 870 cm^{-1} that were absent after annealing are attributed to Si-H (B) vibration modes without and with three O back bonds attached to Si, respectively [131]. The Si-H (B) peaks for vibration

modes with one and two O back bonds, which are expected at $k = 780$ cm^{-1} and 840 cm^{-1}, overlap with the more pronounced Si-O-Si (B) peak centered at around 800 cm^{-1} [132]. The most pronounced asymmetric peak is assigned to the Si-O-Si (S) vibration mode, the position of which is sensitive to the value of the oxygen content and has been correlated to the composition of SiO_x material [133].

In Fig. 4.14(c), the Si-O-Si (S) peak positions $k_{\text{Si-O-Si}}$ are plotted versus c_O for the a-SiO_x:H samples in as-deposited and annealed states. For as-deposited samples, $k_{\text{Si-O-Si}}$ increases by trend with rising c_O due to the increase of O back bonds at the Si sites. Upon annealing, all $k_{\text{Si-O-Si}}$ shifted to higher values approaching those of SiO_2 at 1100 cm^{-1} [134]. Since the layer composition is not expected to change significantly during the annealing, this shift is interpreted as a decomposition of a-SiO_x:H into Si-rich and O-rich regions [129], which gives rise to a predominant generation of Si-O-Si (S) signals in the O-rich regions. The larger scatter in $k_{\text{Si-O-Si}}$ for the annealed samples might be caused by temperature fluctuations between two annealing runs, which is dealt with in Sec. 4.2.4. The phase separation seems to be uncompleted after annealing at 1000 °C for 60 min, since the composition of the O-rich phases still deviates from that of SiO_2 according to $k_{\text{Si-O-Si}}$. Thus, higher annealing temperature $T_a = 1050$ °C or longer annealing time $t_a = 4$ h were applied to the annealing procedure later on.

4.2.3. Deposition in automatic mode

Composition control

Based on the optimized deposition parameters presented in Sec. 4.2.1 and 4.2.2, a automatic deposition sequence was adapted for the growth of SiC/SiO_x HSL structure for the sake of good reproducibility and low expenditure of human labor. After 2 h preheating time, the automatic mode was activated, which controls all processes of the alternating a-SiC:H and a-SiO_x:H layer growth. The automatic deposition ends with the completed HSL sample ready for take out. The substrate temperature and the plasma frequency were set prior to the automatic deposition start. Also the power matching had to be adjusted beforehand to ensure stable plasma at the very low deposition power. Since it was not possible to stabilize the required low power

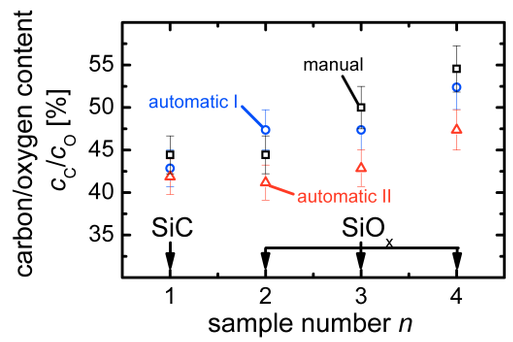

Figure 4.15.: *Compositions of a-SiC:H and a-SiO_x:H single layers deposited either without attenuator in manual mode or with attenuator in automatic mode. The a-SiO_x:H samples were deposited at $r_{CO_2} = 70$ %, 75 % and 80 %, respectively. The automatic I and II series were fabricated under the same deposition condition. The materials deposited in automatic mode with attenuator are comparable to those fabricated in manual mode without attenuator.*

of 1 W at the power source in the automatic mode, a power attenuator was installed between the power source and the matchbox that allows for a set power of 10 W at the power source without increasing the desired power density in the chamber.

Figure 4.15 compares the compositions of a-SiC:H and a-SiO_x:H single layers deposited either without attenuator in manual mode or with attenuator in automatic mode. The a-SiO_x:H samples were deposited at $r_{CO_2} = 70$ %, 75 % and 80 %, respectively. The automatic I and II series were fabricated under the same deposition condition in order to check the reproducibility of the automatic deposition. The results show that the materials deposited in automatic mode with attenuator are comparable to those fabricated in manual mode without attenuator as their differences in carbon or oxygen content lie within the error bars at least for the comparison between the automatic I and the manual series. The discrepancy in c_O between the automatic I series and the automatic II series that were produced one month later implies that a precise control of the oxygen content in a-SiO_x:H layers cannot be sustained over long periodes of time. Thus, test depositions of single layers directly before HSL processing are recommended. Nevertheless, the good adjustability of c_O

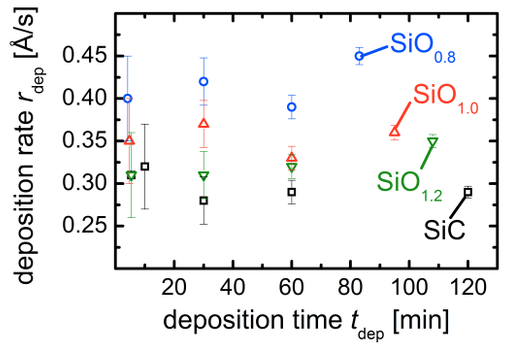

Figure 4.16.: *Deposition rate r_{dep} versus the deposition times t_{dep} for one a-SiC:H and three a-SiO_x:H single layers fabricated using the automatic mode(Fig. 4.15). A clear r_{dep} time dependence was not indicated for all samples. The scatter in r_{dep} values as a function of t_{dep} was mainly within the error bars. The results imply that the deposition rates determined on thick layers are valid for the estimation of sublayer deposition time during HSL fabrication.*

by varying r_{CO_2} during deposition still allows for relative comparisons.

Thickness control

Since the deposition rates at the initial stage of the deposition might be different from those determined on thick layers, a possible time dependence of r_{dep} has to be taken into consideration in order to make sure that the very thin sublayer thicknesses in HSL are precisely realized within a sub-nanometer range. Hence, a-SiC:H and a-SiO_x:H single layers with varying layer thicknesses were fabricated using the automatic mode. Figure 4.16 displays the r_{dep} plotted versus the deposition times t_{dep} for one a-SiC:H and three a-SiO_x:H single layers (see above). The nominal oxygen content $c_{\mathrm{O}} = 45$ %, 50 % and 55 % of the a-SiO_x:H layers were translated into the stoichiometry numbers $x = 0.8$, 1.0 and 1.2 via the equation $x = \frac{c_{\mathrm{O}}}{1-c_{\mathrm{O}}}$, respectively. A clear r_{dep} time dependence was not obeserved for all samples. The scatter in r_{dep} values as a function of t_{dep} was mainly within the error bars. Even the largest r_{dep} discrepancy observed between $t_{\mathrm{dep}} = 60$ min and 83 min ($SiO_{1.2}$) would only result in a thickness deviation of less than 0.5 nm assuming a desired layer thickness of

3 nm. Hence, the results imply that the deposition rates determined on thick layers are valid for the estimation of sublayer deposition time during HSL fabrication.

4.2.4. Optimization of the annealing process

Annealing furnace

At the early stage of this work, the high temperature annealing was carried out in an in-house built quartz tube furnace. Later, the annealing was transfered to a newly installed quartz tube furnace built by the company Linn High Therm due to several drawbacks of the former for the purpose of this work. The HSL samples and their corresponding SiC and SiO_x single layer references presented in Sec. 4.3 were annealed using the in-house built furnace, whereas the samples shown in Sec. 4.4 were thermally treated in the newly installed furnace. The critical differences between the two tube furnaces are discussed below, which should also give an idea about the important features that a annealing system necessitates for the Si-QD formation.

The maximum set temperature is 1050 °C for the old furnace and 1100 °C for the new furnace. For both systems, the maximum real temperature measured with a thermistor at the actual sample positions in the furnace were around 50 °C lower than the maximum set temperature. Thus, the new furnace provides a higher T_a of 1050 °C than the old system with 1000 °C, which makes a considerable difference for precipitation and crystallization of Si-NCs in the SiO_x layers [135]. Since the annealing at 1000 °C for 1 h in the old furnace was found to be insufficient to complete the phase separation in SiO_x layers (Sec. 4.2.2 and 4.3.1), the annealing time t_a was increased to 4 h in order to compensate the low T_a of 1000 °C (Sec. 4.3). With the new furnace being available, the annealing temperature was increased to 1050 °C. At the same time, the annealing time was reduced back to 1 h (4.4), because a longer t_a tends to result in more pronounced surface oxidation and atomic inter-diffusion at the SiC/SiO_x interface.

Another critical issue is the surface oxidation during annealing [136], the formation of which is distinctive especially at high T_a and long t_a. The oxygen source might originate from the ambient air due to leakage of the system or oxygen in-diffusion

through the quartz tube at high temperatures. In addition, the oxygen that exists as impurities in the inert N_2 gas must not be neglected, as oxygen becomes highly reactive with the sample surface at high temperatures. The old furnace operates in an open system at ambient pressure under a continuous N_2 gas flow, which was meant to carry away oxygen out of the quartz tube. However, oxygen back diffusion against the N_2 gas flow cannot be excluded in this open system. On the contrary, the new system operates in a closed system that underwent several evacuation and N_2 flush cycles before heating to eliminate oxygen in the quartz tube. Furthermore, a N_2 gas with a higher purity of 99.9999 % and a higher flow rate of 2 L/min instead of 99.999 % and 0.5 L/min as in the old furnace was used. The higher flow rate might carry away incoming oxygen from the ambient air more efficiently before they reach the sample surface. Even though the thickness of the surface oxide layer was reduced with these optimizations, its complete elimination could not be achieved.

A practical drawback of the old furnace was its small tube diameter and its temperature inhomogeneity along the tube length (measured), which limits the number of 1.5 cm $\times$ 1.5 cm sized samples to 4 that can be processed at $T_a = 1000$ °C simultaneously. Due to this limitation, specimen cut from the same sample and prepared for different measurements were partially annealed in different runs, which is time consuming and might also affect the comparability of the measured results. The new furnace with a larger quartz tube allows for the annealing of samples with diameters up to 140 mm. Even though a temperature inhomogeneity along the tube length was detected in the new furnace as well, it was possible to position more 1.5 cm $\times$ 1.5 cm specimen within an area with $T_a = 1050$ °C due to its larger tube diameter. For example, up to 20 pieces of HSL samples as well as SiC and SiO_x single layer references were processed at the same time in the new system.

Heating ramp

The PECVD grown layers with hydrogen incorporation require an initial low temperature annealing to release the hydrogen out of the material, in order to avoid bubble formation at high temperatures [23]. Figure 4.17 shows the hydrogen effusion rate dN_H/dt of a-SiC:H and a-SiO_x:H single layers versus annealing temperature T_a. At the relatively high heating rate $r_{heat} = 20$ K/min during the hydrogen effu-

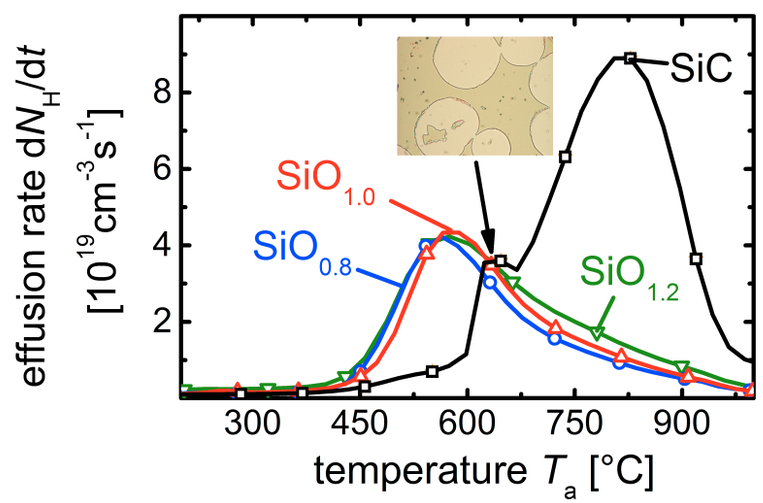

Figure 4.17.: *Hydrogen effusion rate dN_H/dt of a-SiC:H and a-SiO_x:H single layers versus annealing temperature T_a. The inset shows a optical microscopy image of the a-SiC:H surface after the measurement. At the relatively high heating rate r_{heat} = 20 K/min of the hydrogen effusion measurement, blister and bubble formation was detected for the a-SiC:H layer as indicated by the feature between* 600 °C *and* 670 °C *[99]. The release of hydrogen is minute between room temperature and* 400 °C.

sion measurement, blister and bubble formation was detected for the a-SiC:H layer as indicated by the feature between 600 °C and 670 °C [99] and visualized by the optical microscopy image shown as inset in Fig. 4.17. This feature was not observed for a-SiO_x:H layers due to their higher H_2 solubility and diffusion coefficient than the a-SiC:H single layer [137]. The general difference of the temperature dependent effusion characteristics between a-SiC:H and a-SiO_x:H materials is discussed in Sec. 4.4.2. Based on these results, the heating ramp of the high-temperature annealing step was adjusted. Between room temperature and 400 °C, where the release of hydrogen is minute, a high r_{heat} of 10 K/min was applied in order to reduce the total heating time. Above 400 °C, a low r_{heat} of 1 K/min was found to completely eliminate blistering and bubble formation in the a-SiC:H layers.

4.3. Silicon quantum dot formation in SiC/SiO_x HSL

After the development of SiC and SiO_x single layers, SiC/SiO_x hetero-superlattice films were prepared using the optimized process parameters. The first part of this section presents the HRTEM and EFTEM images of the first HSL test samples. In the second part, HSL samples with different combinations of various SiC thicknesses, SiO_x thicknesses and SiO_x compositions were fabricated and characterized together with their corresponding thick single layers. In addition, the suitable composition range of the SiO_x layer, within which the formation of sufficiently confined Si-QDs is feasible, is discussed with the aid of a theoretical model.

4.3.1. HSL structure

Before and after annealing

The first HSL test sample consists of 10 periods of SiC and SiO_x sublayer with thicknesses each above 10 nm. According to the single layer results (Sec. 4.2), the used deposition parameters should result in an carbon and oxygen content of around 45 % (Fig. 4.15) and 20 % (Fig. 4.12) in the SiC and SiO_x sublayer, respectively. The deposition was followed by annealing in the in-house built furnace at $T_a = 1000$ °C for $t_a = 1$ h (Sec. 4.2.4). The cross-sectional structure of the sample stack before and after annealing was visualized by HRTEM and EFTEM measurements.

The HRTEM images of two different magnification as well as the C and Si distribution determined from EFTEM measurements are shown in Fig. 4.18 for the (left) as-deposited and (right) annealed samples. As a first approach, the sublayer thicknesses that largely exceed the thicknesses relevant for any Si-QD superlattice application (Sec. 4.3.2) allow for easier inspection of the multilayer structure. In the as-deposited state, the alternating carbide and oxide layers on top of a c-Si substrate, starting with a-SiC:H and ending with a-SiO_x:H, are clearly visible (Fig. 4.18(a)). In Fig. 4.18(b), a blurring of the SiC/SiO_x interfaces is observed after annealing, which is accompanied by a shrinkage of the total layer thickness by 13 %. Since the sample ends with a thick SiO_x layer, a clear surface oxide formation could not be detected. At higher magnification (Fig. 4.18(c,d)), an extensive amount of

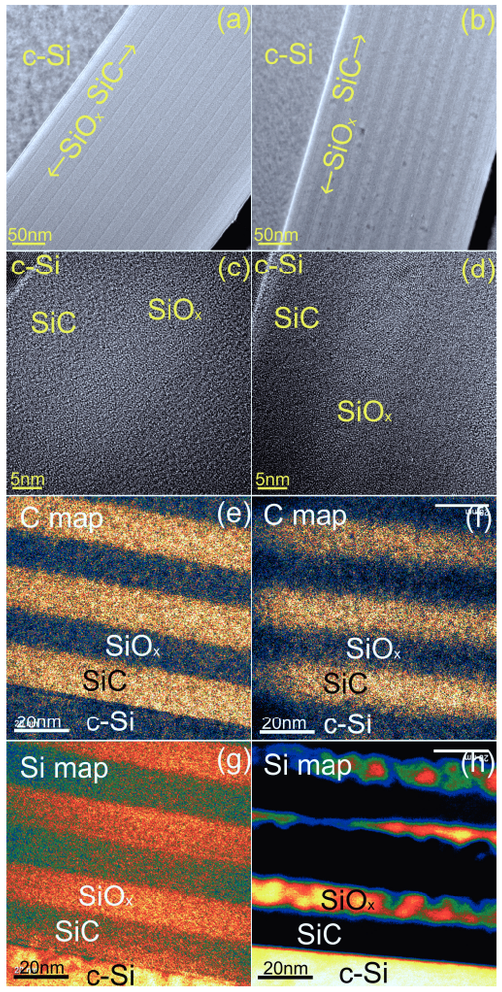

Figure 4.18.: *(a-d) Cross-sectional HRTEM images of two different magnifications as well as (e,f) carbon and (g,h) silicon atom distribution determined from EFTEM measurements for the (left) as-deposited and (right) annealed first HSL samples. The results suggest that alternating deposition of SiC and SiO_x thin layers with sharp interfaces is feasible. Ongoing phase separation of SiO_x and Si crystallization in SiO_x upon annealing can be identified.*

lattice fringes were detected only in the SiO_x layers after annealing. The SiC layers in annealed state as well as both SiC and SiO_x layers in the as-deposited state consist of amorphous phase only, which is in agreement with corresponding GIXRD and Raman spectroscopy results. As expected, the C map (Fig. 4.18(e)) and the Si map (Fig. 4.18(g)) of the as-deposited sample reveal high C and Si intensities (brighter area) in the SiC and SiO_x layers. The transition of the C intensities at the SiC/SiO_x interfaces became less abrupt upon annealing (Fig. 4.18(f)). In addition, areas with very high Si intensities appeared locally in the SiO_x layers after annealing (Fig. 4.18(h)).

First of all, the results suggest that alternating deposition of SiC and SiO_x thin layers with sharp interfaces is feasible. However, the annealing gave rise to a structural densification of the material as indicated by the shrinkage of the total layer thickness. This is likely related to the release of hydrogen (Sec. 4.2.4). The inhomogeneous distribution of Si atoms in the annealed SiO_x layers suggests an ongoing phase separation of SiO_x into Si and SiO_2 [138]. Due to the large amount of Si excess, Si-NC formation in the SiO_x layers was already initiated for annealing at $T_a = 1000$ °C for $t_a = 1$ h as indicated by the lattice fringes in the SiO_x sublayers. It is important to note that the SiC layers remained amorphous after annealing at $T_a = 1000$ °C, which is beneficial for their function as barrier layers [38]. However, the Si content in the oxide layers of the present HSL sample is too high to enable the formation of small and isolated Si-QDs. The blurring of the SiC/SiO_x interfaces might be due to the lateral inhomogeneity in layer thickness induced by the phase segregation and/or due to the inter-diffusion of, e.g., C atoms across the interface (Fig. 4.18(f)). In conclusion, the Si-QD formation in SiC/SiO_x HSL seems feasible according to the present results.

Reasonable silicon oxide composition range

In order to locate the composition range, in which the formation of sufficiently confined Si-QDs is theoretically feasible, the effective band gap energy $E_{g,eff}$ was calculated as a function of Si-QD size d_{dot} and oxygen content c_O (stoichiometry number x) for the SiC/SiO_x structure. In the first step, the spacing between two adjacent Si-QDs d_{sp} was derived from d_{dot} and x by assuming complete phase separation of

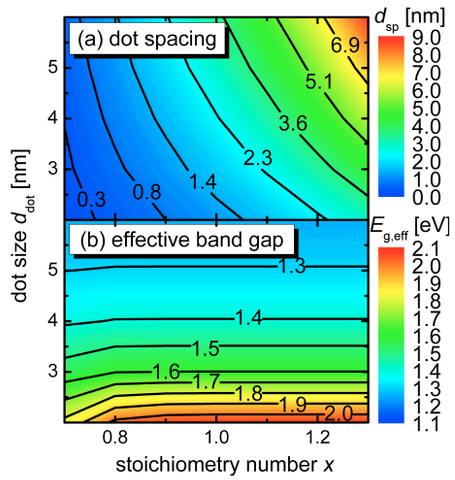

Figure 4.19.: *Contour map of (a) Si-QD spacing d_{sp} and (b) effective band gap energy $E_{g,eff}$ versus Si-QD size d_{dot} and stoichiometry number x. (a) The strong increase of d_{sp} with increasing d_{dot} and x is due to the higher Si consumption needed for larger Si-QDs and the less Si supply from the initial SiO_x material. (b) Unlike for Si-QD formation in SRC materials (Sec. 4.1.2), it is theoretically possible to achieve $E_{g,eff} \geq 1.8$ eV for $d_{dot} \geq 2$ nm due to the high band offset between Si-QD and a-SiO_2.*

SiO_x into spherical Si-QDs and a-SiO_2 matrix. The required atomic densities of the different phases were taken from Ref. [132] (Sec. 4.1.2). Figure 4.19(a) shows the contour map of d_{sp} plotted versus d_{dot} and x. The strong increase of d_{sp} with increasing d_{dot} and x is due to the higher Si consumption needed for larger Si-QDs and the smaller Si supply from the initial SiO_x material, respectively, as a consequence of which the SiO_2 matrix volume becomes larger. It is worthwhile to note that d_{sp} falls below 0 nm for $x \leq 0.6$, which is interpreted as the undesired agglomeration of Si-NCs.

In the next step, the $E_{\mathrm{g,eff}}$ was calculated for the different d_{dot} and d_{sp} configurations using the 3D superposition of the Kronig-Penny model (Sec. 4.1.2). The lateral two dimensions utilize an a-SiO_2 band gap of 7.8 eV with symmetrical conduction and valence band offsets towards the band gap of Si-QD (1.1 eV). In the vertical dimension, a realistic a-SiC layer with $c_{\mathrm{C}} = 45$ % was applied (Sec. 4.2.3),

which provides a E_g of 2.3 eV (Fig. 4.6) and therefore a symmetrical band offset of 0.6 eV. Figure 4.19(b) shows the contour map of $E_{g,eff}$ plotted versus d_{dot} and x for $d_{SiC} = 5$ nm. The difference in $E_{g,eff}$ for $d_{SiC} = 2$ nm (not shown) and $d_{SiC} = 5$ nm were negligbly small indicating a weak contribution of SiC to the quantum confinement beyond a thickness of 2 nm. Unlike for Si-QD formation in SRC materials (Sec. 4.1.2), it is possible to achieve $E_{g,eff} \geq 1.8$ eV for $d_{dot} \geq 2$ nm due to remarkably high band offset between Si-QD and a-SiO_2. The E_g increases with decreasing d_{dot} due to enhanced carrier localization. The noticable deterioration of E_g for $x < 0.8$ originates from pronounced wavefunction overlap of two adjacent Si-QDs as d_{sp} decreases (Fig. 4.19(a)). Thus, SiO_x materials with $x < 0.8$ are not recommended for Si-QD absorber applications. Furthermore, SiO_x materials with $x > 1.2$ are not recommended either, since the Si-QD density will decrease rapidly with higher x as indicated by the strong increase of d_{sp} and therefore the a-SiO_2 volume fraction. For $x > 1.2$, the c-Si volume fraction falls below 25%.

Reduced thickness and Si excess

The sublayer thicknesses and the Si excess in SiO_x layers were reduced to more relevant values as compared to those of the test sample presented in Sec. 4.3.1, while all other deposition and annealing parameters were kept the same. The new HSL sample consisting of 15 periods of nominally 4 nm thick SiC and SiO_x sublayers starting with a thick SiO_x layer. The SiO_x sublayers were deposited at $r_{CO_2} = 70$ %, which should yield in a c_O of around 45 % ($x = 0.8$). Figure 4.20 presents the cross-sectional HRTEM and EFTEM images with two different magnifications for the annealed HSL sample. First of all, the thinner alternating SiC and SiO_x layer structure is still clearly visible after annealing in Fig. 4.20(a,b). Unlike for the first HSL sample that is terminated with a thick SiO_x layer, a clear surface oxide layer has formed in the second HSL sample, consuming the three uppermost SiO_x/SiC/SiO_x layers. The sublayer thicknesses of 3.9 nm and 4.0 nm for SiC and SiO_x, respectively, were estimated from the HRTEM images. Assuming a thickness reduction of 13 % upon annealing (see above), the sublayer thicknesses in the as-deposited state are expected to be 4.5 nm and 4.6 nm for SiC and SiO_x, respectively, which is in good agreement with the expected thickness of 4 nm and thus confirming a sufficient

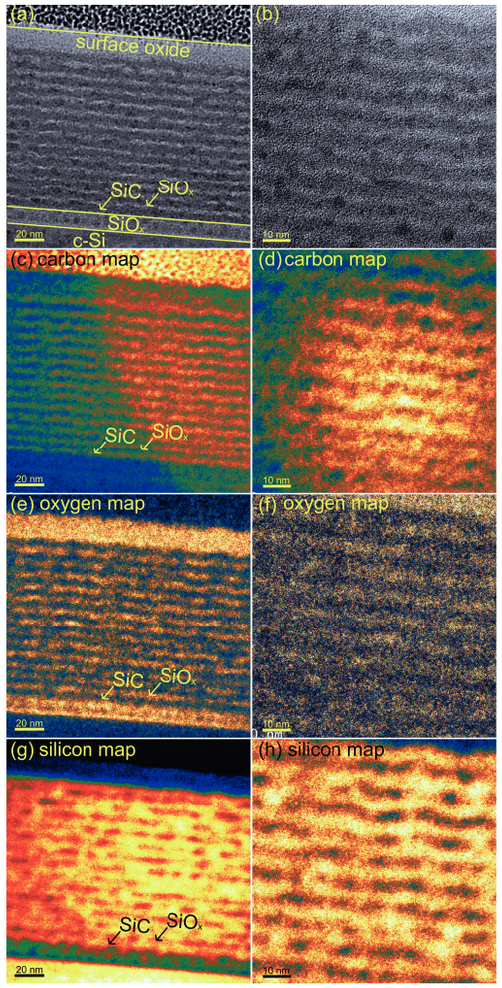

Figure 4.20.: *(a-b) Cross-sectional HRTEM images as well as atom distributions for (c,d) carbon, (e,f) oxygen and (g,h) silicon determined from EFTEM measurements for the annealed second HSL samples in two different magnifications (left/right). The thinner SiC and SiO_x layer structure is still clearly visible after annealing. A clear phase separation in the thin and O-rich SiO_x layers is visible. However, only a few isolated lattice fringes can be observed in the SiO_x layers.*

thickness control.

The C maps (Fig. 4.20(c,d)) and the O maps (Fig. 4.20(e,f)) show clear restriction of C atoms to the SiC layers and O to the SiO_x layers after annealing with some blurring of the SiC/SiO_x interfaces, which excludes a pronounced element intermixing even in the HSL sample with very thin sublayers. In addition, an inhomogeneous O distribution appeared in the SiO_x layers as an indication of phase segregation upon annealing. The large-area intensity inhomogeneity in the C maps arises from measurement artifacts. The Si maps (Fig. 4.20(g,h)) reveal high Si intensities homogeneously distributed in the SiC layers and locally present in the SiO_x layers, which hints at a successful precipitation of laterally isolated Si in the SiO_x layer only. Thus, the Si-QD formation in SiC/SiO_x HSL seems also applicable for thinner sublayer thicknesses and lower Si excess in SiO_x layers.

However, only a few isolated lattice fringes in the SiO_x layers can be observed in Fig. 4.20(b), even though a clear phase separation in the SiO_x layers is apparent. This small amount of Si-NCs could not be detected by Raman spectroscopy or XRD (not shown). Thus, the annealing at $T_a = 1000$ °C for $t_a = 1$ h is probably unable to complete the phase separation and Si crystallization due to the higher oxygen content of the SiO_x layers as compared to those in the first HSL sample, which suggests to use a higher T_a or a longer t_a for later experiments.

4.3.2. Thickness and composition variations

Impact on structural properties

SiC/SiO_x hetero-superlattice films with different combinations of various SiC thicknesses d_{SiC} (6 nm, 2 nm), SiO_x thicknesses d_{SiO_x} (5 nm, 3 nm) and SiO_x compositions c_O (45 %, 50 %, 55 %) were fabricated together with their corresponding thick SiC, $SiO_{0.8}$, $SiO_{1.0}$ and $SiO_{1.2}$ single layers, respectively. The HSL sample numbers and the corresponding sample specifications are listed in Tab. 4.1. All HSL samples consist of 20 bi-layers starting with a SiC layer and ending with a SiO_x layer. Except for the gas flow rates, all deposition parameters were kept constant at $P = 15.3$ mW/cm^2, $f = 81.4$ MHz, $p = 0.25$ mbar, $T_{sub} = 350$ °C and $d_{ele} = 16$ mm. For the SiC layers, H_3SiCH_3 and H_2 gas flow rates of 0.5 sccm and 19.5 sccm were

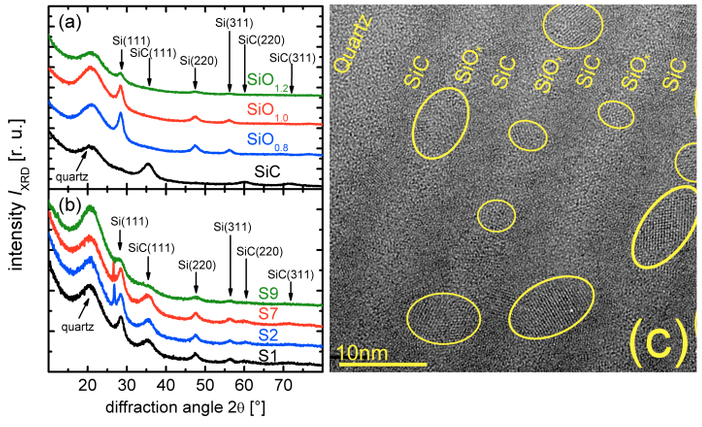

Figure 4.21.: *GIXRD patterns of (a) the thick single layers and (b) a selection of four characteristic HSL samples all after annealing. Reflexes around the diffraction angles* $2\theta = 35.4\,^\circ$, $60.0\,^\circ$ *and* $71.8\,^\circ$ *are assigned to (111), (220) and (311) oriented SiC crystals, while reflexes at* $2\theta = 28.5\,^\circ$, $47.6\,^\circ$ *and* $56.3\,^\circ$ *are attributed to (111), (220) and (311) oriented Si crystals [29]. (c) Cross-sectional HRTEM image of the sample S*1 *after annealing. The isolated lattice fringes of different orientations in the* SiO_x *layers are highlighted with circles.*

used, respectively. For the $SiO_{0.8}$ ($SiO_{1.0}$, $SiO_{1.2}$) layers, CO_2, SiH_4 and H_2 gas flow rates of 3.5 sccm (3.75 sccm, 4.0 sccm), 1.5 sccm (1.25 sccm, 1.0 sccm) and 45 sccm (45 sccm, 45 sccm) were employed, respectively. The deposition was followed by a thermal treatment in an annealing furnace at $T_\mathrm{a} = 1000\,^\circ\mathrm{C}$ for $t_\mathrm{a} = 4$ h.

Figures 4.21(a,b) present the GIXRD patterns of the thick single layers and a selection of four characteristic HSL samples all after annealing. As compared to S1, the sample S2 contains thinner oxide layers of the same oxygen content, while S7 exhibits higher oxygen content at the same oxide layer thicknesses as S1. The sample S9 exhibits thinner carbide layers as compared to S7. The GIXRD patterns of the SiC single layer show peaks around diffraction angles $2\theta = 35.4\,^\circ$, $60.0\,^\circ$ and $71.8\,^\circ$, which are assigned to (111), (220) and (311) oriented SiC crystals, respectively [29]. For all three SiO_x single layers, reflexes appear at $2\theta = 28.5\,^\circ$, $47.6\,^\circ$ and $56.3\,^\circ$, which are attributed to (111), (220) and (311) oriented Si crystals [29]. As the

Table 4.1.: *HSL films with different combinations of SiC thicknesses, SiO_x thicknesses and SiO_x compositions.*

sample number	S1	S2	S3	S4	S5	S6	S7	S8	S9
content c_C [%]	45	45	45	45	45	45	45	45	45
content c_O [%]	45 ($x = 0.8$)	45	45	50 ($x = 1.0$)	50	50	55 ($x = 1.2$)	55	55
thickness d_{SiC} [nm]	6	6	2	6	6	2	6	6	2
thickness d_{SiO_x} [nm]	5	3	5	5	3	5	5	3	5

c_O continuously increases from $SiO_{0.8}$ to $SiO_{1.2}$, the intensity of these Si crystals-related reflexes is weakest (strongest) for the $SiO_{1.2}$ ($SiO_{0.8}$) single layer with the lowest (highest) Si excess. The broad peak centered at 21.0 ° that is present in all samples originates from the amorphous quartz substrate. The average SiC-NCs size in the SiC single layer is 3.0 nm, while the Si-NCs in the $SiO_{0.8}$, $SiO_{1.0}$ and $SiO_{1.2}$ single layers have an average size of 7.7 nm, 7.6 nm an 5.5 nm, respectively.

The GIXRD patterns of the HSL samples exhibit diffraction peaks from both SiC- and Si-NCs. Hence, crystallization of SiC took place in HSL that was previously not observed for annealing at 1000 °C for 1 h. According to the GIXRD results of the single layer, the SiC-NCs originate from the SiC sublayers and the Si-NCs are likely formed in the SiO_x sublayers. The average nanocrystal size of the samples S1, S2, S7 and S9 are 4.9 nm, 5.4 nm, 4.4 nm and 3.6 nm for Si crystals and 2.7 nm, 3.0 nm, 2.7 nm and 1.7 nm for SiC crystals, respectively. It is worthwhile to stress that the GIXRD patterns could be fitted without taking into consideration contributions from graphitic phase or amorphous silicon phase. In addition, the samples S2 and S7 exhibit a sharp peak positioned at 26.7 °, which can be attributed to crystalline SiO_2. Since the alternating SiC and SiO_x layer materials likely have different thermal expansion coefficients and thus behave differently upon annealing or cooling, stress will be induced in the layers through the SiC/SiO_x boundary. This stress may induce crystallization of the material, which would have been thermodynamically unfavorable otherwise [139]. This could explain the partial crystallization of the SiO_2 matrix in the case of the samples S2 and S7. Both the reduction of the oxide layer thickness (higher induced stress) and the increase of the oxygen content (larger SiO_2 fraction) support the stress-induced crystallization of the SiO_2 matrix, which is in agreement with the observation that the sample S1 with thicker oxide layers

than S2 and lower oxygen content than S7 does not show any crystalline SiO_2 signal in GIXRD. For the sample S9, the amount of induced stress is probably larger in the thinner SiC layers through SiC/SiO_x boundary, resulting in more relaxed oxide layers, thus no crystalline SiO_2 is observed for the sample S9 either. The sharp peak positioned at 26.7 ° was only observed for HSL samples annealed for $t_a = 4$ h in any case.

Figure 4.21(c) presents a HRTEM image of sample S1 on quartz substrate after annealing, showing many clear lattice fringes in both SiC and SiO_x layers. The isolated lattice fringes of different orientations in the SiO_x layers are highlighted with circles. Some of them are confined in the oxide layers, while some of them extend into adjacent SiC layers or have lateral diameters larger than the SiO_x layer thickness. Their average diameter perpendicular to the film plane is around 5 nm, whereas the diameter in the broadest direction ranges from 4 nm - 10 nm. The HRTEM image of the sample S7 (not shown) with nominally the same SiC/SiO_x thicknesses combination as the sample S1 but with higher c_O reveals mainly spherically constrained lattice fringes in the oxide layer, whereas the density of the lattice fringes is strongly decreased.

Figure 4.22 shows another cross-sectional HRTEM image of the sample S1 with lower magnification and its corresponding EFTEM carbon, oxygen and silicon distribution after annealing. Despite a $t_a = 4$ h, the HSL structure is preserved with clear separation of SiC layers and SiO_x layers as indicated by alternating areas with high C and O intensities, respectively. Inhomogeneous O and Si distributions were again observed in the SiO_x layers as a signature phase segregation upon annealing. Due to the longer annealing time, the atomic inter-diffusion at the SiC and SiO_x interface seems to be more pronounced than in HSL samples shown in Sec. 4.3.1. The average thicknesses of the annealed layers are 5.2 nm for SiC and 4.4 nm for SiO_x. Assuming a thickness reduction of 13 % upon annealing (Sec. 4.3.1), the sublayer thicknesses in the as-deposited state are 6.0 nm for SiC and 5.1 nm SiO_x, which is in excellent agreement with the nominal sublayer thicknesses of 6 nm and 5 nm calculated from deposition times and pre-determined deposition rates. Zooming the HRTEM image into the 12th SiO_x layer, one can see that this layer is completely crystallized with many differently orientated lattice fringes touching each other. According to the

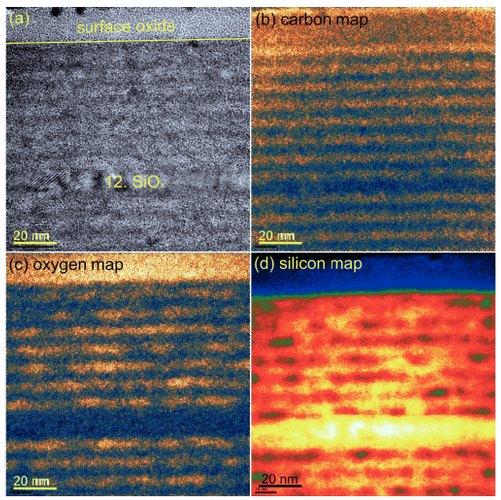

Figure 4.22.: *(a) Cross-sectional HRTEM image of the sample S*1 *with lower magnification and its corresponding EFTEM (b) carbon, (c) oxygen and (d) silicon distribution after annealing. Despite a* $t_a = 4$ h*, the HSL structure is preserved with clear separation of SiC layers and* SiO_x *layers as indicated by alternating areas with high C and O intensities, respectively. Due to the longer annealing time, the atomic inter-diffusion at the SiC and* SiO_x *interfaces seems to be more pronounced than in the HSL samples shown in Sec. 4.3.1.*

Si, C and O mappings, this layer consists of Si atoms only. The formation of such pure Si layers might be due to an infrequent error in the CO_2 gas inlet during SiO_x deposition in automatic mode.

The GIXRD measurements and TEM images suggest that HSL structures with desired thickness and composition variations were achieved. The lattice fringes in the oxide layers shown in HRTEM (Fig. 4.21(c)) are attributed to Si-NCs while the embedding material has a composition close to a-SiO_2, since GIXRD measurements do not show any clear a-Si phase signals. The lattice fringes in the carbide layers shown in HRTEM are attributed to SiC-NCs from the comparison of the carbon mappings from EFTEM. The Si-NCs sizes of S1 determined from HRTEM are in good agreement with those from GIXRD. According to the GIXRD data, the Si-NCs size decreased with increasing oxygen content. The Si-NC sizes of the $SiC/SiO_{1.2}$

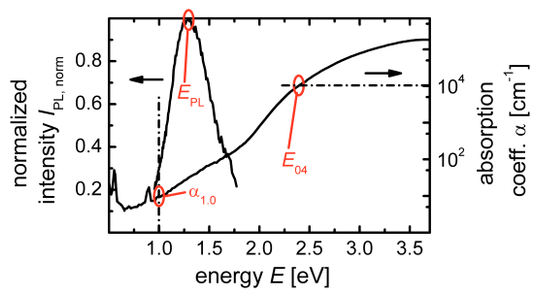

Figure 4.23.: *Normalized PL intensity $I_{PL,norm}$ and the absorption coefficient α from PDS measurements as a function of the photon energy E for the as-deposited sample S1. The optical band gap energy E_{04}, the defect absorption coefficient $\alpha_{1.0}$ and the PL peak energy E_{PL} were extracted from the PDS and PL data for all HSL series samples before and after annealing.*

samples are smaller than their oxide layer thickness indicating an upper limit of the Si-NC size due to the limited amount of excess silicon atoms under the given annealing conditions. Surprisingly, the reduction of the oxide layer thickness from 5 nm (S1) to 3 nm (S2) for the $SiC/SiO_{0.8}$ samples resulted in an increase of the Si-NCs size. This might be an indication that much more Si-NCs extend into adjacent SiC layers when making the oxide layer thinner. These results suggest that the SiC barrier layers are rather poor Si crystallization stops also within the SiC/SiO_x HSL structure (Sec. 2.1.2). Hence, the Si-NC size in the HSL is presumably more strongly determined by the oxygen content and less by the oxide layer thickness. As a consequence, it is not possible to control the Si-QD size and the Si-QD density independently, as both features are determined by the oxygen content. In the case of SiC-NCs, the crystal sizes are always smaller than the respective carbide layer thicknesses according to GIXRD. Accordingly, an extension of SiC-NCs into adjacent SiO_x layers was not observed in HRTEM.

Impact on optical properties

Figure 4.23 shows the normalized PL intensity $I_{\mathrm{PL,norm}}$ and the absorption coefficient α from PDS measurements as a function of the photon energy E for the as-deposited

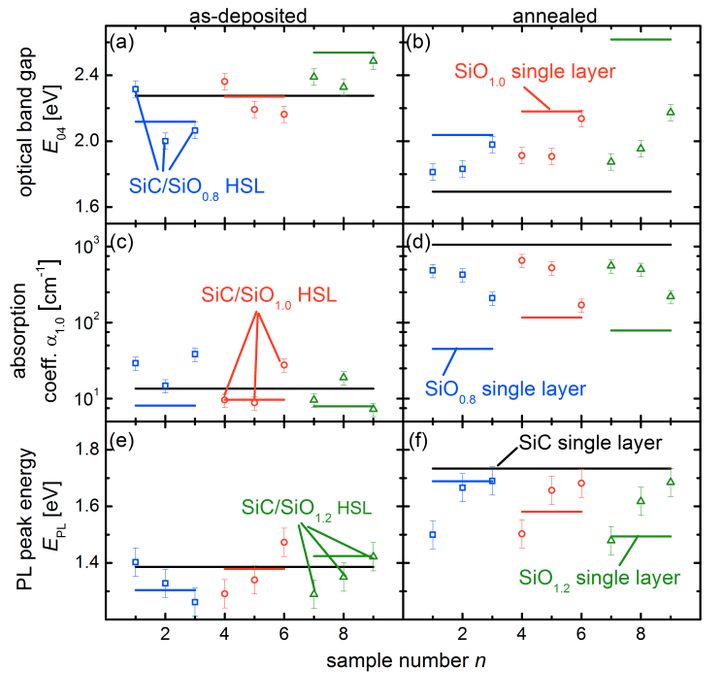

Figure 4.24.: *(a,b) Optical band gap E_{04}, (c,d) defect absorption $\alpha_{1.0}$ and (e,f) E_{PL} for all HSL samples from the composition and thickness series and their corresponding single layers (left) before and (right) after annealing. The decrease of E_{04} as well as the increase of $\alpha_{1.0}$ and E_{PL} upon annealing indicate the formation of annealing-induced defects.*

sample S1. Three characteristic parameters were extracted from the PDS and PL data for all samples before and after annealing, namely the optical band gap energy E_{04}, which is defined as the energy with $\alpha = 10^4$ cm^{-1}, as a measure for the optical band gap, the defect absorption coefficient $\alpha_{1.0}$, which is the absorption coefficient at $E = 1.0$ eV, as a measure for the defect absorption in the case of intrinsic materials, and the PL peak energy E_{PL}. The PL intensities I_{PL} (not shown) of the annealed samples were significantly weaker than those of the as-deposited samples. Compared to the PL signal of the annealed SiC single layer, the PL signals of the annealed SiO_x were more intense.

Figure 4.24 summarizes E_{04}, $\alpha_{1.0}$ and E_{PL} for all HSL samples from the compo-

sition and thickness series (symbols) and their corresponding single layers (horizontal lines) before and after annealing. The E_{04} (Fig. 4.24(a,b)) of the SiC single layer was red-shifted upon annealing. For SiO_x single layers, the E_{04} shows an increasing trend with increasing oxygen content. However, the E_{04} decreased slightly for the $SiO_{0.8}$ and $SiO_{1.0}$ single layers upon annealing, while it increased for the $SiO_{1.2}$ single layer. In Si-richer $SiO_{0.8}$ and $SiO_{1.0}$ layers, the replacement of the Si-H bonds by weaker Si-Si bonds gives rise to the decrease of E_{04} upon annealing, whereas the increase of E_{04} in O-richer $SiO_{1.2}$ layer is attributed to the formation of oxygen-rich matrix phase with higher optical band gap during the phase separation upon annealing (Sec. 4.4.4). After annealing, the E_{04} of the SiC single layer is smaller than those of the SiO_x single layers. All HSL samples have in common that their E_{04} decreased upon annealing. In addition, their E_{04} are arranged between or close to those of the SiC and SiO_x single layer references. This indicates that the optical band gap of the HSL samples might be a effective value of the single layers. Comparison between HSL samples with different oxygen content of the SiO_x sublayers, e.g., S2, S5 and S8, reveals a slightly increasing trend of E_{04} with increasing c_O, which is consistent with the E_{04} trend of the SiO_x single layers. Hence, the E_{04} results are explainable without taking into consideration quantum confinement of Si-QDs.

The $\alpha_{1.0}$ (Fig. 4.24(c,d)) of the SiC single layer increased by nearly three orders of magnitudes upon annealing. Even though the defect absorption did also increase during the annealing for the SiO_x samples, it is still by a factor 10 lower than that of the annealed SiC single layer. All SiO_x single layers exhibit comparable $\alpha_{1.0}$ both in as-deposited state and after annealing. Similar to E_{04}, the $\alpha_{1.0}$ of the HSL samples are arranged between or close to those of the SiC and SiO_x single layer references. An increase of $\alpha_{1.0}$ upon annealing was observed for all HSL samples in agreement with the single layer results. This also indicates that the defect absorption of the HSL samples is determined by those of the single layers. The S3, S6 and S9 with a thinner SiC layer exhibit lower $\alpha_{1.0}$ than other HSL samples after annealing, which supports the idea that the high defect absorption in annealed SiC sublayers dominates the HSL results.

The E_{PL} (Fig. 4.24(e,f)) of the SiC single layer was blue-shifted upon anneal-

ing. Before annealing, the E_{PL} of the SiO_x single layers show an increasing trend. During annealing, the E_{PL} of all SiO_x single layers moved to higher values. However, the PL peak energies of the single layers now show a decreasing trend. The E_{PL} was found to be smaller than the E_{04} both before and after annealing as expected. An increase of E_{PL} upon annealing was observed for all HSL samples in agreement with the single layer results. Before annealing, the PL peaks are in the sub-band gap regimes for both the single layer and the HSL samples. Thus, these PL signals can be attributed to radiative recombination via disorder-related states [140]. Upon annealing, the PL peak energies shift to higher energies. The origin of this PL peak shift is discussed in Sec. 4.4.4. Unfortunately, a clear evidence of enhanced quantum confinement (PL blue-shift) [20] with decreasing Si-QDs sizes is lacking.

The attempt to gather information on Si-QDs from optical properties was hindered by other effects that occurred during annealing. The decrease of E_{04} and I_{PL} as well as the increase of $\alpha_{1.0}$ and E_{PL} mainly in the SiC but also in the SiO_x sublayer might be explained as follows. During annealing, hydrogen is released out of the PECVD grown materials (Sec. 4.2.4), as a result of which the E_{04} decreases due to the reversed hydrogen chemical alloying effect [141]. The hydrogen release depassivates the Dangling Bond (DB), which act as recombination center and thus decreases radiative recombination (I_{PL}) and increases defect absorption ($\alpha_{1.0}$). The apparent blue-shift of E_{PL} might be simply a quenching of radiative recombination at lower energies. Thus, the formation of annealing-induced defects mainly in SiC is evident, which will likely limit the usability of the SiC/SiO_x HSL as a Si-QD absorber.

4.4. Thermal annealing and hydrogen passivation of SiC/SiO_x HSL

Even though the analysis of the structural properties confirms the successful deposition of HSL with desired thicknesses and compositions as well as formation of Si-NCs in the oxide layers, the optical investigations indicate the generation of additional defect states during the post-deposition annealing. In order to verify the aforementioned assumption on the formation of annealing-induced defects and to

gain insight into the nature of the these defects in SiC and SiO_x materials and their multilayer systems, the temperature dependent evolution of the structural, optical and electrical properties of HSL, SiC and SiO_x samples was investigated. In addition, defect passivation by post-annealing hydrogen reincorporation using various techniques was tested for both the HSL samples and single layer reference samples by comparing material properties measured before and after passivation, respectively. The first part of this section deals with the temperature dependence of structural changes needed for later interpretations, followed by the description of thermally activated release of hydrogen as a main source for the defect creation during annealing. Then, the effectiveness of the different passivation techniques on the different types of samples are related to the different hydrogen reincorporation mechanisms. The last part discusses the effects of annealing and passivation on the optoelectronic properties of the samples.

4.4.1. Structural evolution during annealing

Crystallization

$SiC/SiO_{1.2}$ HSL films with 20 periods of nominal 2 nm SiC and 4.5 nm $SiO_{1.2}$ layers and their corresponding SiC (250 nm) and $SiO_{1.2}$ (215 nm) single layers were deposited on amorphous quartz and <100>-oriented mono-crystalline silicon substrates. Details on the PECVD deposition conditions are given in Sec. 4.3.2. The deposition was followed by thermal annealing in the new annealing furnace at various annealing temperatures $T_a = 750$ °C, 850 °C, 950 °C, 1000 °C, and 1050 °C under N_2 flow for an annealing time $t_a = 1$ h. The $SiO_{1.2}$ was used, since the Si-NCs were shown to be mainly constrained in the $SiO_{1.2}$ layer and not extend into adjacent SiC layers (sec. 4.3.2).

Figure 4.25 presents the GIXRD patterns and the FTIR spectra of HSL, SiC and $SiO_{1.2}$ samples for different T_a. In SiC single layers (Fig. 4.25(b)), GIXRD diffraction peaks from SiC crystals start to appear after annealing at $T_a = 950$ °C and become more pronounced towards $T_a = 1050$ °C. In $SiO_{1.2}$ samples (Fig. 4.25(c)), the GIXRD patterns show rising reflexes of Si crystals, as T_a increases from 950 °C to 1050 °C. However, no crystalline signals were observed below $T_a = 950$ °C for

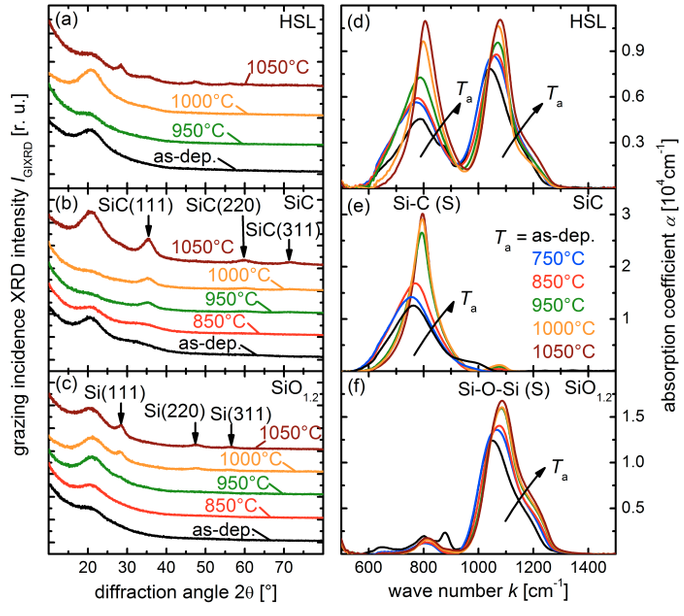

Figure 4.25.: *(a-c) GIXRD patterns and (d-f) FTIR spectra of HSL, SiC and $SiO_{1.2}$ samples after annealing at different temperatures $T_a = 750$ °C, 850 °C, 950 °C, 1000 °C, and 1050 °C under N_2 flow for an annealing time $t_a = 1$ h. The temperature dependence of crystallization, structural densification and phase separation processes is provided. As compared to the single layers, these processes take place in HSL at higher temperatures.*

both single layers. The GIXRD spectra of the HSL samples (Fig. 4.25(a)) do not reveal any crystalline diffraction peaks up to $T_a = 1000$ °C. Only at $T_a = 1050$ °C, reflexes from both SiC and Si crystals are identified. Hence, the crystallization of SiC in SiC sublayers and Si in $SiO_{1.2}$ sublayers is shifted to higher temperatures as compared to the single layers. Besides, the formation of SiC- and Si-NCs always occurs simultaneously at the same temperature. This finding excludes the possibility to realize Si-NCs without the formation of rather unfavored SiC-NCs in the barrier layers (Sec. 2.1.2).

The average size of the crystals was determined using the Scherrer formula (Eq. 4.1). Figure 4.26(a,b) shows increasing nanocrystal size with rising temperature.

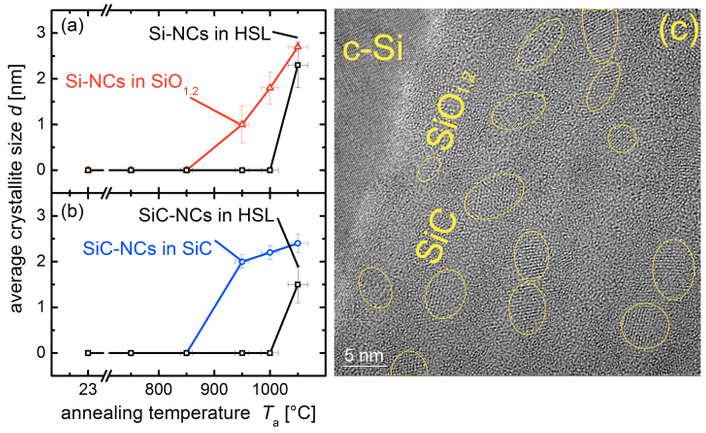

Figure 4.26.: *Average crystallite sizes d determined using the Scherrer formula from GIXRD data (Fig. 4.25(a-c)) as a function of annealing temperature T_a for (a) Si-NCs and (b) SiC-NCs. The formation of SiC- and Si-NCs always occurs simultaneously at the same temperature. (c) Cross-sectional HRTEM of the HSL sample on c-Si substrate after annealing at $T_a = 1050$ °C. The lattice fringes in the $SiO_{1.2}$ layers are highlighted with circles. The formation of isolated Si-NCs constrained in oxide matrix layer is demonstrated.*

The average SiC-NCs size in the SiC single layers annealed at 950 °C, 1000 °C and 1050 °C are 2.0 nm, 2.2 nm and 2.4 nm, respectively. The Si-NCs in the $SiO_{1.2}$ single layers have an average size of < 1.0 nm, 1.8 nm and 2.9 nm for $T_a =$ 950 °C, 1000 °C and 1050 °C, respectively. The HSL sample annealed at 1050 °C contains 1.9 nm sized SiC-NCs and 2.9 nm sized Si-NCs. The GIXRD patterns could be fitted without taking into consideration contributions from graphitic phase. Correspondingly, the cross-sectional HRTEM of the HSL sample on c-Si substrate after annealing at $T_a = 1050$ °C is shown in Fig. 4.26(c). The lattice fringes in the $SiO_{1.2}$ layers are highlighted with circles showing Si-NCs with varying crystal diameters.

Structural densification and phase separation

During annealing, the predominant Si-C (S) peak intensity continuously increases, pointing at an increase of Si-C bond density (Fig. 4.25(e)). These additional Si-C

bonds are created from the breaking of Si-H and C-H bonds, while hydrogen effuse out of the material in form of H_2 [142]. This is consistent with the decrease of Si-H (S) and C-H (S) absorption with increasing T_a (not shown). The thermally activated release of hydrogen is discussed in more detail in Sec. 4.4.2. Besides the increase of intensity, the Si-C (S) peak undergoes change in peak shape with annealing. In particular, the abrupt change of the Si-C (S) peak shape from Gaussian-like to Lorentzian-like was observed between 850 °C and 950 °C, which indicates the formation of crystalline SiC [32] in agreement with the corresponding GIXRD results. Thus, the crystallization of SiC is confirmed as a rather abrupt process in agreement with the observation from Sec. 4.1.1. However, a shift of the Si-C (S) peak to higher wavenumber is already observed at lower temperatures, which suggests an ongoing increase in network order (structural densification) before SiC crystallizes [143]. In addition, an insignificant Si-O-Si (S) peak increases with increasing T_a, which affirms an enhanced surface oxidation at higher temperatures (Sec. 4.2.1). For the $SiO_{1.2}$ single layers (Fig. 4.25(f)), the predominant asymmetric Si-O-Si (S) peak shows both increasing intensity and wavenumber with increasing annealing temperature, which is an unambiguous hint to phase separation of $SiO_{1.2}$ into Si and SiO_2 phases (Sec. 4.2.2) via thermally activated atomic diffusion.

The vibration modes observed in SiC and $SiO_{1.2}$ single layers are superposed in the FTIR spectra of the HSL samples. It is important to note that no additional FTIR signals could be detected. The Si-C (S) mode characteristic for SiC and the Si-O-Si (S) mode characteristic for SiO_x are clearly distinguishable from the mixed spectra. These absorption peaks are still able to deliver information on the SiC and $SiO_{1.2}$ sublayers separately. However, the presented absorption coefficients of the HSL samples were obtained by normalizing the measured FTIR intensity to the total film thickness, which is the sum of both SiC and $SiO_{1.2}$ layer thicknesses. Thus, the α values of the HSL sample appear misleadingly smaller than those of the single layers. Individually normalizing the intensity of SiC-related ($SiO_{1.2}$-related) signals by the sum of the SiC ($SiO_{1.2}$) thicknesses would have been necessary for quantitative comparison with the single layer results. Nevertheless, similar processes that were observed for single layers, e.g., the densification in SiC and the phase separation in $SiO_{1.2}$, were found in the HSL samples as well. However, the change of the Si-C (S) peak shape takes place more smoothly up to $T_a = 1050$ °C, since the SiC-NCs

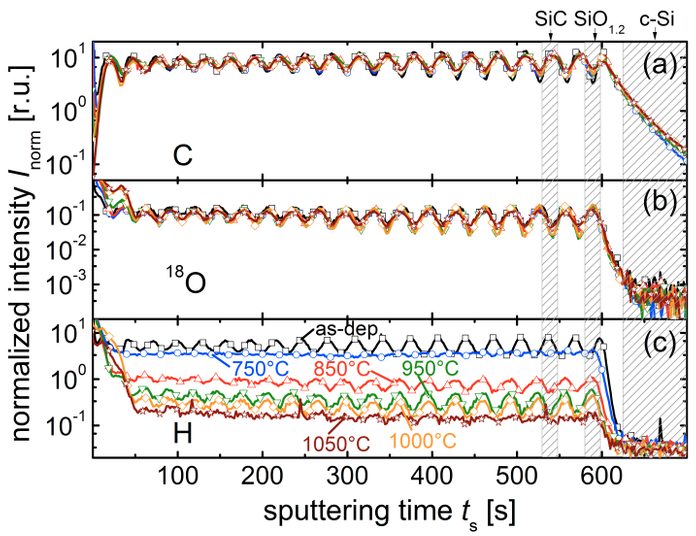

Figure 4.27.: *SIMS depth profiles of the (a) C, (b) ^{18}O and (c) H intensities normalized to the ^{30}Si intensities before and after annealing at various temperatures T_a for the HSL samples introduced in Sec. 4.4.1. The sputtering time $t_{sputter}$ is used for the x-axes. The shaded areas highlight the positions of a SiC and a $SiO_{1.2}$ sublayer as well as the c-Si substrate. The C and ^{18}O intensities show little change upon annealing as compared to the H intensity that continuously decreases as T_a rises.*

formation in HSL is delayed to higher temperature as shown by GIXRD. Moreover, the Si-O-Si (S) peak position was somewhat lower for HSL than for $SiO_{1.2}$ at the same T_a indicating a temperature delay of the phase separation in the oxide sublayers in HSL, which might be the reason for the delayed Si crystallization as compared to $SiO_{1.2}$ single layers.

4.4.2. Hydrogen effusion

Thermally activated release of hydrogen

Figure 4.27 shows the SIMS depth profiles of the C, ^{18}O and H intensities normalized to the ^{30}Si intensities before and after annealing at various temperatures T_a for the

HSL samples introduced in Sec. 4.4.1. The sputtering time t_{sputter} is used for the x-axes instead of a depth, since the sputtering rate is unknown. The shaded areas highlight the positions of a SiC and a $SiO_{1.2}$ sublayer as well as the c-Si substrate. The oscillation of the C and ^{18}O intensities arises from the $SiC/SiO_{1.2}$ multilayer structure. The C intensity maxima (minima) and the ^{18}O intensity minima (maxima) correspond to the SiC ($SiO_{1.2}$) layers. The sputtering rate and thus the depth resolution (the dynamic of the oscillations) depend much on the sputtering energy and the probed material itself. The amplitude of the oscillation is slightly reduced with increasing T_{a} indicating some blurring of the $SiC/SiO_{1.2}$ interfaces. Nevertheless, the C and ^{18}O intensities show little change upon annealing as compared to the H intensity, which excludes a significant inter-diffusion of carbon or oxygen into adjacent layer. The increase (decrease) of ^{18}O (C) intensity towards the sample surface from $t_{\mathrm{sputter}} = 50$ s to 0 s becomes more obvious with rising T_{a}, which indicates an advancing surface oxidation with temperature. Nevertheless, only the uppermost $SiO_{1.2}/SiC/SiO_{1.2}$ layers were affected even at the highest temperature.

The H intensity decreases continuously as T_{a} rises. Prior to annealing, the $SiO_{1.2}$ layers contain less H than the SiC layers, whereas the opposite behavior is observed after annealing. Hence, the as-deposited SiC contains more bonded hydrogen than the as-deposited $SiO_{1.2}$ that was fabricated under similar deposition conditions. The presence of carbon atoms in SiC promotes H incorporation during deposition in the form of strong C-H bonds additionally to the Si atoms [144] (Sec. 4.1.1). Besides, the presence of oxygen atoms in $SiO_{1.2}$ reduces H incorporation during deposition, since OH groups tend to form the energetically more favored H_2O with another H atom [145]. This is consistent with the decrease of H content with increasing oxygen content in PECVD grown a-SiO_x materials (Sec. 5.1.2). However, the solubility for molecular hydrogen H_2 is much higher in silicon oxide with micro-porous cage structure [137] than in silicon carbide with dense diamond structure giving rise to the reversed hydrogen content ratio in SiC and $SiO_{1.2}$ layers after annealing. This is in agreement with the observation that the hydrogen depth profile correlates with the oxygen depth profile after annealing.

In order to analyze the hydrogen release mechanisms in SiC and SiO_x materials and their multilayer systems, hydrogen effusion experiments were carried out. Figure

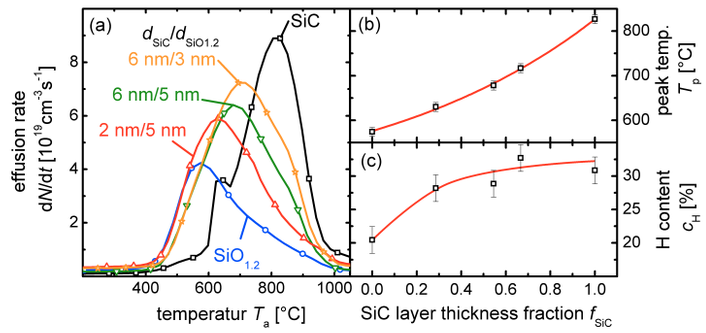

Figure 4.28.: *(a) Hydrogen effusion rate dN_H/dt of as-deposited SiC and $SiO_{1.2}$ single layers as well as of HSL samples with different sublayer thickness combinations versus annealing temperature T_a. (b) Peak temperature T_p and (c) H content c_H versus the SiC layer thickness fraction f_{SiC}. The T_p and c_H decrease with decreasing f_{SiC}, which might be due the relatively thinner SiC layers, in which the hydrogen atoms H can easily diffuse into adjacent relatively thicker $SiO_{1.2}$ layers with higher H_2 solubility and form molecular hydrogen H_2.*

4.28(a) presents the hydrogen effusion rate dN_{H}/dt of as-deposited SiC and $\mathrm{SiO}_{1.2}$ single layers as well as HSL samples with different sublayer thickness combinations versus annealing temperature T_{a}. The general absence of a low temperature peak near 400 °C, which would have been characteristic for the presence of interconnected void network, indicates that the hydrogen release happens only via out-diffusion of atomic H for the present samples [146]. This is, besides the well restricted surface oxidation, another evidence for the high compactness of the deposited materials. The feature between 600 °C and 670 °C of the SiC sample is ascribed to blister and bubble formation [99]. The results also reveal that the hydrogen in SiC is mainly released at higher temperatures than $\mathrm{SiO}_{1.2}$ due to the higher bonding energy of C-H bonds as compared to Si-H bonds [144] as well as due to different H diffusion coefficients for SiC and $\mathrm{SiO}_{1.2}$ materials. The latter is supported by the results of the hydrogen reincorporation experiments (Sec. 4.4.3).

Figures 4.28(b,c) display the peak temperature T_{p} and the H content c_{H} plotted versus the SiC layer thickness fraction f_{SiC}, which is defined as the ratio between d_{SiC} and $d_{\mathrm{SiC}} + d_{\mathrm{SiO}_{1.2}}$. The c_{H} is defined as the ratio between the hydrogen concentration

N_H and the total atomic concentration $N + N_H$, where N is the atomic density of the respective material. Here, the atomic density of silicon ($N = 5 \times 10^{22}$ cm^{-3}) was used as a first approximation. The calculation of N_H from the dN_H/dt data is described in Ref. [146]. The T_p and c_H increase with increasing f_{SiC} from 0 ($SiO_{1.2}$ single layer) to 1 (SiC single layer). The increase of c_H with increasing f_{SiC} is logically related to the increasing volume of SiC material with higher H content. The continuous lowering of T_p for HSL with decreasing f_{SiC} might be due the relatively thinner SiC layers, in which the hydrogen atoms H can easily diffuse into adjacent relatively thicker $SiO_{1.2}$ layers with higher H_2 solubility and form molecular hydrogen H_2. This assumption is in agreement with the evolution of the H depth profiles upon annealing (Fig. 4.27(c)).

Defect creation during annealing

In a first approach towards the understanding of defect creation in these materials, the relationship between the temperature dependence of the defect density and that of the hydrogen effusion was studied with regard to structural evolution during annealing. Figure 4.29(a) displays the temperature dependent dN_H/dt measured on as-deposited HSL, SiC and $SiO_{1.2}$ samples, from which the concentration of the hydrogen N_H that has been released from the samples between room temperature and the annealing temperature T_a was calculated (Fig. 4.29(b)). The amount of effused hydrogen N_H first increases strongly with increasing temperature and then slowly saturates above the peak temperature.

ESR spectra of SiC (not shown) contain a single nearly Lorenzian line with a g-value of 2.0037 - 2.0040 and peak to peak line width of 5.6 G before and throughout the whole annealing procedure. The resonance line of $SiO_{1.2}$ is a single line as well with a peak-to-peak line width of 7.4 G. It has a slightly asymmetric shape similar to the ESR lines of DBs in amorphous silicon. The g-value in the as deposited $SiO_{1.2}$ is 2.0045 and it experiences a slight shift to 2.0047 during annealing. A calibrated sputtered a-Si sample was used as a secondary standard for spin density calibration [100]. The spin density is used as an estimate of the density of spin resonant defect states in SiC, $SiO_{1.2}$ and HSL samples. In Fig. 4.29(d), the spin density N_s from ESR measurements (symbols) is plotted versus the annealing temperature T_a. The

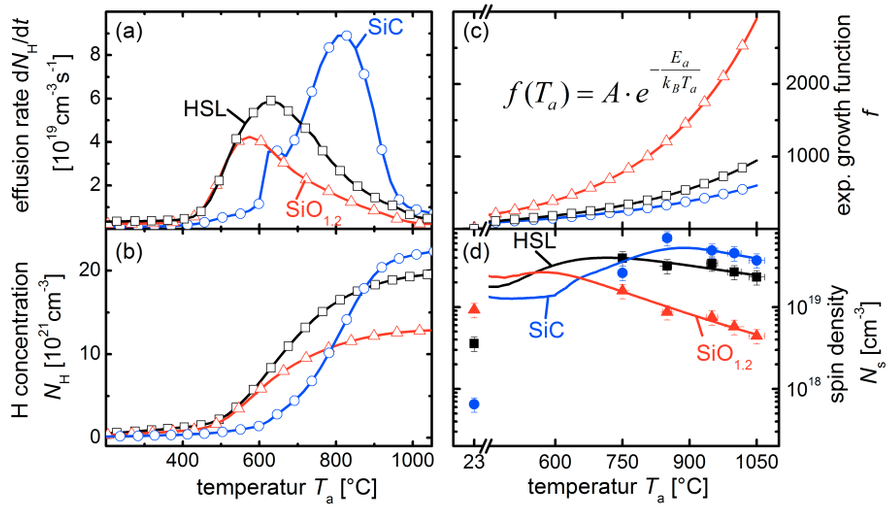

Figure 4.29.: *(a) Temperature dependent dN_H/dt measured on as-deposited HSL, SiC and $SiO_{1.2}$ samples. (b) Effused hydrogen concentration N_H calculated from corresponding dN_H/dt data. (c) Exponential growth functions f as a relative measure of the efficiency of DB healing adjusted for each sample type to fit the ESR results with N_H. (d) Spin density N_s from ESR measurements (symbols) as well as the N_H/f curves versus the annealing temperature T_a. The excellent fits of the ESR results above* 450 °C *for all three types of samples suggest a sufficient description of the temperature dependence of N_s by a simple model.*

as-deposited state is depicted as $T_\mathrm{a} = 23$ °C. It was possible to fit the spin density data by the effused hydrogen concentration N_H from Fig. 4.29(b) divided by a DB recombination probability shown in Fig. 4.29(c) (lines), which is described below.

The spin density in all three sample types increases initially with annealing, but at higher T_a a decreasing trend for N_s is observed. There is no abrupt change of the spin density in the range of T_a where crystallization took place (Sec. 4.4.1). Thus, there is no indication of a formation of defect states specific for the crystalline volume or to the amorphous/crystalline interface. The decrease of N_s in $SiO_{1.2}$ material cannot be attributed to passivation of Si-NC interface by SiO_2 surrounding only, since the decrease of N_s starts at temperatures much below the onset of Si

crystallization. For SiC material and probably also for $SiO_{1.2}$ material, the decrease of N_s is likely due to the recombination of DBs during the structural reconstruction. Inter-diffusion in HSL structure should have minor effect on N_s, since the N_s values of HSL samples are between those of the single layers towards higher temperatures, where inter-diffusion processes are enhanced.

Based on the above considerations, a simple model to describe the temperature dependence of the spin density is proposed. The model includes the temperature dependences of hydrogen effusion and DB healing. Upon annealing, hydrogen effuses out of the films, leaving behind DBs. If the creation of new DBs is proportional to the total amount of hydrogen effused at each temperature, the dependence of hydrogen concentration on temperature in Fig. 4.29(b) represents the DB creation upon annealing. At the same time, some of these DBs are healed due to bond reconstruction. The formation of new bonds is expected to be governed by the thermal motion of the elements. In addition, the reduction of DBs involves sufficient probability for the presence of neighboring DBs, which is likely to increases if atoms can exchange places via diffusion in the material. The phase separation in $SiO_{1.2}$ shows that diffusion processes do take place at least in this material. Since atomic diffusion in $SiO_{1.2}$ due to the strong driven force towards phase separation is expected to be higher than in SiC, reconstruction of DBs in SiC material is considered to be not as efficient as in $SiO_{1.2}$ material. Since the element motion and the atomic diffusion are thermally activated, the healing of DBs is expected to increase exponentially with temperature, which can be expressed by a recombination probability in exponential form:

$$f(T_a) = A \exp\left(\frac{-E_a}{k_B T_a}\right) \quad \forall\ 450\ ^\circ\mathrm{C} \leq T_a \leq 1050\ ^\circ\mathrm{C} \quad , \tag{4.2}$$

where E_a is the activation energy for the DB healing, k_B is the Boltzmann constant and the pre-exponential factor A is a relative measure of the efficiency of DB healing. The annealing temperature T_a in the equation uses Kelvin as unit. By adjusting the parameters E_a and A for each sample type, the effused hydrogen concentrations divided by the exponential growth functions give excellent fits of the ESR results above 450 °C for all three types of samples showing that the very simple model

seems to be sufficient to describe the temperature dependent evolution of N_s. At temperatures below 450 °C, both the hydrogen concentrations and the exponential growth functions are small, hence, division of the two does result in large error bars and cannot be considered to be accurate. The reciprocal of these exponential growth functions describes the reduction of DBs due to the dangling bond healing. The combination of both trends, namely the increase in DB density due to hydrogen effusion and the reduction of the DB density due to the bond reconstruction, would explain the initial increase and then the decreases of N_s with increase of annealing temperature. Furthermore, the fit reproduces the different positions of the maximum N_s located near 700 °C, 900 °C and 570 °C for HSL, SiC and $SiO_{1.2}$, respectively.

It is important to note that this model does not draw conclusions on any information on the exact number of healed DBs from the exponential growth function, since the exact number of created DBs is also unknown despite of the assumed proportionality of the creation of DBs and the total amount of effused hydrogen. Thus, the absolute values of the exponential growth functions cannot be translated into any physical quantities. However, comparison of these values as a relative measure of the efficiency of DB healing between the different sample types appears reasonable. Furthermore, the form of the curves and the exponent are independent from the absolute values. While the activation energies for HSL (0.31 eV) and SiC single layers (0.38 eV) are comparable, the $SiO_{1.2}$ single layer (0.56 eV) needs much higher energy for DB healing. The A for HSL (1.1×10^4) is comparable to that for SiC single layers (1.5×10^4), while a much higher A was need for $SiO_{1.2}$ single layers (3.8×10^5). Since the annealing-induced defect densities in HSL are dominated by the high defect densities from the SiC layers (Sec. 4.3.2), the healing of DBs in SiC sublayer dominates the E_a and A for HSL. The correlation of increasing A with increasing E_a is known as the Meyer-Neldel rule, which is explained by the thermal activation of frozen-in silicon alloy network supporting the assumption of element motion [146]. However, the higher A of the $SiO_{1.2}$ as compared to SiC might partially arise from a more efficient DB healing in $SiO_{1.2}$ due to the higher O diffusion in silicon oxide than Si or C diffusion in SiC.

In conclusion, crystallization, atomic diffusion (phase separation), structural reconstruction (densification) and hydrogen effusion take place upon annealing with

different characteristic temperature dependences, whereas the creation of additional DBs due to hydrogen out-diffusion and the healing of DBs due to element motion during the structural reconstruction likely dominate the annealing-induced defect creation. The more significant increase of spin density upon annealing in SiC as compared to $SiO_{1.2}$ is ascribed to the effusion of a higher amount of hydrogen and the less efficient atomic diffusion up to the annealing temperature of 1050 °C. It is worthwhile to stress that this model does not exclude the presence of other types of paramagnetic defect states reported in the literatures [147–150], which might exist in the SiC and SiO_x volumes as well as at the Si/SiO_x and SiC/SiO_x interfaces for the samples under investigation in this work. This model assumes that in the case of hydrogenated SiC and SiO_x materials containing a high amount of hydrogen, the DB density due to hydrogen out-diffusion during annealing is likely to dominate the spin density.

4.4.3. Hydrogen reincorporation

Hydrogen reincorporation mechanisms

Since dangling bonds were identified as a major source of annealing-induced defects, their passivation is expected to be crucial for the establishment of high quality SiC/SiO_x HSL Si-QD absorber. Hence, hydrogen reincorporation into annealed HSL samples and single layer references was tested using hydrogen plasma in a PECVD reactor, hydrogen dissociation catalysis in a HWCVD reactor and annealing in forming gas atmosphere (Forming Gas Annealing (FGA)). For the post-annealing hydrogen reincorporation using HWCVD, a substrate temperature $T_{sub} = 250$ °C, a H_2 flow rate $f_{H_2} = 30$ sccm, a wire temperature $T_{wire} = 1600$ °C, a deposition pressure $p = 0.1$ mbar and an electrode spacing $d_{ele} = 7$ cm were applied for a treating time of 1 h. For the 1 h PECVD hydrogen plasma passivation, $T_{sub} = 350$ °C, $p = 6$ mbar, plasma frequency $f = 94.7$ MHz, power density $P = 0.54$ W/cm^2, $d_{ele} = 12$ cm and $f_{H_2} = 500$ sccm were used. The forming gas annealing passivation was carried out at $T_a = 450$ °C for $t_a = 1$ h in a quartz tube annealing furnace under 5% H_2 forming gas flow.

Figure 4.30 displays the SIMS depth profiles of the H intensities normalized to

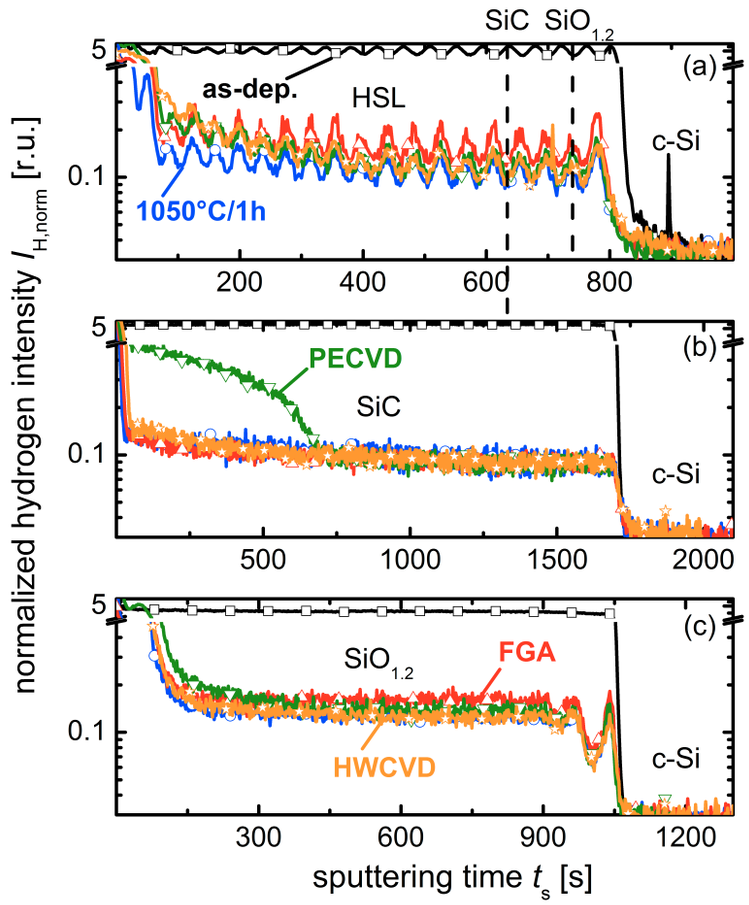

Figure 4.30.: *SIMS depth profiles of the H intensities, normalized to the ^{30}Si intensities, before annealing, after annealing at 1050 °C for 1 h and after passivation using FGA, PECVD and HWCVD techniques for (a) HSL, (b) SiC and (c) $SiO_{1.2}$ samples. Hydrogen in-diffusion with FGA is most effective for $SiO_{1.2}$ single layer and HSL samples, while PECVD is only effective for SiC single layers. The deviating effectiveness of the different techniques on the different types of samples is assumed to arise from the different diffusion mechanisms (hopping or interstitial diffusion) of the different hydrogen sources (atomic or molecular hydrogen).*

the ^{30}Si intensities before annealing, after annealing (1050 °C/1 h) and after passivation (FGA, PECVD and HWCVD) for HSL, SiC and $SiO_{1.2}$, respectively. The H intensities are around 1 - 2 orders of magnitude higher for the as-deposited samples than for the annealed and/or passivated samples. After the FGA passivation, the H intensities increased homogeneously over the whole sample depth for HSL and $SiO_{1.2}$ single layer as compared to the annealed samples, but remain unchanged in the SiC single layer. The PECVD passivation increases the H intensities close to the sample surface for all sample types, but most effectively for the SiC single layer. Passivation with HWCVD incorporates hydrogen only into HSL sample with a comparable H depth profile as in case of PECVD. Thus, passivation with FGA is most effective for $SiO_{1.2}$ single layer and HSL samples, while PECVD is only effective for SiC single layers, which is explained as follows.

During FGA, molecular hydrogen H_2 adsorbs at the surface, desorbs from the surface again or diffuses into the material via interstitials and dissociates into H radicals at vacancies [151]. The H radicals then dock at the dangling bonds and saturate them. A high solubility of H_2 promotes the effectiveness of the FGA passivation in two ways: (1) more H_2 is present in the material, increasing the probability of H_2 to reach a vacancy and to dissociate into H radicals; (2) due to less desorption, a hydrogen-rich layer that acts as a H_2 source for the interstitial diffusion process is produced at the surface. If the H_2 interstitial diffusion coefficient is high enough, hydrogen can be introduced homogeneously over the whole sample thickness, since the in-diffusion of H_2 happens prior to the bonding of the dissociated H radicals. Therefore, FGA effectively reincorporates hydrogen and reduces the spin density in $SiO_{1.2}$ single layers, which have higher hydrogen solubility and higher H_2 interstitial diffusion coefficient than the SiC single layers [137]. Although $SiO_{1.2}$ contains inclusions of Si nanocrystals after annealing, the diffusion of H through the layer during passivation is believed to be primarily determined by the diffusion coefficient of H in the host matrix material. This is due to the fact that the Si nanocrystals are isolated and surrounded by the host $SiO_{1.2}$ tissue (Fig. 4.26(c)).

During PECVD passivation, the H_2 precursor gas is first dissociated into highly reactive H radicals in the plasma, which then reach the sample surface [152] and dock to the dangling bonds. The now bonded atomic hydrogen H then diffuses into

the material via hopping through bonding states or desorbs from the surface again in form of H or H_2 [153]. Since the H hopping diffusion comprises the breaking of existing bonds, weaker bonding energies support the PECVD passivation. Since the bonding energy of Si-C ($E_{\mathrm{bond}} = 3.3$ eV) is lower than that of Si-O ($E_{\mathrm{bond}} = 4.8$ eV) [128], the PECVD passivation is more effective for silicon carbide than for silicon oxide. The experimental observation that hydrogen reincorporation appears only close to the sample surface for PECVD passivation suggests that the H hopping diffusion coefficient is not high enough under the given process conditions. The same explanation is valid for HWCVD passivation, where the molecular hydrogen dissociation is catalytically initiated at the hot wire [154]. The HWCVD passivation is not as effective as PECVD passivation likely because the chosen parameters are not suitable for hydrogen reincorporation.

The surface material of the HSL sample is silicon oxide because of the deposition sequence and the surface oxidation during annealing. Thus, the H_2 solubility and diffusion coefficient are high, but the H diffusion coefficient is low at the surface. The FGA passivation works well for the HSL sample probably because H_2 can be better incorporated into the surface layer than H, which leads to higher probability for H_2 to diffuse to the next $SiC/SiO_{1.2}$ interface, dissociate into H radicals, which then bond to Si or C atoms and diffuse through the adjacent SiC layer via hopping diffusion. At the next $SiC/SiO_{1.2}$ interface, atomic hydrogen will form molecular hydrogen, in order to enter the next $SiO_{1.2}$ layer more effectively. From a more general point of view, the $SiO_{1.2}$ layers with high H_2 solubility can act as H_2 reservoirs for the adjacent SiC layers with low H_2 solubility. Thus, the process with H_2 source (FGA) is more advantageous in passivating HSL samples than that with H radical source (PECVD). The higher process temperature of the FGA annealing may also have contributed to the better hydrogen reincorporation in HSL.

Effectiveness of hydrogen passivation

With the successful in-diffusion of hydrogen into the HSL sample and its single layer references after annealing, the question arises whether these reincorporated hydrogen are able to saturate dangling bonds and thus reduce the defect density. It was possible to give a rough estimate of the hydrogen concentration in the annealed

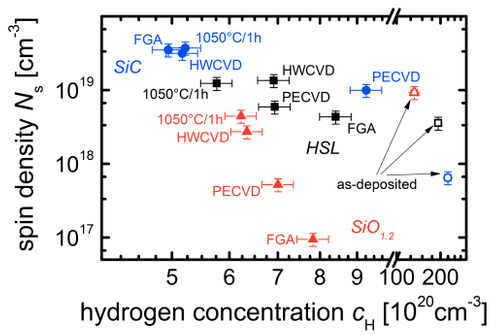

Figure 4.31.: *Hydrogen concentrations c_H plotted versus the spin densities N_s for HSL, SiC and $SiO_{1.2}$ in the as-deposited state, after annealing and after passivation using FGA, PECVD and HWCVD. The c_H is roughly estimated from the mean H intensity of the SIMS data by calibrating them to the hydrogen concentration determined from the effusion measurements. The hydrogen incorporation lowers the defect density as the hydrogen concentration increases, thus confirms the passivation of unsaturated bonds in the material.*

and/or passivated samples from the corresponding mean H intensities (SIMS) using the hydrogen concentration from the effusion measurements (Fig. 4.29(a)) as calibration. The underlying idea is that the hydrogen concentration from the effusion measurements must correlate with the difference between the mean H intensities of the as-deposited samples and of the annealed samples from the SIMS measurements (Fig. 4.30), if the same hydrogen sputtering efficiency in SIMS is assumed. Figure 4.31 shows these estimated hydrogen concentrations c_{H} plotted versus the spin densities N_{s} for HSL, SiC and $\mathrm{SiO}_{1.2}$ in the as-deposited state, after annealing and after passivation using FGA, PECVD and HWCVD.

As already discussed in Sec. 4.4.2, the N_{s} of the $\mathrm{SiO}_{1.2}$ single layer has slightly decreased and the spin density of the SiC single layer has significantly increased upon annealing at $T_{\mathrm{a}} = 1050$ °C. The subsequent passivation lowers the defect density as the hydrogen concentration increases, which confirms the passivation of unsaturated bonds in the material by reincorporated hydrogen. HWCVD passivation produced the smallest improvement, whereas PECVD is most efficient for SiC single layers and FGA is most suitable for $\mathrm{SiO}_{1.2}$ single layers and HSL samples. It is worthwhile to stress that although the passivation processes reduce the spin densities, the lowest

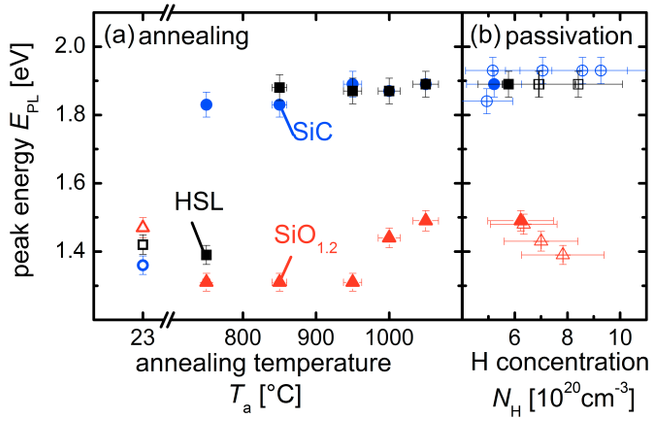

Figure 4.32.: *PL peak energy E_{PL} of SiC, $SiO_{1.2}$ and HSL samples plotted versus (a) the annealing temperature T_a for the annealing series and (b) versus the hydrogen concentration N_H for the passivation series. The as-deposited, annealed and passivated samples are represented by open, full and crossed symbols, respectively. The photoluminescence properties of HSL are more comparable to those of SiC single layers.*

defect density N_s is 10^{19} cm^{-3} for SiC single layer and 4.3×10^{18} cm^{-3} for HSL multilayer, which is still nearly two orders of magnitude higher than the lowest defect density of $N_s = 9.5 \times 10^{16}$ cm^{-3} in $SiO_{1.2}$ single layer.

4.4.4. Effects of annealing and passivation on optoelectronics

Radiative recombination

Figure 4.32 shows the PL peak energy E_{PL} of SiC, $SiO_{1.2}$ and HSL samples plotted versus the annealing temperature T_a for the annealing series (Sec. 4.4.1) and versus the hydrogen concentration N_H for the passivation series (Sec. 4.4.3). The as-deposited samples are represented by open symbols, while the annealed and passivated samples are shown in full and crossed symbols, respectively. In the as-deposited state, the E_{PL} of the $SiO_{1.2}$ single layer is the highest and that of the SiC single layer is the lowest. Upon annealing, the E_{PL} of the $SiO_{1.2}$ samples decreases first and then increases for $T_a \geq 950$ °C. Upon passivation, the E_{PL} is red-shifted

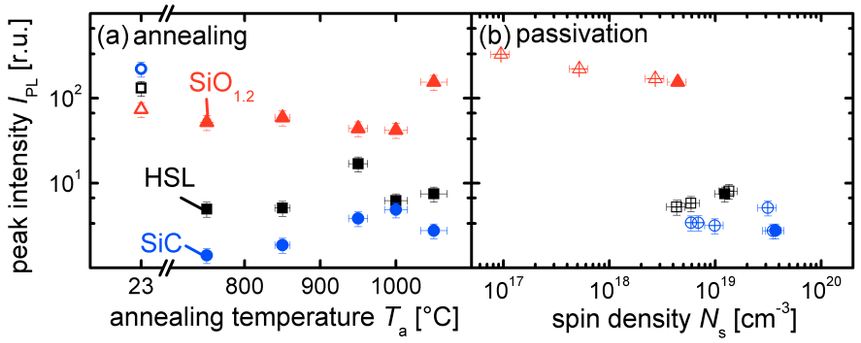

Figure 4.33.: *PL peak intensity I_{PL} of SiC, $SiO_{1.2}$ and HSL samples plotted versus (a) annealing temperature T_a for the annealing series and (b) versus spin density N_s for the passivation series. The as-deposited, annealed and passivated samples are represented by open, full and crossed symbols, respectively. The most intense $SiO_{1.2}$ PL signal at* 1050 °C *is ascribed to the luminescence of quantum confined Si-QDs confirming the excellent Si/SiO_2 interface quality.*

with increasing amount of reincorporated hydrogen. During annealing, the E_{PL} values of the SiC and HSL samples are strongly blue-shifted, both reaching a comparable value of around 1.8 eV - 1.9 eV at $T_{\mathrm{a}} = 750$ °C and 850 °C, respectively. The E_{PL} remains at this value not only upon further increase of T_{a}, but also upon passivation in spite of noticeable hydrogen reincorporation. These PL signals feature a larger broadness than those of the as-deposited samples (not shown).

Figure 4.33 displays the PL peak intensity I_{PL} plotted versus T_{a} for the annealing series and versus N_{s} for the passivation series. In the as-deposited state, the I_{PL} of the $SiO_{1.2}$ single layer is the highest and that of the SiC single layer is the lowest. For $SiO_{1.2}$ single layers, the I_{PL} first decreases slightly with increasing T_{a} and then increases for $T_{\mathrm{a}} \geq 1000$ °C reaching the highest I_{PL} at 1050 °C. During passivation, the I_{PL} increases continuously with decreasing N_{s}. The SiC and HSL samples have in common that I_{PL} first drops drastically from $T_{\mathrm{a}} = 23$ °C to 750 °C and then remains on a low level with further increase of T_{a}. The reduction of N_{s} after passivation does not result in noticeable change in I_{PL}.

For the as-deposited samples, all E_{PL} values lie below the corresponding E_{04}

values (Fig. 4.34). The simultaneous increase in E_{PL} with increasing E_{04} suggests that these as-deposited PL signals arise from radiative recombination via disorder-related band tail states as proposed by Ref. [140]. The higher (lower) I_{PL} at smaller (larger) N_s (Fig. 4.29) is likely a consequence of less (more) non-radiative recombination via dangling bonds.

The PL signals centered at around 1.3 eV observed in $SiO_{1.2}$ single layers is ascribed to the luminescence from a-Si clusters [155]. The emergence of the 1.3 eV signal agrees with the finding that phase separation of $SiO_{1.2}$ has already initiated at $T_a = 750$ °C (Sec. 4.4.1). Since now the $SiO_{1.2}$ material differs structurally from its initial state, the decrease of the pronounced disorder-related PL signal observed in the as-deposited $SiO_{1.2}$ is comprehensible. The subsequent increase of E_{PL} and I_{PL} correlates with the formation of quantum confined Si-QDs [156], which agrees with the fact that Si crystallization has already started at $T_a = 950$ °C (Sec. 4.4.1). Thus, the highest I_{PL} at 1050 °C confirms the excellent Si/SiO_2 interface quality. The hydrogen passivation results in even higher PL intensities. Under the assumption that the reduction of N_s by hydrogen reincorporation is at least partially due to the hydrogen saturation of Si DBs at the Si/SiO_2 interface, known as the P_b type defects [157], the increase in I_{PL} is assigned to higher radiative recombination from Si-QDs. Since the surface area and volume of Si-QDs increases with increasing crystallite size, the probability to contain non-radiative defects before passivation is expected to be higher in larger Si-QDs. Thus, H passivation should have a greater impact on the emission from larger Si-QDs than from smaller ones. A disproportionate increase in emission from larger Si-NCs with weaker quantum confinement then gives rise to an apparent redshift in the composite PL emission spectrum after annealing [158].

The weak PL signals around 1.8 eV observed in both annealed and passivated SiC and HSL samples are attributed to carbon-related defects, that cannot be passivated by hydrogen [159]. This is supported by the unimproved I_{PL} despite of noticeable reduction of N_s in SiC and HSL after passivation. This PL peak becomes visible due to the disappearance of the much more intense as-deposited PL signal as a consequence of significant increase in DB density as non-radiative recombination centers upon annealing (Fig. 4.29). The combination of $SiO_{1.2}$ and SiC layers in HSL is expected to provide PL signals arising from the oxide layers. However, the

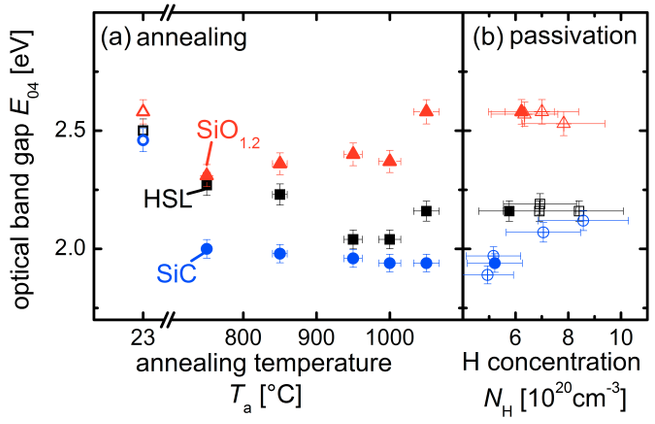

Figure 4.34.: *Optical band gap E_{04} of SiC, $SiO_{1.2}$ and HSL samples plotted versus (a) annealing temperature T_a for the annealing series and (b) versus hydrogen concentration N_H for the passivation series. The as-deposited, annealed and passivated samples are represented by open, full and crossed symbols, respectively. The decrease of E_{04} in SiC, $SiO_{1.2}$ and HSL during annealing as well as the increase of E_{04} in SiC during passivation can be ascribed to the hydrogen chemical alloying effect.*

photoluminescence properties of HSL are more comparable to those of SiC single layers. As a possible explanation, the charge carrier generated in the oxide layers might recombine via non-radiative recombination paths at the SiC/SiO$_{1.2}$ interfaces close to the defects in the carbide layers and thus prevent the luminescence from the oxide layers of the HSL structure.

Optically active defects

In Fig. 4.34(a), the E_{04} values for SiC, SiO$_{1.2}$ and HSL are plotted versus T_a. For SiC single layers, the E_{04} decreases continuously with increasing T_a, whereas for SiO$_{1.2}$ single layers, the E_{04} first decreases upon annealing and then increases continuously for $T_\mathrm{a} \geq 750$ °C. The E_{04} of the HSL samples, for which the values are always between those of the single layers, decreases with increasing T_a up to 1000 °C before it rises again. In Fig. 4.34(b), the E_{04} values for SiC, SiO$_{1.2}$ and HSL are plotted versus N_H. Despite of the large error bars, we observe that the E_{04}

of the SiC single layers increases by trend with increasing amount of reincorporated hydrogen, whereas the E_{04} of the $SiO_{1.2}$ and HSL samples show little change upon passivation.

During annealing, the continuous decrease of the E_{04} in SiC single layers can be ascribed to the inverse of the hydrogen chemical alloying effect. The hydrogen chemical alloying effect describes the widely observed phenomenon of the optical band gap widening of, e.g., hydrogenated amorphous silicon due to the incorporation of hydrogen, which is attributed to the replacement of the Si-Si bonds by stronger Si-H bonds moving states from the top of the valence bands to a position deep inside the valence bands [141]. During annealing, hydrogen effuses out of the films during annealing and creates dangling bonds, which then partially reconstruct by forming new bonds as proposed in Sec. 4.4.2. Thus, besides the increase in DB density, the hydrogen effusion gives rise to the partial replacement of Si-H and C-H bonds by weaker Si-C bonds moving states from a position deep inside the valence bands to the top of the valence bands resulting in the decrease of the E_{04}.

In $SiO_{1.2}$ single layers, the replacement of the Si-H bonds by weaker Si-Si bonds gives rise to the decrease of E_{04} upon annealing for $T_a \leq 850$ °C. The increase of E_{04} at higher T_a can be attributed to the formation of an oxygen-rich matrix phase with higher optical band gap during the phase separation of $SiO_{1.2}$ into Si-NCs and SiO_2 matrix (Sec. 4.4.1). In the case of the HSL samples, all characteristic parameters are between those of the SiC and $SiO_{1.2}$ single layer reference samples. This suggests that the material properties of the thin SiC and $SiO_{1.2}$ sublayers in HSL are comparable to those of the alone-standing references. Under this assumption, the decrease of E_{04} in HSL can be ascribed to the hydrogen chemical alloying effect in both SiC and $SiO_{1.2}$ sublayers. The temperature, at which the E_{04} increases, is shifted to a higher value as compared to that of $SiO_{1.2}$ single layers, which correlates with the delay of the phase separation in $SiO_{1.2}$ sublayers as compared to $SiO_{1.2}$ single layers (Sec. 4.4.1).

After hydrogen reincorporation, the increase of E_{04} for SiC single layers can also be explained by the hydrogen chemical alloying effect. Since the atomic H diffuses into the SiC material via hopping through bonding states, which comprises the breaking of existing bonds (Sec. 4.4.3), the reincorporated hydrogen does not

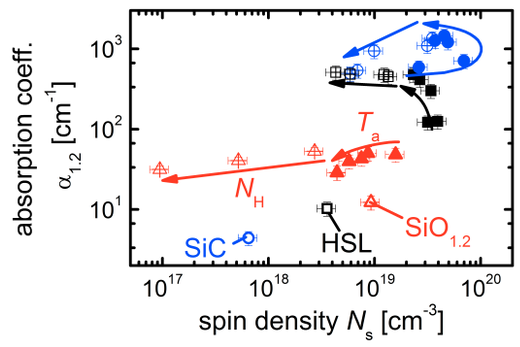

Figure 4.35.: *Sub-band gap absorption $\alpha_{1.2}$ of SiC, $SiO_{1.2}$ and HSL samples plotted versus the spin density N_s in as-deposited states (open symbol), upon annealing (full symbol) and after passivation (crossed symbol).The continuous increase of $\alpha_{1.2}$ with increasing T_a for SiC single layers and HSL samples is ascribed to the increase of dangling bonds at lower temperatures and to the increase of strained bonds at higher temperatures in SiC material.*

only saturate existing DBs, but also break up Si-C bonds by forming Si-H and C-H bonds, which results in the increase of E_{04}. Unlike in SiC material, molecular hydrogen diffuses into SiO_x material via interstitials and dissociates into H radicals at vacancies (Sec. 4.4.3), which implies that the reincorporated hydrogen mainly saturates existing DBs instead of breaking Si-Si bonds. This would explain why E_{04} shows little change upon passivation in $SiO_{1.2}$. Another possible explanation is the high optical band gap of the oxygen-rich matrix phase in the annealed state that prevents the hydrogen chemical alloying from showing any significant effect, even if the breaking of Si-Si bonds by hydrogen reincorporation takes place in SiO_x material. Hydrogen reincorporation into HSL sample is a more complicated process consisting of dissociation of H_2 into H for the hopping diffusion in SiC sublayers and formation of H into H_2 for the interstitial diffusion in $SiO_{1.2}$ sublayers. Since the $SiO_{1.2}$ sublayers with high H_2 solubility act as H_2 reservoirs for the adjacent SiC sublayers with low H_2 solubility (Sec. 4.4.2), the reincorporated hydrogen might exist mainly in the form of H_2 in the $SiO_{1.2}$ sublayers. Therefore, the passivation of SiC sublayers and consequently the hydrogen chemical alloying effect are weak, which explains the unchanged E_{04} for HSL samples upon passivation.

Figure 4.35 shows the sub-band gap absorption $\alpha_{1.2}$ plotted versus the spin density N_s for all three sample types in as-deposited states (open symbol), upon annealing (full symbol) and after passivation (crossed symbol). The arrows indicate the increase of T_a or N_H, respectively. For SiC single layers and HSL samples, upon annealing, the N_H first increases and then decreases, whereas the $\alpha_{1.2}$ continuously rises with increasing T_a. The 1050 °C SiC and HSL samples still exhibit higher N_s than the as-deposited SiC and HSL samples, respectively. For $SiO_{1.2}$ single layers, both $\alpha_{1.2}$ and N_s are increased as T_a rises from as-deposited to 750 °C. A decrease of both quantities is observed from $T_a = 750$ °C to 1050 °C with increasing T_a. It is important to note that the 850 °C $SiO_{1.2}$ sample shows higher sub-band gap absorption as compared to the as-deposited $SiO_{1.2}$ sample despite similar spin density. Overall, the in-crease of $\alpha_{1.2}$ and N_s upon annealing is most pronounced for SiC single layers, followed by HSL samples and $SiO_{1.2}$ single layers.

The SiC single layers show a decrease in $\alpha_{1.2}$ and N_s with the reincorporation of hydrogen. For HSL samples, the presence of reincorporated hydrogen gives rise to decreased N_s and slightly increased $\alpha_{1.2}$. The reincorporated hydrogen in $SiO_{1.2}$ single layers leads to the decrease of N_s. However, the $\alpha_{1.2}$ values of the passivated samples are higher than in the 1050 °C sample before passivation, even though the increasing amount of hydrogen seems to lower the $\alpha_{1.2}$ slightly when comparing only the passivated samples. The effectiveness of the different methods for different materials were discussed in Sec. 4.4.3.

The dependence of N_s as a measure for the DB density on annealing temperature is explained as an overlap of the temperature dependence of the creation of additional DBs due to hydrogen effusion and of the healing of DBs by forming new bonds (Sec. 4.4.2). As the temperature dependence of $\alpha_{1.2}$ does not correlate with that of N_s for SiC single layers and HSL samples, the sub-band gap absorption cannot be regarded as dangling bonds-related absorption only. Unlike for N_s, both the increase of DBs and new bonds might result in the increase of $\alpha_{1.2}$, when considering the newly formed bonds to be partially strained bonds, which can add to the sub-band gap absorption [160]. The probability of creating strained bonds in SiC material with 4-fold coordination is supposed be high due to the lack of efficient bond relaxation. In comparison, the SiO_x material with 2-fold coordination

has more possibilities to release stress. Hence, the continuous increase of $\alpha_{1.2}$ with increasing T_a for SiC single layers and HSL samples is ascribed to the increase of DBs at lower temperatures and to the increase of strained bonds at higher temperatures in SiC material. Since the formation of strained bonds is less pronounced in $SiO_{1.2}$ single layers, the $\alpha_{1.2}$ correlates with N_s during annealing via the amount of DBs. The fact that the 850 °C $SiO_{1.2}$ sample shows higher $\alpha_{1.2}$ as compared to the as-deposited $SiO_{1.2}$ sample despite similar spin density indicates contributions of strained bonds to the sub-band gap absorption even in $SiO_{1.2}$ single layers, which is also proposed by Ref. [161], where the authors supported their assumption with theoretical calculations.

A strong decrease of $\alpha_{1.2}$ with increasing amount of reincorporated hydrogen was observed only for SiC single layers, but not for $SiO_{1.2}$ single layers and HSL samples, even though the reduction of N_s is comparable in all three types of samples. The hydrogen reincorporation in SiC single layers might saturate existing DBs and break up strained Si-C bonds, which are expected to be energetically less favored. Since both processes reduce the $\alpha_{1.2}$ and only the saturation of existing DBs reduces the N_s, the decrease of $\alpha_{1.2}$ as a function of N_s is steep. The hydrogen reincorporation in $SiO_{1.2}$ single layers mainly saturate existing DBs, thus there is hardly any reduction of strained bonds-related absorption upon passivation in $SiO_{1.2}$ single layers resulting in less pronounced decrease of $\alpha_{1.2}$. Due to the weak hydrogen passivation of the SiC sublayers in HSL samples, no significant reduction of the absorption from strained bonds is expected. The higher $\alpha_{1.2}$ of the passivated samples as compared to that of the 1050 °C sample before passivation observed for $SiO_{1.2}$ single layers and HSL samples cannot be explained using the above mentioned models.

Annealing induced doping

Figure 4.36 presents the lateral dark conductivity σ_{dark} of SiC, $SiO_{1.2}$ and HSL samples plotted versus T_a for the annealing series and versus N_s for the passivation series. In the as-deposited state, all three types of samples show σ_{dark} values below 10^{-11} S/cm, which is typical for intrinsic silicon dielectrics. The σ_{dark} remained unchanged during annealing for the $SiO_{1.2}$ single layer, while it increased by several

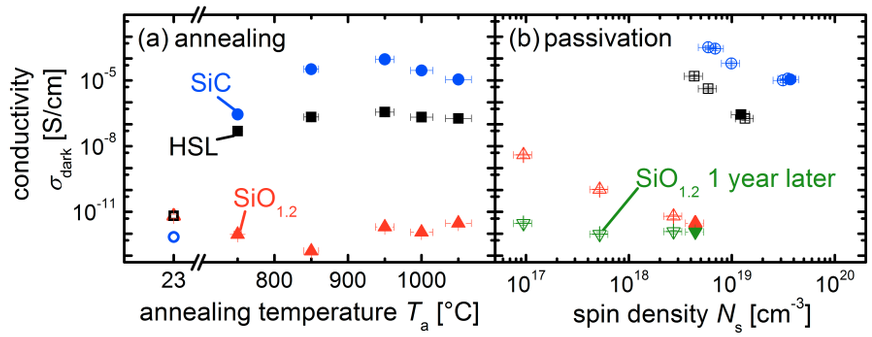

Figure 4.36.: *Dark conductivity σ_{dark} of SiC, $SiO_{1.2}$ and HSL samples plotted (a) versus T_a for the annealing series and (b) versus N_s for the passivation series. In addition, the σ_{dark} of the passivated $SiO_{1.2}$ samples measured after one year storage in ambient air are presented. The as-deposited, annealed and passivated samples are represented by open, full and crossed symbols, respectively. The SiC single layers seem to be unintentionally doped after annealing, whereas the $SiO_{1.2}$ single layers show metastable hydrogen-induced doping after passivation. The change of σ_{dark} upon annealing and/or passivation in the HSL sample seems to be a conjunction of the effects that are also present in SiC and $SiO_{1.2}$ single layers.*

orders of magnitude for the HSL sample and SiC single layer up to $T_\mathrm{a} = 950$ °C before saturating at higher temperatures. For the passivated samples, the decrease of N_s due to the hydrogen reincorporation is always accompanied by a rise in σ_dark irrespective of the sample type. In addition, the σ_dark of all passivated samples were measured again one year after storage in ambient air. Only the $SiO_{1.2}$ samples show large discrepancy between σ_dark measured directly after passivation and after one year storage. During this time, all $SiO_{1.2}$ conductivity values fell below 10^{-11} S/cm. Even though a dominance of the SiC sublayers on the HSL lateral conductivity is indicated, the change of σ_dark upon annealing and/or passivation in the HSL sample seems to be a conjunction of the effects that are also present in SiC and $SiO_{1.2}$ single layers. Thus, the evolution of σ_dark during annealing and passivation were discussed for the single layers only.

The increase of σ_dark in the SiC single layer by several orders of magnitude upon annealing reaching values exceeding those of typical intrinsic silicon dielectrics

indicates that this material is doped after annealing. The assumption of annealing initiated doping is supported by the increase of σ_{dark} with reduced N_{s} after passivation using, e.g., the PECVD technique [162]. In doped semiconductors, an increase of σ_{dark} with the reduction of N_{s} is expected, since the defects, which act as trap states for free charge carriers, counteract the effect of the dopants. In intrinsic materials, a decrease of N_{s} would have resulted in smaller σ_{dark}, because the paths for defect-assisted thermal generation of free charge carrier under dark condition would be partially absent after passivation. In order to verify this assumption, temperature variation during conductivity measurements were carried out on SiC single layers. The significant decrease of the activation energy E_{a} from as-deposited (384 meV) to 850 °C (64 meV) indicates a shift of the Fermi level closer to the conduction or valence band edge and thus supports the doping in annealed SiC material.

Similarly high conductivities have been observed in nominally undoped, HW-CVD grown µc-SiC:H [163]. This unintentional conductivity, which was identified to be n-type, was attributed to impurity doping by nitrogen and/or oxygen incorporated in the c-SiC phase as donor centers [164]. However, the annealing initiated doping observed in the SiC materials under investigation in this work might have a different origin, since SiC-NCs were formed at $T_{\mathrm{a}} \geq 950$ °C (Sec. 4.4.1), whereas the pronounced σ_{dark} increase started at much lower temperatures. Unfortunately, it was not possible to identify the origin and mechanism of annealing initiated doping in SiC material in this work. One possible explanation would be a strained-induced delocalization of carriers, where the strain and therefore the doping concentration is related to the structural densification (increase in network order) in SiC material during annealing (Sec. 4.4.1). An increase of σ_{dark} upon passivation is then due to the dominant reduction of DB trap state density. The reported reduction of the dark conductivity to an intrinsic level by incorporating nitrogen [38] or oxygen [37] atoms might then be due to the O- or N-induced relaxation of the material network. Anyway, the doped character of annealed SiC represents, besides the high defect density and sub-band gap absorption, another obstacle for the realization of SiC/SiO_x HSL structure as a high quality Si-QD absorber. Since both types of carriers have to travel through the SiC barriers, the minority charge carriers will likely recombine with the majority charge carriers in these layers. In addition, the SiC doping might induce band bending near the surface of the Si-QDs giving rise to

handicapped carrier extraction.

The dark conductivity of the $SiO_{1.2}$ single layer increased directly after passivation. According to the discrepancy between σ_{dark} measured directly after passivation and after one year storage, this increase in σ_{dark} might be related to some metastable hydrogen-related doping. Similar hydrogen-induced metastable changes in the electrical conductivity in poly- and microcrystalline Si were reported in Ref. [165, 166]. The authors attributed the metastable conductivity increase upon hydrogen implantation to the formation and dissociation of bond-center hydrogen. This complex consists of a single H atom residing in a Si-Si bond-center site that has been identified as s donor complex in c-Si material [167]. The bond-center hydrogen might form molecular hydrogen H_2 and escape the material with time giving rise to reduced σ_{dark}. The same explanation might be applied to the SiO_x materials under investigation in this work. However, distinct ESR features that could unambiguously identify the presence of bond-center hydrogen [168] were not detected in the passivated $SiO_{1.2}$ single layers. The phenomenon of metastable hydrogen-induced conductivity could not be investigated in depth in this work.

5. Silicon oxide layers in silicon heterojunction solar cell

This chapter deals with the development of SiO_x materials for SHJ solar cells. The first section provides information on the c-Si surface passivation using intrinsic a-SiO_x:H buffer layers from both technical and materials science point of view. In the second section, the dependence of the μc-SiO_x:H layer properties in terms of microstructure, optoelectronics and passivation on the PECVD deposition conditions are presented and discussed. The last two sections describe chronologically the progresses in SiO_x based SHJ solar cell fabrication achieved in this work starting with a prototype SiO_x emitter SHJ solar cell and ending with a state-of-the-art all SiO_x SHJ solar cell.

5.1. Intrinsic amorphous silicon oxide passivation layers

The a-SiO_x:H samples were fabricated in the same multi-chamber deposition system as used for HSL fabrication. The PECVD chamber usually utilized to deposit n-type material was used for a-SiO_x:H growth. This chamber provides the required precursor gases CO_2, SiH_4 and H_2. In the first part, experiments aiming at the reproducibility and controllability of a-SiO_x:H passivation are presented. The second part deals with the development of a-SiO_x:H thin-films taking into account complementary demands for its material properties, which are relevant in the later SHJ solar cells. In particular, the influence of the a-SiO_x:H composition and thickness on the optical, electrical and passivation properties was investigated. In addition,

the impact of post-deposition annealing on the passivation properties of a-SiO_x:H layers is discussed.

5.1.1. Technical aspects

Reproducibility of the passivation quality

For lifetime measurement, a double side polished, <100> orientated, 250 µm thick p-type Float-Zone (FZ) silicon wafers with a diameter of 100 mm was used as substrate. Before transferring the substrate into the deposition system, a SSEC 3300 wafer cleaner was used to treat the wafer first in a mixture of sulphuric acid and hydrogen peroxide to clean off organic residues and then in a diluted hydrofluoric acid to remove the native oxide from the wafer surface. It is important to note that this procedure is adequate only for wafers that were precleaned by the wafer supplier before shipping. Otherwise, a complete RCA cleaning (denotes a standard two-step cleaning process developed at Radio Corporation of America, USA) might be necessary to ensure sufficiently clean and well defined wafer surface conditions. The time of exposure to ambient air after cleaning and before transferring was kept below 10 min, in order to avoid significant surface reoxidation. After the deposition of an intrinsic a-SiO_x:H layer on one side, the wafer is taken out without waiting for cool down, quickly turned to the other side and put back into the system. The whole sequence needed to be as short as possible, since a hot wafer in ambient air tends to oxidize faster than at Room Temperature (RT). The hot turning did not degrade the quality of the uncovered surface as confirmed by similar lifetime values on samples with and without waiting for cooling down before turning. Once the other surface is covered with nominally the same a-SiO_x:H layer as that on the previous side, the lifetime sample is taken out of the system after cooling for 30 min and measured with QSSPC. Effective lifetime τ_{eff} at the light intensity corresponding to the AM1.5 solar spectrum is taken as a measure for the passivation quality.

The deposition conditions were further optimized on the basis of previous work on a-SiO_x:H passivation [103]. Improved lifetime values above 1.5 ms in the as-deposited state were obtained at a power density P of 17 mW/cm^2, a plasma frequency f of 81.40 MHz, a deposition pressure p of 0.25 mbar, a substrate temper-

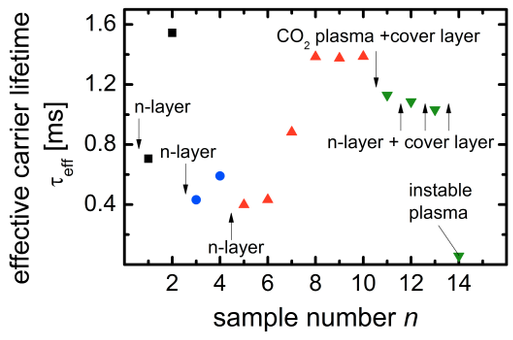

Figure 5.1.: *Effective lifetime τ_{eff} of a-SiO_x:H samples from the passivation reproducibility series. The sample numbers denote the chronological order of their fabrication in the same deposition chamber. Deterioration of the passivation quality is observed for samples fabricated directly after the operation of other processes. Subsequent repetition of the same a-SiO_x:H deposition could restore the high effective lifetime values. The loss of the sensitive optimal power matching when changing the matching conditions or switching the frequency matchbox cable between RF and VHF gave rise to instable plasma conditions and therefore decreased passivation quality.*

ature T_{sub} of 200 °C, an electrode spacing d_{ele} of 16 mm, and a total gas flow f_{total} of 20 sccm. However, lifetime samples prepared under the same cleaning and deposition conditions had large deviation in their results. In order to locate the source of this problem, a systematic study on the reproducibility of the passivation was carried out. Figure 5.1 shows τ_{eff} of a-SiO_x:H lifetime samples fabricated using the same deposition parameters as mentioned above and numerated in the chronological order of their fabrication date. The arrows give information about other processes running in the same chamber between two a-SiO_x:H depositions. The a-SiO_x:H layers had a measured thickness of around 50 nm. Up to the sample 10, the a-SiO_x:H depositions were interrupted by n-type a-Si:H growth. The τ_{eff} decreased as a consequence of this interruption and recovered again upon repetition of the same a-SiO_x:H deposition. Interestingly, a sequence of chamber cleaning by CO_2 plasma treatment and a-SiO_x:H cover layer deposition on a sacrificial substrate between sample 10 and 11 deteriorates the passivation quality as well. Thus, contamination by impurities like the doping gas PH_3 remaining after the n-type a-Si:H deposition is unlikely the

reason. The a-SiO_x:H cover layer deposition seems to prevent pronounced decrease of τ_{eff}, since the samples 12 and 13 fabricated after n-type a-Si:H and cover layer deposition show only slightly lower τ_{eff} than their previous samples.

Unlike for a-SiO_x:H growth, the a-Si:H deposition and the CO_2 plasma treatment were carried out at $f = 13.56$ MHz in RF mode. Together with the observation that an obviously instable plasma resulted in very poor τ_{eff} for sample 14, the decrease of τ_{eff} is associated with the changed power matching conditions after unplugging and plugging the different frequency matchbox cables for RF and VHF, which gave rise to plasma conditions off the optimum. A switch was installed that enables the switching between RF and VHF frequency matchboxes without plugging and unplugging the cables. Now, the a-SiO_x:H lifetime sample prepared at VHF directly after a n-type a-Si:H deposition at RF provided excellent lifetime values, thus confirming the aforementioned assumption. Hence, the passivation quality of a-SiO_x:H layers relies sensitively on a stable plasma condition, which is often delicate at low deposition power used. Since the first mono layers of a-SiO_x:H on the c-Si surface are most important for good passivation, the deposition has to start under a stable plasma condition and there is no time to adjust the matching parameters after the growth has started. In order to find and maintain a stable starting plasma, a-SiO_x:H cover layer depositions after any change in the system are necessary. The implementation of the cable switch was crucial for the later cell fabrication, where the µc-SiO_x:H layers were processed in the same chamber in RF mode. Also the d_{ele} for the µc-SiO_x:H depositions was kept at 16 mm (sec. 5.2), in order to avoid any change to the system.

Deposition rate vs. passivation quality

As the a-SiO_x:H thickness is limited to a few nm when used in SHJ solar cells, a precise thickness control would be beneficial for reproducible results. Reducing the deposition rate r_{dep} is one way to increase the accuracy of the desired thickness. Since the deposition power is already operating at its lower limit, the effect of H_2 gas flow ratio r_{H_2} and CO_2 gas flow ratio r_{CO_2} on the deposition rate were investigated. The r_{H_2} is defined as the ratio between H_2 gas flow rate f_{H_2} and the total gas flow rate f_{total}. Figure 5.2 shows decreasing r_{dep} with increasing r_{H_2}.

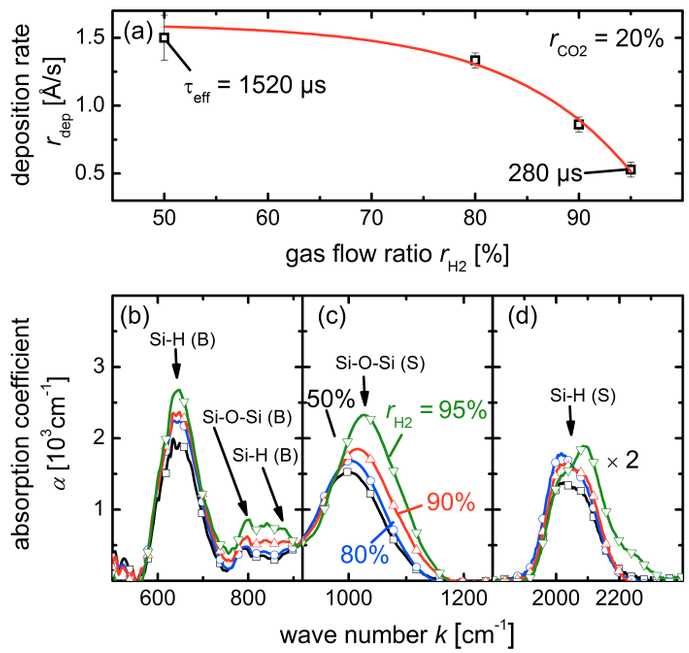

Figure 5.2.: *(a) Deposition rate r_{dep} and (b-d) FTIR data of the H_2 gas flow ratio r_{H_2} series. The r_{dep} decreases with increasing r_{H_2}. The τ_{eff} of two lifetime samples are assigned to the respective data points with the same deposition parameters showing a decreasing trend with rising r_{H_2}. FTIR results reveal increasing H and O content with increasing r_{H_2}.*

However, the τ_{eff} of two lifetime samples assigned to the respective data points with the same deposition parameters suggests that also the passivation quality has decreased with increasing $r_{\mathrm{H_2}}$. This might be due to the higher amount of hydrogen bombarding the c-Si surface and/or due to changed a-SiO_x:H layer properties. In order to check the latter, FTIR measurements were carried out. The absorption coefficients α as a function of the wavenumber k are plotted in Fig. 5.2(b-d). Both the increase of the Si-O-Si stretching (S) mode peak intensity and position with increasing $r_{\mathrm{H_2}}$ indicate an increase of O atoms in the layers [132]. Ref. [108] assigned peaks centered at 2115 cm^{-1}, 2200 cm^{-1} and 2260 cm^{-1} to Si-H (S) modes with

1, 2 and 3 back bonded O atoms, respectively. Thereby, the redistribution of the Si-H (S) intensity from the 2000 cm^{-1} peak to higher wavenumber also suggests higher O content with increasing r_{H_2}. At the same time, the Si-H bending (B) mode peak intensity rises, which suggests more H incorporation with increasing r_{H_2}. Since the chemical passivation of the c-Si surface arises from the saturation of Si DB by hydrogen [169], the higher H content cannot explain the lower τ_{eff} of the $r_{H_2} = 95$ % sample. Based on the FTIR data, the deterioration of the passivation quality might be related to the higher O content of the a-SiO_x:H layers. However, increasing hydrogen bombardment as the reason for decreased τ_{eff} could not be excluded. The decrease of r_{dep} with increasing r_{H_2} might be due to the removal of embedded Si by stronger hydrogen etching [127]. Since the Si-O bonds possess higher bonding energy than the Si-Si bonds in a amorphous network [128], the incorporated O atoms are less likely to be removed by impinging hydrogen, giving rise to higher O incorporation with increasing r_{H_2}.

Figure 5.3 presents the results of the r_{CO_2} series. As shown in Fig. 5.3(a), the r_{dep} decreases linearly with increasing r_{CO_2}. This is explained by the enhanced formation of water vapor (H_2O) as a reaction by-product at the surface, which hinders the docking of reactants from the gas phase [170]. The τ_{eff} corresponding to the $r_{CO_2} = 90$ % sample is much lower than that at $r_{CO_2} = 20$ % reaching a value comparable to those of unpassivated c-Si wafers. Since the hydrogen dilution remained unchanged, the deterioration of τ_{eff} is unlikely due to surface damaging by hydrogen bombardment. The Si-O-Si (B) peak intensity and peak position increased with increasing r_{CO_2}, pointing at growing O content as expected. Simultanously, the Si-H (B) peak intensity decreased with increasing r_{CO_2} as the amount of Si atoms decreased. Since H is unlikely to bond to O atoms [145], the H content is also reduced. The evolution of the Si-H (S) signals with rising r_{CO_2} supports the increase in O as well as the decrease in H. With increasing O content, the Si-H (S) intensity shifted from the 2000 cm^{-1} peak to higher wavenumber, where more O content resulted in larger fraction of Si-H (S) modes with more O back bonds. Due to the decreasing H and Si content, the integrated aera under the Si-H (S) signals was reduced.

Thus, the r_{CO_2} and r_{H_2} series have in common that a higher amount of in-

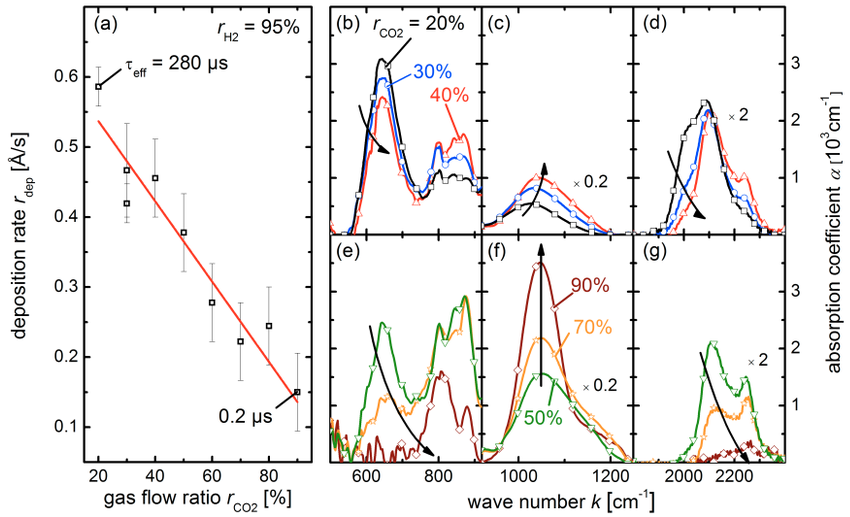

Figure 5.3.: *(a) Deposition rate r_{dep} and (b-g) FTIR data of the CO_2 gas flow ratio r_{CO_2} series. The r_{dep} decreases linearly with increasing r_{CO_2}. The τ_{eff} corresponding to the respective data points show a decrease with rising r_{CO_2}. FTIR results indicate decreasing H and increasing O content with increasing r_{CO_2}. The higher O content correlates with the poorer passivation quality for both r_{H_2} and r_{CO_2} series.*

corporated O atoms correlates with a lower deposition rate. At least for the $r_{\mathrm{CO_2}}$ series, the r_{dep} is lowered due to the participation of O atoms during film growth (see above). For the $r_{\mathrm{H_2}}$ series, the increasing hydrogen dilution is likely the major reason for the reduced r_{dep}. The deposition rate could not be reduced in this work by changing the H_2 or CO_2 gas flow ratio without considerably degrading the passivation quality. The higher O content also seems to correlate with the poorer passivation quality for both series. This can be explained by two reasons. First, the Si content and thus the H content, are lower with higher O content, resulting in higher amount of unsaturated DB as recombination centers at the c-Si surface. Secondly, H atoms that are bonded to Si with the more electronegative O back bonds might be unfavorable for c-Si surface DB saturation due to stronger attraction of the Si-H bonding orbital towards Si as compared to Si-H without O back bonds. Thereby, the deterioration of τ_{eff} is always accompanied by the reduction of

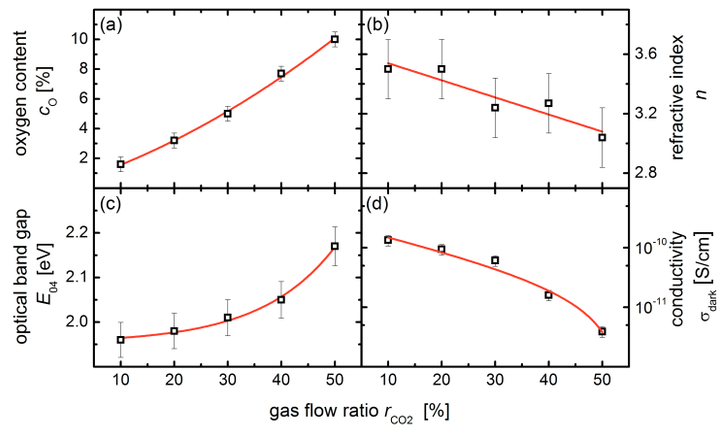

Figure 5.4.: *(a) Oxygen content c_O, (b) refractive index n, (c) optical band gap E_{04} and (d) dark conductivity σ_{dark} of a r_{CO_2} series with thick a-SiO_x:H samples on glass substrates [103]. All a-SiO_x:H samples possess an amorphous phase only, which was checked with Raman spectroscopy. With increasing c_O, the E_{04} shifted to higher energies, the n increased linearly and the σ_{dark} decreased by almost two orders of magnitude.*

the 2000 cm^{-1} peak intensity as shown in the FTIR results. This would explain the lower passivation quality in spite of higher H content for the r_{H_2} series.

5.1.2. Material properties

Oxygen content dependence

According to the findings from Sec. 5.1, the amount of oxygen incorporated in a-SiO_x:H passivation layers should not be too high. Since the optical and electrical properties also rely on the O content, careful adjustment of the a-SiO_x:H composition is required to find a good compromise between the optical, electrical and passivation properties. Therefore, another r_{CO_2} series was fabricated under deposition conditions close to the optimized parameters as mentioned in 5.1, which gave excellent τ_{eff}. The r_{CO_2} was varied between 10 % and 50 %, while the r_{H_2} was kept at 50 %. This series consists of lifetime samples with an a-SiO_x:H layer thickness of

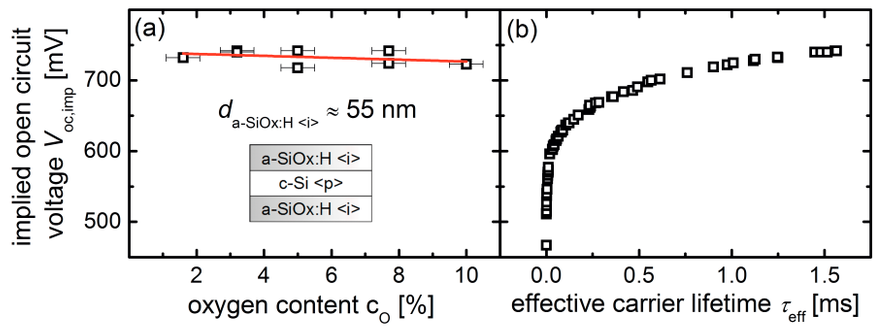

Figure 5.5.: *(a) Implied open circuit voltage $V_{oc,imp}$ at the light intensity corresponding to the AM1.5 solar spectrum versus the oxygen content c_O. Excellent $V_{oc,imp}$ values were achieved for all samples with c_O up to 10 %. (b) Correlation between $V_{oc,imp}$ and effective lifetime τ_{eff} for all lifetime samples prepared in this work. The $V_{oc,imp}$ is a more suitable measure for the passivation property than τ_{eff} with respect to the estimation of solar cell performance.*

around 55 nm.

In Fig. 5.4, the oxygen content c_O, refractive index n, optical band gap E_{04} and dark conductivity σ_{dark} of a similar r_{CO_2} series with thick a-SiO_x:H samples on glass substrates are plotted versus r_{CO_2} [103]. All a-SiO_x:H samples possess an amorphous phase only, which was checked with Raman spectroscopy. The oxygen content c_O increased almost linearly with increasing r_{CO_2}. This indicates that the oxygen atoms, produced during the cracking process of CO_2 into CO and O, are incorporated into the material proportionally to the CO_2 gas flow. SIMS results (not shown) reveal that less than 0.1 % C atoms were embedded into the material, since the C-O bond has high bonding energy and is therefore unlikely to be cracked by the plasma [128]. With increasing c_O, the E_{04}, read from PDS data, shifted to higher energies, the n increased linearly and the σ_{dark} decreased by almost two orders of magnitude.

Figure 5.5(a) shows the implied open circuit voltage $V_{oc,imp}$ at the light intensity corresponding to the AM1.5 solar spectrum versus the c_O for the r_{CO_2} lifetime samples. The $V_{oc,imp}$ of the r_{CO_2} series ranges from 718 mV to 742 mV, which

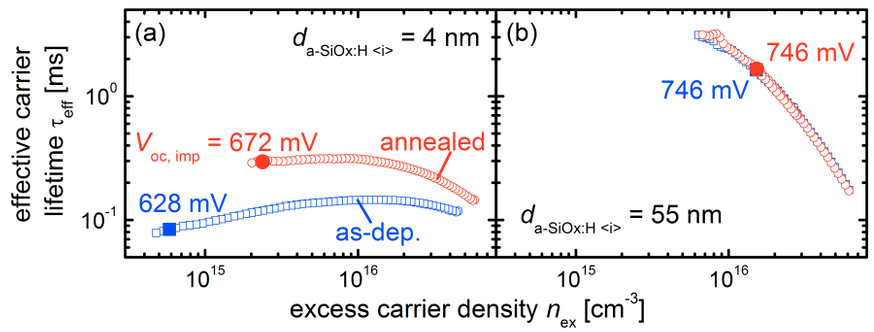

Figure 5.6.: *Injection dependences of two lifetime samples with (a) thin and (b) thick a-SiO_x:H layers before and after annealing. The data points corresponding to one sun reference are highlighted by larger filled symbols together with the respective $V_{oc,imp}$ values. The lifetime values were lower for samples with thinner passivation layers in both as-deposited and annealed states, whereas the annealing resulted in higher relative increase for the thin a-SiO_x:H sample as compared to the thick one.*

correlates with a τ_{eff} of 0.90 ms and 1.56 ms, respectively. Figure 5.5(b) illustrates the correlation between $V_{\text{oc,imp}}$ and τ_{eff} at one reference sun for all lifetime samples prepared in this work. This dependence reveals that a significant increase in τ_{eff} will only result in a small gain in $V_{\text{oc,imp}}$ in the high τ_{eff} range. On the contrary, a slight increase in τ_{eff} is equivalent to a pronounced gain in $V_{\text{oc,imp}}$ in the low τ_{eff} range. Thus, the $V_{\text{oc,imp}}$ is preferably used as a measure for the passivation quality than τ_{eff} in the following, since it is intuitively related to the V_{oc} in SHJ solar cells. Optionally, the τ_{eff} may be plotted on a logarithmic scale. The fact that all samples with c_{O} up to 10 % achieved an excellent $V_{\text{oc,imp}}$ value implies the reachability of high quality a-SiO_x:H passivation layers over a relatively wide range of material composition. However, the linear fit (red line) already visualizes a decreasing trend of the $V_{\text{oc,imp}}$ with increasing c_{O}, which is in agreement with the results from Sec. 5.1. The $c_{\text{O}} = 5$ % a-SiO_x:H material was chosen for further development due to its reasonable trade-off between optical transparency and electrical conductivity for implementation as buffer layer in SHJ solar cells.

Thickness dependence and annealing effect

The τ_{eff} and $V_{\text{oc,imp}}$ values mentioned in the previous sections were obtained on as-deposited lifetime samples with a-SiO_x:H layers thicker than 50 nm. There are at least two effects that can significantly affect the passivation quality for the same a-SiO_x:H materials. For a-Si:H passivation layers, an increased layer thickness and/or a post-deposition annealing are known to give a more effective surface passivation [75, 171]. Similar behaviors were reported for a-SiO_x:H passivation layers as well [80,172]. In order to check these effects for the a-SiO_x:H passivation layers fabricated in this work, several lifetime samples with reduced layer thicknesses were fabricated and subsequently annealed at 200 °C on a hot plat under ambient air for up to 30 min. Since 50 nm thick intrinsic a-SiO_x:H would result in unacceptably high series resistance in a SHJ solar cell, the verification of the passivation property on thinner a-SiO_x:H is indispensable.

Figure 5.6 shows the injection dependences of two lifetime sample with thick (55 nm) and thin (4 nm) a-SiO_x:H layers before and after annealing. The data points corresponding to one sun reference are highlighted by larger filled symbols together with the respective $V_{\text{oc,imp}}$ values. The lifetime values were lower for samples with thinner passivation layers in both as-deposited and annealed states, whereas the annealing resulted in higher relative increase for the thin a-SiO_x:H sample as compared to the thick one. Thereby, the loss of the passivation quality by reducing the buffer layer thickness could be partially compensated by the gain in τ_{eff} due to post-deposition annealing. The τ_{eff} and $V_{\text{oc,imp}}$ values at one sun reference are affected by Auger recombination in case of the thick sample with a higher injection level and limited by Shockley-Read-Hall (SRH) recombination in case of the thin sample with a lower injection level [173]. Since the passivation improvement due to annealing was assumed to arise from the thermally activated reconfiguration of di-hydrides SiH_2 into mono-hydrides SiH that are more suitable for dangling bond saturation [174], the annealing could reduce the SRH recombination only. This would explain the deviating behavior of the two different samples on the annealing treatment.

The a-Si:H thickness dependence of the surface passivation was assigned to the initial growth of a SiH_2-rich layer and the stabilization of a SiH-rich layer with further growth [175]. This is consistent with the higher DB density measured in

ultra thin a-Si:H films as compared to their thicker counterparts [176]. However, this assumption implies a non-locality of the surface passivation by hydrogen from the a-Si:H layers, since the situation at the very interface is the same for thin and thick buffer layers. A more intuitive explanation would be the transport of both types of charge carriers generated in the c-Si absorber through the passivation layer and recombination at the next defect-rich interface [177]. With increasing layer thickness, the tunnel probability decreases exponentially giving rise to lower recombination rate. This explanation may presumably applied to a-SiO_x:H passivation as well.

5.2. Doped microcrystalline silicon oxide contact layers

This section deals with the development of µc-SiO_x:H layers for the implementation as an emitter or a BSF in SHJ solar cells using a-SiO_x:H buffer layers. The µc-SiO_x:H samples were fabricated in the same PECVD chamber of the multi-chamber deposition system as for a-SiO_x:H. The compatibility to the a-SiO_x:H deposition was thus taken into consideration during the µc-SiO_x:H process development. In this section, the technology transfer of n-type µc-SiO_x:H deposition from another deposition system [88] is reviewed, followed by the evaluation of the structural, optical and electrical properties as a function of varying precursor gas flow rates for n- and p-type µc-SiO_x:H. Finally, the impact of n- and p-type µc-SiO_x:H the on wafer passivation is discussed.

5.2.1. Deposition parameters

The µc-SiO_x:H deposition uses CO_2, SiH_4 and H_2 as process gases and phosphine PH_3 and trimethylborane (TMB) $B(CH_3)_3$ as doping gases. All µc-SiO_x:H samples were deposited at a power density P of 337 mW/cm^2, a plasma frequency f of 13.56 MHz, a deposition pressure p of 4.00 mbar, a substrate temperature T_{sub} of 200 °C, and an electrode spacing d_{ele} of 16 mm. Only the gas flow rates were varied between the different samples. Figure 5.7 shows the H_2 gas flow ratio $r_{H_2} = f_{H_2}/(f_{H_2} + f_{CO_2} + f_{SiH_4} + f_{PH_3})$ as a function of the CO_2 gas flow ratio $r_{CO_2} =$

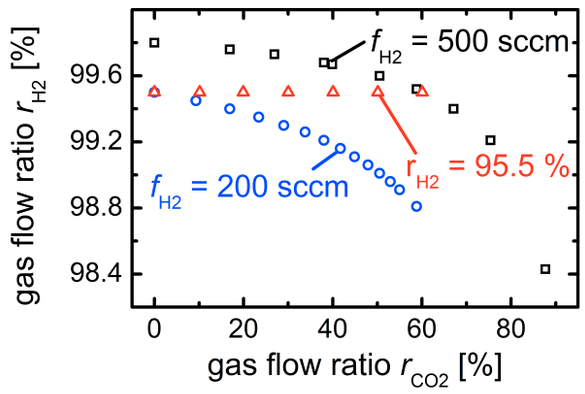

Figure 5.7.: *H_2 gas flow ratio r_{H_2} as a function of the CO_2 gas flow ratio r_{CO_2} for three n-type µc-SiO_x:H r_{CO_2} series with different r_{H_2} dependence on r_{CO_2}. The PH_3 gas flow ratio r_{PH_3} remained constant at 2 % for all three series. The r_{H_2} values of the $r_{H_2} = 95.5$ % series intersect those of the $f_{H_2} = 200$ sccm and $f_{H_2} = 500$ sccm series at the r_{CO_2} of 0 % and 60 %, respectively.*

$f_{CO_2}/(f_{SiH_4} + f_{CO_2})$ for three different n-type µc-SiO_x:H r_{CO_2} series. In the r_{CO_2} series with a constant H_2 gas flow rate f_{H_2}, the r_{CO_2} was varied by changing the CO_2 gas flow rate f_{CO_2}, while the SiH_4 gas flow rate f_{SiH_4} and the PH_3 gas flow rates f_{PH_3} were kept constant as well. Consequently, the r_{H_2} decreases with increasing r_{CO_2} according to the definition of r_{H_2}. The r_{H_2} is higher for the $f_{H_2} = 500$ sccm series than for the $f_{H_2} = 200$ sccm series. The r_{CO_2} series with a constant $r_{H_2} = 95.5$ % was realized by keeping f_{H_2} and f_{total} constant and adjusting f_{CO_2}, f_{SiH_4} and f_{PH_3} in a way that r_{CO_2} is the only changing parameter. Importantly, the PH_3 gas flow ratio $r_{PH_3} = f_{PH_3}/(f_{SiH_4} + f_{PH_3})$ remained constant at 2 % for all three series. The r_{H_2} values of the $r_{H_2} = 95.5$ % series intersect those of the $f_{H_2} = 200$ sccm and $f_{H_2} = 500$ sccm series at the r_{CO_2} of 0 % and 60 %, respectively.

Figure 5.8 displays the deposition rate r_{dep}, the Raman intensity ratio f_c, the optical band gap E_{04} and the dark conductivity σ_{dark} of the three r_{CO_2} series measured on n-type µc-SiO_x:H layers with glass substrates. The r_{dep} shows deviating r_{CO_2} dependence between the different series. For the $r_{H_2} = 95.5$ % series, r_{dep} decreases with increasing r_{CO_2}, which was also observed for the a-SiO_x:H deposition

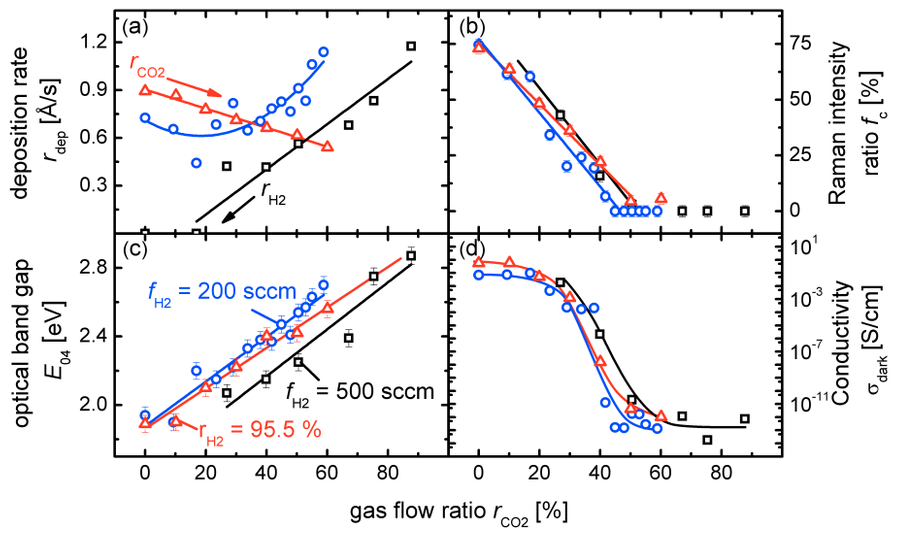

Figure 5.8.: *(a) Deposition rate r_{dep}, (b) Raman intensity ratio f_c, (c) optical band gap E_{04} and (d) dark conductivity σ_{dark} of three r_{CO_2} series each with constant $r_{H_2} = 95.5$ %, $f_{H_2} = 500$ sccm and $f_{H_2} = 200$ sccm. The characteristics of the material properties for the $r_{H_2} = 95.5$ % series represent the real dependence on r_{CO_2}, whereas an additional dependence on r_{H_2} is involved for the $f_{H_2} = 200$ sccm and 500 sccm series.*

(Sec. 5.1). For the $f_{\mathrm{H_2}} = 500$ sccm series, r_{dep} shows an increasing trend with increasing $r_{\mathrm{CO_2}}$, which is rather due to the reduction of $r_{\mathrm{H_2}}$ and therefore weaker hydrogen etching effect [127]. For the $f_{\mathrm{H_2}} = 200$ sccm series with overall lower $r_{\mathrm{H_2}}$, the decrease of r_{dep} in the lower $r_{\mathrm{CO_2}}$ range due to increasing $r_{\mathrm{CO_2}}$ is progressvely overcompensated by the increase of r_{dep} in the higher $r_{\mathrm{CO_2}}$ range due to decreasing $r_{\mathrm{H_2}}$. Since the $r_{\mathrm{H_2}} = 95.5$ % series was able to reveal the true impact of $r_{\mathrm{CO_2}}$ on r_{dep} and probably also on other material properties, keeping $r_{\mathrm{H_2}}$ constant while varying the $r_{\mathrm{CO_2}}$ is more recommendable than keeping $f_{\mathrm{H_2}}$ constant only. The characteristics of the material properties for the $r_{\mathrm{H_2}} = 95.5$ % series in Fig. 5.8(b-d) represent their real dependence on $r_{\mathrm{CO_2}}$, whereas an additional dependence on $r_{\mathrm{H_2}}$ is involved for the $f_{\mathrm{H_2}} = 200$ sccm and 500 sccm series. Comparison between the three series in conjunction with Fig. 5.7 suggests a higher f_{c} and σ_{dark} as well as a lower E_{04}

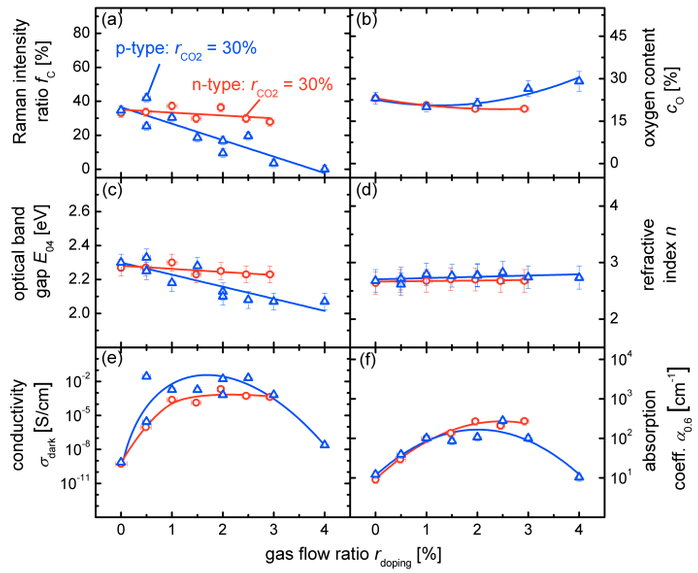

Figure 5.9.: *(a) Raman intensity ratio f_c, (b) oxygen content c_O, (c) optical band gap E_{04}, (d) refractive index n, (e) dark conductivity σ_{dark} and (f) free carrier absorption $\alpha_{0.6}$ versus doping gas flow ratio r_{doping} for a n-type r_{PH_3} series and a p-type $r_{B(CH_3)_3}$ series. The f_{H_2}, r_{H_2} and r_{CO_2} were kept constant at 500 sccm, 95.5 % and 30 %, respectively.*

with increasing $r_{\mathrm{H_2}}$, which can be related to a lower c_{O} (Sec. 5.2.2). Unlike for a-SiO$_x$:H deposition (Sec. 5.1), a higher hydrogen dilution enhances the growth of crystalline Si phase more than the incorporation of oxygen into the amorphous SiO$_x$ phase [178]. The influence of $r_{\mathrm{CO_2}}$ on the µc-SiO$_x$:H material properties are discussed in Sec. 5.2.2 in more detail.

5.2.2. Structural, optical and electrical properties

Effect of doping gas flow

In order to investigate the effect of doping on µc-SiO$_x$:H material properties, a $r_{\mathrm{PH_3}}$ series for n-type material and a $r_{\mathrm{B(CH_3)_3}}$ series for p-type material were fabricated. The $f_{\mathrm{H_2}}$, $r_{\mathrm{H_2}}$ and $r_{\mathrm{CO_2}}$ were kept constant at 500 sccm, 95.5 % and 30 %,

respectively. The layers were deposited on glass substrates with a layer thickness of 390 nm-660 nm. Figure 5.9 presents the measured structural, optical and electrical properties represented by f_c and c_O, E_{04} and n as well as σ_{dark} and $\alpha_{0.6}$, respectively. The $\alpha_{0.6}$ denotes the absorption coefficient at the photon energy of 0.6 eV, which is attributed to free carrier absorption and thus considered a measure for the active doping concentration. The contribution of defect absorption is assumed to be inferior as compared to that of free carrier absorption for doped materials, which is supported by the increase of α with decreasing photon energy in the lower sub-band gap range observed in the present samples as a characteristic feature of the free charge carrier exitation (not shown).

For n-type μc-SiO_x:H, the structural and optical properties are hardly affected by the variation of the r_{doping}. Only a slight decrease of f_c and c_O indicate a minute reduction of the c-Si phase fraction and the O amount in SiO_x phase (Fig. 5.9(a,b)). The E_{04} decreases and the n increases slightly as a consequence of the oxygen depletion, which is in agreement with the composition dependence of a-SiO_x:H materials (Sec. 5.1.2). However, the electrical properties changes with r_{doping}. The σ_{dark} increases first with increasing r_{doping} and saturates with further increase of r_{doping} above 2 %. Since the negligible reduction of c-Si phase fraction with increasing r_{doping} is unlikely to result in noticeable change of the carrier mobility μ, the σ_{dark} behavior is mainly attributed to the variation of the active doping concentration with changing r_{doping}, which is confirmed by the same increase and saturation of $\alpha_{0.6}$ with rising r_{doping}. While the increase of doping concentration in the material with rising dopant gas flow in the gas phase is intuitively understood, the subsequent saturation of the doping concentration might be due to the incorporation of inactive interstitial dopants or the creation of impurity defects at higher r_{doping}. Therefore, the $r_{doping} = 2$ % sample seems to be most suitable for further development.

For p-type μc-SiO_x:H, the f_c decreases strongly with increasing r_{doping}. Beyond $r_{doping} = 3$ %, the material consists of amorphous phase only. The loss of high mobility c-Si phase is likely to result in the decrease the carrier mobility μ as well. The deterioration of the crystalline growth by the usage of $B(CH_3)_3$ as a doping gas is known for p-type μc-Si:H deposition [179]. Based on the present results, this statement is also valid for p-type μc-SiO_x:H growth. At the same time, the c_O in-

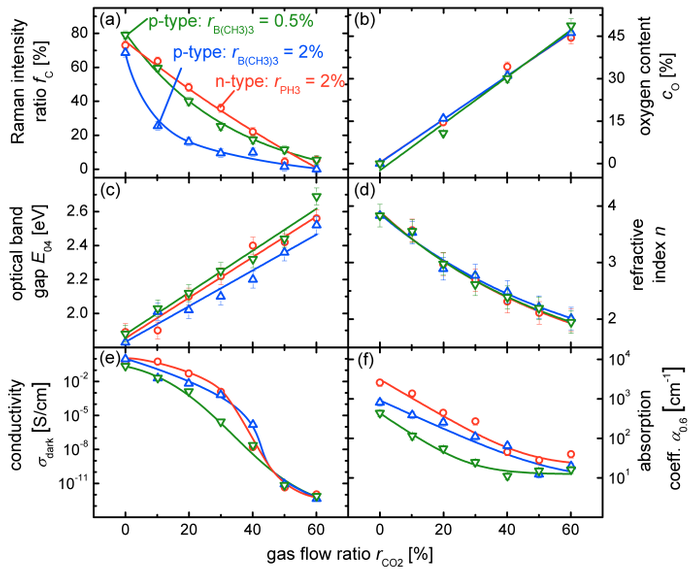

Figure 5.10.: *(a) Raman intensity ratio f_c, (b) oxygen content c_O, (c) optical band gap E_{04}, (d) refractive index n, (e) dark conductivity σ_{dark} and (f) free carrier absorption $\alpha_{0.6}$ versus CO_2 gas flow ratio r_{CO_2} for one n-type r_{CO_2} series with the optimum $r_{doping} = 2$ % and two p-type r_{CO_2} series each with $r_{doping} = 0.5$ % and $r_{doping} = 2$ %. The f_{H_2} and r_{H_2} were kept constant at 500 sccm and 95.5 %, respectively.*

creases by trend. However, the E_{04} declines and the n rises with increasing r_{doping}, which disagrees with their c_{O} dependence as mentioned above. This behavior of the optical properties as a function of r_{doping} suggests an enrichment of the a-SiO_x:H phase with excess Si that were not incorporated into the c-Si phase as compared to other samples with less $B(CH_3)_3$ addition involved. An initial increase and a subsequent decrease of $\alpha_{0.6}$ towards higher r_{doping} is observed, where the increase is attributed to the incorporation of more active B atoms due to the higher amount of doping gas and the decrease is assigned to the reduced doping efficiency due to vanishing c-Si phase fraction. As a product of the carrier mobility and carrier concentration, the σ_{dark} increases strongly from intrinsic $r_{\mathrm{doping}} = 0$ % to a little B doping $r_{\mathrm{doping}} = 1$ %, then remains on a high level without pronounced change

before it significantly deteriorates from $r_{\mathrm{doping}} = 3$ % to $r_{\mathrm{doping}} = 4$ %. Unlike for the n-type μc-SiO_x:H r_{doping} series, the choice of suitable r_{doping} for further development necessitates a compromise between optical and electrical properties. Thus, the $r_{\mathrm{doping}} = 0.5$ % sample with higher E_{04} but lower σ_{dark} and the $r_{\mathrm{doping}} = 2$ % sample with lower E_{04} but higher σ_{dark} are taken into consideration later on.

Effect of oxygen content

In order to investigate the effect of oxygen content on μc-SiO_x:H material properties, one r_{CO_2} series for n-type material with the optimum $r_{\mathrm{doping}} = 2$ % and two for p-type material each with $r_{\mathrm{doping}} = 0.5$ % and $r_{\mathrm{doping}} = 2$ % were fabricated. The f_{H_2} and r_{H_2} were kept constant at 500 sccm and 95.5 %, respectively. The layer thickness ranged from 230 nm to 1080 nm. Figure 5.10 displays the f_c, c_O, E_{04}, n, σ_{dark} and $\alpha_{0.6}$ as a function of r_{CO_2} for the three series. Starting from μc-Si:H at $r_{CO_2} = 0$ % and ending with a-SiO_x at $r_{CO_2} = 60$ %, the c-Si phase fraction is reduced with increasing r_{CO_2}, while the oxygen incorporation rises. The successive substitution of the c-Si phase by a-SiO_x phase gives rise to the increase of E_{04} and the decrease of n, σ_{dark} and $\alpha_{0.6}$, which is in agreement with the observation in r_{doping} series and with Ref. [180]. Comparison between the series reveals higher crystallinity for n-type material, which results in higher conductivity and doping concentration as compared to p-type material. Comparison between the two p-type μc-SiO_x:H series confirms the aforementioned effect of $B(CH_3)_3$ doping gas on the material properties. The impact of the varying optoelectronic properties on device parameters when applying the μc-SiO_x:H layers as BSF or emitter to SHJ solar cells is presented in Sec. 5.4.2 and Sec. 5.4.3.

5.2.3. Impact on passivation quality

Passivation without a-SiO_x:H buffer layer

Since a-SiO_x:H passivation layers feature remarkable lifetime values (Sec. 5.1.2), the a-SiO_x phase of the μc-SiO_x:H material might contribute to excellent surface passivation as well. If so, SHJ solar cells with doped μc-SiO_x:H as a combined passivation and contact layer would not only allow a simpler device processing, but also bene-

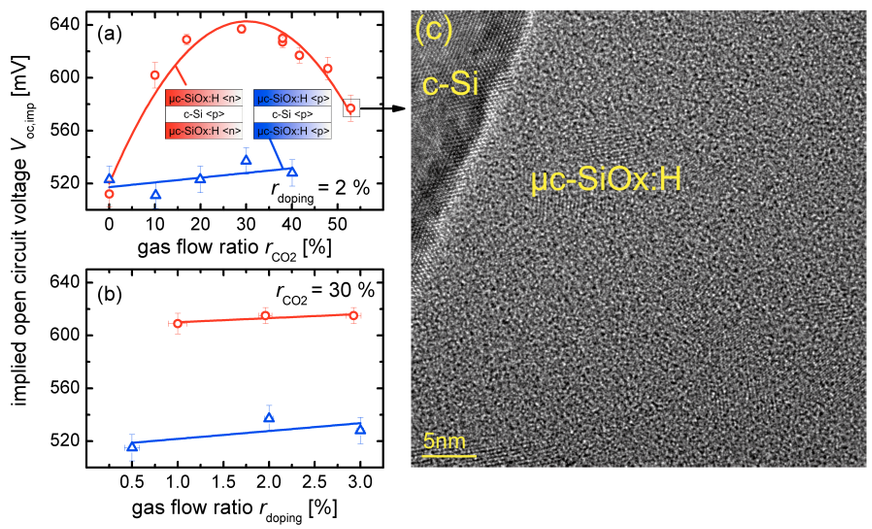

Figure 5.11.: *Implied open circuit voltage $V_{oc,imp}$ measured on lifetime samples with bi-facially deposited n- or p-type µc-SiO_x:H layers on p-type wafer versus (a) r_{CO_2} and (b) r_{doping} used during the deposition of these layers with a thickness of around* 55 nm. *The large discrepancy between n- and p-type µc-SiO_x:H passivation is attributed to the different field effect passivation on p-type wafer. (c) Cross-sectional HRTEM image of a c-Si/µc-SiO_x:H interface.*

fit from lower series resistance R_s as compared to cells with an additional intrinsic a-SiO_x:H buffer. Thus, the c-Si surface passivation properties of µc-SiO_x:H layers deposited directly on c-Si wafer without a-SiO_x:H buffer layers were investigated. Figure 5.11 shows the implied open circuit voltage $V_{oc,imp}$ measured on lifetime samples with bi-facially deposited n- or p-type µc-SiO_x:H layers on p-type wafer versus r_{CO_2} and r_{doping} used during the deposition of these layers with a thickness of around 55 nm. In addition, the cross-sectional HRTEM image of a c-Si/µc-SiO_x:H interface is presented. For the r_{CO_2} series, the r_{doping} was kept constant at 2 %, whereas for the r_{doping} series, the r_{CO_2} remained at 30 %.

Unfortunately, the obtained $V_{oc,imp}$ values indicate a passivation quality inferior to that achieved with intrinsic a-SiO_x:H. A maximum $V_{oc,imp}$ of only 637 mV was found for n-type µc-SiO_x:H with a $r_{CO_2} = 30$ % and a $r_{doping} = 2$ %. The fact

that the passivation quality of n- and p-type μc-SiO_x:H shows large discrepancy between each other suggests that the main passivation mechanism here is the field effect passivation, whereas the chemical passivation is insufficient. The band bending at the μc-SiO_x:H <n>/c-Si <p> interface is expected to be more pronounced than the band bending at the μc-SiO_x:H <p>/c-Si <p> interface with the n- and p-type μc-SiO_x:H having comparable doping concentrations (Sec. 5.2.2). Thereby, the holes are more effectively reflected away from the interface for μc-SiO_x:H <n> passivation than the electrons for μc-SiO_x:H <p> passivation. The poor chemical passivation might be a consequence of (i) the high c_O up to 46 % largely exceeding that in well passivating a-SiO_x:H samples, giving rise to very low hydrogen content needed for passivation, (ii) the unavoidable incorporation of P or B as impurities also in the a-SiO_x phase lowering its passivation quality, (iii) the stronger surface damaging due to the significantly higher hydrogen dilution and deposition power used as compared to a-SiO_x:H deposition and/or (iv) the formation of epitaxial Si as well as the presence of highly impurity doped c-Si crystallites at the interface, which contain a very low amount of hydrogen and thus do not passivate the surface sufficiently [181].

For $r_{CO_2} \leq 30$ %, the $V_{oc,imp}$ of the n-type μc-SiO_x:H samples decreases with decreasing r_{CO_2} (Fig. 5.11(a)), which might be correlated with the increase of epitaxial Si growth and/or the formation of Si crystallites at the interface, since the f_c increases with decreasing r_{CO_2} (Sec. 5.2.2). This assumption is supported by the annealing experiments of these n-type samples discussed below. The field effect passivation is not the $V_{oc,imp}$ limiting factor in this regime, since the doping concentration and therefore the band bending rather increases with decreasing r_{CO_2} (Fig. 5.10(f)). For $r_{CO_2} \geq 30$ %, the $V_{oc,imp}$ decreases with increasing r_{CO_2}. This might be assigned to the decrease of the total hydrogen concentration as well as the diminish of the Si-H configuration favorable for DB passivation (Sec. 5.1.1). In addition, the reduction of the doping concentration with increasing r_{CO_2} (Fig. 5.10(f)) might contribute to the loss in $V_{oc,imp}$ due to deteriorated field effect passivation. The fact that the $V_{oc,imp}$ of all p-type μc-SiO_x:H samples are around a very low value of 520 mV independent of r_{CO_2} and r_{doping} might be a consequence of the poorer field effect passivation as compared to n-type μc-SiO_x:H passivation. Since the material properties of the n-type μc-SiO_x:H did not noticeably change between $r_{doping} = 1$ %

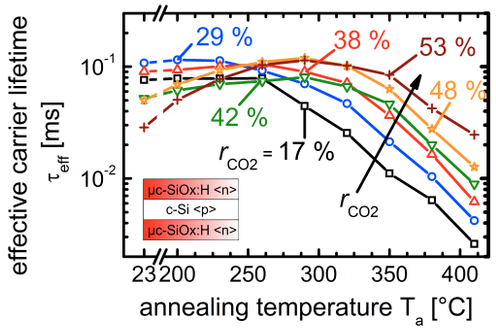

Figure 5.12.: *Evolution of the effective carrier lifetime τ_{eff} with increasing annealing temperature T_a for the n-type µc-SiO_x:H r_{CO_2} series. The samples were stepwise annealed at higher T_a on a hot plate under ambient air each for* 1 min. *QSSPC measurements were carried out after each annealing step. The increasing maximum gain of τ_{eff} as compared to the as-deposited state with rising r_{CO_2} suggests a reduction of c-Si phase at the interface. The thermal stability of the passivation quality is better for samples with higher oxygen content as indicated by the τ_{eff} values at, e.g.,* 400 °C.

and 3 % (Fig. 5.9), the $V_{\mathrm{oc,imp}}$ remained unchanged within this r_{doping} regime (Fig. 5.11(b)) as well.

Figure 5.12 shows the evolution of the effective carrier lifetime τ_{eff} with increasing annealing temperature T_{a}. The samples were stepwise annealed at higher T_{a} on a hot plate under ambient air each for 1 min. QSSPC measurements were carried out after each annealing step. As mentioned in Section 5.1.2, hydrogen is released from higher hydride states during annealing. However, a fraction of the saturated DB at the interface may become dehydrogenated too. While a sufficiently large H source is present in the amorphous film to guarantee re-passivation of these defect states, the H source at an epitaxial Si interface or within Si crystallites is probably too small for such repassivation [182]. Therefore, the passivation quality is expected to decrease upon annealing in case of epitaxial Si or Si crystallites at the interface, which is indeed observed for the highly crystalline $r_{\mathrm{CO_2}} = 17$ % sample. Otherwise, an improvement of the passivation quality is expected with annealing. With increasing $r_{\mathrm{CO_2}}$, the maximum gain of τ_{eff} as compared to the as-deposited state increases, which suggests a reduction of c-Si phase at the interface. The $r_{\mathrm{CO_2}} = 53$ % sample

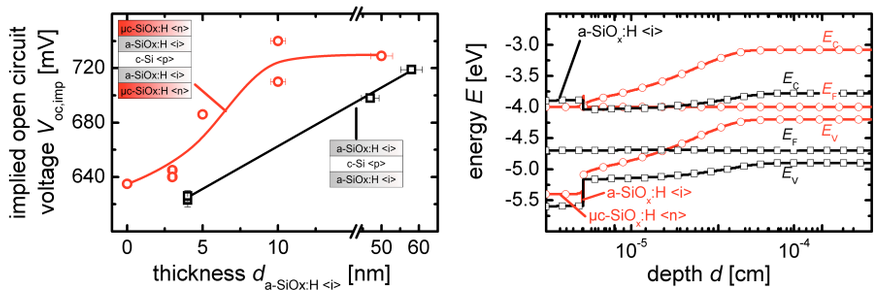

Figure 5.13.: *(a) Implied open circuit voltage $V_{oc,imp}$ versus a-SiO_x:H buffer layer thickness $d_{a\text{-}SiOx:H\ <i>}$ for lifetime samples with and without an additional* 50 nm *thick* µc-SiO_x:H <n> *layer on top of the a-SiO_x:H <i> layer. (b) The valence band edge E_V, the Fermi level E_F and the conduction band edge E_C of both structures as a function of the sample thickness in logarithmic scale. The increase of the $V_{oc,imp}$ at the same $d_{a\text{-}SiOx:H\ <i>}$ with an additional* µc-SiO_x:H <n> *layer is likely due to the enhanced built-in electrical field.*

with the overall lowest as-deposited τ_{eff} of 30 µs and the overall highest annealed τ_{eff} of 115 µs features a clear amorphous phase at the µc-SiO_x:H <n>/c-Si <p> interface as proven by HRTEM measurement (Fig. 5.11(c)). It is important to note, that the $r_{CO_2} = 53$ % sample is still a µc-SiO_x:H material, since lattice fringes of Si crystallites could be observed in its bulk. In addition, even though the τ_{eff} starts to decrease at a certain T_a for all samples due to dehydrogenation, the thermal stability of the passivation quality is better for samples with higher oxygen content as indicated by the τ_{eff} values at, e.g., 400 °C. This is in agreement with the reported results on a-SiO_x:H passivation layers [80].

Passivation with a-SiO_x:H buffer layer

Since the µc-SiO_x:H material was not able to passivate Si wafer surface sufficiently, the usage of intrinsic a-SiO_x:H/doped µc-SiO_x:H double layer in SHJ solar cells seems more promising. In order to investigate the passivation quality of this double layer structure, corresponding lifetime samples were fabricated. As a first approach, 50 nm thick n-type µc-SiO_x:H layers with a r_{CO_2} of 30 %, which yielded the best

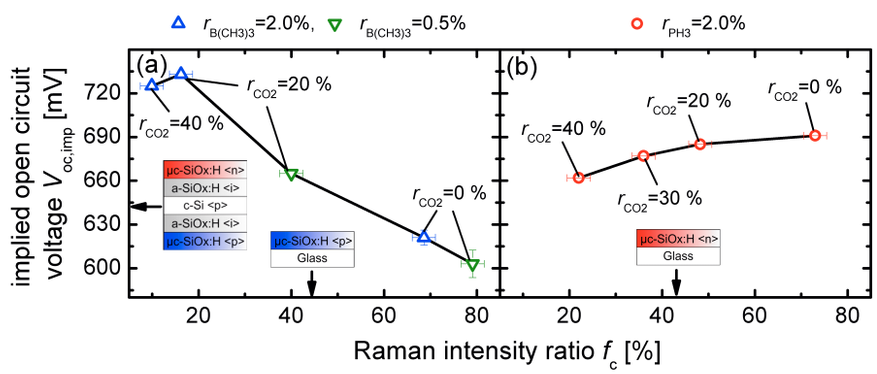

Figure 5.14.: *Implied open circuit voltage $V_{oc,imp}$ measured on asymmetric lifetime samples versus the Raman intensity ratio f_c of the respective single layer samples on glass for (a) a µc-SiO_x:H <p> series and (b) a µc-SiO_x:H <n> series. The different behavior of $V_{oc,imp}$ as a function of f_c for the two different series is tracked back to their different field effect passivation on p-type wafer.*

as-deposited $V_{\mathrm{oc,imp}}$, were put on top of an $c_O = 5$ % a-SiO_x:H buffer layer of variying thicknesses. Figure 5.13(a) compares $V_{\mathrm{oc,imp}}$ versus a-SiO_x:H buffer layer thickness $d_{\text{a-SiOx:H <i>}}$ of lifetime samples with and without an additional µc-SiO_x:H <n> layer. The increase of $V_{\mathrm{oc,imp}}$ with increasing $d_{\text{a-SiOx:H <i>}}$ was already discussed in Sec. 5.1.2. An increase of the $V_{\mathrm{oc,imp}}$ at the same $d_{\text{a-SiOx:H <i>}}$ is observed as the additional µc-SiO_x:H <n> layer is deposited onto the a-SiO_x:H layer, which is likely due to the enhanced built-in electrical field, which reflects the majority holes in the c-Si bulk from the heterojunction interface [183]. This effect is illustrated in Fig. 5.13(b) showing the valence band edge E_{V}, the Fermi level E_{F} and the conduction band edge E_{C} of an a-SiO_x:H <i>/c-Si <p> structure (black solid line) as well as an µc-SiO_x:H <n>/a-SiO_x:H <i>/c-Si <p> structure (red dashed line) as a function of sample depth in logarithmic scale, respectively. Moreover, the $V_{\mathrm{oc,imp}}$ seems to saturate at around 730 mV at $d_{\text{a-SiOx:H <i>}} = 10$ nm for the a-SiO_x:H <i>/µc-SiO_x:H <n> double layers, which indicates that the $V_{\mathrm{oc,imp}}$ is no more longer limited by interface recombination beyond this i-layer thickness [184].

Next, two series of lifetime samples with a more solar cell relevant structure consisting of a µc-SiO_x:H <n>/a-SiO_x:H <i>/c-Si <p>/a-SiO_x:H <i>/µc-SiO_x:H

<p> stack were processed. In the first series, combinations of $r_{CO_2} = 0\ \%, 20\ \%, 40\ \%$ and $r_{doping} = 0.5\ \%, 2.0\ \%$ during the deposition of μc-SiO_x:H <p> layer were tested. For this series, the μc-SiO_x:H <n> layers were deposited at $r_{CO_2} = 30\ \%$ and $r_{doping} = 2.0\ \%$. The thicknesses of the a-SiO_x:H <i> layers were kept constant at around 8 nm. With a-SiO_x:H <i> layers on both sides having the same thickness and thus comparable chemical passivation, the interface recombination at the μc-SiO_x:H <p>/a-SiO_x:H <i> side is likely to limit the passivation quality due to the weaker field effect passivation of μc-SiO_x:H <p> as compared to μc-SiO_x:H <n> as mentioned above. The second series contains four lifetime samples with a r_{CO_2} of 0 %, 20 %, 30 % and 40 % at a fixed r_{doping} of 2.0 % for the μc-SiO_x:H <n> layer. In this series, the μc-SiO_x:H <p> layer used $r_{CO_2} = 20\ \%$ and $r_{doping} = 0.5\ \%$. In order to make the impact of the μc-SiO_x:H <n> composition on the passivation quality stronger and clearer, the thickness of the a-SiO_x:H <i> layer next to the μc-SiO_x:H <n> layer is reduced to 4 nm, while the thickness of the a-SiO_x:H <i> on the opposite side of the wafer is kept at 8 nm. By doing so, the interface recombination at the μc-SiO_x:H <n>/a-SiO_x:H <i> side is expected to limit the passivation quality. Thereby, the absolute $V_{oc,imp}$ values are not directly comparable between the two series. Nevertheless, the comparison of $V_{oc,imp}$ values within the series is valid.

The $V_{oc,imp}$ values of these two series were compared with the material properties of the corresponding samples from Sec. 5.2.2. In Fig. 5.14, the $V_{oc,imp}$ is plotted versus the f_c for μc-SiO_x:H <p> and μc-SiO_x:H <n> variations. While the $V_{oc,imp}$ decreases with increasing f_c for the μc-SiO_x:H <p> series (Fig. 5.14(a)), the opposite behavior is observed for the μc-SiO_x:H <n> series (Fig. 5.14(b)). For μc-SiO_x:H <p> series, the f_c is the only parameter among the material properties presented in Sec. 5.2.2 that can directly be correlated to the $V_{oc,imp}$. This correlation might be explained as follows. In Sec. 5.1.2, the transport of photo generated electrons and holes through the buffer layer, which leads to recombination at the next defect-rich interface, was suggested to explain the thickness dependence of a-SiO_x:H passivation. Based on this model, the quality of the μc-SiO_x:H <p>/a-SiO_x:H <i> interface may affect the passivation quality. Since the field effect passivation of μc-SiO_x:H <p> for p-type wafer was found to be insufficient, which is again supported by the fact that $V_{oc,imp}$ does not correlate with $\alpha_{0.6}$ (not shown), the obtained $V_{oc,imp}$ might be mainly a consequence of the chemical passivation at the a-SiO_x:H <i>/c-Si

<p> and μc-SiO_x:H <p>/a-SiO_x:H <i> interfaces. The decrease of $V_{oc,imp}$ with increasing f_c of the μc-SiO_x:H <p> layer can then be attributed to the increase of c-Si phase with low hydrogen content and consequently higher DB density at the μc-SiO_x:H <p>/a-SiO_x:H <i> interface. Thus, the present results are consistent with the assumptions proposed in Sec. 5.2.3. Moreover, the subsequent decrease of $V_{oc,imp}$ from $f_c = 16$ % to 10 % (Fig. 5.14(b)) is consistently explained by the increase of c_O and thus reduction of hydrogen content, which was already proposed for μc-SiO_x:H passivation without a-SiO_x:H <i> buffer layer (Sec. 5.2.3).

On the contrary, the $V_{oc,imp}$ increases with increasing f_c for the μc-SiO_x:H <n> series (Fig. 5.14(b)). This opposite trend as compared to that observed for the μc-SiO_x:H <p> series suggests that the dominant passivation effect is a different one. The evolution of $V_{oc,imp}$ for the μc-SiO_x:H <n> series is consistently explained in connection with the parameter $\alpha_{0.6}$ as follows. Since the field effect passivation of μc-SiO_x:H <n> material for p-type wafer was found to be significantly higher than that of μc-SiO_x:H <p> material (Sec. 5.2.3), the $V_{oc,imp}$ in this case is likely a product of both the chemical passivation due to the a-SiO_x:H <i> buffer layer and the field effect passivation due to the μc-SiO_x:H <n> contact layer. Since the field effect passivation is prominent, the probability for holes to reach and recombine at the μc-SiO_x:H <n>/a-SiO_x:H <i> interface is low. Therefore, the quality of the μc-SiO_x:H <n>/a-SiO_x:H <i> interface is less important here. This would explain, why the $V_{oc,imp}$ increases with increasing f_c due to the increase of the doping concentration and consequently the field effect passivation, as indicated by the linear dependence between $\alpha_{0.6}$ and f_c (Fig. 5.12), and not decrease due to the worse μc-SiO_x:H/a-SiO_x:H interface quality towards higher f_c as in the case of μc-SiO_x:H <p> series.

In conclusion, the importance of the μc-SiO_x:H/a-SiO_x:H interface passivation is governed by the strength of the field effect passivation. With a strong band bending, the probability for the wrong type of charge carrier to travel through the buffer layer and recombine at the μc-SiO_x:H/a-SiO_x:H interface is reduced, thus the impact of this interface on the eventual passivation quality is minute, and vice versa. This model consistently links the results of the lifetime samples with and without the intrinsic buffer layer. In addition, it supports the idea proposed to explain

the thickness dependence of the a-SiO_x:H passivation (Sec. 5.1.2). However, the µc-SiO_x:H <p> BSF does not seem to be sufficiently doped to provide a strong electron reflexion at the back side of a SHJ solar cell according to the obtained results. A higher doping concentration of the µc-SiO_x:H <p> material is challenging due to the crystallization inhibiting nature of boron (Sec. 5.2.1). One possibility to circumvent this problem is to use n-type wafer instead, where the BSF requires a n-type µc-SiO_x:H layer, that might be processed with higher doping concentration more easily.

5.3. Development of silicon oxide SHJ solar cells

The µc-SiO_x:H/a-SiO_x:H double layer structure demonstrated excellent c-Si surface passivation with as-deposited $V_{oc,imp}$ value above 720 mV. Encouraged by these results, a-SiO_x:H buffer and µc-SiO_x:H contact layers were implemented into SHJ solar cell. This section presents the preliminary development of silicon oxide SHJ solar cells before the systematic optimization of the SiO_x:H layers. The first part deals with the fabrication and characterization of SHJ solar cells consisting of a silicon oxide heterojunction front contact and a fired aluminum (Al) BSF rear contact [185] (heterojunction emitter solar cell) as a proof of concept, followed by SHJ solar cells with silicon oxide heterojunction contacts on both sides (full heterojunction solar cell). In the second part, the choice of the TCO material was motivated with respect to the solar cell performance before and after annealing. In the last part, the origin of the efficiency improvement due to post-deposition annealing was discussed.

5.3.1. Fabrication of SHJ solar cells

Heterojunction emitter solar cell

Limiting the heterojunction contact to only one side by keeping, e.g., a conventional fired aluminum BSF rear contact [185] was expected to be a beneficial first approach that allows for easier interpretation of the influence of the SiO_x:H layers on the SHJ solar cell performance. Figure 5.15 illustrates a schematic drawing of the so called heterojunction emitter solar cell before and after processing the illuminated side. Here, the p-type wafer features the same specification at those used in lifetime

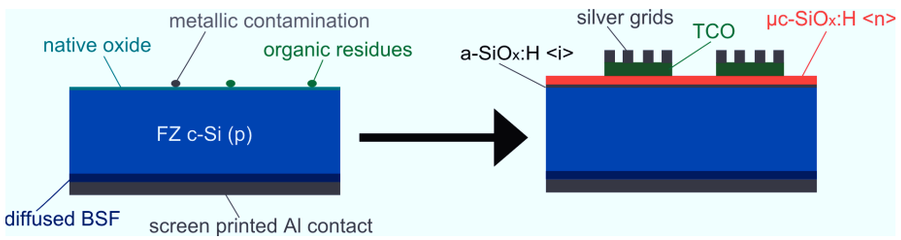

Figure 5.15.: *Schematic drawing of a heterojunction emitter solar cell structure before and after the processing of the illuminated side. First, Al paste was screen printed on the rear side of a flat p-type wafer and subsequently fired at high temperatures to form the diffused BSF. Then, the opposite side of the wafer was freed from native oxide, organic residues and metallic contaminants by chemical cleaning. After the deposition of the a-SiO_x:H <i> buffer and the μc-SiO_x:H <n> emitter layer, ZnO:Al was sputtered through a shadow mask, which defines a cell area of* 1 cm × 1 cm*. The front metalization was realized by thermally evaporated silver grids or silver dots.*

samples. After the screen printing of the aluminum (Al) paste and the subsequent firing at high temperatures to form the full area diffused AlSi BSF, the unprocessed side of the wafer was freed from native oxide and organic residues by wet-chemical cleaning similar to the lifetime sample preparation (Sec. 5.1). A special wafer holder was constructed to protect the processed rear side during the cleaning. In a later stage, it turned out that the front side suffered heavily from metallic contamination caused by the previous rear contact process, which could be partially removed by an additional RCA cleaning step. After the full area PECVD deposition of a-SiO_x:H <i> buffer and μc-SiO_x:H <n> emitter, a number of isolated 1 cm × 1 cm area Al-doped zinc oxide (ZnO:Al) was sputtered through a shadow mask, which defines the cell area. The front metalization was realized by thermally evaporating silver grids or silver dots on top of the ZnO:Al through a shadow mask.

The first cells used an μc-SiO_x:H <n>/a-SiO_x:H <i> configuration that corresponds with that of the $r_{CO_2} = 30$ % sample presented in Fig. 5.14(b). If the rear interface recombination is not the limiting factor, an V_{oc} above 670 mV is expected for these cells according to the $V_{oc,imp}$ of the corresponding lifetime sample. However, a much lower V_{oc} of 563 mV was obtained. With a additional RCA cleaning, known to be effective in removing ionic contaminants [186], the V_{oc} increased to

606 mV. After the subsequent annealing at 200 °C, the V_{oc} further increased to 615 mV, which is the highest value achieved for the heterojunction emitter solar cells in this work. Cells with an significantly thicker a-SiO_x:H <i> layer could not provide higher V_{oc}, which is either an indication that the rear interface with the diffused BSF is limiting the V_{oc} or an hint that the c-Si surface is still not sufficiently clean even with RCA cleaning. In either way, the heterojunction emitter solar cell concept with a fired Al BSF rear contact exhibits unexpected drawbacks.

Full heterojunction solar cell

Based on the experience from the lifetime sample preparation and the heterojunction emitter solar cell fabrication, an optimized process for the fabrication of full heterojunction solar cells with a-SiO_x:H <i> buffer, µc-SiO_x:H <n> emitter and µc-SiO_x:H <p> BSF layers was established. Figure 5.16 shows the process flow chart, respectively. The absorber material is a double side polished, <100> orientated, 250 µm thick p-type FZ Si wafers with a diameter of 100 mm. First, the organic residues on the wafer surface were cleaned using a mixture of sulphuric acid and hydrogen peroxide solution, followed by the removal of the native oxide using a diluted hydrofluoric acid. This wet-chemical procedure was carried out in an automated wafer cleaner in order to guarantee highest reproducibility of the cleaned surface quality. Then, the wafer was quickly transfered into the PECVD system to avoid reoxidation. The preheating time at a substrate temperature of 200 °C was at least 2 hours. After the first a-SiO_x:H <i> layer deposition, the wafer is taken out without waiting for cool down, quickly turned to the other side and put back into the system. After the deposition of the second a-SiO_x:H <i> layer, the chamber is switched to RF mode for the µc-SiO_x:H deposition. Since the front interface quality was found to be less critical than the rear interface quality (Sec. 5.2.3), the µc-SiO_x:H <n> layer was put on top of the second a-SiO_x:H <i> layer, where minute reoxidation during the hot turning might have taken place. After the second hot turning, the µc-SiO_x:H <p> layer was deposited onto the first a-SiO_x:H <i> layer. By processing both a-SiO_x:H <i> layers before µc-SiO_x:H deposition, the reproducibility of the critical a-SiO_x:H <i> deposition is optimal (Sec. 5.1) and the contamination of the a-SiO_x:H <i> layer with impurity dopants is avoided.

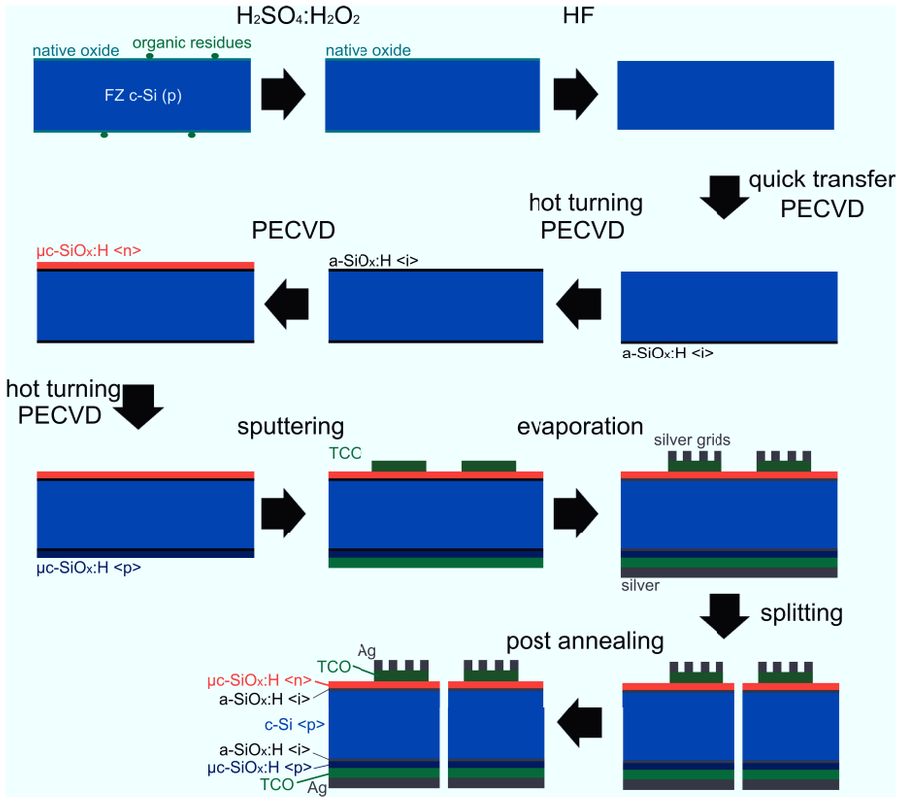

Figure 5.16.: *Process flow chart for the fabrication of full heterojunction solar cells with a-SiO_x:H <i> buffer, µc-SiO_x:H <n> emitter and µc-SiO_x:H <p> BSF layers. Since the front interface quality was found to be less critical than the rear interface quality, the µc-SiO_x:H <n> layer was put on top of the second a-SiO_x:H <i> layer, where minute reoxidation during the hot turning might have taken place. The µc-SiO_x:H <p> layer was then deposited onto the first a-SiO_x:H <i> layer. After the wet-chemical cleaning and the deposition of the SiO_x:H layers, the cell is finished by TCO sputtering and Ag evaporation.*

After the deposition of the PECVD layers, a 70 nm thick full area rear TCO layer was sputtered on top of the μc-SiO_x:H <p> layer, whereas several isolated 1 cm^2 squares of a 70 nm thick front TCO layer was sputtered through a shadow mask on top of the μc-SiO_x:H <n> layer. Both ZnO:Al (2% Al) and Indium Tin Oxide (ITO) (In_2O_3 95%:SnO_2 5%) as TCO material were tested (Sec. 5.3.2). The cell is finished with thermally evaporated silver grids (active area = 0.67 cm^2) or silver dot through a shadow mask on the front TCO and full area silver on the rear TCO. The individual cells, defined by the front TCO area, were then separated by splitting the wafer substrate and annealed on a hot plate at 200 °C under ambient air.

Heterojunction emitter vs. full heterojunction

For the cells with silver grids with a cell coverage of around 33 %, the JV characteristics under illumination was measured to determine the solar cell parameters V_{oc}, J_{sc} and FF. During the measurement, the cell is illuminated through a mask with an opening slightly smaller than the cell area in order to avoid parasitic lateral current collection. The current density values from the solar simulator are corrected to the size of the illuminated areas. The spectrally resolved external quantum efficiency EQE was measured by positioning a focused light spot between two silver grids. The integrated short circuit current density $J_{sc,\,int}$ was determined by integrating the product of EQE under short circuit and AM1.5G solar spectrum over the wavelength range from 300 nm to 1150 nm [187]. Considering $J_{sc,\,int}$ from DSR being more accurate than J_{sc} from the solar simulator [188], the efficiency η_{act} of the active area was recalculated from FF, V_{oc} and $J_{sc,int}$. The cells with a silver dot in the corner of the cell were used to determine the spectrally resolved reflectance R and EQE with an larger light spot. This information is required to calculate the internal quantum efficiency $IQE = EQE/(1-R)$, where $1-R$ is denoted as the cell absorptance A_{cell} later on. It is worthwhile to note that the EQE spectra at short circuit case showed only slight gain as compared to those under negative bias voltage for all cell fabricated in this work. Thus, only the EQE spectra at a bias voltage of 0 V were presented in the following sections.

Capacitance/voltage CV measurements were carried out on silver grid cells

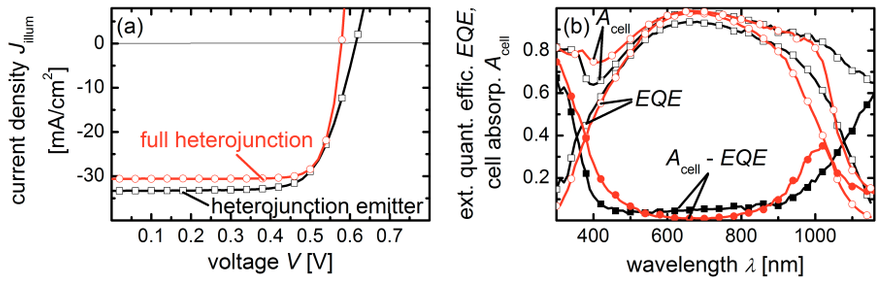

Figure 5.17.: *(a) JV characteristic under illumination. An active area efficiency* $\eta_{act} = 14.70$ % *(14.20 %) with* $FF = 71.8$ % *(80.3 %),* $V_{oc} = 615$ mV *(579 mV) and* $J_{sc,int} = 33.3$ mA/cm^2 *(30.6 mA/cm*^{2}*) was achieved on the heterojunction emitter (full heterojunction) solar cell. The lower* V_{oc} *and* $J_{sc,int}$ *of the full heterojunction solar cell are mainly due to its poorer rear interface passivation. (b)* EQE, A_{cell} *and* $A_{cell} - EQE$ *for an annealed heterojunction emitter and an annealed full heterojunction solar cell both using ZnO:Al as TCO material. The differences in* A_{cell} *and* $A_{cell} - EQE$ *in the long wavelength range is attributed to the different back contact geometry.*

fabricated on several wafers with the nominally same specifications. An average wafer doping concentration N_A of 4.62×10^{15} cm^{-3} with a small standard deviation of 0.15×10^{15} cm^{-3} was obtained from the Moss-Schottky-plot [189, 190]. This confirms the equivalence of the wafer used in this work, which is an important prerequisite for the comparison of the different cells. Presuming a hole-mobility of 425 cm^2/Vs for bulk c-Si, the N_A could be translated into a wafer resistivity ρ of 3.18 ± 0.11 Ωcm.

Figure 5.17 compares the JV under illumination as well as the EQE and A_cell for an annealed heterojunction emitter and an annealed full heterojunction solar cell both using ZnO:Al as TCO material. The $A_\mathrm{cell} - EQE$ is a measure for the optical and electrical losses within the cells. A highest active area efficiency η_act of 14.70 % with $FF = 71.8$ %, $V_\mathrm{oc} = 615$ mV and $J_\mathrm{sc,int} = 33.3$ mA/cm^2 was achieved on the heterojunction emitter solar cell, which clearly demonstrates the processability of working photovoltaic devices using a-SiO$_\mathrm{x}$:H buffer and μc-SiO$_\mathrm{x}$:H contact layers and motivates their implementation also on the rear side of the cell. Therefore, full heterojunction solar cell were fabricated with the nominally same

μc-SiO_x:H <n> ($d = 20$ nm, $r_{CO_2} = 30$ %, $r_{PH_3} = 2.0$ %)/a-SiO_x:H <i> ($d = 4$ nm, $c_O = 5$ %) configuration as that of the heterojunction emitter solar cell. The rear side, however, used an a-SiO_x:H <i> ($d = 4$ nm, $c_O = 5$ %)/μc-SiO_x:H <p> ($d = 50$ nm, $r_{CO_2} = 20$ %, $r_{B(CH_3)_3} = 0.5$ %) stack. On this yet not optimized cell, an active area efficiency η_{act} of 14.20 % with $FF = 80.3$ %, $V_{oc} = 579$ mV and $J_{sc,int} = 30.6$ mA/cm^2 was obtained. The choice of a rather thick μc-SiO_x:H <p> layer of $d = 50$ nm arises from the consideration that a thin μc-SiO_x:H <p> layer might not be able to build up an effective BSF due to insufficient doping of μc-SiO_x:H <p>. Beside, a thick μc-SiO_x:H <p> BSF layer reduces the negative influence of the TCO on the band bending at the c-Si/a-SiO_x:H interface.

The lower V_{oc} of the full heterojunction solar cell indicates a higher rear interface recombination by using the heterojunction rear contact instead of the diffused one. On the contrary, the FF of the full heterojunction solar cell largely exceeds that of the heterojunction emitter solar cell, which suggests an excellent contact forming using a-SiO_x:H <i>/μc-SiO_x:H <p> double layer. However, the solar cell parameters are closely related to the specification of the intrinsic buffer and doped contact layers as shown later on in Sec. 5.4. For example, a significantly higher V_{oc} than 615 mV can be achieved on full heterojunction solar cell by making the rear buffer layer thicker, however, at the cost of the FF (Sec. 5.4.1). Nevertheless, the comparison of EQE and A_{cell} reveals some fundamental differences between the two similar solar cell devices (Fig. 5.17(b)). The EQE of the full heterojunction sample in the wavelength range between 900 nm and 1150 nm lies below that of the heterojunction emitter solar cell due to the lower A_{cell} (higher cell reflectance) between 1000 nm - 1150 nm and/or the higher parasitic loss $A_{cell} - EQE$ between 900 nm and 1050 nm of the former. This remarkable differences in A_{cell} and $A_{cell} - EQE$ is explained as follows.

The penetration depth of the light impinging on bulk c-Si, where, e.g., 99 % of the light is absorbed, is determined as $d(\lambda) = -\ln(0.99)/\alpha(\lambda)$ assuming Lambert-Beer-law, with $\alpha(\lambda)$ the spectrally resolved absorption coefficient of the c-Si material. As $\alpha(\lambda)$ decreases strongly with increasing λ, $d(\lambda)$ gets larger towards higher λ. At a λ of around 1020 nm, the $d(\lambda)$ reaches 250 μm, which is the thickness of the c-Si wafer used in this work. Since light trapping does not occur in the flat

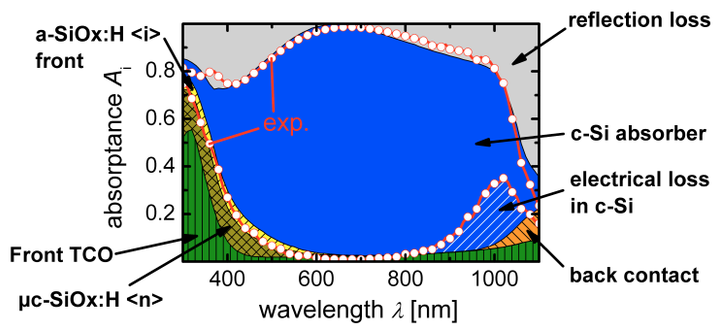

Figure 5.18.: *Simulated absorptance distribution together with the measured $A_{cell} - EQE$ and A_{cell} of the full heterojunction solar cell from Fig. 5.17. The experimental results are sufficiently, although not perfectly, reproduced by the simulation. The sum of the optical losses in the front and back contacts obviously deviates from the measured $A_{cell} - EQE$ in the long wavelength range, which is likely due to electrical losses at the rear interface.*

cell under investigation and the light falls perpendicular onto the sample during the measurements, only the light with $\lambda \leq 1020$ nm entering the c-Si absorber is absorbed before reaching the rear interface. In the case of full heterojunction solar cell, a major part of the light with $\lambda \geq 1020$ nm is reflected back at the rear interface due to the abrupt refractive index change between c-Si and a-SiO_x:H <i>. Since the light in this wavelength range is hardly absorbed even during the subsequent passages through the c-Si bulk due to the low α, the cell reflectance increases rapidly beyond the wavelength of around 1000 nm as observed in Fig. 5.17(b). In the case of heterojunction emitter solar cell, the diffused AlSi BSF induces a refractive index grating between c-Si and Al, which gives rise to lower back reflexion (higher A_{cell}) as compared to the full heterojunction solar cell and higher optical loss (higher $A_{\text{cell}} - EQE$) at the rear side with increasing λ, e.g., in form of plasmonic exitations in aluminum [191].

In order to understand the wavelength dependence of the losses $A_{\text{cell}} - EQE$ within the full heterojunction solar cell, optical simulation was carried out using the device simulator Afors-HET [192] and the Multiple Reflexion and Coherence model. The procedure to obtain the required optical data and the description of the optical model can be found in Ref. [187]. Figure 5.18 displays the simulated absorptance

distribution together with the measured $A_{\text{cell}} - EQE$ and A_{cell} of the corresponding full heterojunction solar cell. As indicated by the comparison between simulated reflexion loss and measured cell absorptance, the experimental results are sufficiently, although not perfectly, reproduced by simulation. The sum of the optical losses in the front and back contacts obviously deviates from the measured $A_{\text{cell}} - EQE$ in the long wavelength range (the deviation is highlighted by the area shaded with white lines). Therefore, this part is likely attributed to the electrical losses. Since this electrical loss has a maximum at $\lambda = 1020$ nm, it presumably originates from rear interface recombination of charge carriers generated in the c-Si bulk close to the rear interface. For wavelengths smaller than 1020 nm, the electron hole pairs are generated closer to the rear interface as the wavelength increases and thus more likely to recombine at this interface. For wavelengths larger than 1020 nm, the place of the photo generation moves away from the rear interface, since the light with longer wavelength is reflected back at the abrupt interface. As a consequence, $A_{\text{cell}} - EQE$ decreases again with further increasing λ. The fact that this decrease of $A_{\text{cell}} - EQE$ is not observed for heterojunction emitter solar cell is consistent with the assumption that the interface with the diffused BSF does not feature pronounced light back reflexion. In addition, the higher $A_{\text{cell}} - EQE$ of the full heterojunction solar cell between 900 nm and 1050 nm supports its lower V_{oc} due to higher rear interface recombination as compared to the heterojunction emitter solar cell.

The differences in the short wavelength range are surprising, since the front side of both devices uses the same layer stacks and therefore the optical behavior in this wavelength range should be comparable. The higher EQE and lower $A_{\text{cell}} - EQE$ of the heterojunction emitter solar cell between 500 nm - 900 nm suggests a overall better carrier extraction property than in full heterojunction solar cell. Unfortunately, this observation could not be explained within the present work.

5.3.2. Choice of TCO and effect of annealing

ZnO:Al vs. ITO

In this work, the ZnO:Al layers were produced at a substrate temperature of 150 °C required to provide good optoelectronic properties [193]. However, the TCO growth

at temperatures above room temperature implies the heating (cooling) of the sample before (after) the ZnO:Al sputtering, which is time consuming and would have delayed the cell throughput. Hence, ITO produced at room temperature was tested on full heterojunction solar cells (later on simply denoted as SHJ solar cell) and compared with those using ZnO:Al as TCO. Figure 5.17 shows the JV characteristics under illumination as well as the EQE and A_{cell} for two SHJ solar cells each with ZnO:Al or RT-ITO (room temperature ITO) before and after annealing at 200 °C for 1 min, whereas the specification of all other layers were kept nominally the same. The corresponding solar cell parameters are listed in Tab. 5.1.

The post-deposition annealing significantly improved the efficiency by raising V_{oc}, $J_{\mathrm{sc,int}}$ and especially FF for both cells. Although the cell performance of the RT-ITO sample was clearly inferior to that of the ZnO:Al sample before annealing, the solar cell parameters of both samples became comparable after the annealing. Even though the increase of $J_{\mathrm{sc,int}}$ after annealing is not as pronounced as the other parameters, the comparison of EQE and A_{cell} between the two samples reveals different behavior of RT-ITO and ZnO:Al upon thermal treatment. While the change after annealing is almost negligible for the ZnO:Al sample, there seems to be a shift and a simultaneous increase of the interference maximum in the EQE and A_{cell} spectra for the RT-ITO sample. In the wavelength range between 300 nm and 400 nm, the EQE of the annealed RT-ITO sample is higher than the as-deposited one, which is not the case for A_{cell}. This implies a reduced optical loss in the short wavelength range with annealing.

Table 5.1.: *Solar cell parameters of SHJ solar cells with ZnO:Al and RT-ITO as TCO layers in as-deposited and annealed states.*

TCO	state	$\eta_{\mathbf{act}}$ [%]	FF [%]	$V_{\mathbf{oc}}$ [mV]	$J_{\mathbf{sc,int}}$ [mA/cm^2]
ZnO:Al	as-dep.	11.6	68.7	558	30.3
	annealed	14.2	80.3	579	30.6
RT-ITO	as-dep.	9.54	62.3	520	29.4
	annealed	13.9	79.0	568	30.9

These observations are conclusively explained by the change of the optical properties of the TCO layers. Transmission and reflexion measurements on ZnO:Al

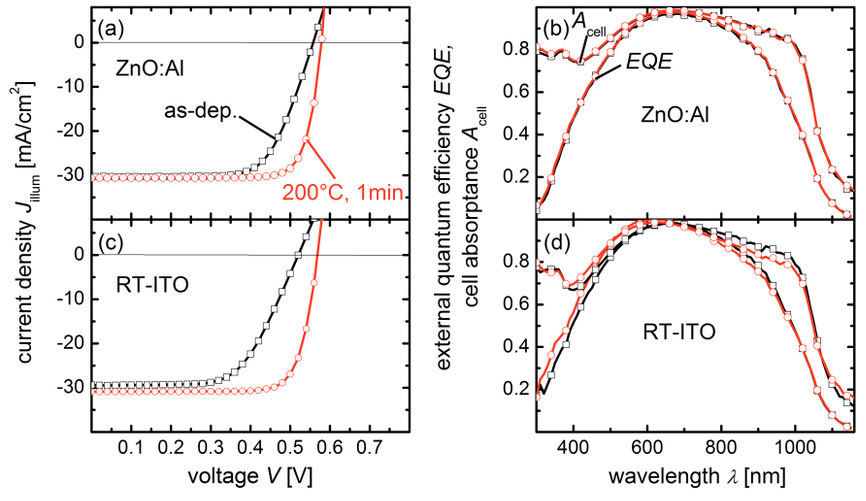

Figure 5.19.: *(a,c) JV characteristics under illumination. The post-deposition annealing significantly improved the efficiency by raising V_{oc}, $J_{sc,int}$ and especially FF for both cell. (b,d) EQE and A_{cell} for two SHJ solar cells each with ZnO:Al or RT-ITO before and after annealing at* 200 °C *for* 1 min*, whereas the specification of all other layers were kept nominally the same. While the change after annealing is almost negligible for the ZnO:Al sample, there seems to be a shift and a simultaneous increase of the interference maximum in the EQE and A_{cell} spectra as well as a reduced optical loss in the short wavelength range for the RT-ITO sample.*

layers showed that the optical properties of ZnO:Al remained unaffected by the annealing procedure at 200 °C, which is not surprising due to the fact that the substrate temperature was already 150 °C during the deposition. An annealing at 200 °C for a short time will unlikely induce any optical change to this material. On the contrary, the room temperature ITO was changed with respect to its optical and electrical properties. Figure 5.20 presents the refractive index n and the absorptance A of a 70 nm thick RT-ITO layer in the as-deposited and annealed states. The n was measured using spectroscopic ellipsometry [194] on sample with c-Si substrate and the A was determined using optical photometry on samples with glass substrate. In agreement with the EQE and A_{cell} data, the thermally induced change in n of the front ITO over the whole spectral range is responsible for the shift of the

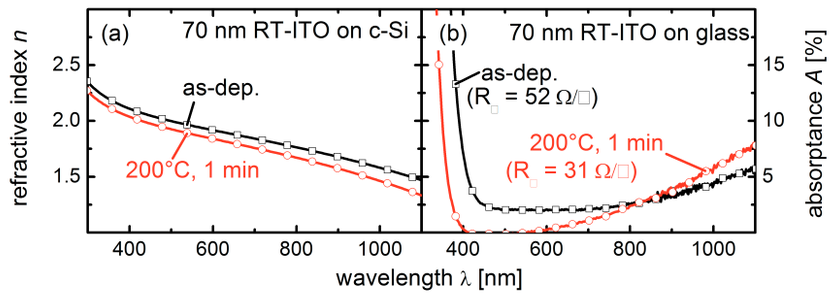

Figure 5.20.: *(a) Refractive index n and (b) absorptance A of a* 70 nm *thick RT-ITO layer in the as-deposited and annealed states. The n was measured using spectroscopic ellipsometry [194] on samples with c-Si substrate and the A was determined using optical photometry on sample with glass substrate. The thermally induced change in n of the front ITO over the whole spectral range is responsible for the shift of the interference pattern and the reduction of reflexion loss in the EQE and A_{cell} spectra (Fig.5.19(d)), while the Burstein-Moss-shift due to thermally activated doping accounts for the reduced optical loss in the short wavelength range upon annealing (Fig.5.19(d)).*

interference pattern and the reduction of reflexion loss. The decrease of A in the short wavelength range and its increase in the long wavelength range are typically assigned to the increase of free charge carriers in TCO, which induces a Burstein-Moss-shift and enhances the free carrier absorption, respectively [195]. Thus, the thermal treatment might have excited inactive dopants that release electrons into the conduction band. This assumption is supported by the sheet resistance R_{sheet} values measured on as-deposited (52 Ω/□) and annealed (31 Ω/□) RT-ITO samples on glass substrates as displayed in Fig 5.20. Hence, the Burstein-Moss-shift accounts for the reduced optical loss in the short wavelength range upon annealing (Fig. 5.19(d)).

Origin of efficiency improvement upon annealing

The sheet resistance of ZnO:Al layers on glass substrate was also determined. Although the R_{sheet} of the as-deposited RT-ITO layer (52 Ω/□) is lower than the as-deposited ZnO:Al layer (107 Ω/□), the FF of the latter is higher. This suggests

that the difference in FF does not result from the sheet resistance of the TCO layers, but the potential barrier at the TCO/µc-SiO_x:H contacts, which depends on the work function of TCO material. According to this R_{sheet} comparison between ZnO:Al and RT-ITO, the decrease of the RT-ITO R_{sheet} from 52 Ω/□ to 31 Ω/□ cannot exclusively explain the remarkable increase of FF upon annealing. In principle, there are 7 constituents at each side of the c-Si absorber that might have been changed due to the annealing in terms of transport properties. These are the TCO, µc-SiO_x:H and a-SiO_x:H layers as well as the Ag/TCO, TCO/µc-SiO_x:H, µc-SiO_x:H/a-SiO_x:H and a-SiO_x:H/c-Si interfaces. In addition to the electrical properties of the TCOs, the dark conductivity σ_{dark} values of µc-SiO_x:H and a-SiO_x:H layers on glass substrates was checked before and after annealing. While the σ_{dark} of the a-SiO_x:H layer remained below 10^{-10}S/cm even after annealing, the µc-SiO_x:H layer gained in σ_{dark} from 2.6×10^{-3}S/cm to 7.2×10^{-3}S/cm. The reduction of its activation energy E_a from 71 meV (as-deposited) to 66 meV (annealed) determined from the slope of the temperature dependent conductivity in the Arrhenius-plot suggests that an increase in doping concentration due to the annealing-induced activation of dopants is the reason for the improved conductivity. Increase in carrier mobility would have required structural change of the µc-SiO_x:H material, which is unlikely to occur during annealing at 200 °C. In conclusion, the insignificant conductivity improvement in all layers might have contributed to some part of the increase in FF during annealing.

The Ag/RT-ITO contact resistance measured with TLM structures (Sec. 3.2) changed marginally from 7.0 Ω in the as-deposited state to 7.2 Ω in the annealed state, which can be thus excluded as a source for higher FF upon annealing. As already discussed in Sec. 5.1.2, the number of defect states at the a-SiO_x:H/c-Si interface is reduced via thermally activated reconfiguration of SiH_2 into SiH. Accordingly, the transport of charge carriers across this interface takes place with less recombination loss after annealing, giving rise to increased FF and V_{oc}. A reduction of recombination loss at the a-SiO_x:H/c-Si interface is also expected due to a higher field effect passivation induced by the higher doping concentration of the µc-SiO_x:H layer after annealing (Sec. 5.2.3). The increase of doping concentration in the RT-ITO upon annealing correlates with a shift of the Fermi level towards higher energies and consequently a reduction of its work function. The decrease of

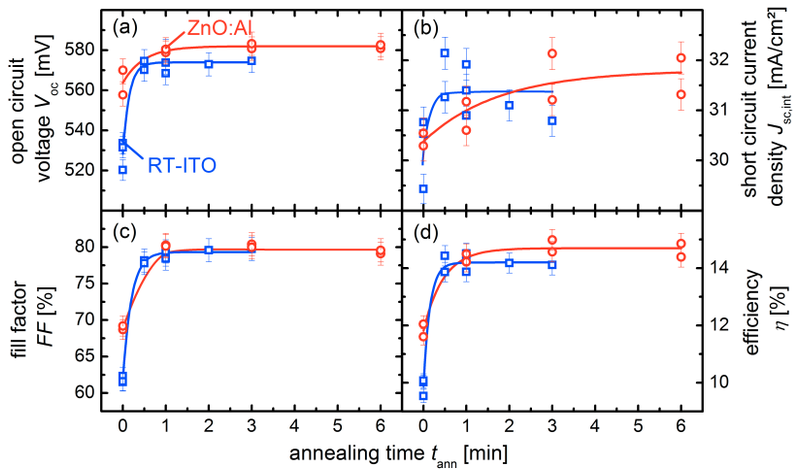

Figure 5.21.: *Solar cell parameters (a) V_{oc}, (b) $J_{sc,int}$, (c) FF and (d) η_{act} of SHJ solar cells with ZnO:Al and RT-ITO as TCO layers versus annealing time t_a. The lines serve as a guide to the eye. The annealing temperature T_a was kept constant at* 200 °C. *The improvements take place between as-deposited and* 1 min *annealing, whereas the effect of annealing seems to be saturated after the* 1 min *annealing. Since the η_{act} did not deteriorate with longer annealing, an t_a of* 2 min *was chosen for later SHJ solar cell processing in order to guarantee stabilized efficiencies.*

the TCO work function results then in higher FF due to improved RT-ITO/μc-SiO_x:H contact [196]. Since the RT-ITO might have shifted its work function closer to that of the ZnO:Al during annealing, the annealed FF values of both samples became comparable (Fig. 5.19). Thus, the work function of the ZnO:Al might have been smaller than that of the RT-ITO in the as-deposited state, which gave rise to higher initial FF of the ZnO:Al sample. In addition, the thermally induced doping activation in μc-SiO_x:H layers might affect the transport properties at the TCO/μc-SiO_x:H and μc-SiO_x:H/a-SiO_x:H interfaces as well. Although several possible causes of the annealing-induced efficiency improvement were identified, their quantitative attribution to the solar cell parameters requires more systematic studies, which is beyond the scope of this work.

Annealing time dependence

Since the post-deposition annealing is a crucial step to obtain high efficiency SHJ solar cells, a closer look at the annealing time t_a dependence of the solar cell performance is indicated. Figure 5.21 shows the solar cell parameters of several ZnO:Al and RT-ITO samples gradually annealed up to 6 min. The cell improvements take place between as-deposited and 1 min annealing, whereas the effect of annealing seems to be saturated after the 1 min annealing. The observation that the solar cell performance did not deteriorate with longer annealing indicates a good thermal stability of the SiO_x:H layers. It is worthwhile to note that the $J_{sc,int}$ values are plotted within a narrow range, because they did not change as pronounced as the other parameters. As a consequence, the scatter between the different samples fabricated under the same deposition conditions appears to be large, which explains the alleged decrease of $J_{sc,int}$ with increasing t_a for RT-ITO. Since the η_{act} did not deteriorate with longer annealing, an t_a of 2 min was chosen for later SHJ solar cell processing, in order to guarantee stabilized efficiencies and avoid operations in the critical range around $0.5\ \mathrm{min} - 1\ \mathrm{min}$. Although the stabilized efficiency values of the ZnO:Al samples are still higher than those of the RT-ITO samples, the difference lies within the fluctuation of statistics and the error bars. Since the difference in the performance of SHJ solar cells with ZnO:Al and RT-ITO is within the experimental scatter, it is preferable to use RT-ITO in future simply due to the economy of time, as the heating (cooling) of samples before (after) the ZnO:Al sputtering is time consuming.

5.4. Optimization of the silicon oxide layers

This section deals with the optimization of the PECVD grown SiO_x:H layers in SHJ solar cells. Figure 5.22 shows a schematic illustration of the SHJ solar cell structure, on which the optimization of the emitter, BSF and buffer layers was carried out. The variations in the SiO_x:H layers that were studied in this work are summarized on the right side of the drawing in chronological order. In the following, systematic variations of the thickness of the a-SiO_x:H front and rear buffer layers, the CO_2 and $B(CH_3)_3$ gas flow ratios of the µc-SiO_x:H <p> BSF as well as the thickness and

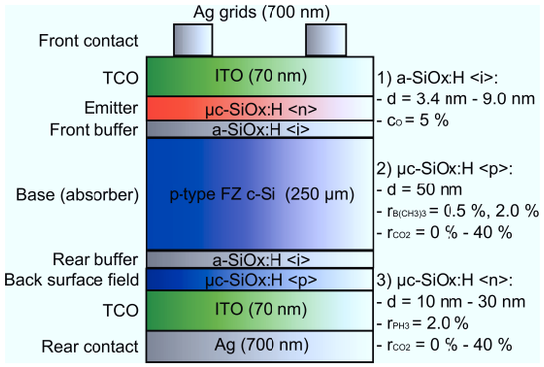

Figure 5.22.: *Schematic illustration of the SHJ solar cell structure with PECVD grown emitter, BSF and buffer layers on flat p-type wafer covered with sputtered TCO and thermally evaporated silver, on which the optimization of the PECVD layers was carried out. The variations in the SiO_x:H layers that were studied in this work are summarized on the right side of the drawing in chronological order.*

CO_2 gas flow ratio of the µc-SiO_x:H <n> emitter are presented. The impact of these variations on the SHJ solar cell performance is discussed in correlation with the corresponding layer properties provided in previous sections. In the last part, the SHJ solar cell with the highest efficiency achieved in this work is presented and compared with the record Sanyo HIT solar cell (Sec. 2.2.1).

5.4.1. Optimization of intrinsic a-SiO_x:H buffer layer

Buffer layer thickness

Figure 5.23 displays the solar cell parameters plotted versus the rear buffer layer thicknesses for three different SHJ solar cell series each with the front buffer layer thickness d_{front} kept at the same size (1), half the size (1/2) or a third of the size (1/3) of that of the rear buffer layer thickness d_{rear}. The thicknesses were estimated from deposition times and the pre-determined deposition rate. The µc-SiO_x:H layers were deposited under the same gas flow rates as those in the first full heterojunction solar cell from Sec. 5.3.1. Within each series, the V_{oc} and the $J_{\text{sc,int}}$ increase with thicker buffer layers, whereas the FF, first remaining at a high value showing only slight

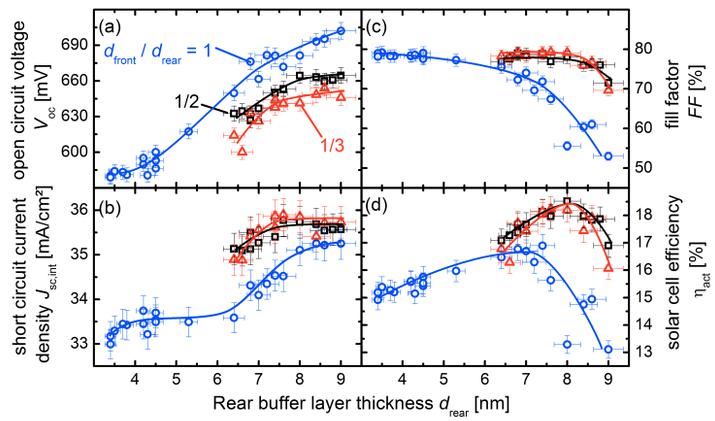

Figure 5.23.: *Dependence of the SHJ solar cell parameters on the thickness of the rear a-SiOx:H <i> buffer layer for three different SHJ solar cell series each with the front buffer layer thickness d_{front} kept at the same size (1), half the size (1/2) or a third of the size (1/3) of that of the rear buffer layer thickness d_{rear}. The η_{act} first increases with increasing buffer layer thickness due to the improvement of interface passivation, but then decreases due to higher series resistance from the buffer layers.*

deterioration with thickness, decreases strongly upon a critical rear buffer thickness. Thereby, the efficiency η_{act} first increases with increasing buffer layer thickness due to the increase in V_{oc} and $J_{\mathrm{sc,int}}$, but then decreases due to significant loss in FF. Comparison between the series (1) and (1/2) shows a decrease in V_{oc} and an increase in $J_{\mathrm{sc,int}}$ as the d_{front} is reduced. The critical rear buffer thickness, upon which the FF starts to strongly deteriorate, shifts to higher d_{rear} values. Consequently, the maximum η_{act} increases and shifts to thicker rear buffer layers with thinner front buffer layers for the series (1) and (1/2). Comparing the series (1/2) and (1/3), it is found that the decrease in V_{oc} and the increase in $J_{\mathrm{sc,int}}$ continue with further reduction of the d_{front}. However, no significant change in the FF was observed for these two series. Since the loss in V_{oc} and the gain in $J_{\mathrm{sc,int}}$ compensate each other, the η_{act} as a function of the d_{rear} was similar for the series (1/2) and (1/3). The highest efficiency was obtained for the 4.0 nm front and 8.0 nm rear buffer layer thickness SHJ solar cell of the (1/2) series with $V_{\mathrm{oc}} = 664$ mV, $J_{\mathrm{sc,int}} = 35.7$ mA/cm^2,

$FF = 78.0$ % and $\eta_{\mathrm{act}} = 18.5$ %.

Figure 5.24 shows the IQE of a selection of SHJ solar cells from the three series. Figure 5.24(a) compares the IQE of two cells with same d_{front} but different d_{rear}, showing an increase of the carrier extraction especially in the long wavelength range with increasing d_{rear}. Figure 5.24(b) compares the IQE of three cells with same d_{rear} but different d_{front}, showing a decrease of the carrier extraction over the whole spectral range with increasing d_{front}. It is important to note that the cells achieved a highest EQE value of 98.7 % $\pm$ 1.0 % at the wavelength around 630 nm. This surprisingly high EQE at the wavelength of 630 nm is verified by optical photometry measurements on annealed RT-ITO layers deposited on glass substrates (Fig. 5.20) showing an absorptance of less than 0.05 % and on SHJ solar cells showing a cell reflectance of 1.3 %.

The increase in V_{oc} with thicker d_{front} at constant d_{rear}, when comparing between the solar cell series (1), (1/2) and (1/3) (Fig. 5.23(a)), can be attributed to improved front interface passivation, which is in agreement with the QSSPC results of the μc-SiO_x:H <n>/a-SiO_x:H <i> lifetime samples with varying i-layer thickness (Sec. 5.2.3). At the same time, the $J_{\mathrm{sc,int}}$ decreases with thicker d_{front} (Fig. 5.23(b)), which can be assigned to higher parasitic absorption losses from the front buffer layer, which is supported by the decreasing IQE in the short wavelength range with increasing d_{front} as shown in Fig. 5.24(b) and confirmed by device simulation using AFORS-HET (not shown). However, the simulation results do not show any change of IQE in the long wavelength range with varying d_{front}. This disagreement with the experimental observation is explained below. Device simulation also reveals that a reduced front interface passivation does not deteriorate $J_{\mathrm{sc,int}}$, since the pronounced band bending at the emitter <n>/base <p> interface in the short circuit case effectively reflects majority holes and extracts minority electrons close to this interface before the charge carriers recombine at the heterojunction interface. In difference to the situation at the front interface, the rear interface passivation will likely affect the IQE in the long wavelength range due to the weaker band bending at the base <p>/BSF <p> interface as compared to the emitter <n>/base <p> interface in the short circuit case.

In order to verify this assumption, the effect of varying d_{rear} at constant d_{front}

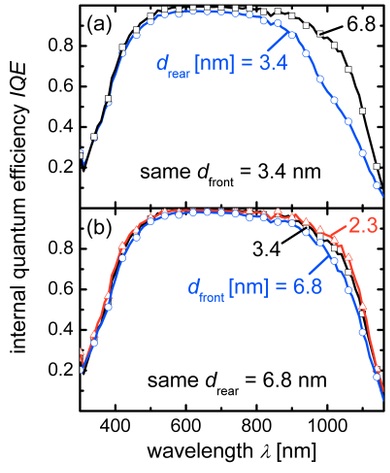

Figure 5.24.: *Internal quantum efficiency IQE of the SHJ solar cells with different (a) rear and (b) front a-SiO_x:H <i> buffer layer thicknesses. The strong increase of the carrier extraction in the long wavelength range with increasing d_{rear} at constant d_{front} is attributed to the reduction of the rear interface recombination. The decrease of IQE in the short wavelength range with increasing d_{front} at constant d_{rear} suggests higher parasitic absorption losses from the front buffer layer. The noticeable change of the IQE in the long wavelength range for SHJ solar cells with thicker d_{front} at constant d_{rear} is attributed to the small thickness variation of d_{rear} within the error bars as indicated in Fig. 5.23(b).*

was analyzed by comparing the solar cells with $d_{\mathrm{rear}} = 3.0\ \mathrm{nm} - 4.5\ \mathrm{nm}$ from the series (1) with those with $d_{\mathrm{rear}} = 6.0\ \mathrm{nm} - 9.0\ \mathrm{nm}$ from the series (1/2). With thicker d_{rear} at constant d_{front}, V_{oc} (Fig. 5.23(a)) and $J_{\mathrm{sc,int}}$ (Fig. 5.23(b)) increase significantly, which can be attributed to the reduction of the rear interface recombination. This is consistent with the comparison of the IQE of two SHJ cells with the same d_{front} but different d_{rear} (Fig. 5.24(a)), showing strong increase of the carrier extraction especially in the long wavelength range with increasing d_{rear}. Therefore, the noticeable change of the IQE in the long wavelength range for SHJ solar cells with thicker d_{front} at constant d_{rear} (Fig. 5.24(b)) is attributed to the small thickness variation of d_{rear} within the error bars as indicated in Fig. 5.23(b).

Within the series with simultaneous increase of both buffer layer thicknesses,

the current gain at long wavelengths due to improved rear interface passivation (thicker d_{rear}) overcompensates the current loss at short wavelengths due to higher parasitic absorption loss (thicker d_{front}), giving rise to a total gain in $J_{\mathrm{sc,int}}$ with increasing buffer layer thickness. The increase of V_{oc} with thicker d_{front} and d_{rear} within the series is then attributed to the improved passivation of both heterojunction interfaces. The higher FF (Fig. 5.23(c)) with thinner d_{front} and/or d_{rear} can be assigned to the lower series resistance of the buffer layers, which overcompensates the deterioration of the FF due to reduced buffer layer thickness and thus increased interface recombination (Sec. 5.3.2). However, the FF does not exceed the value of 78 % for all three series, which is an indication for the limitation of the FF by other sources of series resistance as listed in Sec. 5.3.2.

5.4.2. Optimization of p-type μc-SiO$_x$:H back surface field layer

BSF layer doping concentration

Figure 5.25 compares the solar cell parameters of the (1/2) buffer layer thickness series from Sec. 5.4.1, where the μc-SiO$_x$:H <p> BSF was deposited at $r_{\mathrm{CO_2}} = 20$ % and $r_{\mathrm{B(CH_3)_3}} = 0.5$ %, with another (1/2) buffer layer thickness series, where the μc-SiO$_x$:H <p> BSF was deposited at $r_{\mathrm{CO_2}} = 20$ % and $r_{\mathrm{B(CH_3)_3}} = 2.0$ %. The V_{oc} of the latter is higher over the whole d_{rear} range, whereas the difference between the V_{oc} of both series increases with decreasing d_{rear}. A similar behavior is observed for $J_{\mathrm{sc,int}}$. The higher V_{oc} and $J_{\mathrm{sc,int}}$ of the 2.0 % samples as compared to those of the 0.5 % samples suggest a better rear interface passivation of the former. This is in agreement with the QSSPC results shown in Fig. 5.14 (Sec. 5.2.3), where the higher $V_{\mathrm{oc,imp}}$ of the lifetime sample with μc-SiO$_x$:H <p> deposited at $r_{\mathrm{B(CH_3)_3}} = 2.0$ % was assigned to the lower c-Si phase fraction of the p-layer giving rise to less defect-rich a-SiO$_x$:H <i>/μc-SiO$_x$:H <p> interface. The observation of an increasing difference in V_{oc} between the two series with decreasing d_{rear} supports this explanation, since a thinner buffer layer increases the probability of electrons to penetrate through the buffer layer and recombine with holes at the a-SiO$_x$:H <i>/μc-SiO$_x$:H <p> interface. In other words, the quality of the i/p interface becomes increasingly important as this probability increases with decreasing d_{rear}.

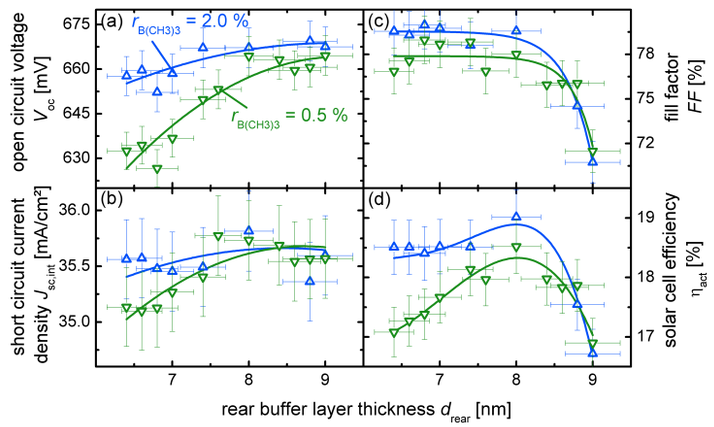

Figure 5.25.: *Solar cell parameters plotted versus rear buffer layer thickness d_{rear} for two buffer layer thickness series with the µc-SiO_x:H <p> BSF deposited at r_{CO_2} = 20 %/$r_{B(CH_3)_3} = 0.5$ % and $r_{CO_2} = 20$ %/$r_{B(CH_3)_3} = 2.0$ %, respectively. The front buffer layer thickness d_{front} was kept at half the size of that of d_{rear}. All relevant solar cell parameters were improved by substituting the µc-SiO_x:H <p> layer with $r_{B(CH_3)_3} = 0.5$ % by one with 2.0 % in a d_{rear} range before the buffer layer thickness deteriorates the solar cell performance.*

Since the field effect passivation was found to play an minor role at the rear side (Sec. 5.2.3), the improvement in rear interface passivation is unlikely to be related to stronger field effect passivation, even though the doping concentration increased as $r_{\mathrm{B(CH_3)_3}}$ changed from 0.5 % to 2.0 % (Sec. 5.2.2).

The FF values of the $r_{\mathrm{B(CH_3)_3}} = 2.0$ % series are higher than those of the 0.5 % series for $d_{\mathrm{rear}} \leq 8$ nm, which is likely due to the higher σ_{dark} (lower series resistance) of the µc-SiO_x:H <p> layer deposited at $r_{\mathrm{B(CH_3)_3}} = 2.0$ % (Sec. 5.2.2). The improvement in rear interface passivation might also have contributed to the higher FF. For $d_{\mathrm{rear}} \geq 8$ nm, the series resistance of the buffer layers limits the carrier transport in the cells, as a consequent of which the FF values of both series become comparably low. In conclusion, all relevant solar cell parameters were improved by substituting the µc-SiO_x:H <p> layer with $r_{\mathrm{B(CH_3)_3}} = 0.5$ % by one with 2.0 % in a d_{rear} range before the buffer layer thickness deteriorates the solar cell

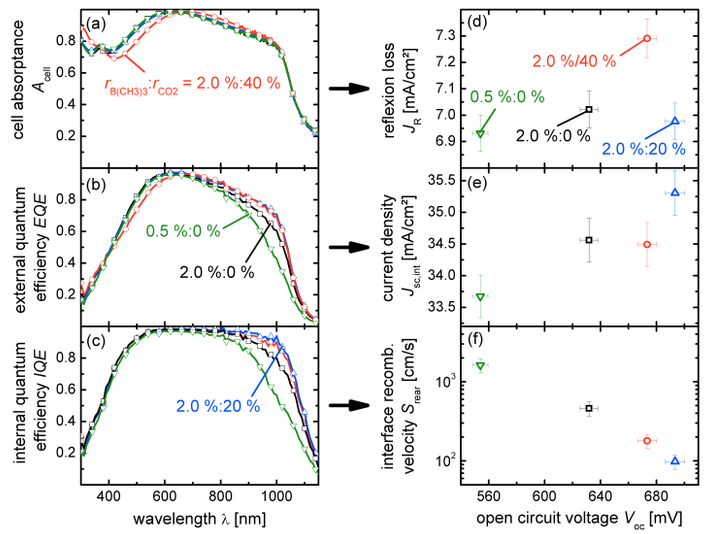

Figure 5.26.: *(a) Cell absorptance A_{cell}, (b) EQE and (c) IQE as well as (d) integrated reflexion loss J_R, (e) $J_{sc,int}$ and (f) rear interface recombination velocity S_{rear} plotted versus the V_{oc} for SHJ solar cells with $r_{CO_2} = 0$ %, 20 % and 40 % during the p-layer deposition and $r_{B(CH_3)_3}$ kept constant at 2.0 %. A $r_{CO_2} = 0$ % cell with $r_{B(CH_3)_3} = 0.5$ % is additionally included. The $r_{CO_2} = 20$ % sample shows the best solar cell performance due to its lowest rear interface recombination velocity and relatively low reflexion loss.*

performance. The new highest efficiency was obtained on the SHJ solar cell of the $r_{\mathrm{B(CH_3)_3}} = 2.0$ % series with $V_{\mathrm{oc}} = 667$ mV, $J_{\mathrm{sc,int}} = 35.8$ mA/cm^2, $FF = 79.6$ % and $\eta_{\mathrm{act}} = 19.0$ %. The optimum buffer layer thickness combination remained at 4.0 nm and 8.0 nm for front and rear buffer layer thickness, respectively.

BSF layer oxygen content

In order to investigate the effect of oxygen content in the μc-SiO_x:H <p> layer on device level, SHJ solar cells with $r_{\mathrm{CO_2}} = 0$ %, 20 % and 40 % during the p-layer deposition were fabricated, while the $r_{\mathrm{B(CH_3)_3}}$ was kept constant at 2.0 %. In addition, a $r_{\mathrm{CO_2}} = 0$ % cell at $r_{\mathrm{B(CH_3)_3}} = 0.5$ % was prepared. Since the resulting FF values of these cells are easily correlated with σ_{dark} of the corresponding μc-SiO_x:H

<p> layers (Fig. 5.10), the focus of this study lies on the optics and passivation-related effects. Figure 5.26 displays the A_{cell}, EQE and IQE of these four samples as well as the integrated reflexion loss in form of current density J_{R}, the $J_{\mathrm{sc,int}}$ and the rear interface recombination velocity S_{rear} versus the V_{oc}. The J_{R} was derived from cell reflectance $R_{\mathrm{cell}} = 1 - A_{\mathrm{cell}}$ by integrating the product of R_{cell} and AM1.5G spectrum over the spectral range from 300 nm to 1150 nm. For the determination of S_{rear}, the effective diffusion length L_{eff} was extracted from the IQE spectra via the equation [197]

$$IQE^{-1}(L_\alpha) = 1 + \frac{L_\alpha}{L_{\mathrm{eff}}} \quad , \tag{5.1}$$

where $L_\alpha = \alpha^{-1}$ is the absorption length in the c-Si absorber. The S_{rear} is derived from L_{eff} via the equation [197]

$$L_{\mathrm{eff}} = L_{\mathrm{n}} \frac{S_{\mathrm{rear}} \sinh(w/L_{\mathrm{n}}) + D_{\mathrm{n}}/L_{\mathrm{n}} \cosh(w/L_{\mathrm{n}})}{S_{\mathrm{rear}} \cosh(w/L_{\mathrm{n}}) + D_{\mathrm{n}}/L_{\mathrm{n}} \sinh(w/L_{\mathrm{n}})} \quad , \tag{5.2}$$

by assuming an electron diffusion length L_{n} significantly larger than the wafer thickness w and an electron diffusion coefficient D_{n} of around 29 cm^2/s for the high quality p-type FZ wafer absorber with an electron lifetime $\tau_{\mathrm{n}} >> 1$ ms [103].

The method to extract L_{eff} from IQE spectra was proposed for first generation c-Si solar cells [197], where parasitic absorption loss in the long wavelength range is negligibly small. However, the TCO layers in SHJ solar cells, which do not exist in conventional c-Si solar cells, exhibit non-negligible and wavelength dependent absorption at long wavelengths (Fig. 5.18). Thus, the TCO absorption A_{TCO}, which would have falsified the L_{eff} results, has to be taken into consideration when using this method for SHJ solar cells. As an example, Fig. 5.27(a) shows the A_{ITO} of a 70 nm thick front ITO from device simulation, the measured IQE of one SHJ solar cell that already includes the TCO absorption and the sum $IQE + A_{\mathrm{ITO}}$. The $IQE + A_{\mathrm{ITO}}$ spectrum between 700 nm and 1000 nm is assumed to be the expected IQE of the same SHJ solar cell, if the ITO layer at the emitter side would be completely transparent. This assumption is at least true for the wavelength range

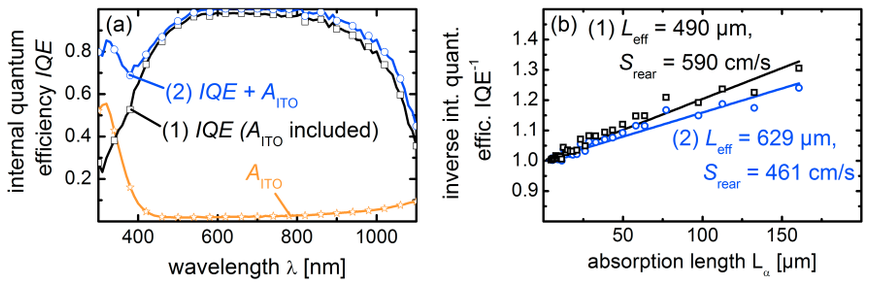

Figure 5.27.: *(a) The A_{ITO} of a* 70 nm *thick front ITO from device simulation, the measured IQE of one SHJ solar cell that already includes the A_{ITO} and the sum $IQE + A_{ITO}$. The $IQE + A_{ITO}$ spectrum between* 700 nm *and* 1000 nm *is assumed to be the expected IQE of the same SHJ solar cell, if the ITO layer at the emitter side would be completely transparent. (b) The IQE^{-1} versus L_α for (1) IQE and (2) $IQE + A_{ITO}$ for the wavelength range $\lambda = 700$ nm $- 1000$ nm. The L_{eff} values were derived from the slope of the fitting lines within this range. The considerable difference between S_{rear} before and after ITO correction confirms the importance of excluding A_{ITO} before L_{eff} determination from IQE spectra.*

between 700 nm and 1000 nm. For $\lambda \leq 700$ nm, the light that was originally absorbed by the ITO would be mainly absorbed by the emitter and front buffer layers instead of by the c-Si wafer (Fig. 5.18). For $\lambda \geq 1000$ nm, the additionally available light would result in more absorption in the back ITO and/or higher cell reflectance, since the light at these wavelengths with low α of the c-Si cannot be absorbed completely during the first passage through the wafer (Sec. 5.3.1). Figure 5.27(b) presents the IQE^{-1} versus L_α for (1) IQE and (2) $IQE + A_{\mathrm{ITO}}$ for the wavelength range $\lambda = 700$ nm $- 1000$ nm. The L_{eff} values were successfully derived from the slope of the fitting lines within this range. The considerable difference between S_{rear} before and after ITO correction confirms the importance of excluding A_{ITO} before L_{eff} determination from IQE spectra.

The A_{cell} spectra reveal a shift of the interference pattern (Fig. 5.26(d)) with varying $r_{\mathrm{CO_2}}$, which is likely a consequence of changing refractive index n in the µc-SiO$_x$:H <p> BSF (Fig. 5.10(d)). In particular, the reflexion loss J_{R} is the highest for the $r_{\mathrm{CO_2}} = 40$ % cell, while J_{R} of other cells remain comparable on a

lower level. The shift of the interference pattern affects the EQE spectra mostly in the short wavelength range. At long wavelengths, the difference in EQE between the cells is dominated by the difference in IQE. The increasing trend of $J_{\mathrm{sc,int}}$ with increasing V_{oc} (Fig. 5.26(e)) mainly arises from the increase of EQE in the long wavelength range. The lower $J_{\mathrm{sc,int}}$ of the $r_{\mathrm{CO_2}} = 40$ % cell, which deviates from a linear dependence between $J_{\mathrm{sc,int}}$ and V_{oc}, originates from its higher J_{R}. Hence, V_{oc} and $J_{\mathrm{sc,int}}$ perfectly correlate with each other when omitting reflexion losses. This suggests that, within the solar cell device, the variation of these two cell parameters have the same origin. The V_{oc} increases from $r_{\mathrm{CO_2}} = 0$ % to 20 % and decreaes from 20 % to 40 % (Fig. 5.26), which is in agreement with the QSSPC results shown in Fig. 5.14 (Sec. 5.2.3). The hydrogen content at the a-SiO_x:H <i>/μc-SiO_x:H <p> interface was assumed to be the key parameter, which first increases with increasing oxygen content due to less H-poor c-Si phase and then decreases due to less H bonding silicon atoms. Thus, the variation of both V_{oc} and $J_{\mathrm{sc,int}}$ for different cells is attributed to their corresponding rear interface passivation quality. The exponentially decreasing S_{rear} as a function of increasing V_{oc} (Fig. 5.26(f)) strongly supports this assumption.

As a result of this study, the application of μc-SiO_x:H <p> BSF did not result in any optical gain in the SHJ solar cell as compare to its μc-Si:H <p> reference, this might be due to the fact that the back reflexion is mainly determined by the abrupt flat a-SiO_x:H/c-Si rear interface, which is already very efficient as indicated by the high cell reflectance for $\lambda \geq 1000$ nm (Fig. 5.26(a)). An improved absorption in the c-Si absorber is expected when combining this efficient back reflexion with light scattering at the a-SiO_x:H/c-Si rear interface by using textured wafers due to enhanced light trapping. In addition, the cells cannot profit from the higher band gap of the μc-SiO_x:H <p> layers, since light in the short wavelength range do not reach the back side of the cell (Fig. 5.18). In conclusion, the $r_{\mathrm{CO_2}} = 20$ % sample shows the best solar cell performance due to its low rear interface recombination velocity $S_{\mathrm{rear}} = 98$ cm/s and reflexion loss $J_{\mathrm{R}} = 7.0$ mA/cm^2 combined with an sufficient $\sigma_{\mathrm{dark}} = 6.8 \times 10^{-3}$ S/cm of the BSF layer.

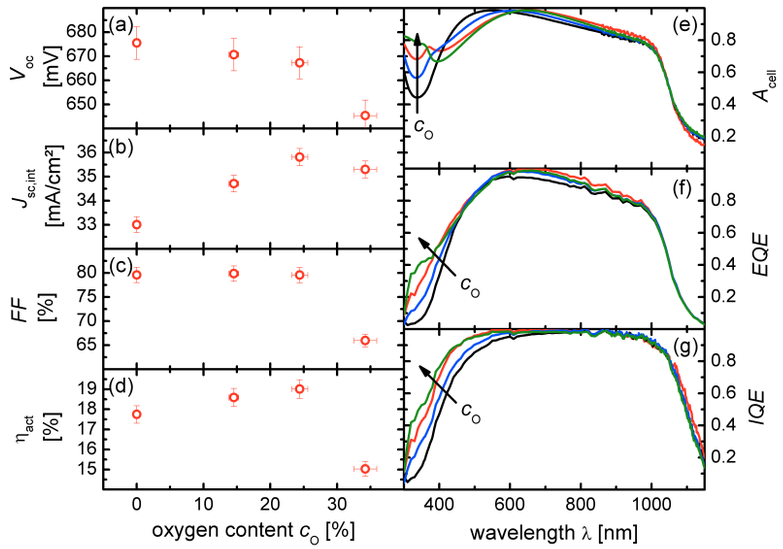

Figure 5.28.: *(a-d) Solar cell parameters plotted versus the oxygen content c_O as well as corresponding (e) A_{cell}, (f) EQE and (g) IQE for SHJ solar cell series with varying r_{CO_2} during the deposition of the* 20 nm *thick* µc-SiO_x:H <n> *emitter layer. The r_{PH_3} was kept constant at* 2.0 %*. The c_O values correlate with the $r_{CO_2} = 0$ %, 20 %, 30 % and* 40 %*, respectively. The optimal oxygen content for emitter layer remained at $c_O = 24\%$ ($r_{CO_2} = 30$ %) with a η_{act} of* 19 %*.*

5.4.3. Optimization of n-type µc-SiO_x:H emitter layer

Emitter layer oxygen content

On the basis of optimized a-SiO_x:H <i> buffer and µc-SiO_x:H <p> BSF layers, SHJ solar cells with varying r_{CO_2} during the deposition of the 20 nm thick µc-SiO_x:H <n> emitter layer were fabricated. Here, the r_{PH_3} was kept constant at 2.0 %, which is considered the optimum doping gas flow ratio (Sec. 5.2.2). Figure 5.28 shows the solar cell parameters plotted versus the oxygen content c_O as well as the A_{cell}, EQE and IQE for the corresponding SHJ solar cells. The increasing c_O values correlate with the CO_2 gas flow ratio $r_{CO_2} = 0$ %, 20 %, 30 % and 40 %, respectively (Fig.

5.10(b)).

The series reveals decreasing V_{oc} with increasing c_O, which is in agreement with the QSSPC results shown in Fig. 5.14. Accordingly, this trend with increasing c_O is attributed to the reduction of doping concentration resulting in deteriorated field effect passivation. The evolution of $J_{sc,int}$ in correlation with c_O comprises two overlapping effects. On the one hand, the optical loss in the emitter layer is noticeably reduced with increasing c_O due to increased optical band gap as reflected in the gain of the IQE in the short wavelength range (Fig. 5.28(g)). On the other hand, the interference patterns are different for varying c_O, since the refractive index n is reduced with rising c_O. A shift of the interference maximum can be clearly observed on the A_{cell} shown in Fig. 5.28(e). Thus, the initial increase of $J_{sc,int}$ with increasing c_O is predominantly due to the optical gain from the emitter. The subsequent drop is attributed to less beneficial interference patterns with higher reflection loss. Up to a c_O of 24%, which corresponds to a r_{CO_2} of 30 %, the FF remains on a high level, suggesting that the series resistance of the emitter layer is not limiting the FF yet. The pronounced decrease of FF from 24% to 34% c_O is explained by the decrease of the corresponding σ_{dark} from around 10^{-3} S/cm to 10^{-8} S/cm, respectively (Fig. 5.10(e)). As a compromise between the aforementioned competing effects, the optimal oxygen content for emitter layer remained at $c_O = 24\%$ ($r_{CO_2} = 30$ %) with a η_{act} of 19 %.

Emitter layer thickness

In addition, SHJ solar cells with varying µc-SiO_x:H <n> emitter layer thickness $d_{emitter}$ were processed. The r_{CO_2} and r_{PH_3} during n-layer deposition were kept constant at the optimal 30 % and 2.0 %, respectively. Figure 5.29 displays the solar cell parameters plotted versus $d_{emitter}$ as well as the A_{cell}, EQE and IQE for the corresponding SHJ solar cells. The series, consisting of three samples with $d_{emitter} = 10$ nm, 20 nm and 30 nm, shows increasing V_{oc} with increasing $d_{emitter}$, which is likely due to the higher charge accumulation in the space-charge region within the c-Si absorber. As $d_{emitter}$ increases, the space-charge region x_p within the c-Si absorber increases in order to maintain the charge neutrality at the junction. Thus, the band bending in c-Si at the front interface that is propotional to $N_A x_p^2$

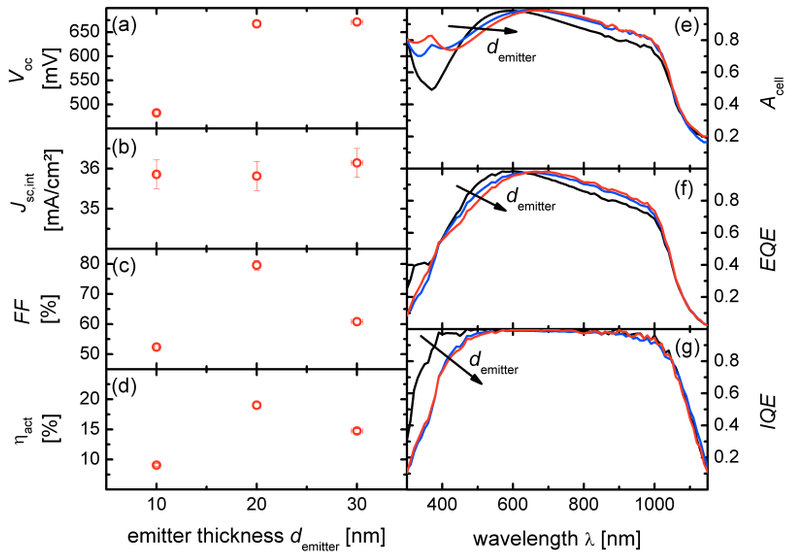

Figure 5.29.: *(a-d) Solar cell parameters plotted versus the* µc-SiO_x:H <n> *emitter layer thickness* $d_{emitter}$ *as well as (e)* A_{cell}*, (f) EQE and (g) IQE for a SHJ solar cell series consisting of three samples with* $d_{emitter} = 10$ nm*,* 20 nm *and* 30 nm*. The* r_{CO_2} *and* r_{PH_3} *during n-layer deposition were kept constant at the optimal* 30 % *and* 2.0 %*, respectively. As a trade-off between insufficient passivation, if* $d_{emitter}$ *is too thin, and pronounced series resistance, if* $d_{emitter}$ *is too thick, the* η_{act} *was the highest at* $d_{emitter} = 20$ nm*.*

increases with increasing d_{emitter} giving rise to higher field effect passivation. The very low V_{oc} at $d_{\mathrm{emitter}} = 10$ nm indicates an insufficient field effect passivation for this sample. The evolution of $J_{\mathrm{sc,int}}$ in correlation with d_{emitter} also comprises two overlapping effects similar as observed for the c_{O} series. While the optical loss in the emitter layer is reduced with decreasing d_{emitter} as indicated by the IQE in the short wavelength range (Fig. 5.29(g)), the reflexion loss increases with decreasing d_{emitter} as indicated by the A_{cell} in the short wavelength range. In total, the $J_{\mathrm{sc,int}}$ remains on a comparably high level independent from the emitter layer thickness.

The low FF at $d_{\mathrm{emitter}} = 10$ nm might come along with the very low V_{oc} as a result of poor field effect passivation. As expected, an insufficient field effect

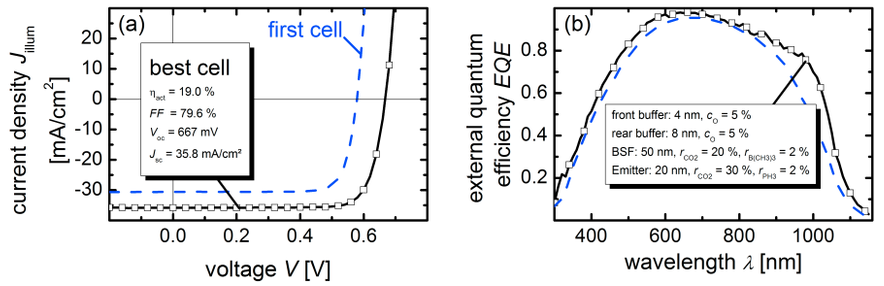

Figure 5.30.: *(a) JV characteristic under illumination and (b) EQE in short circuit case of the best SHJ solar cell using a-SiO_x:H <i> buffer, µc-SiO_x:H <n> emitter and µc-SiO_x:H <p> BSF layers fabricated in this work. The front and rear a-SiO_x:H <i> buffer layers both with an oxygen content of* 5 % *were* 4 nm *and* 8 nm *thick, respectively. The* 20 nm *thick* µc-SiO_x:H <n> *emitter layer and the* 50 nm *thick* µc-SiO_x:H <p> *BSF layer feature an oxygen content of* 24 % *and* 16 %*, an optical band gap of* 2.22 eV *and* 2.04 eV *as well as a dark conductivity of* 1.2×10^{-3} S/cm *and* 6.8×10^{-3} S/cm*, respectively. For comparison, the cell results of the first full heterojunction solar cell (Fig. 5.17) fabricated in the work is included.*

passivation at the emitter side is more critical than at the BSF side, since the major part of the light-induced charge carrier generation takes place in the c-Si absorber very close to the front interface. The low FF at $d_{\text{emitter}} = 30$ nm might be attributed to a pronounced series resistance arising from the thick µc-SiO_x:H <n> layer. As a trade-off between insufficient passivation and pronounced series resistance, the FF at $d_{\text{emitter}} = 20$ nm reached an excellent value close to 80 %. For the same reason, the η_{act} was the highest at $d_{\text{emitter}} = 20$ nm.

5.4.4. Highest efficiency silicon oxide SHJ solar cell

In this work, the best SHJ solar cell using a-SiO_x:H <i> buffer, µc-SiO_x:H <n> emitter and µc-SiO_x:H <p> BSF layers on flat p-type wafer yielded an active area efficiency $\tau_{\text{act}} = 19.0\%$ with $V_{\text{oc}} = 667$ mV, $J_{\text{sc,int}} = 35.8$ mA/cm^2 and $FF = 79.6$ %. This is up to now the highest efficiency shown for SHJ solar cells with µc-SiO_x:H contact layers. Figure 5.30 displays the JV characteristic under illumination and the

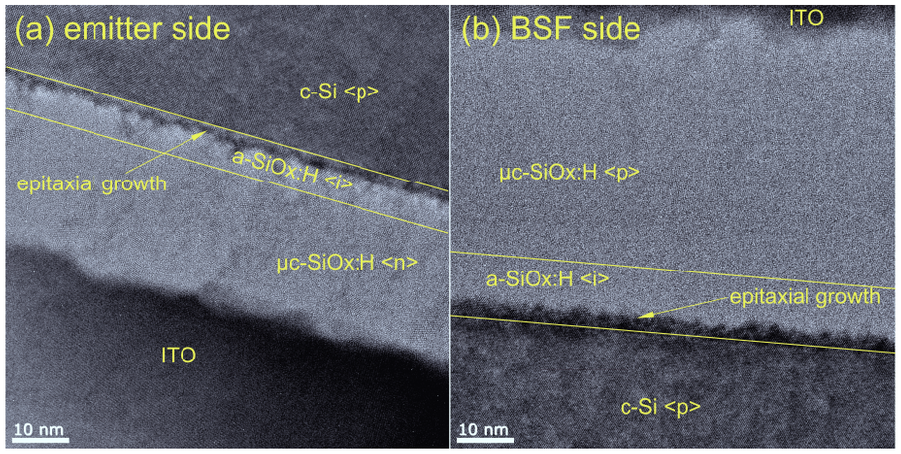

Figure 5.31.: *Cross-sectional HRTEM images of the (a) front and (b) rear side of the best SHJ solar cells. Undesired Si epitaxial growth was observed at the a-SiO_x:H/c-Si interface. The thicknesses of the front buffer, rear buffer, emitter and BSF layers are* 4nm, 8 nm, 23 nm *and* 46 nm, *respectively. The crystalline fraction of the* µc-*SiO_x:H <n> emitter is higher than* µc-*SiO_x:H <p> BSF.*

EQE in short circuit case of this cell. The front and rear a-SiO_x:H <i> buffer layers, both with an oxygen content of 5 %, are 4 nm and 8 nm thick, respectively. The 20 nm thick µc-SiO_x:H <n> emitter layer and the 50 nm thick µc-SiO_x:H <p> BSF layer feature an oxygen content of 24 % and 16 %, an optical band gap of 2.22 eV and 2.04 eV as well as a dark conductivity of 1.2×10^{-3} S/cm and 6.8×10^{-3} S/cm, respectively. For comparison, the cell results of the first full heterojunction solar cell (Fig. 5.17) fabricated in the work is included. Figure 5.31 shows the cross-sectional HRTEM images of the front and rear side of the best cell. Except for a roughly 3 nm thick epitaxial Si layer (see below), the real thicknesses of the front buffer (4 nm), rear buffer (8 nm), emitter (23 nm) and BSF (46 nm) layers are in very good agreement with the nominal ones estimated from deposition times and the pre-determined deposition rate. In addition, the real crystalline fraction of the µc-SiO_x:H <n> emitter is higher than µc-SiO_x:H <p> BSF, which is in agreement with the Raman intensity ratios determined on thick single layer samples.

The obtained V_{oc} is lower than the record V_{oc} of 745 mV reported on Sanyo

HIT solar cells [64] due to several reasons. (i) One major cause for the low V_{oc} was identified as Si epitaxial growth at the a-SiO_x:H/c-Si interface during the deposition of front and rear buffer layers according to the HRTEM images (Fig. 5.31). This means that the epitaxial growth is not always completely suppressed during a-SiO_x:H deposition. Thus, Si epitaxial growth may also occur during a-SiO_x:H deposition depending on the exact deposition parameters, e.g., the CO_2 gas flow ratio. Nevertheless, this problem is solvable by using <111>-orientated wafers instead [198] and/or by adjusting the deposition conditions, e.g., the power density and the substrate temperature [74]. (ii) Even though the incorporation of oxygen into a-Si:H material increased its transparency and improved its thermal stability, the a-SiO_x:H is presumably never as good as an optimized a-Si:H due to less effective c-Si surface passivation as denoted in Sec. 5.1. (iii) SHJ solar cells on n-type wafers achieved higher V_{oc} than those on p-type wafers. This discrepancy might be due to (i) the larger electron than hole capture cross-sections of transition metal point defects, which gives rise to lower minority carrier lifetime in p-type wafers [199], (ii) the photodissociation of iron-boron pairs [200] and the light-induced formation of boron-oxygen complexes [201] resulting in additional recombination centers in p-type wafers, (iii) a higher electron-to-hole capture cross-section of surface dangling bonds, which implies a more difficult p-type wafer passivation [202], and (iv) a better band alignment with higher built-in voltage for n-type wafer proposed to produce the deviation by means of simulation study [184]. Thus, a higher V_{oc} is expected when transferring the present concept from p-type onto n-type wafer. (iv) As already stated in Sec. 5.2.3, the μc-SiO_x:H <p> BSF does not seem to be sufficiently doped due to the crystallization inhibiting nature of boron. One possibility to circumvent this problem is to use n-type wafer instead, where the BSF is a μc-SiO_x:H <n> layer, that might be processed with higher doping concentration more easily. (v) The record V_{oc} cell used a thin c-Si absorber with a thickness of 98 μm. A thinner absorber thickness results in lower bulk recombination, which gives rise to higher V_{oc} under the precondition that the surface passivation is sufficient to maintain low interface recombination even for reduced wafer thickness.

The excellent $J_{sc,int}$ value for flat cells was mainly attributed to the low optical losses in the μc-SiO_x:H <n> emitter layer (Fig. 5.28). Optical advantages by the application of μc-SiO_x:H <p> BSF layer was not observed due to the usage of rather

thick wafers (250 µm). Since the a-SiO_x:H <i> buffer layers consist of a small oxygen content only, the optical gain through the substitution of a-Si:H by a-SiO_x:H should be minute. However, once applied to bifacial SHJ solar cells based on thin, textured wafers [64], the optical gain with SiO_x:H layers on both sides of the wafer instead of a-Si:H should be more significant. Together with the improvements proposed for V_{oc} to reduce recombination loss, the J_{sc} might outperform the 39.4 mA/cm^2 of the Sanyo HIT solar cells. The FF is already at an excellent level, which has to be maintained or even improved during further development.

6. Summary and Outlook

The objective of this thesis was to fabricate and characterize silicon nanostructures embedded in a silicon alloy matrix and implement these materials into silicon based photovoltaic devices. In particular, (i) silicon quantum dots in a silicon carbide/silicon oxide hetero-superlattice structure as top cell absorber in all-Si tandem solar cells and (ii) nanocomposite microcrystalline silicon oxide as contact layers in silicon heterojunction solar cells have been investigated. Both approaches aim at the exploration of novel Si photovoltaic device concepts with the potential to combine high performance and low-cost production. This chapter summarizes the main results of this thesis and gives recommendations for further activities.

6.1. Silicon carbide/silicon oxide hetero-superlattice

6.1.1. Summary

Inadequacy of SiC as matrix material

The original task of the this topic was to develop high quality Si-QD absorbers via the high-temperature annealing of Si-rich carbide/stoichiometric SiC superlattices. However, both experimental results and theoretical considerations indicate that it is almost impossible to produce usable Si-QD absorber materials that possess the desired effective band gap with this approach. (i) Even though the phase separation of Si-rich carbide into Si and SiC phases takes place during annealing, the SiC matrix phase was found to fully crystallize in form of small and differently orientated crystallites that is likely to induce undesired barrier height fluctuation at the Si-QDs interface. Besides, Si-QD formation without crystallization of the SiC matrix seems infeasible, since the formation of both Si- and SiC-NCs always occurred simultane-

ously at the same temperature. (ii) The incorporation of carbon inhibits a complete crystallization of the Si phase, which might be interpreted as the surrounding of Si-NCs by an a-Si phase that was not able to crystallize due to influences (e.g., strains) from the adjacent SiC matrix. In this case, the quantum confinement is expected to be weak due to the low band offset between c-Si and a-Si. (iii) Even from a theoretical point of view neglecting c-SiC and a-Si formation, the rather small band offset of the SiC matrix towards Si gives rise to the determining conflict between Si-QD density and quantum confinement. While large Si-QDs with small spacing are needed for a high Si-QD density, only small Si-QDs with large spacing can provide sufficient quantum confinement. This conflict is accentuated as the carbon content and thus the band offset of the SiC matrix additionally depends on the Si-QD size and spacing as well as the carbon content of the as-deposited layers.

This work introduced the novel SiC/SiO_x HSL with near-stoichiometric SiC as vertical barrier layer and Si-rich SiO_x as lateral matrix layer for the quantum dot formation. Unlike Si-rich carbide, the Si-rich oxide is considered a more promising matrix due to the thermodynamically favored phase separation into Si and SiO_2, the high persistence of the amorphous SiO_2 phase at high temperatures, the pronounced band offset giving rise to high quantum confinement and the excellent Si/SiO_2 interface quality. The conflict between Si-QD density and quantum confinement is considerably relaxed in the case of silicon oxide matrix material due to its significantly higher band offsets towards Si than silicon carbide. The SiC with low band gap should lead to low band offset between Si and SiC and thus give rise to high tunnel probability and easy carrier transport. Here, the crystallization of SiC upon annealing should be less critical for the Si-QDs, since the Si/SiC contact area is rather limited.

Hetero-superlattice process development

Considerable effort was put into the development of high quality, laterally uniform and low rate depositions of SiC and SiO_x layers that are fully compatible with each other. The obtained optimal set of deposition parameters that were able to fulfill all these requirements simultaneously were transfered into an automatic deposition sequence, which allows the successive fabrication of high quality SiO_x and SiC sublayer

with good control over the composition and the thickness in the nanometer range as confirmed by HRTEM and EFTEM images. Moreover, the annealing procedure was optimized in a way that surface oxidation is minimized (furnace preconditioning, high purity N_2 gas, high N_2 gas flow) and blister/bubble formation is avoided (adjusted heating ramps). The temperature inhomogeneity along the tube length was taken into account when positioning the samples in the furnace.

The theoretical oxygen content range of the SiO_x sublayers relevant for Si-QD formation was found between 45 % and 55 %. Below 45 %, the expected Si-QD spacing is too small so that the wavefunctions of two adjacent Si-QDs show a consideable overlap resulting in deteriorated quantum confinement. Above 55 %, the expected Si-QD spacing is too large so that the Si-QD density and thus the c-Si volume fraction will decrease below 25%. The optimum annealing temperature and annealing time for HSL structures based on SiO_x sublayers with oxygen content within this range and near-stoichiometric SiC sublayers were found at 1050 °C and 1 h. A longer annealing time is not recommended, because it resulted in more pronounced surface oxidation and atomic inter-diffusion at the SiC/SiO_x interface as well as stress-induced crystallization of the SiO_2 matrix phase. Annealing at lower temperatures was not sufficient to complete the phase separation and to induce any crystallization in HSL.

Challenging features

Even though the analysis of the structural properties confirms the successful deposition of HSL with desired thicknesses and compositions as well as formation of Si-NCs in the oxide layers, the high-temperature annealing step induced several processes that might limit the usability of the SiC/SiO_x HSL as a photovoltaic quantum dot absorber.

(i) Si-NCs extended into adjacent SiC layers from SiO_x layers towards smaller layer thickness or higher silicon excess, which confirms that near-stoichiometric SiC is an insufficient Si diffusion barrier. As a consequence, the Si-NC size in the HSL is more strongly determined by the oxygen content and less by the oxide layer thickness.

(ii) The hydrogen release from SiC sublayers was identified as the main cause for the decrease of the optical band gap, the increase of the defect density and the increase of the sub-band gap absorption in HSL, which conflicts with the important optical precondition (high transparency) for the dielectrics in Si-QD absorbers.

(iii) Charge carriers generated in the oxide layers might recombine via non-radiative recombination paths at the SiC/SiO_x interfaces close to the defects in the carbide layers as indicated by the suppressed luminescence from Si-QDs in the oxide layers. This implies unacceptably high electrical losses in the HSL material as an absorber.

(iv) The annealing-induced doping character of SiC represents another obstacle, since the minority charge carriers will likely recombine with the majority charge carriers in these layers during carrier transport.

Fundamental differences between carbide and oxide

The systematic analysis of HSL and single layers of SiC and SiO_x annealed at various temperatures and passivated by various techniques using a number of characterization methods yielded a consistent picture of the fundamental differences between SiC and SiO_x. The hydrogen effusion mechanisms during annealing and the hydrogen reincorporation mechanisms during passivation in HSL are well understood. The annealing temperature dependence of the spin densities is explained as an overlap of the temperature dependence of the creation of additional dangling bonds due to hydrogen effusion and of the healing of dangling bonds due to element motion during the structural reconstruction. The stronger increase of spin density upon annealing in SiC as compared to SiO_x is ascribed to the effusion of a higher amount of hydrogen and the less efficient atomic diffusion up to the annealing temperature of 1050 °C.

The much lower optical band gap and the significantly higher sub-band gap absorption of SiC in the annealed state as compared to SiO_x can be traced back to the lower flexibility of its relatively dense 4-fold coordinated atomic structure, which is closely related to the low band gap of SiC. In the more flexible 2-fold coordinated cage structure of the SiO_x material, the easier diffusion of the oxygen

atoms promotes the phase separation giving rise to oxygen rich matrix phase with high optical band gap. This enhanced diffusion also supports the healing of dangling bonds, which reduces the sub-band gap absorption. The more efficient stress relaxation reduces the probability of creating strained bonds, which would have additionally contributed to the sub-band gap absorption.

6.1.2. Outlook

Although the results on SiC/SiO_x hetero-superlattice presented in this thesis represent a self-contained piece of work, this novel material system is not yet fully understood. Its quality is still far away from being sufficient for the usage as a Si-QD top cell absorber in all-Si tandem solar cells. Recommendations for further activities are given in the following.

Extended investigations

Detailed electron spin resonance and photoluminescence investigations on SiC/SiO_x HSL samples can provide more insight into the nature of annealing-induced defects. From temperature dependent PL measurements, the freezing-in or the activation of photoluminescence signals at distinctive measurement temperatures may contain information on the defect characteristics. Combined with the time dependent PL decay measurements, the location of non-radiative recombination centers and the dynamics of the electron-hole pair migration into these states might be identified [156]. ESR results measured in the dark and under illumination with light of different wavelengths, preferably at low measurement temperatures, would allow for the comparison of defects at different electronic states. Multifrequency pulsed ESR measurements might help to increase the resolution of hyperfine data [203].

Alternative annealing techniques to the conventional furnace annealing, e.g., the rapid thermal annealing and the laser annealing can be tested on existing HSL samples. For example, deviating crystallization mechanisms of Si-NCs in Si-rich carbide by rapid thermal annealing [204] and in Si/SiO_2 quantum wells by laser annealing [205] have been reported. For example, comparing the evolution of the unintentional doping in SiC upon annealing using different techniques might provide

more hints for the understanding of this phenomenon.

Solving critical issues

The conclusions drawn from this work are valid for PECVD grown layers annealed at temperatures up to 1050 °C only. A decrease of the defect density with increasing temperature at high temperatures was indicated in this work. Annealing at temperatures above 1050 °C was not carried out due to the temperature limitation of the annealing furnace. Higher temperatures might provide more energy for the inflexible SiC material network to relax its stress and heal its dangling bonds. The quality of annealed SiC in terms of low defect density might then become comparable with that of annealed SiO_x. In addition, the post-annealing H passivation needs to be optimized to further decrease the defect density. The forming gas annealing approach, which was found to be most effective for HSL samples, should be tested at higher annealing temperatures and/or longer treating times. Optionally, a combination of H plasma passivation and forming gas annealing might be beneficial, as the former is especially effective for SiC passivation.

Device realization

This work did not deal with the fabrication of photovoltaic devices using SiC/SiO_x HSL Si-QD absorber. The development of such devices is reasonable if the critical material issues are solved and a high photo-sensitivity is provided. The choice of doped contact layers is not evident. Due to the low doping efficiency of Si-QDs, a huge level of impurity incorporation is required to realize sufficient active Si-QD doping [206]. However, such high impurity doping is questionable. Hence, contact layers free of Si-QDs, e.g., P or B doped a-SiC:H layers are recommended [45]. The band gap of a-SiC:H can be adjusted via composition variation to match the effective band gap of the Si-QDs in the intrinsic absorber region.

It is crucial to somehow isolate the high-temperature Si-QD formation step from all other processes [45], since (i) strong inter-diffusion of impurity dopants into the intrinsic region is unavoidable when carrying out the annealing after the formation of the pin stack and (ii) the surface passivation of the c-Si bottom cell in a

conceivable Si-QD/c-Si tandem device is unlikely to survive the annealing procedure. Hence, novel device structures and/or processing sequences need to be developed in the first place. In addition, wet-chemical removal of surface oxide will definitively be necessary before the deposition of the doped layers.

6.2. Silicon oxide/silicon heterojunction solar cells

6.2.1. Summary

In this topic, the fabrication of SHJ solar cell using intrinsic a-SiO_x:H buffer, n-type µc-SiO_x:H emitter and p-type µc-SiO_x:H <p> BSF layers on flat p-type wafer yielding an active area efficiency $\tau_{eta} = 19.0\%$ with $V_{oc} = 667$ mV, $J_{sc} = 35.8$ mA/cm^2 and $FF = 79.6$ % was achieved. This is up to now the highest efficiency shown for SHJ solar cells with µc-SiO_x:H contact layers. The main attainments are summarized in the following.

Amorphous silicon oxide buffer layer

Comparison with reported advantages The original task of this topic was to develop doped µc-SiO_x:H materials that should combine good c-Si surface passivation with high optical transparency and sufficient electrical conductivity. However, the passivation quality of n- and p-type µc-SiO_x:H was shown to be poor due to several reasons: (i) the high oxygen content giving rise to very low hydrogen content needed for passivation, (ii) the incorporation of P or B as impurities in the a-SiO_x:H phase, (iii) the surface damaging due to the high hydrogen dilution and deposition power, and (iv) the formation of epitaxial Si and/or c-Si crystallites with a very low amount of hydrogen at the interface that cannot passivate the surface sufficiently. Hence, intrinsic a-SiO_x:H was implemented as a passivating buffer layer. The reported advantages of a-SiO_x:H, e.g., higher optical band gap and higher thermal stability as compared to a-Si:H, were independently confirmed by analyzing the optical properties of a-SiO_x:H layers and by showing improved surface passivation on material and device level upon annealing, respectively. However, HRTEM images reveal that Si epitaxial growth is not always completely suppressed during a-SiO_x:H deposition

unlike reported. Thus, this work suggests that Si epitaxial growth may also occur during a-SiO_x:H deposition depending on the exact deposition parameters.

Critical issues Reproducibility tests provided insight into the critical issue of c-Si surface passivation using a-SiO_x:H. Since the first mono layers of a-SiO_x:H on the c-Si surface are most important and there is no time to adjust the matching parameters after the growth has started, careful preconditioning of the deposition system before a-SiO_x:H growth was found to be crucial to guarantee high quality passivation. In addition, system changes need to be avoided on all accounts, which was taken into consideration during the development of μc-SiO_x:H layers that were processed in the same chamber. The preconditioning by a-SiO_x:H cover layer depositions after any change in the system was also required to maintain precisely controllable buffer layer thicknesses, which are immensely important for the solar cell performance.

In fact, SHJ solar cells with front and rear a-SiO_x:H layer thicknesses varying from 3.4 nm to 9.0 nm showed largely deviating efficiency values ranging from 13.1 % to 18.5 %. The highest efficiency was obtained for 4 nm front and 8 nm rear buffer layer thicknesses. An increase in front buffer layer thickness resulted in losses in fill factor (higher series resistance) and short circuit current density (higher parasitic absorption), whereas a decrease gave rise to deteriorated open circuit voltage (higher front surface recombination). An increase in rear buffer layer thickness resulted in fill factor drop (higher series resistance), whereas a decrease gave rise to reduced open circuit voltage (higher rear surface recombination) and short circuit current density (higher rear surface recombination).

Choice of composition Lifetime and infrared measurements for a-SiO_x:H layers with oxygen contents varying over a large range indicated that poor passivation quality correlates with high O content, since (i) the H content decreases with decreasing Si content, which then results in higher amount of unsaturated dangling bonds as recombination centers at the c-Si surface and (ii) H atoms that are bonded to Si with more electronegative O back bonds might be unfavorable for the saturation of c-Si surface dangling bonds due to stronger attraction of the Si-H bonding orbital towards Si as compared to Si-H without O back bonds. Nevertheless, the

fact that a-SiO_x:H layers with O content up to 10 % achieved excellent implied open circuit voltages above 718 mV demonstrated a good reachability of high quality a-SiO_x:H passivation within a low O content range. However, a decreasing trend of the implied open circuit voltage with increasing O content was also observed in this small composition range. Thus, a-SiO_x:H with O content above 10 % are not recommended for usage as passivation layer.

Microcrystalline silicon oxide contact layer

Material properties Structural, optical and electrical properties of n- and p-type μc-SiO_x:H layers with varying H_2, CO_2 and $PH_3/B(CH_3)_3$ gas flow ratios have been systematically investigated. The material properties varied strongly depending on the fraction of c-Si and a-SiO_x:H phases. A higher CO_2 (H_2) gas flow gave rise to higher a-SiO_x:H (c-Si) fraction and thus higher (lower) optical band gap, lower (higher) refractive index, lower (higher) dark conductivity, and lower (higher) doping concentration. The PH_3 doping gas for n-type μc-SiO_x:H hardly affected the a-SiO_x:H and c-Si fraction. While the optical properties remained unchanged, the doping concentration and thus the dark conductivity increased first with rising PH_3 gas flow due to incorporation of active P atoms and then saturated due to the formation of inactive interstitial dopants and/or the creation of impurity defects. The $B(CH_3)_3$ doping gas for p-type μc-SiO_x:H, however, tends to inhibit the Si crystallization and enrich the a-SiO_x:H phase with Si atoms that could not be embedded into the c-Si phase resulting in deteriorated optical and electrical properties at the same time. The choice of suitable $B(CH_3)_3$ gas flow ratio requires a compromise between deteriorated optoelectronic properties when increasing the $B(CH_3)_3$ gas flow and reduced B atom supply when decreasing the $B(CH_3)_3$ gas flow.

Passivation mechanisms Field effect passivation was unambiguously identified for n-type μc-SiO_x:H layers with and without a-SiO_x:H buffer layer, whereas it was found to be insufficient for p-type μc-SiO_x:H layers with comparable doping concentrations as the n-type ones. This discrepancy is due to the more pronounced band bending in c-Si at the n/p interface as compared to that at the p/p interface. Based on this finding, the present work was able to provide several hints to consistently

explain the buffer layer thickness dependence of the surface passivation. Assuming electrons and holes to be able to transport from the c-Si absorber through the buffer layer and recombine at the next defect-rich interface, a thicker a-SiO_x:H layer decreases the recombination rate at this interface by lowering the probability of the wrong type of charge carriers to penetrate the layer.

Based on this model, the quality of the μc-SiO_x:H/a-SiO_x:H interface may affect the passivation quality. Indeed, the passivation quality diminished with higher c-Si fraction of the μc-SiO_x:H p-layer, since the H content, needed to passivate dangling bonds, decreased with the c-Si fraction. As the field effect passivation using μc-SiO_x:H n-layers is prominent, the probability for holes to reach and recombine at the μc-SiO_x:H/a-SiO_x:H interface is low. Therefore, the quality of this interface is less important, which explains why the implied open circuit voltage did not decrease due to worse interface quality towards higher c-Si fraction as in the case of the p-layer, but improved with increasing c-Si fraction due to higher doping concentration and consequently better field effect passivation. The importance of the μc-SiO_x:H/a-SiO_x:H interface passivation is therefore governed by the strength of the field effect passivation. The model also implies that the quality of the μc-SiO_x:H/a-SiO_x:H interface should become more important with decreasing a-SiO_x:H layer thickness. This was confirmed on device level by comparing two SHJ solar cell buffer layer thickness series with different c-Si fractions of the p-type μc-SiO_x:H back surface field. In agreement with the model, the difference in open circuit voltage and short circuit voltage between the two series increased with decreasing rear buffer layer thickness.

Solar cell parameters Variations of CO_2 and $B(CH_3)_3$ gas flow ratios during BSF deposition yielded a consistent picture of the relationship between p-type μc-SiO_x:H material properties and solar cell parameters. The V_{oc} correlates with the rear interface recombination velocity, which is mainly determined by the H content at the μc-SiO_x:H/a-SiO_x:H interface as a measure for the passivation quality of this interface. The evolution of J_{sc} composes two overlapping effects, namely (i) the variation of rear interface recombination loss due to varying H content in agreement with the V_{oc} variations and (ii) the changes in total reflexion loss due to changing refractive index. Optical advantages by the application of p-type μc-SiO_x:H BSF

was not observed due to the usage of thick flat wafers. The FF is correlated to the series resistance of the SHJ solar cells, which is linked to the dark conductivity of the BSF.

The dependences of n-type μc-SiO_x:H emitter material properties on solar cell parameters observed upon CO_2 and thickness variations were consistently explained. The increase of doping concentration and/or layer thickness leads to higher V_{oc} due to stronger band bending in c-Si at the hetero-interface and thus improves the field effect passivation. The evolution of J_{sc} in correlation with O content and layer thickness composes also two overlapping effects. On the one hand, the optical loss in the emitter layer was noticeably reduced with increasing optical band gap or decreasing thickness. On the other hand, the interference pattern in cell reflectance and thus the reflexion loss changed with varying refractive index and thickness of the emitter. The excellent $J_{sc,int}$ values for flat cells was mainly attributed to the low optical losses in the wide-gap μc-SiO_x:H emitter layer. A pronounced decrease of FF was observed (i) with the deterioration of the dark conductivity with increasing O content, (ii) with an emitter layer that is too thin to provide reasonable field effect passivation and (iii) with a thick emitter layer that contributes to high series resistance.

6.2.2. Outlook

This work delivered promising results and encourages further development of SHJ solar cell using SiO_x layers. Recommendations for further activities on both fundamental and device level are given in the following.

Technology

As a general remark, it was not possible to extensively optimize the whole device in this work. The impact of the a-SiO_x:H layer composition on the cell performance needs to be explored. SHJ solar cells with μc-SiO_x:H emitter and BSF layers on top of well passivating a-Si:H buffer layers should be targeted in future as well, in order to find out whether the advantageous features of a-SiO_x:H, e.g., higher optical band gap and higher thermal stability can overcompensate its drawbacks, e.g., poorer wafer

passivation and lower electrical conductivity as compared to a-Si:H. In addition, extended thickness, doping and oxygen content series for the μc-SiO_x:H emitter and BSF layers might help to find better optimum with higher efficiency values. As already indicated in this work, the TCO properties are important for SHJ solar cells. Systematic investigation of the effect of work function, conductivity, transparency and thickness of the ITO and/or ZnO:Al layers on solar cell parameters stands for another crucial part for further improvements. When moving towards real cell efficiencies instead of active area efficiency, one has to focus on a metalization process capable of forming metal grids with a high aspect ratio. The patterning via photo lithography and the more industry-relevant screen printing are two options. For the latter, a low temperature paste should be used to avoid degradation of the surface passivation during the firing step. In addition, the screen printing method is more suitable for larger cell areas.

In order to improve the surface passivation, it is mandatory to deal with the epitaxial growth first. This problem is solvable by using <111>-orientated wafers instead [198] and/or by adjusting the deposition conditions, e.g., the CO_2 gas flow ratio, the power density and the substrate temperature [74]. Further improvement in passivation is expected when hydrogen plasma treatments are used during the buffer layer deposition [207]. Stable and reproducible depositions will become more and more important towards higher passivation quality. Reducing the deposition rate is one way to control the deposition process, which could not be achieved in this work without considerably degrading the passivation quality. Decoupling the deposition rate from the plasma condition, e.g., by using remote plasma or triode electrode PECVD is one option. Hot-wire CVD is another attractive alternative method as it is ion-bombardment free yielding good quality films over a wide range of deposition rates [208].

Device simulation

In this work, it was not possible to elaborately deal with the device simulation of SHJ solar cells using SiO_x layers. Only preliminary optical simulations were carried out and briefly presented in this work. Optical simulation with systematic composition and thickness variations of the a-SiO_x:H and μc-SiO_x:H layers should be

compared with experimental results for further investigation. The required optical data can be extracted from the optical measurements of the corresponding single layers [187]. While the optical simulation for flat cells using the device simulator Afors-HET [192] is rather simple, the electrical simulation lacks a reasonable model to describe the important tunneling processes for charge carrier transport through the hetero-interface [209]. Without taking into account the tunneling effects, the buffer layer thickness dependence of the passivation cannot be reproduced and the large band offsets at the a-SiO_x:H/c-Si interface give FF values much lower than experimentally observed.

It is interesting to note that the SHJ solar cells with a-SiO_x:H buffer and μc-SiO_x:H contact layers are perfectly suitable for the development of device simulations and for a better understanding of the device working principles, since systematic variations of band gap, electron affinity and so on can be experimentally realized and compared with simulations. Thus, the determination of the electrical parameters (extended states and defect states) needed for the electrical simulation is of great academic interest. However, this task is challenging, especially for μc-SiO_x:H, where only part of its phase mixture is believed to contribute to the carrier transport.

Wafer specification

The specifications of the c-Si absorber has major impact on the SHJ solar cell performance and should be investigated. The transfer of the present concept from p-type onto n-type wafer is strongly recommended due to several reasons. (i) Wafer passivation in SHJ solar cells on n-type wafers is easier than in those on p-type wafers as indicated by the comparison of state of the art SHJ solar cells to date [210]. (ii) CZ wafers can be used instead of the much more expensive FZ wafers without much loss in electronic properties, since iron and oxygen impurities are less critical in n-type c-Si material due to the absence of boron-iron pairs and boron-oxygen complexes. (iii) The μc-SiO_x:H <p> BSF does not seem to be sufficiently doped due to the crystallization inhibiting nature of boron. One possibility to circumvent this problem is to use n-type wafer instead, where the BSF is a μc-SiO_x:H <n> layer, that might be processed more easily with higher doping concentration.

In addition, the use of thinner c-Si wafers is recommended, since a thinner

absorber thickness is expected to result in lower bulk recombination, which gives rise to higher V_{oc} under the precondition that the surface passivation is sufficient to maintain low interface recombination even for reduced wafer thickness. When using textured wafers, the current collection will likely increase due to enhanced light trapping. With proper surface texturing, smoothing and wet-chemical oxidation prior to deposition, a good passivation quality of the a-SiO_x:H layers on textured wafers should result in similar or even improved passivation as compared to that on flat wafers. Optionally, novel light trapping concepts, e.g., by means of localized surface plasmon polaritons [211] and/or anti-reflective textured covers [212], can be tested on thin and flat wafers. Finally, the optical gain with SiO_x:H layers on both sides of the wafer instead of a-Si:H should be more significant once the SiO_x:H layers are applied to bifacial SHJ solar cells using thin and textured wafers.

A. Abbreviations and symbols

α	absorption coefficient
$\alpha_{0.6}$	sub-band gap absorption at the photon energy of 0.6 eV
η	solar cell efficiency
η_{act}	active area efficiency
λ	wavelength
ρ	mass density
Θ	diffraction angle
σ	electrical conductivity
σ_{dark}	dark conductivity
τ_{eff}	effective carrier lifetime
A	absorptance
A_{cell}	cell absorptance
A_{ITO}	ITO absorptance
c_{C}	carbon content
$c_{\mathsf{C,initial}}$	initial carbon content before annealing
$c_{\mathsf{C,matrix}}$	matrix carbon content after annealing
c_{H}	hydrogen content
c_{O}	oxygen content
$d_{\mathsf{a\text{-}SiOx:H}\ <\mathsf{i}>}$	silicon sub-oxide passivation layer thickness
d_{BSF}	BSF layer thickness
$d_{\mathsf{c\text{-}Si}}$	average Si crystallite size
$d_{\mathsf{c\text{-}SiC}}$	average SiC crystallite size
d_{dot}	Si-QD diameter
d_{ele}	electrode spacing
d_{emitter}	emitter layer thickness

d_{front}	front buffer layer thickness
d_{rear}	rear buffer layer thickness
d_{SiC}	SiC sublayer thickness
$d_{\mathsf{SiO_x}}$	SiO_x sublayer thickness
d_{sp}	spacing between two adjacent Si-QDs
E_{04}	optical band gap
E_{a}	activation energy
E_{C}	conduction band edge
E_{F}	Fermi level
E_{g}	band gap energy
$E_{\mathsf{g,eff}}$	effective band gap energy
E_{PL}	PL peak energy
EQE	External Quantum Efficiency
E_{V}	valence band edge
f	frequency
f_{c}	Raman intensity ratio
$f_{\mathsf{c\text{-}Si}}$	crystalline Si volume fraction
$f_{\mathsf{c\text{-}SiC}}$	crystalline SiC volume fraction
f_{i}	gas flow rate, where i denotes the chemical formula of the gas
f_{SiC}	SiC layer thickness fraction
FF	fill factor
I_{PL}	PL intensity
$I_{\mathsf{PL,norm}}$	normalized PL intensity
IQE	Internal Quantum Efficiency
J	current density
J_{R}	reflexion loss in form of current density
J_{sc}	short circuit current density
$J_{\mathsf{sc,int}}$	integrated short circuit current density from EQE
k	wavenumber
L_{eff}	effective diffusion length
n	refractive index (real part)
N_{A}	acceptor doping concentration
N_{H}	hydrogen concentration

N_{i}	atomic density, where i denotes the respective element
N_{s}	spin density
p	deposition pressure
P	power density
$r_{\mathsf{B(CH_3)_3}}$	$B(CH_3)_3$ gas flow ratio
$r_{\mathsf{CO_2}}$	CO_2 gas flow ratio
r_{dep}	deposition rate
r_{doping}	doping gas flow ratio
$r_{\mathsf{H_2}}$	H_2 gas flow ratio
r_{heat}	heating rate
$r_{\mathsf{PH_3}}$	PH_3 gas flow ratio
$r_{\mathsf{SiH_4}}$	SiH_4 gas flow ratio
R	reflectance
R_{cell}	cell reflectance
R_{s}	series resistance
R_{sh}	shunt resistance
R_{sheet}	sheet resistance
S_{rear}	rear interface recombination velocity
T	transmittance
t_{a}	annealing time
T_{a}	annealing temperature
t_{dep}	deposition time
T_{p}	peak temperature
t_{sputter}	sputtering time
T_{sub}	substrate temperature
T_{wire}	hot-wire temperature
V	voltage
V_{oc}	open circuit voltage
$V_{\mathsf{oc,imp}}$	implied open circuit voltage
V_{built}	open circuit voltage
x	stoichiometry number
:H	hydrogenated
μc-	microcrystalline

a-	amorphous
Al	aluminum
AlO_x	off-stoichiometric aluminum carbide
Ag	silver
B	boron
$B(CH_3)_3$	trimethylborane
c-	crystalline
C	carbon
CH_3	monomethyl
CH_4	methane
CO_2	carbon dioxide
H	hydrogen
H_2	molecular hydrogen
H_2O	water
H_3SiCH_3	monomethylsilane
<i>	intrinsic
<n>	n-type doped
N	nitrogen
N_2	molecular nitrogen
O	oxygen
O_2	molecular oxygen
<p>	p-type doped
P	phosphorus
PH_3	phosphine
Si	silicon
SiC	silicon carbide
SiC_x	sub-stoichiometric silicon carbide
SiH	mono-hydride
SiH_2	dihydride
SiH_4	silane
Si_3N_4	silicon nitride
SiN_x	sub-stoichiometric silicon nitride
SiO_2	silicon dioxide

SiO_x	sub-stoichiometric silicon oxide
ZnO:Al	Al-doped zinc oxide
AM	Air-Mass
(B)	bending
BSF	Back Surface Field
CV	Capacitance Voltage Measurement
CZ	Czochralski
DB	Dangling Bond
EFTEM	Energy Filtered Transmission Electron Microscopy
ESR	Electron Spin Resonance
FGA	Forming Gas Annealing
FTIR	Fourier Transform Infrared Spectroscopy
FZ	Float-Zone
GI-XRD	Grazing Incidence X-Ray Diffraction Spectroscopy
HIT	Heterojunction with Intrinsic Thin layer
HRTEM	High Resolution Transmission Electron Microscopy
HSL	Hetero-Superlattice
HWCVD	Hot-Wire Chemical Vapor Deposition
ITO	Indium Tin Oxide
MMS	monomethylsilane
NC	nanocrystallite
PDS	Photothermal Deflection Spectroscopy
PECVD	Plasma Enhanced Chemical Vapor Deposition
PERL	Passivated Emitter and Rear Locally diffused
PL	Photoluminescence
QD	Quantum Dot
QSSPC	Quasi Steady-State Photo Conductance
RBS	Rutherford Backscattering Spectrometry
RCA	standard cleaning process developed at Radio Corporation of America
RF	Radio Frequency
RT	Room Temperature
SHJ	Silicon Heterojunction

SIMS	Secondary Ion Mass Spectrometry
(S)	stretching
SRC	Silicon Rich Carbide
SRH	Shockley-Read-Hall
SRN	Silicon Rich Nitride
SRO	Silicon Rich Oxide
TCO	Transparent Conducting Oxide
TEM	Transmission Electron Microscopy
TLM	Transfer Length Method
TMB	trimethylboron
VHF	Very High Frequency
XPS	X-ray Photoelectron Spectroscopy

B. List of Publications

Publications related to this work

1. K. Ding, U. Aeberhard, O. Astakhov, F. Koehler, W. Beyer, F. Finger, R. Carius, and U. Rau, *Silicon quantum dot formation in SiC/SiO_x hetero superlattice*, Energy Procedia 10, 249 – 254 (2011)
2. K. Ding, U. Aeberhard, O. Astakhov, U. Breuer, M. Beigmohamadi, S. Suckow, B. Berghoff, W. Beyer, F. Finger, R. Carius, and U. Rau, *Defect passivation by hydrogen reincorporation for silicon quantum dots in SiC/SiO_x heterosuperlattice*, J. Non-Cryst. Solids 358, 2145 – 2149 (2012)
3. K. Ding, U. Aeberhard, W. Beyer, O. Astakhov, F. Köhler, U. Breuer, F. Finger, R. Carius, and U. Rau, *Annealing induced defects in SiC, SiO_x single layers and SiC/SiO_x hetero-superlattices*, Phys. Status Solidi A 209, 1960 – 1964 (2012)
4. K. Ding, U. Aeberhard, O. Astakhov, W. Beyer, F. Finger, R. Carius, and U. Rau, *Optically active defects in SiC, SiO_x single layers and SiC/SiO_x hetero-superlattices*, Sol. Energ. Mat. Sol. C. 129, 3 – 6 (2014)
5. K. Ding, U. Aeberhard, F. Finger, and U. Rau, *Silicon heterojunction solar cell with amorphous silicon oxide buffer and microcrystalline silicon oxide contact layers*, Phys. Status Solidi RRL 6, 193 – 195 (2012)
6. K. Ding, U. Aeberhard, F. Finger, and U. Rau, *Optimized amorphous silicon oxide buffer layers for silicon heterojunction solar cells with microcrystalline silicon oxide contact layers*, J. Appl. Phys. 113, 134501 (2013)
7. A. Lambertz, V. Smirnov, T. Merdzhanova, K. Ding, R.E.I. Schropp, F. Finger, and U. Rau, *Microcrystalline silicon-oxygen alloys for application in sili-*

con solar cells and modules, Sol. Energ. Mat. Sol. C. 119, 134 – 143 (2013)

8. K. Ding, U. Aeberhard, V. Smirnov, B. Holländer, F. Finger, and U. Rau, *Wide gap microcrystalline silicon oxide emitter for a-SiO_x:H/c-Si heterojunction solar cells*, Jpn. J. Appl. Phys. 52, 122304 (2013)
9. K. Ding, U. Aeberhard, A. Lambertz, V. Smirnov, B. Holländer, F. Finger, and U. Rau, *Impact of doped microcrystalline silicon oxide layers on crystalline silicon surface passivation*, Can. J. Phys. 92, 758 – 762 (2014)

Other publications

1. C. Ulbrich, T. Kirchartz, K. Ding, B.E. Pieters, A. Gerber, and U. Rau, *Spectrally dependent optimization of multi-junction solar cells*, Proceeding 24th European Photovoltaic Solar Energy Conference, Hamburg, Germany (2009)
2. K. Ding, T. Kirchartz, B.E. Pieters, C. Ulbrich, S. Schicho, A. Lambertz, R. Carius, and U. Rau, *Detailed analysis of a-Si:H/µc-Si:H tandem solar cell characterization data using numerical simulation*, Proceedings 25th European Photovoltaic Solar Energy Conference, Valencia, Spain (2010)
3. K. Ding, T. Kirchartz, B. E. Pieters, C. Ulbrich, A. M. Ermes, S. Schicho, A. Lambertz, R. Carius, and U. Rau, *Characterization and simulation of a-Si:H/µc-Si:H tandem solar cells*, Sol. Energ. Mat. Sol. C. 95, 3318 – 3327 (2011)

C. Curriculum Vitae

Personal details

Name	Kaining Ding
Date of birth	October 8th, 1983
Place of birth	Taiyuan, China
Citizenship	German

Education

1990-1996	Primary school in China
1996-1997	Luisen Gymnasium, Düsseldorf
1997-2004	Gymnasium Ohmoor, Hamburg
2004-2007	Bachelor of Science in Material Science at the RWTH-Aachen Bachelor thesis at I.Institute of Physics Title: Struktur und Optische Charakterisierung Neuartiger Binärer Oxide
2007-2009	Master of Science in Material Science at the RWTH-Aachen Main subject: nanotechnology and electronic materials Master thesis at IEK5-Photovoltaics Title: Characterisierung und Simulation von a-Si:H/µc-Si:H Tandem Solarzellen
01/2010-now	PhD student at the IEK5-Photovoltaics

References

[1] M. A. Green, Prog. Photovoltaics **9**, 123 (2001).

[2] G. Conibeer et al., Thin Solid Films **511**, 654 (2006).

[3] G. Conibeer et al., Thin Solid Films **516**, 6748 (2008).

[4] F. Meillaud, A. Shah, C. Droz, E. Vallat-Sauvain, and C. Miazza, Sol. Energ. Mat. Sol. C. **90**, 2952 (2006).

[5] J. Meier et al., Energy Procedia **15**, 179 (2012).

[6] H. Harrison, *Quantum Well, Wires and Dots: Theoretical and Computational Physics*, John Wiley & Sons, Ltd, Chisester, 2000.

[7] K. Böer, *Survey of Semiconductor Physics*, van Nostrand Reinhold, New York, 1990.

[8] O. L. Lazarenkova and A. A. Balandin, J. Appl. Phys. **89**, 5509 (2001).

[9] V. Badescu and M. Paulescu, *Physics of Nanostructured Solar cells*, Nova Science Publishers, Inc., New York, 2010.

[10] M. Zacharias et al., Appl. Phys. Lett. **80**, 661 (2002).

[11] X. J. Hao et al., Sol. Energ. Mat. Sol. C. **93**, 1524 (2009).

[12] G. Cantele et al., Phys. Rev. B **72**, 113303 (2005).

[13] Z. H. Lu, D. J. Lockwood, and J.-M. Baribeau, Nature **378**, 258 (1995).

[14] U. Kahler and H. Hofmeister, Optical Materials **17**, 83 (2001).

[15] X. J. Hao et al., Nanotechnology **20**, 485703 (2009).

[16] M. Peralvarez et al., Appl. Phys. Lett. **89**, 51112 (2006).

[17] T. Arguirov et al., Appl. Phys. Lett. **89**, 53111 (2006).

[18] D. Di et al., Nanoscale Res. Lett. **5**, 1762 (2010).

[19] X. J. Hao et al., Nanotechnology **19**, 424019 (2008).

[20] J. Heitmann, F. Müller, M. Zacharias, and U. Gösele, Adv. Mater. **17**, 795 (2005).

[21] S. Mirabella et al., J. Appl. Phys. **106**, 103505 (2009).

[22] D. Hiller et al., Phys. Rev. B **82**, 195401 (2010).

[23] Y. Cho et al., Silicon quantum dots in SiNx matrix for thrid generation photovoltaics, in *Proceedings of the 20th European Photovoltaic Solar Energy Conference and Exhibition, Barcelona, Spain, June 6-10, 2005*, pages 47–50, 2005.

[24] T. W. Kim, C. H. Cho, B. H. Kim, and S. J. Park, Appl. Phys. Lett. **88**, 123102 (2006).

[25] Y. H. So, A. Gentle, S. Huang, G. Conibeer, and M. A. Green, J. Appl. Phys. **109**, 64302 (2011).

[26] A. K. Panchal, D. K. Rai, M. Mathew, and C. S. Solanki, Nano **4**, 265 (2009).

[27] Y. Kurokawa, S. Miyajima, A. Yamada, and M. Konagai, Nanocrystalline silicon in amorphous silicon carbide matrix for Si quantum dots superlattice, in *Proceedings of the 4th World Conference on Photovoltaic Energy Conversion, Waikoloa, Hawaii, May 7-12, 2006*, volume 1-2, pages 138–141, 2006.

[28] E.-C. Cho et al., Adv. OptoElectronics **2007**, 1 (2007).

[29] D. Song et al., J. Appl. Phys. **103**, 83544 (2008).

[30] M. Künle, A. Hartel, and S. Janz, Analysis of Microstructural Transformations during Annealing of a-SiC:H/a-SiCx:H Layer Stacks for the Preparation Silicon Quantum Dot Superlattices, in *Proceedings of the 23rd European Photovoltaic Solar Energy Conference and Exhibition, Valencia, Spain, Sep 1-5, 2008*, page 1CV.1.58, 2008.

[31] B. H. Kim et al., Appl. Phys. Lett. **86**, 091908 (2005).

[32] M. Künle et al., Mater. Sci. Eng. B-Adv. **159-60**, 355 (2009).

[33] C. Q. Sun, Prog. Solid State Ch. **35**, 1 (2007).

[34] Q. Cheng, E. Tam, S. Xu, and K. K. Ostrikov, Nanoscale **2**, 594 (2010).

[35] G. Scardera, T. Puzzer, I. Perez-Wurfl, and G. Conibeer, J. Cryst. Growth **310**, 3680 (2008).

[36] D. Song et al., J. Vac. Sci. Technol. B **25**, 1327 (2007).

[37] Y. Kurokawa, S. Yamada, S. Miyajima, A. Yamada, and M. Konagai, Curr. Appl. Phys. **10**, S435 (2010).

[38] Y. Kurokawa, S. Tomita, S. Miyajima, A. Yamada, and M. Konagai, Effects of Nitrogen on the Electrical Properties of Si Quantum Dots Superlattice Using a-SiC Matrix, in *Proceedings of the 24th European Solar Energy Conference and Exhibition, Hamburg, Germany, Sep 21-25, 2009*, page 1CV.3.68, 2009.

[39] Z. Wan, R. Patterson, S. Huang, M. Green, and G. Conibeer, EPL **95**, 67006 (2011).

[40] D. Di, H. Xu, I. Perez-Wurfl, M. A. Green, and G. Conibeer, Nanoscale Res. Lett. **6**, 612 (2011).

[41] J. F. Lelievre et al., Thin Solid Films **511**, 103 (2006).

[42] E.-C. Cho et al., Nanotechnology **19**, 245201 (2008).

[43] S. Yamada, Y. Kurokawa, S. Miyajima, A. Yamada, and M. Konagai, High open-circuit voltage oxygen-containing silicon quantum dots superlattice solar cells, in *Proceedings of the 35th IEEE Photovoltaic Specialists Conference Honolulu, Hawaii, June 20-25, 2010*, pages 766–769, 2010.

[44] I. Perez-Wurfl et al., Sol. Energ. Mat. Sol. C. **100**, 65 (2012).

[45] P. Loeper et al., Adv. Mater. **24**, 3124 (2012).

[46] J. Knobloch et al., Solar cells with efficiencies above 21% processed from Czochralski grown silicon, in *Proceedings of the 25th IEEE Photovoltaic Specialists Conference, Washington DC, USA, May 13-17, 1996*, pages 405–408, 1996.

[47] M. J. Kerr and A. Cuevas, Semicond. Sci. Tech. **17**, 35 (2002).

[48] J. H. Zhao, A. H. Wang, and M. A. Green, Sol. Energ. Mat. Sol. C. **65**, 429 (2001).

[49] J. Schmidt and A. G. Aberle, J. Appl. Phys. **85**, 3626 (1999).

[50] A. G. Aberle and R. Hezel, Prog. Photovoltaics **5**, 29 (1997).

[51] M. J. Kerr and A. Cuevas, Semicond. Sci. Tech. **17**, 166 (2002).

[52] J. Bernat et al., Solid State Electron. **47**, 2097 (2003).

[53] S. Dauwe, L. Mittelstadt, A. Metz, and R. Hezel, Prog. Photovoltaics **10**, 271 (2002).

[54] S. Miyajima, J. Irikawa, A. Yamada, and M. Konagai, Appl. Phys. Express **3**, 012301 (2010).

[55] G. Dingemans, M. C. M. van de Sanden, and W. M. M. Kessels, Electrochem. Solid St. **13**, 76 (2010).

[56] P. Saint-Cast et al., Appl. Phys. Lett. **95**, 151502 (2009).

[57] T. Saga, NPG Asia Materials **2**, 96 (2010).

[58] W. Brendle et al., Prog. Photovoltaics **14**, 653 (2006).

[59] W. Fuhs, K. Niemann, and J. Stuke, Heterojunctions of Amorphous Silicon and Silicon Single Crystals, in *Tetrahedrally-Bonded Amorphous Semiconductors: International Conference*, volume 20, pages 345–350, 1974.

[60] K. Wakisaka et al., More than 16% solar cells with a new 'HIT' (doped a-Si/nondoped a-Si/crystalline Si) structure, in *Proceedings of the 22th IEEE Photovoltaic Specialists Conference, Las Vegas, NV, Oct 7-11, 1991*, pages 887–892, 1991.

[61] M. Tanaka et al., Jpn. J. Appl. Phys. **31**, 3518 (1992).

[62] T. Sawada et al., High-efficiency a-Si/c-Si heterojunction solar cell, in *Proceedings of the 1st World Conference on Photovoltaic Energy Conversion, Waikoloa, Hawaii, Dec 4-9, 1994*, volume 2, pages 1219–1226, 1994.

[63] Y. Tsunomura et al., Sol. Energ. Mat. Sol. C. **93**, 670 (2009).

[64] T. Kinoshita et al., The Approaches for High Efficiency HIT Solar Cell with Very Thin (<100 mucm) Silicon Wafer over 23%, in *Proceedings of the 26nd European Photovoltaic Solar Energy Conference, Hamburg, Germany, Sep 5-9, 2011*, pages 871–874, 2011.

[65] M. Taguchi, A. Terakawa, E. Maruyama, and M. Tanaka, Prog. Photovoltaics **13**, 481 (2005).

[66] E. Maruyama et al., Sanyo's Challenges to the Development of High-efficiency

HIT Solar Cells and the Expansion of HIT Business, in *Proceedings of the 4th World Conference on Photovoltaic Energy Conversion, Waikoloa, Hawaii, May 7-12, 2006*, pages 1455–1460, 2006.

[67] D. Bätzner et al., Energy Procedia **8**, 153 (2011).

[68] W. G. J. H. M. van Sark, L. Korte, and F. Roca, *Physics and Technology of Amorphous-Crystalline Heterostructure Silicon Solar Cells*, Springer Verlag, Berlin, 2011.

[69] T. Mueller, *Heterojunction solar cells (a-Si/c-Si): Investigation on PECV deposited hydrogenated silicon alloys for use as high-quality surface passivation and emitter/BSF*, PhD thesis, University of Hagen, 2009.

[70] W. Kern, J. Electrochem. Soc. **137**, 1887 (1990).

[71] H. Angermann et al., Thin Solid Films **516**, 6775 (2008).

[72] H. Angermann et al., Mat. Sci. Eng. B **159-160**, 219 (2009).

[73] M. Taguchi et al., Prog. Photovoltaics **8**, 503 (2000).

[74] H. Fujiwara and M. Kondo, Appl. Phys. Lett. **90**, 13503 (2007).

[75] S. De Wolf, S. Olibet, and C. Ballif, Appl. Phys. Lett. **93**, 032101 (2008).

[76] D. Pysch et al., Appl. Phys. Express **94**, 093510 (2009).

[77] D. Pysch, M. Bivour, M. Hermle, and S. W. Glunz, Thin Solid Films **519**, 2550 (2011).

[78] T. Mueller, S. Schwertheim, and W. R. Fahrner, J. Appl. Phys. **107**, 14504 (2010).

[79] H. Fujiwara, T. Kaneko, and M. Kondo, Appl. Phys. Lett. **91**, 133508 (2007).

[80] F. Einsele, W. Beyer, and U. Rau, Phys. Status Solidi C **7**, 1021 (2010).

[81] M. W. M. van Cleef et al., J. Appl. Phys. **82**, 6089 (1997).

[82] T. Mueller et al., High efficiency silicon heterojunction solar cell using novel structure, in *Proceedings of the 35th IEEE Photovoltaic Specialists Conference Honolulu, Hawaii, June 20-25, 2010*, pages 683–688, 2010.

[83] S. Miyajima, K. Haga, A. Yamada, and M. Konagai, Jpn. J. Appl. Phys. 2 **45**, L432 (2006).

[84] T. Chen, Y. Huang, D. Yang, R. Carius, and F. Finger, Phys. Status Solidi RRL **2**, 160 (2008).

[85] T. Chen, D. Yang, R. Carius, and F. Finger, Jpn. J. Appl. Phys. **49**, 041303 (2010).

[86] J. Irikawa, S. Miyajima, T. Watahiki, and M. Konagai, Appl. Phys. Express **4**, 092301 (2011).

[87] A. Lambertz et al., Microcrystalline Silicon oxide as intermediate reflector for thin film silicon solar cells, in *Proceedings of the 22nd European Photovoltaic Solar Energy Conference, Milano, Italy, Sep 3-7, 2007.*, pages 1839–1842, 2007.

[88] V. Smirnov et al., Phys. Status Solidi C **7**, 1053 (2010).

[89] J. Sritharathikhun, F. Jiang, S. Miyajima, A. Yamada, and M. Konagai, Jpn. J. Appl. Phys. **48**, 101603 (2009).

[90] C. Banerjee, J. Sritharathikhun, A. Yamada, and M. Konagai, J. Phys. D Appl. Phys. **41**, 185107 (2008).

[91] S. Rattanapan, T. Watahiki, S. Miyajima, and M. Konagai, Jpn. J. Appl. Phys. **50**, 082301 (2011).

[92] B. Holländer, H. Heer, M. Wagener, H. Halling, and S. Mantl, Nucl. Instrum. Meth. B **161-163**, 227 (2000).

[93] M. Roczen et al., Appl. Phys. A **108**, 719 (2012).

[94] H. Schmidt et al., Appl. Surf. Sci. **252**, 1460 (2005).

[95] F. Köhler, *Zur Mikrostruktur siliziumbasierter Dünnschichten für die Phoovoltaik*, PhD thesis, RWTH-Aachen, 2012.

[96] D. Long, *Raman Spectroscopy*, Mcraw-Hill International Book Company, New York, 1977.

[97] T. Grundler, Silicon Oxide as an Intermediate Reflector in Silicon Thin Film Solar Cells, Bachelor's thesis, RWTH-Aachen, 2009.

[98] A. A. Langford, M. L. Fleet, B. P. Nelson, W. A. Lanford, and N. Maley, Phys. Rev. B **45**, 13367 (1992).

[99] W. Beyer, H. Wagner, and H. Mell, Solid State Commun. **39**, 375 (1981).

[100] C. Malten, *Pulsed electron spin resonance of amorphous and microcrystalline semiconductors*, Phd, Forschungszentrum Jülich, Germany, 1996.

[101] W. B. Jackson, N. M. Amer, A. C. Boccara, and D. Fournier, Applied Optics **20**, 1333 (1981).

[102] R. A. Sinton and A. Cuevas, Appl. Phys. Lett. **69**, 2510 (1996).

[103] F. Einsele, *Amorphe Siliziumoxidschichten zur Oberflächenpassivierung und Kontaktierung von Heterostruktur-Solarzellen aus amorphem und kristallinem Silizium*, PhD thesis, RWTH-Aachen, 2010.

[104] W. Reetz, H. Stiebig, and T. Brammer, Spectral responce of stacked solar cells based on a-Si:H, in *Proceedings of the 2nd ISEC-Europe Solar Congress, Eurosun98*, pages V.1.5–1, 1999.

[105] D. Song et al., Thin Solid Films **516**, 3824 (2008).

[106] S. Klein, *Microcrystalline silicon prepared by hot wire CVD*, PhD thesis, TU München, 2003.

[107] H. Wieder, M. Cardona, and C. R. Guarnieri, Phys. Status Solidi B **92**, 99 (1979).

[108] G. Lucovsky, Solid State Commun. **29**, 571 (1979).

[109] S. Hasegawa, S. Watanabe, T. Inokuma, and Y. Kurata, J. Appl. Phys. **77**, 1938 (1995).

[110] F. Koehler et al., J. Non-Cryst. Solids **358**, 2011 (2012).

[111] M. Dkaki, L. Calcagno, A. M. Makthari, and V. Raineri, Mat. Sci. Semicon. Proc. **4**, 201 (2001).

[112] D. Polk, J. Non-Cryst. Solids **5**, 365 (1971).

[113] J. Robertson, Philos. Mag. B **66**, 615 (1992).

[114] I. Solomon, Appl. Surf. Sci. **184**, 3 (2001).

[115] C. Summonte et al., J. Appl. Phys. **96**, 3987 (2004).

[116] F. Demichelis, F. Giorgis, C. F. Pirri, and E. Tresso, Philos. Mag. A **72**, 913 (1995).

[117] W. Beyer and H. Wagner, J. Non-Cryst. Solids **59-60**, 161 (1983).

[118] F. Fujimoto et al., Jpn. J. Appl. Phys. **23**, 810 (1984).

[119] J. Bullot and M. P. Schmidt, Phys. Status Solidi B **143**, 345 (1987).

[120] G. Bastard, Phys. Rev. B **25**, 7584 (1982).

[121] C. W. Jiang and M. A. Green, J. Appl. Phys. **99**, 114902 (2006).

[122] H. Takagi, H. Ogawa, Y. Yamazaki, A. Ishizaki, and T. Nakagiri, Appl. Phys. Lett. **56**, 2379 (1990).

[123] J. A. Bucaro and H. D. Dardy, J. Appl. Phys. **45**, 5324 (1974).

[124] M. N. P. Carreno, I. Pereyra, M. C. A. Fantini, H. Takahashi, and R. Landers, J. Appl. Phys. **75**, 538 (1994).

[125] P. Pan, L. Nesbit, R. Douse, and G. RT, J. Electrochem. Soc. **132**, 2012 (1985).

[126] T. Chen, *Microcrystalline Silicon Carbide Thin Films Prepared by Hot-Wire Chemical Vapor Deposition and Their Application in Silicon Thin Film Solar Cells*, PhD thesis, FZ-Jülich, 2009.

[127] C. Tsai, G. Anderson, R. Thompson, and B. Wacker, J. Non-Cryst. Solids **114**, 151 (1989).

[128] R. T. Sanderson, *Chemical Bonds and Bond Energy*, Academic Press, New York, 1976.

[129] F. Iacona, C. Bongiorno, C. Spinella, S. Boninelli, and F. Priolo, J. Appl. Phys. **95**, 3723 (2004).

[130] S. Lombardo and S. Campisano, Mater. Sci. Eng. R **17**, 281 (1996).

[131] D. V. Tsu, G. Lucovsky, and B. N. Davidson, Phys. Rev. B **40**, 1795 (1989).

[132] L. He, T. Inokuma, Y. Kurata, and S. Hasegawa, J. Non-Cryst. Solids **185**, 249 (1995).

[133] P. G. Pai, S. S. Chao, Y. Takagi, and G. Lucovsky, J. Vac. Sci. Technol. **4**, 689 (1986).

[134] Y. H. Seo et al., Appl. Phys. Lett. **62**, 1812 (1993).

[135] F. Gourbilleau, C. Ternon, D. Maestre, O. Palais, and C. Dufour, J. Appl. Phys. **106**, 13501 (2009).

[136] D. Hiller, *The influence of interface defects on the optical properties of silicon nanocrystals*, PhD thesis, University Freiburg, 2011.

[137] W. Beyer, J. Non-Cryst. Solids **266**, 845 (2000).

[138] M. Zacharias, Adv. Solid State Phys. **44**, 351 (2004).

[139] J. Park et al., Thin Solid Films **517**, 3222 (2009).

[140] R. Carius, Philos. Mag. B **80**, 741 (2000).

[141] L. Ley, *The Physics of Hydrogenated Amorphous Silicon II*, Springer, Berlin, 1983.

[142] A. L. B. Neto, S. S. Camargo, R. Carius, F. Finger, and W. Beyer, Surf. Coat. Tech. **120**, 395 (1999).

[143] A. Oliveira and M. Carreño, J. Non-Cryst. Solids **352**, 1392 (2006).

[144] R. Saleh, L. Munisa, and W. Beyer, Sol. Energ. Mat. Sol. C. **90**, 3449 (2006).

[145] G. Lucovsky, J. Yang, S. Chao, J. Tyler, and W. Czubatyj, Phys. Rev. B **28**, 3225 (1983).

[146] W. Beyer, Sol. Energ. Mat. Sol. C. **78**, 235 (2003).

[147] E. Janzén et al., Physica B **340-342**, 15 (2003).

[148] Y. Kamigaki, K. Yokogawa, T. Hashimoto, and T. Uemura, J. Appl. Phys. **80**, 3430 (1996).

[149] M. Jivanescu, A. Stesmans, and M. Zacharias, J. Appl. Phys. **104**, 103518 (2008).

[150] F. Devynck, A. Alkauskas, P. Broqvist, and A. Pasquarello, Phys. Rev. B **84**, 235320 (2011).

[151] B. Sopori, M. I. Symko, R. Reedy, K. Jones, and R. Matson, Mechanism(s) of hydrogen diffusion in silicon solar cells during forming gas anneal, in *Proceedings of the 26rd IEEE Photovoltaic Specialists Conference, Anaheim, CA, Sep 29-Oct 03, 1997*, pages 25–30, 1997.

[152] J. E. Greene and S. A. Barnett, J. Vac. Sci. Technol. **21**, 285 (1982).

[153] W. Beyer and U. Zastrow, Plasma post-hydrogenation of hydrogenated amorphous silicon and germanium, in *Proceedings of the 1996 MRS Spring Meeting:*

Symposium on Amorphous Silicon Technology, San Francisco, CA, Apr 08-12, 1996, volume 420, pages 497–502, 1996.

[154] H. Matsumura, Jpn. J. Appl. Phys. 1 **37**, 3175 (1998).

[155] G. Allan, C. Delerue, and M. Lannoo, Phys. Rev. Lett. **78**, 3161 (1997).

[156] J. Heitmann, *Größenkontrollierte Herstellung von Silizium-Nanokristalliten und Ihre Charakterisierung*, PhD thesis, MLU Halle-Wittenberg, 2003.

[157] M. Jivanescu, A. Stesmans, S. Godefroo, and M. Zacharias, J. Optoelectron. Adv. M. **9**, 721 (2007).

[158] S. Cheylan and R. G. Elliman, Appl. Phys. Lett. **78**, 1225 (2001).

[159] A. V. Vasin et al., J. Appl. Phys. **103**, 123710 (2008).

[160] K. Jun, R. Carius, and H. Stiebig, Phys. Rev. B **66**, 1 (2002).

[161] B. G. Lee et al., Adv. Funct. Mater. **22**, 3223 (2012).

[162] D. A. Anderson and W. E. Spear, Philos. Mag. **36**, 695 (1977).

[163] F. Finger et al., Thin Solid Films **517**, 3507 (2009).

[164] L. Xiao et al., Phys. Status Solidi C **7**, 778 (2010).

[165] N. Nickel and M. Rakel, Phys. Rev. B **65**, 041301 (2001).

[166] N. Nickel, N. Johnson, and C. Van de Walle, Phys. Rev. Lett. **72**, 3393 (1994).

[167] C. Van de Walle, P. Denteneer, Y. Bar-Yam, and S. Pantelides, Phys. Rev. B **39**, 10791 (1989).

[168] Y. Gorelkinskii and N. Nevinnyi, Phys. Lett. A **99**, 117 (1983).

[169] S. Olibet et al., Phys. Status Solidi A **207**, 651 (2010).

[170] K. E. Mattsson, J. Appl. Phys. **77**, 6616 (1995).

[171] H. Fujiwara and M. Kondo, J. Appl. Phys. **101**, 54516 (2007).

[172] J. Sritharathikhun, H. Yamamoto, S. Miyajima, A. Yamada, and M. Konagai, Jpn. J. Appl. Phys. **47**, 8452 (2008).

[173] A. G. Aberle, *Crystalline Silicon Solar Cells - Advanced Surface Passivation and Analysis*, University of New South Wales, Sydney, 1999.

[174] M. Z. Burrows, U. K. Das, R. L. Opila, S. De Wolf, and R. W. Birkmire, J.

Vac. Sci. Technol. A **26**, 683 (2008).

[175] H. Fujiwara and M. Kondo, Appl. Phys. Lett. **86**, 032112 (2005).

[176] L. Korte, A. Laades, and M. Schmidt, J. Non-Cryst. Solids **352**, 1217 (2006).

[177] F. Einsele, P. J. Rostan, M. B. Schubert, and U. Rau, J. Appl. Phys. **102**, 94507 (2007).

[178] M. Fang, J. Chevrier, and B. Drevillon, J. Non-Cryst. Solids **137-138**, 791 (1991).

[179] A. Dasgupta et al., P-layers of microcrystalline silicon thin film solar cells, in *Proceedings of the 16h European Photovoltaic Solar Energy Conference, Glasgow, UK, May 1 - 5, 2000*, page 557, 2000.

[180] T. Grundler, A. Lambertz, and F. Finger, Phys. Status Solidi C **7**, 1085 (2010).

[181] C. Tsai, G. Anderson, and R. Thompson, J. Non-Cryst. Solids **137-138**, 673 (1991).

[182] S. De Wolf and M. Kondo, Appl. Phys. Lett. **90**, 042111 (2007).

[183] L. Korte, E. Conrad, H. Angermann, R. Stangl, and M. Schmidt, Sol. Energ. Mat. Sol. C. **93**, 905 (2009).

[184] N. Jensen, R. A. Hausner, R. B. Bergmann, J. H. Werner, and U. Rau, Prog. Photovoltaics **10**, 1 (2002).

[185] G. Che, R. Mertens, R. Van Overstraeten, and L. Frisson, IEEE T. Electron. Dev. **31**, 602 (1984).

[186] W. Kern, *Handbook of Semiconductor Wafer Cleaning Technology*, William Andrew Inc., New York, 1993.

[187] K. Ding et al., Sol. Energ. Mat. Sol. C. **95**, 3318 (2011).

[188] W. Reetz, T. Kirchartz, A. Lambertz, J. Hüpkes, and A. Gerber, Current-Voltage and Spectral Response Based Characterization of Thin Film Silicon Solar Cells - Investigation of Primary Error Sources, in *Proceedings of the 24th European Solar Energy Conference and Exhibition, Hamburg, Germany, Sep 21-25, 2009*, pages 2784–2788, 2009.

[189] N. F. Mott, Proceedings of the Royal Society of London. Series A: Mathemat-

ical and physical sciences **171**, 27 (1939).

[190] W. Schottky, Zeitschrift für Physik **113**, 367 (1939).

[191] U. W. Paetzold et al., Localized plasmonic losses at metal back contacts of thin-film silicon solar cells, in *Proceedings of SPIE: Photonics for Solar Energy Systems III, Brussels, Belgium, Apr 12-15, 2010*, page 772517, 2010.

[192] A. Froitzheim, R. Stangl, L. Elstner, M. Kriegel, and W. Fuhs, AFORS-HET: A computer-program for the simulation of heterojunction solar cells to be distributed for public use, in *Proceedings of the 3rd World Conference on Photovoltaic Energy Conversion, Osaka, Japan, May 11-18, 2003*, pages 279–282, 2003.

[193] W. Böttler, V. Smirnov, A. Lambertz, J. Hüpkes, and F. Finger, Phys. Status Solidi C **7**, 1069 (2010).

[194] H. Fujiwara, *Spectroscopic Ellipsometry*, John Wiley & Sons, Ltd, Chichester, UK, 2007.

[195] M. Berginski, *Lichtstreuende Oberflächen, Schichten und Schichtsysteme zur Verbesserung der Lichteinkopplung in Silizium-Dünnschichtsolarzellen*, PhD thesis, RWTH-Aachen, 2007.

[196] L. Zhao, C. L. Zhou, H. L. Li, H. W. Diao, and W. J. Wang, Phys. Status Solidi A **205**, 1215 (2008).

[197] P. Basore, Extended spectral analysis of internal quantum efficiency, in *Proceedings of the 23th IEEE Photovoltaic Specialists Conference, Louisville, KY, May 10-14, 1993*, pages 147–152, 1993.

[198] H. Yamamoto et al., Sol. Energ. Mat. Sol. C. **74**, 525 (2002).

[199] D. Macdonald and L. J. Geerligs, Appl. Phys. Lett. **85**, 4061 (2004).

[200] J. Lagowski et al., Appl. Phys. Lett. **63**, 3043 (1993).

[201] J. Schmidt and A. Cuevas, J. Appl. Phys. **86**, 3175 (1999).

[202] Y. Bai, J. Phillips, and A. Barnett, IEEE T. Electron. Dev. **45**, 1784 (1998).

[203] M. Fehr et al., Phys. Rev. B **84**, 245203 (2011).

[204] Z. Wan, S. Huang, M. A. Green, and G. Conibeer, Nanoscale Res. Lett. **6**, 129 (2011).

[205] T. Mchedlidze et al., Phys. Status Solidi A **208**, 588 (2011).

[206] A. Stegner et al., Phys. Rev. B **80**, 165326 (2009).

[207] A. Descoeudres et al., Appl. Phys. Lett. **99**, 123506 (2011).

[208] J. Gielis, B. Hoex, P. van den Oever, M. van de Sanden, and W. Kessels, Thin Solid Films **517**, 3456 (2009).

[209] A. Kanevce and W. K. Metzger, J. Appl. Phys. **105**, 094507 (2009).

[210] S. D. Wolf, A. Descoeudres, Z. C. Holman, and C. Ballif, Green **2**, 7 (2012).

[211] U. W. Paetzold, E. Moulin, B. E. Pieters, R. Carius, and U. Rau, Optics Express **19**, 1219 (2011).

[212] C. Ulbrich, A. Gerber, K. Hermans, A. Lambertz, and U. Rau, Prog. Photovoltaics , in press, DOI: http://doi.wiley.com/10.1002/pip.22.

Acknowledgments

I would like to thank all those who made this work possible. Specific thanks are due to the following people for their contribution:

- Prof. Dr. Uwe Rau for the supervision and examination of this thesis, for providing the opportunity to work at his institution and for his constant confidence in me.
- Dr. Urs Aeberhard for being an excellent supervisor who struck the perfect balance between supporting self-directed working and keeping me on the right track, for his continuous encouragement and for being a good friend.
- Dr. Friedhelm Finger and Prof. Dr. Reinhard Carius for being experienced and uncomplicated group leaders who provided valuable knowledge and infrastructure needed for this thesis.
- Dr. Wolfhard Beyer for many fruitful, instructional and enlightening discussions that gave direction for the works on SiC/SiO_x hetero-superlattice.
- Jana Mohr from PGI-PT, FZJ for the instruction to the working in the clean room and for the wafer cleaning in the early stage of the thesis.
- Oliver Thimm for carrying out all the high-temperature annealing and forming gas annealing processes and for being permanently reliable in everything he does.
- Dr. Vladimir Smirnov and Andreas Lambertz for sharing their expertise concerning the deposition of μc-SiO_x layers.
- Dr. Florian Einsele for his groundwork in c-Si surface passivation using a-SiO_x:H layers and for the instruction to the QSSPC measurement setup.
- Horst Windgassen from IHT, RWTH-Aachen for preparing the rear contact of heterojunction emitter solar cells, Juray Hotovy and Alain Doumit for TCO

depositions.

- The many who assisted with sample characterization: Dr. Florian Köhler for XRD measurements; Dr. Oleksandr Astakhov for ESR measurements; Dorothea Lennartz for hydrogen effusion measurements; Jan Flohre and Dr. Stephan Suckow from IHT, RWTH-Aachen for photoluminescence measurements; Mauriozio Roczen from Helmholtz-Zentrum Berlin for XPS measurements; Dr. Bernd Holländer from PGI9-IT, FZJ for RBS measurements; Dr. Uwe Breuer from ZCH, FZJ for SIMS measurements; Dr. Maryam Beigmohamadi from ER-C, FZJ and Dr. Martin Schade from IZM, MLU Halle for TEM measurements; Oliver Thimm, Josef Klomfass and Maurice Nuys for PDS measurements;
- Johannes Wolff and Frank Pennartz for their technical support with the deposition systems and Wilfried Reetz for helping with the solar cell characterization setups.
- Dr. Birger Berghoff from IHT, RWTH-Aachen, Dr. Daniel Hiller from IMTEK, Freiburg University and Philipp Löper from Fraunhofer ISE for fruitful discussions during conference or project meetings.
- Finally, I would like to express my deepest thanks to my family for emotional support and encouragement in good times as in bad.

Band / Volume 232
Lattice-Boltzmann-Simulation in faserbasierten Mikrostrukturen
J. P. Brinkmann (2014), viii, 129 pp
ISBN: 978-3-89336-995-9

Band / Volume 233
Numerische Simulationen von Abfallgebinden aus der Wiederaufarbeitung von Kernbrennstoffen
S. Schneider (2014), 201 pp
ISBN: 978-3-89336-998-0

Band / Volume 234
Materials for Advanced Power Engineering 2014
J. Lecomte-Beckers, O. Dedry, J. Oakey, B. Kuhn (Ed.)
(2014), xxi, 930, viii pp
ISBN: 978-3-95806-000-5

Band / Volume 235
Untersuchungen zur Abtrennung, Konversion und Transmutation von langlebigen Radionukliden
Ein Beitrag zur fortschrittlichen Entsorgung von hochradioaktiven Abfällen
G. Modolo (2014), 291 pp
ISBN: 978-3-95806-005-0

Band / Volume 236
Keramische Membranen für die H_2-Abtrennung in CO-Shift-Reaktoren
D. van Holt (2014), IV, 169 pp
ISBN: 978-3-95806-007-4

Band / Volume 237
Entwicklung von porösen Silica-Membranen zur CO_2-Abtrennung aus dem Rauchgas fossil befeuerter Kraftwerke
J. S. Eiberger (2014), II, 163 pp
ISBN: 978-3-95806-008-1

Band / Volume 238
Development of a highly sensitive and versatile mass spectrometer system for laboratory and atmospheric measurements
S. Albrecht (2014), iv, 171 pp
ISBN: 978-3-95806-009-8

Band / Volume 239
High Temperature Corrosion of Alloys and Coatings in Gas-Turbines Fired with Hydrogen-Rich Syngas Fuels
W. Nowak (2014), 201 pp
ISBN: 978-3-95806-012-8

Schriften des Forschungszentrums Jülich
Reihe Energie & Umwelt / Energy & Environment

Band / Volume 240
Einfluss neuer Membranmaterialien auf Herstellung und Betrieb von Direktmethanol-Brennstoffzellen
S. Hürter (2014), V, 164 pp
ISBN: 978-3-95806-013-5

Band / Volume 241
Spannungsinduziertes Versagen in Hochtemperaturschichtsystemen
C. Nordhorn (2014), v, 118 pp
ISBN: 978-3-95806-016-6

Band / Volume 242
Änderungsdetektion digitaler Fernerkundungsdaten mittels objekt-basierter Bildanalyse
C. Listner (2014), 176 pp
ISBN: 978-3-95806-017-3

Band / Volume 243
Räumlich hoch aufgelöste Modellierung des Spaltprodukt-verhaltens in einem HTR-Core mit kugelförmigen oder prismatischen Brennelementen
A. Xhonneux (2014), viii, 239 pp
ISBN: 978-3-95806-020-3

Band / Volume 244
Effects of Cercospora leaf spot disease on sugar beet genotypes with contrasting disease susceptibility
S. Schmittgen (2015), 121 pp
ISBN: 978-3-95806-021-0

Band / Volume 245
Light scattering and trapping in thin film silicon solar cells with an n-i-p configuration
W. Böttler (2015), 132 pp
ISBN: 978-3-95806-023-4

Band / Volume 246
Nanostructured Si-alloys for silicon solar cells
K. Ding (2015), 210 pp
ISBN: 978-3-95806-024-1

Weitere ***Schriften des Verlags im Forschungszentrum Jülich*** unter
http://wwwzb1.fz-juelich.de/verlagextern1/index.asp

Energie & Umwelt
Energy & Environment
246

Nanostructured Si-alloys for silicon solar cells

Kaining Ding

Member of the Helmholtz Association

Energie & Umwelt / Energy & Environment
Band / Volume 246
ISBN 978-3-95806-024-1

JÜLICH
FORSCHUNGSZENTRUM

Nanostructured Si-alloys for silicon solar cells

Kaining Ding

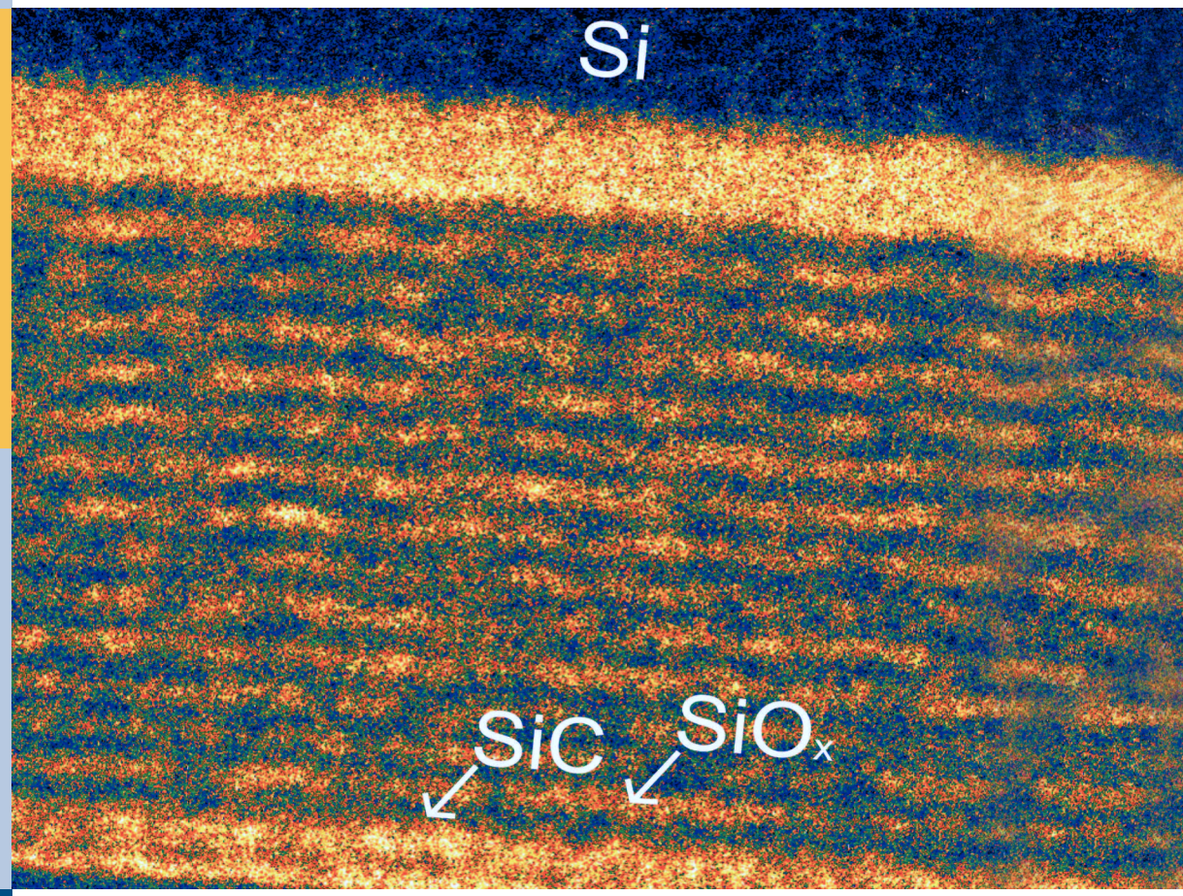

Energie & Umwelt / Energy & Environment
Band / Volume 246
ISBN 978-3-95806-024-1

JÜLICH
FORSCHUNGSZENTRUM